11-8-2012

Nanoporous Gold as a Solid Support for Protein Immobilization for the Development of Immunoassays, and for Biomolecular Interaction Studies

Binod Prasad Pandey
University of Missouri-St. Louis, bppfg8@mail.umsl.edu

Nanoporous Gold as a Solid Support for Protein Immobilization for the Development of Immunoassays, and for Biomolecular Interaction Studies

By

Binod Prasad Pandey

M.S., (Chemistry/Biochemistry), University of Missouri-St. Louis, MO, 2009

M. Sc., (Physical Chemistry), Tribhuvan University, 2004

B. Sc., (Chemistry/Biology), Tribhuvan University, 2001

A Dissertation Submitted to The Graduate School at

The University of Missouri-St. Louis

In Partial Fulfillment of The Requirements for The

Doctor of Philosophy in Chemistry November 2012

Advisory Committee

Dr. Keith J. Stine

(Chair and Advisor)

Dr. Alexei V. Demchenko

Dr. James Chickos

Dr. Michael Nichols

ABSTRACT

Nanoporous Gold as a Solid Support for Protein Immobilization for the Development of Immunoassays, and for Biomolecular Interaction Studies

November 2012

Binod Prasad Pandey, MS, University of Missouri-St. Louis, MO, USA

Chairperson: Dr. Keith J. Stine

Nanoporous gold (NPG) is a nanostructured form of gold with a bicontinuous network of interconnected pores and ligaments. NPG has been an attractive substrate for several studies including biomolecule immobilization, assay development, electrode material development, catalysis etc. The increased surface to volume ratio, electrical conductivity, inertness at ambient conditions, biocompatibility, electrocatalytic activity, simple procedure for preparation and functionalization etc. are some of the notable properties of NPG that have made NPG an attractive substrate for several studies. This study is directed towards the understanding of NPG for use as a substrate for biomolecule immobilization, assay development, biomolecular interaction studies, and its application as an electrode material.

Direct kinetic electrochemical immunoassays were developed on NPG for prostate specific antigen (PSA) and carcinoembryonic antigen (CEA). This novel immunoassay was based on the decrease in rate of enzymatic conversion of p-aminophenylphosphate to p-aminophenol, by alkaline phosphatase conjugated to an

antibody, due to steric hindrance caused by the presence of antigen bound to the antibody. The difference in rate of reaction before and after antigen binding to the enzyme conjugated antibody was observed as a decrease in peak current in square wave voltammetry. Detection limits of these assays were 0.75 ng mL^{-1} and 0.015 ng mL^{-1} for CEA and PSA, respectively. Similarly, the linear range of determination of these biomarkers extended up to 30 ng mL^{-1} and 10 ng mL^{-1} for PSA and CEA, respectively. Unlike traditional immunoassays involving multiple antibodies, this immunoassay involved only one antibody and hence should be an alternative cost effective immunoassay. Minimal interference was observed using new born calf serum as a substitute for the human serum matrix.

Carbohydrates are one of the most abundant biomolecules in earth. Carbohydrates are involved in different biological events such as cell-cell communications, cell recognition, host pathogen interactions etc. Different carbohydrates are involved at different stages of cell growth and differentiations. Differential carbohydrate expressions have been reported at different malignant stages and tumorigenic conditions. Protein glycosylation is one of the most frequent post translational modifications and correct glycosylation is essential for the appropriate conformations and functions of a protein. Several proteins are being studied as biomarkers of diseases because of the differences in glycosylation for different disease conditions. Thus protein glycosylation, and glycan analysis is an important aspect of the proper understanding of protein function in biological systems. With an aim to incorporate unique features of NPG for bioassays, enzyme linked lectinsorbant assays were also developed for the study of glycoprotein-lectin interaction on the NPG surface. These electrochemical lectin assays on NPG were a

sensitive and fast method which could possibly be applied for the high throughput screening of glycan epitopes in glycoproteins. Three different formats of electrochemical assays: traditional type, direct kinetic, and competitive ELLSA were developed on NPG. The kinetic ELLSA was based on the decrease in enzymatic reaction rate of alkaline phosphatase conjugated to the Con A after glycoprotein binding to the lectin Con A.

The other aspect of the research was electrochemical characterization of self-assembled monolayers (SAMs) of alkanethiols on the NPG surface by cyclic voltammetry and electrochemical impedance spectroscopy. Comparison was made with SAMs on the relatively well studied smooth surface of gold wire. Some similarities and differences in behavior of molecular assembly were observed depending on the nature of the surface. Similarly, the applicability of this surface for the formation of carbohydrate monolayers and its application for lectin carbohydrate interaction were also studied. Pure and mixed SAMs of 8-mercaptooctyl α-D-mannopyranoside (αMan-C_8-SH) and α-D-Gal-(1→4)-β-D-Gal-(1→4)-β-D-Glc-1-O-mercaptooctane (Gb3-C_8-SH) with thiols having varying tail groups were prepared. Binding affinity and binding kinetics of concanavalin A to mannoside and soybean agglutinin to galactose in the SAM were affected by the nature and chemistry of the underlying surface.

DEDICATION

To my parents

ACKNOWLEDGEMENTS

I would like to express my sincere gratitude to my Advisor Professor Keith J. Stine for his valuable suggestions and guidance during this research.Without which this work would not have been possible. His scientific excellence and deep understanding of the chemistry was always inspiring and made me realize I was fortunate to work under his supervision. I am grateful to him for taking me into his group and providing valuable guidance and suggestions without a single word of frustration even when it was hard to obtain meaningful results out of experiments. I would like to thank Professor Alexei V. Demchenko for collaboration and valuable guidance for the synthesis of carbohydrate molecules and other synthetic molecules used in the current study. As a director of graduate studies he has been very helpful during my graduate studies at critical points.

I am thankful to all the faculty members at University of Missouri-St. Louis who has put their valuable time and efforts during teaching, and helped me to strengthen my foundation of chemistry. I am also grateful to my dissertation committee, Professor Michael Nichols and Professor James Chickos for taking time to read my dissertation and for the valuable suggestions.

My current and former lab members are important part of my research, they have been very helpful for training me during early days and valuable discussions at the later part of the time. Dr. Yih Horng Tan, Mr. Jay K. Bhattarai, Ms. Abeera Sharma, Mr. Allan Alla, Dr. Kenise Jefferson were very helpful in assisting me in various aspects of my research. I would like to thank Dr. Kohki Fujikawa, Dr. Papapida Pornsuriyasak, Dr. Archana Parameswar and Dr. Vijaya Ganesh Narayanswamy for the synthesis of thiolated glycosides ad PEG derivatives. All the faculties, graduate students and staff

members at UMSL have always been helpful and cooperative for which I will always be grateful to them. I would like to thank Center for Nanoscience and Dr. David Osborn for help in taking some SEM images.

Thanks to my family, my wife Sunita, my brother, my sisters and friends who has always been supportive when in need. Every week, my mother's questioning on the graduation date made me realize it has been a very long time since I haven't visited my home, and I felt more nostalgic and encouraged to work hard expecting to finish my thesis on time.

TABLE OF CONTENTS

LIST OF FIGURES

LIST OF TABLES

LIST OF ABBREVIATIONS

NPG	Nanoporous gold
GW	Gold wire
SAM	Self assembled monolayer
LPA	Lipoic acid
ALP	Alkaline phosphatase
Con A	Concanavalin A
SBA	Soybean agglutinin
IgG	Immunoglobulin G
FET	Fetuin
ASF	Asialofetuin
TSF	Transferrin
BSA	Bovine serum albumin
TEG (HO-PEG2-SH)	8-mercapto-3,6-dioxaoctanol
αMan-C_8-SH	8-Mercaptooctyl α-D-mannopyranoside
Gb3-C_8-SH	(α-D-Gal-(1→4)-β-D-Gal-(1→4)-D-Glc1-O-mercaptooctane
PSA	Prostate specific antigen
CEA	Carcinoembryonic antigen
EIS	Electrochemical impedance spectroscopy
SWV	Square wave voltammetry
CV	Cyclic voltammogram
MAb	Monoclonal antibody
MAb-ALP	Monoclonal antibody and alkaline phosphatase conjugate
BCA	Bicinchoninic acid
OCT	Octanethiol

MDDA	Mercaptododecanoic acid
ELISA	Enzyme linked immunosorbant assay
ELLSA	Enzyme linked lectinsorbant assay
SEM	Scanning electron microscope
Con A-ALP	Concanavalin A and alkaline phosphatase conjugate
p-APP	Para aminophenyl phosphate
p-AP	Para aminophenol

CHAPTER I

INTRODUCTION

1.1 General introduction

The presented study is aimed at understanding molecular assembly behavior and its impact on biomolecular interactions on the nanoporous gold (NPG) surface, compared to that on a relatively flat polycrystalline gold surface. Compared to the flat gold surface, NPG as a substrate is believed to result in different behavior with respect to molecular assembly, and hence the overall behavior of the modified surface is expected to be different. Nanoporous gold was utilized as an electrode material for the immobilization of biomolecules via linking to self-assembled monolayers, for the development of immunoassays, and for the study for lectin-carbohydrate interactions. Thus, nanoporous gold served dual purposes, both as a solid support and as an electrode material for signal transduction. Chapter I presents an introduction to nanoporous gold and its applications to; self-assembled monolayers on gold surfaces, various aspects of protein immobilization on these surfaces, methods of covalent attachment, recent developments in immunoassays, and applications of nanoparticles in immunoassays. The materials and methods applied in this research are detailed in chapter II. Chapter III presents results and discussion on the self-assembled monolayers of alkanethiols on nanoporous gold surfaces and comparisons with those on the relatively flat gold wire surface. Chapter IV concerns the results and discussion of the study of carbohydrate-lectin interaction on carbohydrate presenting SAMs. Comparative study of the carbohydrate-lectin interaction on NPG and gold wire surfaces in also presented. Results and discussion on a novel direct

electrochemical enzyme linked immunosorbant assayfor the cancer biomarkers prostate specific antigen (PSA) and carcinoembryonic antigen (CEA) on NPG are discussed in chapter V. Chapter VI presents results and discussion on the enzyme-linked lectinsorbant assay on NPG. Three different formats of lectin assays are presented in chapter VI: traditional, direct kinetic and competitive assays.

1.2 Nanoporous gold

Nanoporous gold is a nanostructured form of gold, prepared by the selective removal of less noble metal(s) from an alloy of gold and other metal(s). Historically, nanoporous gold was prepared in a process called depletion gilding [1, 2]. Scientific interest in nanoporous gold has been extensive because of some of its unique properties such as large surface to volume ratio [3], chemical inertness at ambient condition, electrocatalytic activity [4], plasmonic properties [5], biocompatibility [6], and ease of functionalization [7]. Gold has been a favorite substrate for the study of molecular assemblies of thiols on its surfaces [8], immobilization of biomolecules, and for biomolecular interaction studies [9, 10]. Recent advances in nanotechnology have attracted interest in the nanostructured forms of gold such as gold nanoparticles [11, 12], gold nanorods [13, 14], gold nanocubes [15, 16], gold nanostars [17, 18], and nanoporous gold [19, 20]. All of these gold nanostructures have their own importance, but preparation and functionalization of NPG involves the simplest procedures, which makes it a highly attractive substrate for conducting biomolecular interaction studies. NPG consists of a three-dimensional bicontinuous distribution of pores and ligaments [2, 20, 21]. These pores and ligaments can be prepared with various sizes by varying the conditions of alloy preparation [22-25], dealloying conditions and post dealloying treatments, including

thermal annealing [26], and electrochemical roughening [27, 28]. Pore sizes are an important parameter for different applications of NPG; for example, relatively small and subnanometer sized pores are essential to achieve the highest possible surface area of a material and for the application towards supercapacitor development [29, 30] and relatively larger pore sizes are required for the study of biomolecular interactions [31], to allow free diffusion of large molecules such as proteins through pores [32]. One of the most attractive and unique features of these noble metal nanoparticles is their plasmonic property [33], which make them potential candidates for the development of label-free assays [34]. Some of the advantages of NPG against the conventional flat gold surfaces are,

a) Nanoporous gold provides cheaper gold surface per unit area [35].

b) The three-dimensional network of pores and ligaments increases the surface to volume ratio [28].

c) Ligaments and pores of some hundreds of nanometers in radius of curvature could be a better mimic of a cell surface.

d) NPG also possesses plasmonic properties which could be useful for development of label-free assays [36].

e) NPG is electrocatalytically active and can be applied directly as a catalyst or as an electrocatalyst for oxidation reactions [37].

1.3 Preparation of NPG

A common strategy of NPG preparation involves preparation of an alloy of gold and selective leaching of other metals from the alloy. Au-Ag alloy is the most favored alloy system for the preparation of NPG. Some of the reasons for silver being a most

attractive component of the binary alloy system with gold include compatibility of gold and silver due to their similar crystal structure (FCC), the complete miscibility of gold and silver at all compositions, highly selective etching of silver from the alloy, and mechanical compatibility in the form of similar yield stress, and similar thermal expansion [38]. Some of the other alternate binary and ternary alloy systems used to prepare NPG include, Au-Zn [39], Au-Al [40], Au-Ni [41], Au-Ag-Pt [42] etc. The most commonly used alloy structures, as a precursor of NPG, are gold-silver ingot, rods and sheets [38]. These alloys can be prepared in any desired sizes and shapes by mechanical treatments. These alloy structures are prepared from a binary mixture of gold and silver, by melting these metals together, followed by mechanical treatment to generate different shapes of the gold and silver alloy. White gold sheet, yellow gold sheet and gold leaf are convenient and commercially available sources of alloys of gold for NPG preparation. Another convenient way of generating a gold and silver alloy is by electrodeposition of gold and silver at various compositions. Electrodeposition is an easy technique for a laboratory setup with electrochemical instrumentations, as various parameters can be controlled and alloys can be generated at desired compositions. Other microfabrication techniques involve sputtering [43], and thermal evaporation [44]. These techniques are attractive for the deposition of relatively thin layers of the metal(s) on the surface because this simultaneous magnetron sputtering of alloy composition allows precise control of the deposited film on the substrate as film composition, thickness, grain size etc. can be controlled by varying the sputtering conditions. One of the drawbacks of this technique is that it is not suitable for the deposition of relatively thick layers due to the low deposition rate, waste of material and increased cost of deposition [38]. Once the alloy of gold and

suitable less noble metal is prepared, the next step involves selective removal of the less noble metal from the alloy. Acid dealloying in nitric acid is the most commonly employed method for dealloying, as concentrated nitric acid almost completely dissolves silver and helps to obtain a surface without any impurities [2, 45]. Electrochemical dealloying has some advantages over the acid dealloying as control over the applied potential and time of dealloying lets one to create NPG of different pores and ligament characteristics, but the process could be slower and inconvenient for dealloying a large number of thicker alloy structures. Various processes and methods for fine tuning pore and ligament sizes and shapes have been studied; the most common processes involve coarsening in acid or thermal annealing [26], varying dealloying conditions and temperatures, or varying the parameters of electrochemical dealloying [28, 39].

1.4 Mechanism of NPG formation

Formation of NPG nanopores is a dynamic process, and does not result from just the removal of one component from a microstructured alloy. The process involves dissolution of exposed silver, and diffusion and agglomeration of gold adatoms clustering together into a two dimensional gold island by a phase separation process at the metal-electrolyte interface [1]. Erlebacher et al. performed kinetic Monte Carlo simulation of the evolution of pores during dealloying [46]. The stepwise process of dissolution was summarized as follows: the process of pore formation begins with the removal of silver atoms at the flat alloy surface of close packed (111) orientation. The dissolution of neighboring silver generates terrace vacancies, making nearby silver atoms more vulnerable to acid dissolution, compared to those on flat terraces. Once the dissolution of the uppermost layer is complete, gold atoms at this layer start to diffuse and agglomerate

into gold islands. Two types of surfaces are generated by this agglomeration process, one consisting of pure gold, which is resistant to further corrosion, and the other surface is the now freshly exposed alloy surface. Corrosion of the successive layers adds more and more gold atoms to the initially formed gold islands, exposing another layer for further corrosion. Structurally, these gold islands consist of pure gold atoms at the top and alloy at the bottom. Finally pits start to form due to undercutting of these gold islands, and porosity formation takes place. Schematic representation of the process is shown in **Figure 1.1** [46].

In-situ studies of the dealloying process by X-ray diffraction on $Au_{30}Ag_{70}$ polycrystalline ingots showed preservation of grain morphology and original crystallographic structure, but small changes in orientation within the grain take place [47]. The same study pointed out that the previous observation on the change in grain structure, during dealloying, was due to the artifacts of TEM. Three-dimensional structural reconstruction by electron tomography in TEM of the NPG formed by dealloying gold leaf showed a continuous branched network of ligaments, irregular distribution of pores and ligaments, larger average surface area compared to that expected based on the ligament size, and average convex surface curvature, close to that of the convex objects of similar size as ligaments [48]. An almost 30% decrease in volume was observed during electrochemical dealloying, which was attributed to the plastic deformation arising from the homogenous slip of small ligaments or due to the climb of lattice dislocations [49].

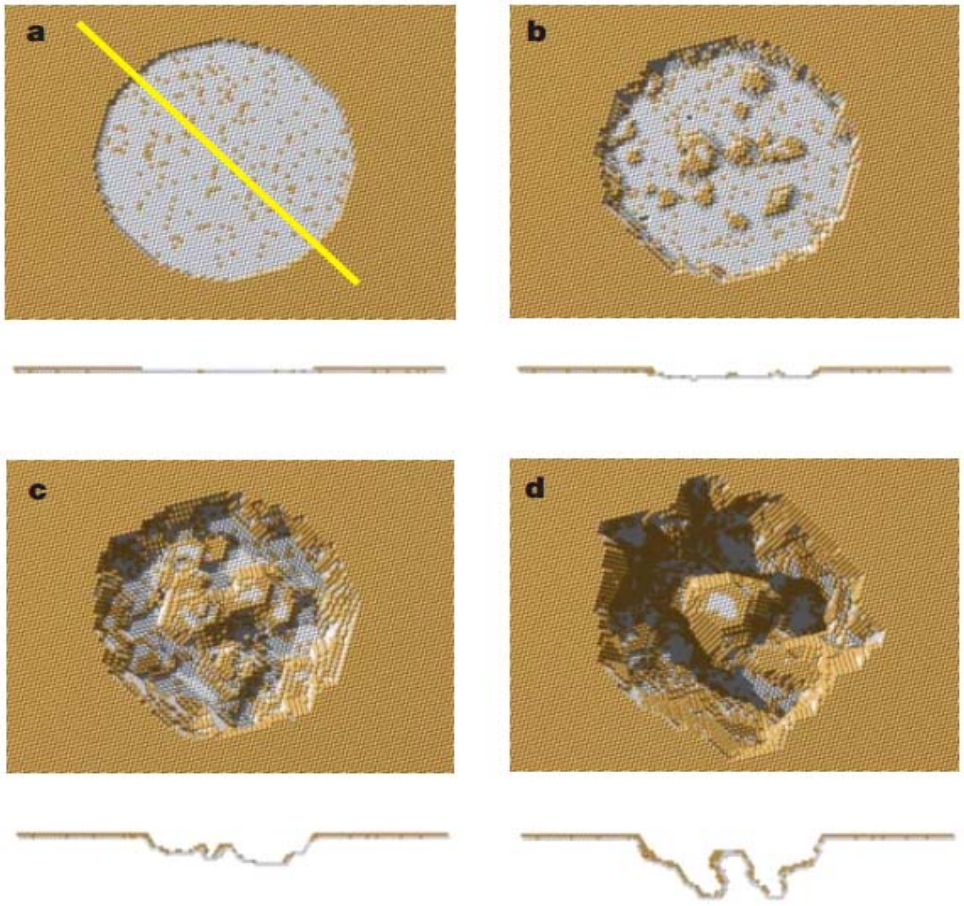

Figure 1.1. Nanopore formation during dealloying of gold and silver alloy. Schemes were generated from Monte Carlo simulation for the pit formation, and porosity evolution, during NPG formation. Initially, the alloy surface is passivated by gold atoms (a), and as pit formation is initiated by dissolution of a few silver atoms this passes through a few monolayers within 1s (b). The porosity evolution begins to take shape with the formation of gold clusters and nucleation of released gold atoms at the center of the pit, which occurs within 10 s. Finally multiple pits are formed by splitting of pits, which progresses towards the bulk of the alloy to form a porous structure; this processes takes around 100 s. Cross-sectional views along the Au(111) plane represented by the yellow line in figure 1.1(a) are shown beneath each panel (ref. 46).

1.5 Applications of NPG

NPG has attracted more research interest in recent years, and the number of publications on NPG is increasing every year. Some of the notable applications of NPG include catalysis [50, 51], sensing [52, 53], biosensing [54-56], in fuel cells [57], development of bioassays [58, 59], study of carbohydrate-lectin interactions [21] etc.

1.5.1 Catalytic properties

NPG has been applied in several studies involving its catalytic properties. The mechanism of the catalytic activity of NPG is not very well understood, but it is believed that the catalytically active surface defect sites with lower bond coordination could possibly interact with adsorbed reactants because of electronic or steric reasons [50, 51, 60]. Residual silver on the NPG surface plays an important role in catalysis and is believed to be responsible for providing oxygen to gold through spillover or at perimeters [60]. Some of the important catalytic applications of NPG involve low temperature oxidation of CO to CO_2 [51], glucose electrooxidation [61], reduction of oxygen and hydrogen peroxide [62], gas phase selective oxidative coupling of methanol to methyl formate [50] and aerobic oxidation of glucose to gluconic acid [63]. Seo et al. reported structure dependent oxidation of glucose on NPG, and NPG with smaller pores and ligaments was shown to be more effective for the electrooxidation of glucose near -0.1 V (vs. Ag|AgCl), whereas NPG with larger features showed an electrooxidation peak near 0.25 V [61]. Ding et al. reported determination of p-nitrophenol on the NPG electrode. One interesting observation on NPG was the appearance of two symmetrical peaks of the 4-(hydroxyamino)phenol/4-nitrosophenol couple, which was not observed on polycrystalline gold [53]. Ge et al. reported simultaneous determination of dopamine and

ascorbic acid utilizing electrocatalytic activity of the NPG film, and an increased signal compared to that on the flat gold surface was observed [64].

1.5.2 Plasmonic properties

a) Localized surface plasmon resonance (LSPR): Particles in the size range below a few hundred nanometers, less than the wavelength of the incident light, show oscillation of their surface plasmons, in a frequency range commonly referred to as the localized surface plasmon resonance (LSPR) absorbance [65]. This frequency is sensitive to the local dielectric environment and is being actively pursued for the development of label-free bioassays [66-68]. NPG with pores and ligaments in the tens to hundreds of nm size range has been shown to exhibit LSPR [5, 36]. Usually the wavelength shift is measured as a probe for the change in the dielectric constant of the environment surrounding the nanoparticles, such as occurs when molecules bind to the gold surface [65]. Localized surface plasmon resonance properties of NPG of variable pore sizes were studied by Lang et al.; they reported appearance of two absorption bands, one at 490 nm (L1) and another at 550-650 (L2) nm. L1 did not show any changes in spectral properties with the change in dielectric constant of the medium, on the vicinity of the surface, whereas L2 showed a significant shift in peak position with the change in dielectric constant of the medium. Larger pore size material was reported to have higher sensitivity compared to the small pore size material [36]. Based on the change in absorption of NPG with the dielectric constant of the surrounding, it has been suggested to be a possible substrate for application in plasmonic sensors and biosensors [5]. Localized surface plasmon resonance is the main factor for the electromagnetic field enhancement in surface

enhanced optical techniques such as surface-enhanced Raman spectroscopy (SERS) [65, 69].

b) Surface-enhanced raman scattering (SERS): Nanoporous gold with its highly rough surface features has been shown to be an excellent substrate for surface-enhanced Raman scattering [27]. Kucheyev et al. reported the highest SERS signal for crystal violet adsorbed on 250 nm pore size NPG and reported a detection limit of 10^{-7} M for crystal violet in solution [70]. Qian et al. reported a contrasting result showing the highest SERS enhancement with smaller pore size NPG, which was attributed to surface contamination, surface heterogeneities, and ultrafine pimple like irregularities on the NPG surface [27]. They also reported one to two orders of magnitude enhancement compared to that of the annealed NPG and a 5×10^{-10} M detection limit for rhodamine 6G. SERS enhancement has been reported to be at least 10 fold higher at the hot spots, at the vicinity of the narrow nanosize gaps between sharp corners and edges of the noble metal nanostructures, compared to the regular NPG surface. Almost 100 times higher sensitivity was observed on wrinkled NPG, prepared on the prestrained polymer substrate with thermal treatment, compared to that of the as prepared NPG [71]. A patterned NPG substrate was prepared by simple stamping of the NPG and was reported to enhance the SERS signal by a factor of 10^7. Qian et al. reported a detection limit of 10^{-11} mol L^{-1}, a huge enhancement by a factor of about 1.5×10^{13}, by incorporating gold nanoparticles in nanoporous gold modified with mercaptopyridine [72].

1.5.3 NPG for enzyme immobilization/bioassay/biosensor development

NPG has a higher surface to volume ratio compared to that of flat gold of similar geometric surface area. Increased surface area is an important factor for increasing

protein loading on the surface and hence for increasing sensitivity of bioassays on surfaces. In addition to surface area, pore size is an important factor for enzyme immobilization and ultimate application in bioassays. Qiu et al. immobilized laccase on NPG samples of various pore sizes, by physisorption, and reported that 40-50 nm pore sizes were better for enzyme activity compared to the 10-20 nm and 90-100 nm pores in NPG [73]. Chen et al. reported immobilization of glucose oxidase on NPG modified with dithiobis(succinimidyl undecanoate) for glucose determination, based on the reaction between glucose and glucose oxidase and detection of generated peroxide [74]. Their study showed pore size dependent amperometric signals, with relatively larger pore size (30 nm) giving a higher response compared to the smaller pores (18 nm). Scanlon et al. characterized NPG as a support for electron transfer to cytochrome c and found that the area accessible for the immobilization of biomacromolecule was up to 40% lower than that of the true area of NPG [75]. Kafi et al. reported immobilization of hemoglobin on NPG directly grown NPG on the Ti surface and then applied it for the electrochemical determination of hydrogen peroxide [76]. Another electrochemical biosensor based on immobilized alcohol dehydrogenase and glucose oxidase was prepared for the determination of ethanol and glucose [56]. NPG was shown to be more sensitive and electrocatalytically active for the determination of NADH and hydrogen peroxide by Qui et al. An enzyme biosensor for glucose was developed based on the electrostatic immobilization of glucose oxidase in Prussian blue modified NPG [77]. Qiu et al. reported a study of three different strategies for the immobilization of laccase on the NPG surface and showed that enzyme loading was similar for both covalent coupling and adsorption whereas it was significantly lower on the enzyme immobilized via

electrostatic interaction [73]. They also showed that almost 70 percent of the NPG surface was unavailable for protein immobilization. Qiu et al. reported immobilization of lignin peroxidase on NPG and showed that thermal stability of the enzyme on NPG was better than that of the free enzyme in solution [78]. They also showed high activity of lignin peroxidase by coimmobilization of glucose oxidase and in situ release of the hydrogen peroxide. Shulga et al. studied immobilization of acetylcholine esterase on NPG surface and various aspects of enzyme kinetics were studied on different pore sized NPGs [79]. Yan et al. reported excellent stability of the immobilized xylanase on NPG surface and reported retention of almost 80% of the initial activity of the enzyme in solution [80].

1.5.4 Application of NPG as a support for immunoassay development

In addition to enzyme/protein immobilization, for various purposes, NPG is being actively studied as a substrate for immunoassay development. An immunoassay for hepatitis B surface antigen was developed, based on the antibody immobilized via linkage to SAMs on NPG, and signal amplification was achieved by immobilizing an antibody horseradish peroxidase conjugate on the gold nanoparticle surface [58]. An impedimetric immunosensor, for the C-reactive protein that is a cardiac biomarker, based on three-dimensional macroporous gold was reported by Zhu et al. [81] An electrochemiluminescence immunoassay for CEA was achieved by immobilizing anti-CEA antibody on NPG and using quantum dot labeled secondary antibodies, as reported by Li et al. [82] This immunoassay based on the electrochemiluminescence enhancement on the NPG surface had a detection limit of 0.01 ng mL^{-1} CEA, with the linear response range from 0.05 to 200 ng mL^{-1}. Li et al. reported development of an electrochemical

immunosensor for human chorionic gonadotrophin, based the relative blockage of the electron transfer process of the hydroquinone probe molecule, on the GCE|graphene sheet|NPG|anti hCG antibody electrode surface after antibody immobilization and antigen binding to the antibody [83]. A kinetic immunoassay strategy was reported on NPG by immobilization of anti-PSA antibody-ALP conjugate on lipoic acid modified NPG [20].

1.6 Self-assembled monolayers on gold

The molecular assembly formed by the interaction of surface reactive molecules with a solid substrate is generally referred to as a self-assembled monolayer or SAM [84]. Thiol or disulfide species on gold and siloxanes on glass surfaces are the most commonly studied SAMs [85]. An unequivocal explanation for the interaction between head-group of thiol and gold has not yet been achieved. There are several controversial results and explanations for the mechanism of gold-thiol interaction. Some of the still debated questions are: Is the thiol physisorbed or chemisorbed? Does the S-H bond dissociate during gold-sulfur interaction? What happens to the hydrogen atom? Does it adsorb to the gold or get associated with the neighboring hydrogen to form a hydrogen molecule? More recent studies indicate dissociation of S-H bonds and hydrogen evolution during gold-sulfur interaction for the case of gold nanoparticles [86]. A density functional theory based study has shown that the chemisorption of R-S-H on Au takes place in two steps, the first energetically unfavorable step, by 0.32 eV, is the dissociation of the S-H bond which is accompanied by the spontaneous interaction of R-S radicals with the gold surface. The energetics of the different steps of bond dissociation and bond formation are listed below [87].

$$R - SH \rightarrow R - S^{\bullet} + H^{\bullet} \qquad \Delta E_r = 3.73\ eV$$

$$H \rightarrow \frac{1}{2}H_2 \qquad \Delta E_r = -2.27\ eV$$

$$R - S^{\bullet} + Au\ (slab) \rightarrow R - SAu(slab) \qquad \Delta E_r = -1.35\ eV$$

$$Total: R - SH + Au(slab) \rightarrow R - SAu(slab) + \frac{1}{2}H_2 \qquad \Delta E_r = 0.11\ eV$$

$$R - S \rightarrow R - S^{\bullet} + H^{\bullet} \qquad \Delta E_r = 3.73\ eV$$

$$H^{\bullet} \rightarrow H_{ads)}\ on\ Au \qquad \Delta E_r = -1.88\ eV$$

$$R - S^{\bullet} + Au\ (slab) \rightarrow R - SAu\ (slab) \qquad \Delta E_r = -1.35\ eV$$

$$Total: R - SH + Au\ (slab) \rightarrow R - SAu(slab) + H_{ads} \qquad \Delta E_r = 0.50\ eV$$

A simplified model for the chemisorption of thiol on a gold surface would be

$$R - SH \rightarrow R - S^{\bullet} + H^{\bullet}$$

$$H \rightarrow \tfrac{1}{2}H_2$$

$$R - S^{\bullet} + Au(slab) \rightarrow R - SAu\ (slab)$$

$$Total: R - SH + Au(slab) \rightarrow R - SAu(slab) + \tfrac{1}{2}H_2$$

1.7 Structure of SAM on the gold surface

Alkanethiols self-assemble, and form a well packed semicrystalline structure, on the gold surface [88, 89]. The general bonding pattern of the thiols on gold surface is generally accepted to be $\sqrt{3} \times \sqrt{3}R30^{\circ}$ (R = rotated). The secondary ordering of the chain in a c(4 × 2) superlattice is also well accepted. Both experiments and theoretical calculation have suggested binding of thiolate on both the three fold hollow sites and at the bridge sites. A general schematic structure of the alkanethiol on gold surface is given in **Figure 1.2** (adapted from ref [88]). Alkanethiol SAM on gold surface is tilted at an angle of 30^{o}. The two-dimensional structure of SAM evolves on the gold surface through

several molecular interactions such as van der Waals interactions, electrostatic interactions, steric interactions [8] etc. The packing and ordering of molecules on the surface is determined by the combination of all the forces listed above.

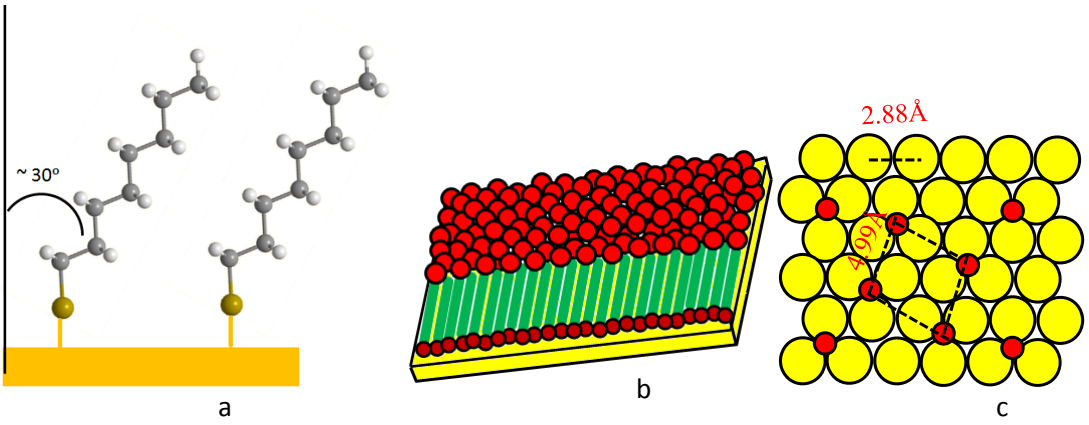

Figure 1.2. Structure of thiols on the gold surface. a) Orientation of a thiol molecule on the gold surface, b) close packing of the thiols, and c) bonding pattern of thiols on the surface (adapted from ref. 88).

1.8 Mechanism of SAM formation on the gold surface

Two distinct kinetic mechanisms are observed in the SAM formation process. The initial fast process involves the quick adsorption of thiols onto the gold surface, which is usually completed within a few minutes. The second step is relatively slow and can last for several hours and may last even for days [90]. The initial step of self-assembly is the transport of the adsorbate molecule to the solid-liquid interface via diffusion and or convection. As soon as the adsorbate reaches the metal surface, adsorption starts at a certain rate determined by the nature of the substrate, nature of the adsorbate, solvent, concentration, solution viscosity, temperature etc. The initial step generates a random distribution of the diverse conformations of the alkanethiols on the surface. Initially these

molecules are lying down on the surface and as more and more molecules come closer they start to interact with their neighboring molecules and adopt an upright orientation, finally rearranging themselves in two dimensions to generate conformationally favorable states for the intermolecular interactions [91]. Thus, three different stages can be envisioned in the process of SAM formation: 1) a low density vapor phase in which isolated, mobile adsorbate molecules are randomly deposited on the surface, 2) an intermediate density phase in which adsorbate molecules are conformationally disordered and are lying flat on the surface, and 3) a final high density state in which molecules are conformationally well ordered, close packed and approximately standing at a tilt angle of 30^{o}. Some differences in the adsorption mechanism and structure have been reported depending on the chain length of alkanethiols [92-94]. The effect of the disordered orientation of the thiols and tailgroups in the adsorption mechanism is not significant in the case of simple alkanethiols, but in case of the thiols with bulkier tail groups masking of the adsorption sites becomes an issue [84, 95].

1.9 Applications of SAMs for biosensors and enzyme immobilization

Modification of the surface with appropriate molecules to prevent direct contact between surface and biomolecules is an attractive way of preserving biomolecular activity on the solid surface. Self-assembled monolayer formation is a convenient approach for surface modification. Using alkanethiols with appropriate terminal functional groups, surfaces with any desired functionality can be generated simply by dipping gold surfaces into the alkanethiol solution. Different methods of biomolecule immobilization can be adopted, based on the nature of the modified surfaces for protein immobilization to the SAM-modified surface. Advantages of self-assembled monolayers

in electrochemical detection include the reduction of background current by hindering close approach of ions and solvents to the metal surface [96]. Faradaic background current is reduced by creating an interface that limits electron transfer close to the surface and long-range electron transfer and electron transfer through the pits and defect sites become alternate paths of electron transfer at the interface. Additional advantages of SAMs include availability of easy detection techniques and compatibility with most analytical techniques such as AFM [97], STM [88], quartz crystal microbalance (QCM) [98], electrochemical methods [99], mass spectrometry [100], thermogravimetric methods [99], differential scanning calorimetry [101-103], etc.

1.10 Biomolecule immobilization on the solid surface

Biomolecule immobilization and active display of biomolecules on the solid surface is an important aspect of the current high throughput studies of biomolecular interaction [104], assay development [105], biomarker screening [106], diagnostic [107], biomaterial [108], tissue engineering [109, 110], etc. Almost every biological process involves interaction of one or multiple biomolecules. Study of these interactions is essential for the proper understanding of protein-protein interactions, protein-DNA interactions, transcription, translation, signal transduction, disease mechanism and several other biological processes. Because of the complexity of the biological system, single processes can involve multi-molecule interactions involving protein, DNA, RNA, carbohydrate, etc. High throughput screening of all these interactions of biomolecules demands efficient and active immobilization as well as efficient detection technology for biomolecular interaction studies [111-113]. The general strategy for the study of biomolecular interaction on the solid surface involves immobilization of one of the

molecules (antibody, DNA, antigen, aptamer or biotin/avidin labeled biomolecules, carbohydrate, lectin etc.) on the surface, followed by the binding of the other molecule to the immobilized partner and generation of a signal as a result of the biomolecular interaction [114-118]. Proteins and DNA immobilized on the solid surface in an array format has substantially improved current understanding of the biological processes involving proteins and DNA [115, 119]. MacBeath et al. reported development of the concept of protein microarray technology by immobilizing proteins on aldehyde functionalized glass slides followed by the binding of fluorescently labeled protein, protein substrate, and small molecules, to the surface bound protein [120]. Protein and DNA immobilization in the array format has started to become a routine technique for the high-throughput studies of these biomolecules. Carbohydrate based studies, on the other hand, are still lagging behind [121, 122]. Some of the reasons for the complexity of carbohydrate based studies involve weak interactions between carbohydrates and proteins, which is overcome in nature by multivalent interaction and the presence of carbohydrate clusters in the biological system [123]. This multivalent interaction has been achieved by immobilizing carbohydrates at a suitable density on the surface, and by immobilizing carbohydrate on dendrimers [124]. Gold is an attractive material for biomolecule immobilization. The spontaneous interaction between gold and sulfur in thiols makes gold an attractive substrate as gold surfaces can be created with many terminal functional groups which can further be utilized for the immobilization of any kind of biomolecule through well-designed surface chemistry [89].

Several methods have been applied for protein immobilization on the surface, and choice of a method depends upon the physicochemical characteristics of the material as

well as of the protein. The most frequently used immobilization methods are based on physical adsorption (based on electrosatatic, hydrophilic or hydrophobic interaction), covalent attachment via generation of covalent bonds between protein and functional groups of molecules already attached to the surface, and by biorecognition or affinity fixation, based on the immobilization of one molecule to the surface followed by affinity interaction between that molecule and the agonist molecule [125-127]. Affinity or bioaffinity based immmobilization methods include immobilization via biotin-streptavidin chemistry, via metal chelators, and by immobilized ligands and immobilized protein counterparts. Even though it is the most challenging part, the most important aspects of protein immobilization are the retention of protein structural and functional integrity. Several approaches have been applied and some progress made in this direction, but none of the methods developed so far are ideal.

1.10.1 Adsorption and physical immobilization

Presumably this is the easiest method of protein immobilization on the surface, but several problems are associated with this method. Protein conformational changes, weak attachment and protein leaching during washing steps, random and heterogeneous protein distribution, effect of size of the protein and loss of protein functionality at high surface density due to the steric hindrance between proteins are some of the pitfalls of this method [128]. In order to increase protein loading on the surface, surfaces are usually modified with polymers and hydrogels [129, 130]. Although these porous matrices help to retain protein integrity, providing a relatively congenial environment, compared to that of the bare surfaces, there are some concerns due to mass transport and high background signals [125].

1.10.2 Nonspecific covalent immobilization of protein

Protein immobilization to the surface via covalent coupling involves reaction between accessible functional groups of the protein amino acid side chains such as -NH_2, -COOH, -OH, -SH and the appropriate complementary functional groups on the surface [125]. Because of the multiple functional groups available on the protein surface, this type of protein immobilization is usually random and multiple attachments are possible. Modification of certain functional groups in the protein and correspondingly engineered surface chemistry will help in site specific and oriented immobilization of proteins to the surface with minimal loss of protein activity and conformation. One of the most commonly used functional groups on the protein surfaces are the amino groups. Among all other possible amino acids with an amine side chain, lysine is the most accessible amino acid for protein immobilization due to its presence on the outer surface of the protein. Application of this strategy demands generation of a carboxyl (or a carbonyl aldehyde, ketone etc.) functionalized surface and activation of the surface, usually via EDC/NHS chemistry generating activated esters with the carboxyl groups on the surface forming an amide bond. Aldehydes react readily with the amino groups of the protein generating a labile Schiff's base or an imine bond, which can be further reduced to generate a stronger secondary amine linkage [131]. Another common functional group on the protein surface is the carboxyl group, which can analogously be applied for protein fixation reactions with amine terminated surfaces, after activation of the protein carboxyl groups by carbodiimides. One possible drawback of this method however, is the cross reactivity between proteins and successive polymerizations. Thiols have also been utilized as a functional group for protein immobilization. One advantage of thiol over

carboxyl or amino group is the presence of a limited number of thiols on the protein, which reduces multiple attachment and generation of a heterogeneous surface [132, 133]. Different approaches of thiol chemistry involve exchange of sulfide between protein and the surface disulfides and thioether bond formation [132]. Sulfide exchange between disulfides on the surface and thiol groups of the protein generates mixed disulfides on the surface with protein immobilized on the surface. A stable thioether linkage can be generated between maleimide and protein thiols via an addition reaction between the double bond of maleimide and the thiols [134]. Maleimide and vinyl sulfone derivatized surfaces both generate thioether linkages between protein and the surface [135]. Thiol linkage and reaction is affected by several factors such as the electrostatic environment of the thiols, reversibility of the linkage, etc. Epoxy groups on the surface can be applied for coupling to –OH groups of serine and threonine, but this reaction is relatively slower [125]. Other approaches involve photochemistry via commonly used reagents such as, arylazides, diazirines, benzophenone and nitrobenzyls by irradiation at wavelength $\geq$ 350 nm [125, 136]. Some site specific chemoligation or protein immobilization involves click chemistry via appropriate labeling of proteins and preparation of surfaces with the complementary functional groups. Another strategy involves Diels-Alder coupling [137], which also requires labeling of biomolecules with a suitable functional group. Staudinger ligation [138] requires two functional groups, one azide group and a functionalized-phosphine containing thioester. Some other approaches involve peptide ligation and α-oxo semicarbazone ligation [125].

1.10.3 Affinity based immobilization

Affinity based ligation is an attractive approach for the generation of homogenous protein functionalized surfaces via oriented assembly of biomolecules on the surface. Affinity based approaches involves immobilization of one affinity partner to the surface and another attached to the protein surface. Some of the most commonly applied approaches include biotin-streptavidin, the His tag - Ni^{2+} nitrilotriacetic acid chelating system [139], DNA directed immobilization [140], and targeting of carbohydrate moieties [132] etc. Other approaches for the directional immobilization of proteins on the surface involves preparation of thiol (cysteine) modified proteins through genetic engineering [133]. Unnatural amino acids have also been applied for protein immobilization on the surface [141]. These modified proteins can form self-assembled monolayers via the thiol units of their structure. Expressed protein ligation, i.e. a genetic engineering approach that expresses thioesters on the protein surface, which react with N-terminal cysteines on the solid surface, generating amide linkages between proteins and the surface is another approach [142]. Fusion proteins prepared by linking a protein of interest with the mutant of human DNA repair protein O6-alkylguanine DNA alkyltransferase (hAGT) have also been applied for site specific protein immobilization [143]; hAGT transfers alkyl groups from O6-alkyl guanine to the cysteine residue. Protein immobilization can then be performed using this property of the enzyme. O6-Benzyl alkylguanine substituted at the 4-position of the benzene ring tethered to a polyethylene glycol linked with an amine head-group was generated and immobilized on the carboxymethylated dextran surface. Protein immobilization based on the above principle was achieved using glutathione S-transferase-hAGT fusion protein [143]. SPR

studies were done to probe immobilized proteins, using anti-GST antibody to bind to the surface bound GST. Another similar approach involved calmodulin cutinase fusion protein. Cutinase was applied because of its reactions with phosphonate to form a covalent adduct [144]. After cutinase active site binding to the phosphonate ligand, an adduct was formed between the phosphonate and the serine residue of the enzyme resulting in a covalent linkage between the enzyme and the surface immobilized phosphonates. Intermediate proteins, such as protein A, protein G and F_c binding antibody can be attached on the surface that bind to the F_c region of the antibody for the oriented immobilization of antibodiesy on the surface [125].

Mac Beath et al. reported one of the pioneering works in modern protein microarray technology. Their work was based on the immobilization of proteins onto aldehyde functionalized glass slides generated from the self-assembly of aldehyde terminated silanes. Three different aspects of protein interactions, protein-protein interaction, protein-substrate interaction and protein-small molecule interactions were studied in a microarray format [145]. Recent advances in microarray based proteomic analysis have taken a leap, and whole cell proteomic analysis has been performed on a single microarray. Another aspect of the immobilization of biomolecules on solid substrates for high throughput screening is DNA microarrays, which has found widespread application in gene expression, point mutation, single nucleotide polymorphism detection and drug discovery [115]. Similar studies involving glycan based analysis are being actively researched through the development of glycan arrays and lectin arrays [117, 118]. Biomolecular interaction on the solid surface involves immobilization of one of the components on the surface followed by the binding of

another molecule to the surface-bound molecule. The most common pairs of complementary biomolecules include antibody-antigen, DNA-DNA, DNA-protein, DNA-RNA, carbohydrate-protein, glycoprotein-lectin, etc. One of the most commonly used pairs of biomolecules are antibody-antigen pairs, they are favored because of their biological significance as well as because of their strong binding affinity, which makes them a model system for most studies. Lectins, on the other hand are equally important biomolecules for glycan-based analysis.

1.11 Antibodies

Antibodies or immunoglobulins are one of the principal effector proteins of the adaptive immune system. Antibodies have found widespread application in scientific research and development, therapeutics, diagnosis, analysis, purification, enrichment, etc. Their application in diagnostics has greatly improved the human healthcare system. Chemically these antibodies are glycoproteins, secreted by the B lymphocyte cells also known as plasma cells [146]. Each antibody consists of four polypeptide chains consisting of two heavy chains (55 kDa) and two light chains (25 kDa) held together by disulfide bonds, hydrogen bonds and van der Waals interactions [147-149]. Mammalian antibodies are divided into five classes: IgA, IgD, IgE, IgG and IgM [150]. Depending upon the species, IgG and IgA could also be divided into several isotypes [151]. Each of the two antigen binding domains is formed by the combination of the NH_2 terminus of both the light and heavy chains and the carboxyl terminus from the F_c domain. Each light chain has one variable and one constant region each consisting of approximately 110 amino acids. The heavy chain, on the other hand, has one variable chain and three constant regions, each consisting of approximately 110 amino acids. Each antigen-

binding domain is generated by binding of the variable region of both the heavy and light chains. The epitope binding site or the complementarity determining region (CDR) is formed by at least three hyper variable regions consisting of approximately 5 to 10 amino acids on each chain. Recognition of the epitope site by an antibody can be variable so all six or some of the CRDs can be used during antigen binding. Structure of IgG with different fragments is shown in **Figure 1.3** [152].

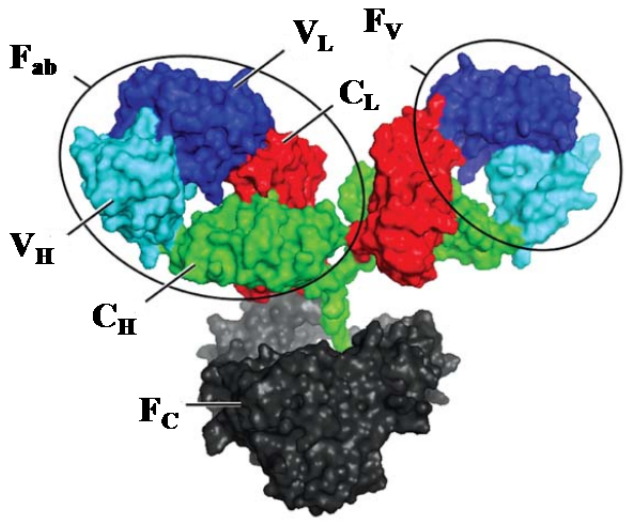

Figure 1.3. Structure of IgG. F_{ab}-antigen binding fragment, F_c-fragment crystallization, F_v- variable fragment, C_L-constant region of the light chain, C_H-constant region of the heavy chain, V_H-variable region of the heavy chain, V_L-variable region of the light chain.

Polyclonal antibodies are produced as a result of the interaction of a complex antigen with multiple lymphocytes and their activation to proliferate and differentiate into plasma cells; on the other hand, monoclonal antibodies are generated from a single lymphocyte [153]. Polyclonal antibodies recognize multiple epitopes in an antigen whereas monoclonal antibodies recognize only one epitope in an antigen. One of the most common applications of antibodies is in protein analysis and diagnosis, in the form of

enzyme-linked immunosorbant assays (ELISA) [154]. Structures of different proteins used in this study are given in **Figure 1.4.**

1.12 Lectins

Lectins are non-enzymatic proteins of nonimmune origin, and bind to specific carbohydrates with high selectivity [155]. Lectins are found to be involved in several biological processes, including the clearance of glycoproteins from biological systems, adhesion of infectious agents to the host cell surface, recruitment of leukocytes to inflammatory sites, and cell interaction in the immune system, in malignancy and metastasis [156, 157]. The presence of multiple binding sites in lectins leads to the crosslinking of several eryhtrocytes and finally precipitation, commonly known as the hemagluttination assay, which used to be commonly employed in the identification of cell types, and glycan units on cell surfaces [158, 159]. Based on the carbohydrate ligands to which lectins exhibit highest specificity, lectins can be classified into four classes: mannose, galactose/N-acetyl galactosamine, N-acetyl glucosamine, fucose and N-acetyl neuraminic acid binding lectins. Even though lectin affinity for carbohydrates is fairly low, in the mM range, the lectin-carbohydrate interaction is fairly specific [160, 161]. Apart from some exceptions, a glucose binding lectin doesn't bind to galactose and vice versa. It is reported that the variation in C2 position of a carbohydrate is tolerated to some extent thus, a galactose binding lectin can bind to N-acetyl galactosamine. Some proteins have anomeric specificity as they bind to the α or the β anomer with higher affinity, whereas some lectins lack this specificity [162]. Lectin-carbohydrate binding affinity has been found to be higher for oligosaccharides compared to that of the monosaccharides [162, 163]. Usually lectins exist as dimers or as tetramers, with nearly

250 amino acids and 25-30 kDa molecular weights, per monomer. Although primary, secondary and tertiary structures of monomeric lectins are fairly similar, the quaternary structure of lectins varies significantly among different lectins. Carbohydrate binding pockets of lectins are shallow depressions on the protein surface. Four invariant residues, aspartic acid, asparagines, glycine and an aromatic amino acid or leucine have been observed in the binding pocket of almost all lectins except Concanavalin A (Con A). Conformational changes of the lectin after carbohydrate binding are very small. One Ca^{2+} and a transition metal, usually Mn^{2+}, are required for lectin-carbohydrate interaction, which is believed to bring about suitable conformational changes of lectin for carbohydrate binding [164-166]. Lectins have been an important analytical tool for the identification of glycan moieties on glycoproteins. Lectins are being actively researched for the development of lectin arrays for high throughput screening of glycan epitopes in glycoproteins and related studies. Lectins are important recognition elements for carbohydrate-lectin interaction because of the lack of high affinity antibodies of carbohydrates [160].

1.13 Prostate specific antigen (PSA)

Prostate specific antigen is a protein belonging to the family of kallikrein (a subgroup of serine protease) like peptidases of serine protease. It is produced by the prostate gland, and its physiological role is to liquefy seminal fluid [167]. Development of prostate cancer causes a significant increase in PSA level, in blood, by up to 10^5 fold. The PSA level in blood is fairly small, almost 10^6 fold less, compared to that of the seminal fluid. PSA in serum exists in various forms such as free PSA, and in the bound form with protease inhibitors such as α1-antichymotrypsin and α2-macroglobulin, as a

proprotein or a mature protein, and intact or a nicked PSA. PSA level in human serum is affected by various factors such as benign prostate diseases, prostatitis, benign prostatic hypertrophy (BPH), age, race, body mass index and smoking, non smoking behavior, etc. Increased levels of PSA could be because of the changes in prostate architecture such as changes in order of the basement membrane and loss of the basal cell layer, changes in ductal lumen architecture and epithelial cell polarity, rather than due to the increased protein expression during prostate cancer development [168].

PSA is one of the most studied biomarkers and is used for diagnosis and monitoring of prostate cancer before and after cancer treatment. The normal level of PSA in healthy individuals is less than 4 ng mL^{-1}; 4-10 ng mL^{-1} is the so called gray zone and more than 10 ng mL^{-1} is regarded to indicate a high risk for prostate cancer; more than 100 ng mL^{-1} has been observed in cases of advanced stage prostate cancer [169]. In addition to the PSA test, different variations of PSA tests are being actively studied to increase the predictivity of prostate cancer, using PSA as a biomarker. The PSA density test is based on the amount of PSA and the size of prostate gland. Complexed and free PSA has been compared to total PSA; the percentage of fPSA is lower in prostate cancer than in BPH (benign prostatic hypertrophy), thus information on total PSA and fPSA makes distinction of BPH and prostate cancer possible. PSA dynamics/PSA velocity is also used, and a strong correlation has been reported between PSA velocity and prostate cancer progression and is the most advocated test for the diagnosis of prostate cancer [170, 171]. The PSA test is also performed after disease diagnosis and treatment. PSA levels more than 0.2 to 0.5 ng mL^{-1} after prostatectomy is taken as a measure of the recurrence of prostate cancer because after prostatectomy only metastatic cells could be

producing PSA. There have been a huge controversy over the PSA test, and the United States Preventive Services Task Force (USPSTF) recommends against PSA test [172]. Their recommendation against PSA screening on healthy individual regardless of age, sex or risk level was also criticized [173]. However, the USPSTF recommendation doesn't apply for PSA monitoring for individuals already diagnosed with prostate cancer. Undoubtedly PSA is a biomarker for prostate cancer; however, testing for it has not been able to reduce the mortality rate. One of the reasons for the USPSTF recommendation is the harm caused by misdiagnosis and subsequent treatment, which can cause several side effects such as, discomfort, impotency, erectile dysfunction, etc. These side effects should not be taken as a major factor in expense to the life-threatening condition of prostate cancer. In absence of any other reliable biomarker of prostate cancer, the PSA test should be taken as an indicator of prostate health for informed decision making for further treatment, and will be applied to thousands of clinics all around the world. There are still ongoing debates on the recommendations of USPSTF and its impact in prostate health care [174-176]. Catalona criticized the recommendation and published a report criticizing flaws in the study and its potential impact in the health care [173]. Some other molecules such as prostatic acid phosphatase (p-AP) and prostate specific membrane antigens (PMP) are also considered as biomarkers for prostate cancers but PSA outweighs their applicability for diagnostic purposes [177-180]. Prostate specific membrane antigen is actively being studied for the immunotherapy of prostate cancer [181].

1.14 Carcinoembryonic antigen (CEA)

Carcinoembryonic antigen (CEA) is a biomarker for gastrointestinal cancer, specifically colorectal cancer. CEA is a 180-200 kDa, highly glycosylated protein, with almost 60% carbohydrate units by molecular weight. Carbohydrate monomers in CEA are mannose, galactose, N-acetylglucosamine, fucose and sialic acid. CEA is attached to the cell membrane via a glycosylated phosphatidylinositol anchor [182]. CEA consists of seven immunoglobulin-like domains, and the N-terminal domain is homologous to the variable domain of IgG, and the other six domains are homologous to the constant domains of a C2 set. Normal level of CEA in healthy non-smokers is less than 3 ng mL^{-1} but its value could rise up to 6.4 ng mL^{-1} in male smokers and 4.9 ng mL^{-1} in female smokers [183-185]. An elevated CEA level has also been found to be associated with malignancies such as lung cancer, breast cancer, coronary artery disease etc. [186-188]

1.15 Transferrin (TSF)

Transferrin is commonly known as an iron binding protein and is a glycoprotein with 679 amino acid residues, and a molar mass of 79 kDa. Transferrin has three carbohydrate chains, two of them are N-linked at Asn-413 and Asn-611 and the third carbohydrate chain is O-linked (at Ser-32). Transferrin has been observed in several body fluids such as plasma, bile, amniotic, cerebrospinal, lymph and breast milk [189, 190]. The plasma level is fairly constant throughout life, ranging from 2 to 3 ng mL^{-1}. Lower concentrations of transferrin (less than 0.1 ng mL^{-1}) have been reported to be associated with increased infection rate, growth retardation and anemia. Changes in glycosylation, or of the carbohydrate units in transferrin have been associated with several malignant

conditions such as hepatocellular carcinoma, and carbohydrate deficient (desialylated TSF) TSF has been found to be associated with alcoholism [191].

1.16 Immunoglobulin G (IgG)

Glycan units in an IgG are attached to the highly conserved fragment crystallization site (F_c) region. IgG is abundantly present in human serum at a very high concentration of 10 mg mL^{-1} in different subclasses. Glycan structures of N-glycans of IgG are mostly of the biantennary, complex type with core fucosylated units [146]. Differences from normal glycosylation of IgG are associated with several autoimmune and chronic inflammatory diseases such as rheumatoid arthritis [192, 193].

1.17 Fetuin (FET)

Fetuin is a circulating acute phase glycoprotein, belonging to the cystatin superfamily of cysteine protease inhibitors [194]. An inverse correlation between mitral and aortic valve calcification and fetuin serum level has been observed [195]. It is an insulin inhibitor and an increased level of fetuin has been found to be associated with diabetes mellitus and hyperglycemia [196].

1.18 Alkaline phosphatase (ALP)

Calf intestine alkaline phosphatase is a 69 kDa, non-specific phosphomonoesterase, purified from calf intestinal mucosa [197]. It has been one of the most favored enzymes in enzyme-linked lectinsorbant assays, and in dephosphorylation of DNAs and RNAs [198-200].

Carcinoembryonic antigen (PDB:1E07)

Immunoglobulin G (1HZH)

Concanavalin A (3CNA)

Transferrin (1LFG)

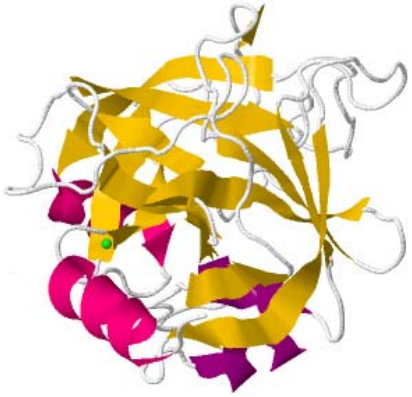

Prostate Specific antigen (PSA-2ZCH)

Alkaline Phosphatase (1B8J)

Figure 1.4. Structures of some of the proteins or their isoforms used in this study.

PDB code is also shown for each protein.

1.19 Immunoassays

Application of antibodies in immunoprecipitation of antigens, and quantitation started early in the nineteenth century. Yalow and Berson showed increased sensitivity of the immunoassay for insulin with antiserum with the use of ^{131}I radiolabel, which became a fairly popular analytical technique in bioanalysis, as a radioimmunoassay [201]. Enzyme-coupled antibodies were used in histochemistry to detect antigens in tissue sections. Utilizing similar concepts, the enzyme-linked immunoassay was introduced by Engvall and Perlmann in 1971 and reported to have similar precision and sensitivity to that of the radioimmunoassay [202]. In this study, they allowed antigen to adsorb on polystyrene tubes followed by the addition of antibody-alkaline phosphatase conjugate and measurement of the activity of the enzyme. Catt and Treager reported a solid phase radioimmunoassay, done by immobilization of antibodies on disposable tubes, in a competitive format [203]. Most of the common ELISA protocols are based on these early developments of immunoassays, both for radioimmunoassay and enzyme linked immunosorbant assays. With the development of modern instrumentation and analytical techniques, some modifications and development have taken place, and commonly used immunoassay formats are of the following three types: sandwich, antigen capture and direct [204, 205]. In a sandwich immunoassay, the primary antibody is immobilized onto the surface and then incubated with the antigen solution, with the final and detection steps consisting of the enzyme labeled secondary antibody binding to the antigen already bound to the primary antibody. Rinsing off any unbound enzyme conjugate and incubation with the enzyme substrate gives the measurement of the amount of antigen bound to the surface bound antibody [206]. In the antigen capture strategy, the

complex mixture of the protein solution (detection solution) needs to be labeled. Antibody is immobilized on the surface and then labeled antigen or protein solution is incubated. In the direct measurement strategy, a protein or the antigen is immobilized on the surface and then incubated with the labeled antibody.

1.19.1 Immunoassay strategies

Sandwich immunoassays involving multiple antibodies are described in the later phase of immunoassay development. Maiolini et al. reported a sandwich immunoassay for an antigen having at least two antibody binding sites; this procedure is fairly similar to the common ELISA protocol adopted today [204, 205, 207]. The initial step involved immobilization of an antibody to the substrate followed by antigen binding, and finally another antibody labeled with enzyme is allowed to bind to the antigen in solution. The final detection step involved measurement of the enzymatic activity of the enzyme. Later versions of the immunoassay involved multiple antibodies [206]. Schematic representations of different strategies of immunoassay are shown in **Figure 1.5.**

Other types of immunoassays include:

a) Competitive assay for antigen: Labeled antigen competes with the unlabeled antigen for binding to the antibody. Amount of the labeled antigen bound to the antibody is detected after appropriate separation procedures [208].

b) Immunoenzymometric assay for antigen: In this procedure, antigen is allowed to react with an excess of labeled antibody. In the second step, an excess of solid phase antigen is allowed to bind with the unreacted labeled antibodies in solution. After separation of the solid phase antibody, the amount of solution phase antigen is determined based on the enzymatic activity associated with them [209].

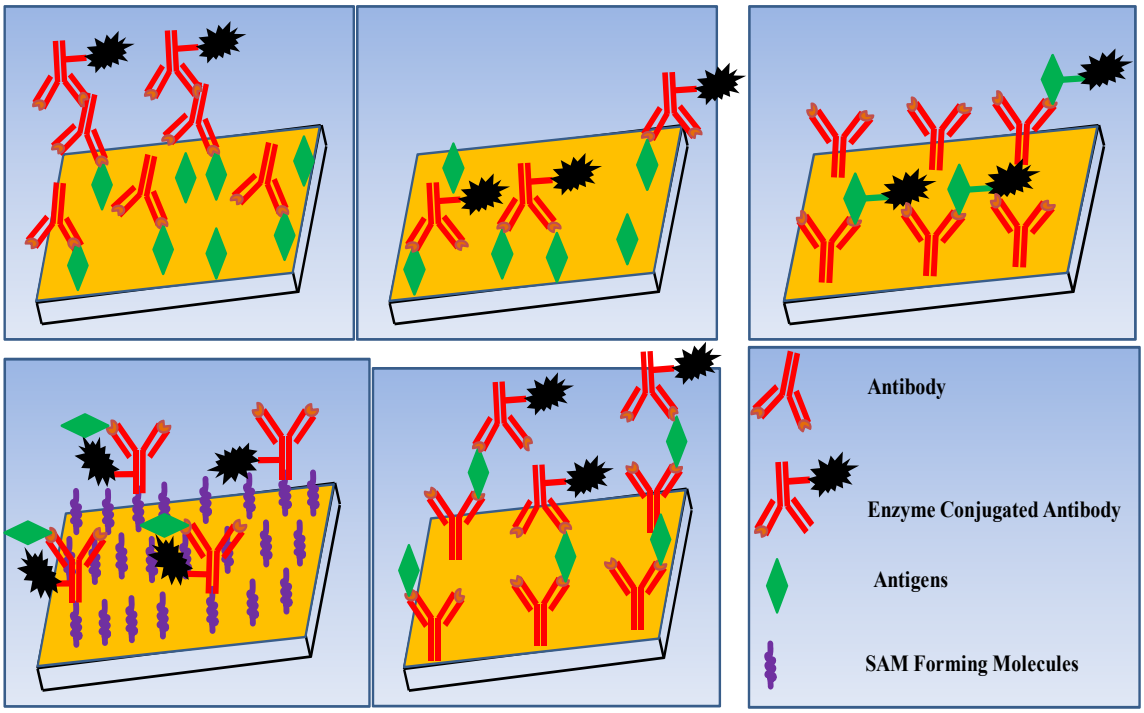

Figure 1.5. Schematic representations of the some of the most common types of immunoassays.

c) Enzyme immunoassay for antibody: This is another version of the enzyme immunoassay, where instead of antibody coating to the surface, antigen is coated and antibody is allowed to bind to the solid phase antigen. The amount of antibody bound to the surface is detected after final step of incubation with the labeled antibody [210].

d) Homogeneous enzyme immunoassay for antigens and haptens: This immunoassay doesn't require separation of the analyte mixture, because the detection strategy is based on the activation or reduction of the enzymatic activity of an enzyme after antibody binding. Briefly, this method consists of preparation of enzyme conjugate with a haptenic group; when the antibody binds to the antigen, enzymatic activity is reduced due to the presence of a large antibody near the enzyme. When excess antigen is

allowed to bind to the antibody, free antigen-enzyme conjugate is released into the solution, and hence enzymatic activity increases [211]. Rowley et al. reported similar studies in which a morphine derivative was attached to malate dehydrogenase and their report showed that the loss of enzymatic activity was because of the conformational freezing of the malate dehydrogenase, rather than due to the presence of the bulkier group, i. e. the antibody [212]. They also pointed out that the conjugation sites in the enzyme is important for the effective loss of the enzymatic activity, after antibody binding [213]. Conjugation of morphine with malate dehydrogenase via tyrosine and amino groups of lysine showed only a moderate loss of activity with an increasing number of morphine molecules substituted to the enzyme; whereas, conjugation via a disulfide bond showed an initial increase in enzymatic activity which dropped sharply with increasing number of molecules. Tryptic digestion, immunoprecipitation and mass spectrometric characterization of morphine glucose 6-phosphate dehydrogenase has been reported recently, for the improvement of current understanding of the mechanism of enzyme inhibition by antibody-hapten interaction [214]. This study also identified that catalytically important lysine residues were among the 26 possible conjugation sites. This assay approach was applied for the determination of several other analytes, as well as using different enzyme labels [215-217].

1.20 Solid surfaces for immunoassays

Different surfaces have been employed for the immobilization of antibodies or antigen depending upon the requirements of the detection techniques. With the development of modern instrumentation and with a continued effort to create novel ways of detecting immunogenic reactions, new surfaces are continuously building up in the

library of surfaces. Historically some of the popular solid phases employed in enzyme immunoassays and ELISAs include polystyrene plates [218], beads and tubes [199, 219], plastic [220], cellulose [221], nitrocellulose [222], agarose [113], dextran [223], latex [113], polydimethylsiloxane [224], nylon membranes, beads and microparticles of methyl methacrylate coated surfaces [225], etc. Polystyrene is one of the most ubiquitous materials used in research laboratories, it is available untreated or treated for optimal protein adsorption on its surface. Irradiated or plasma treated polystyrene and functionalized polystyrenes are commercially available [226]. Chemically modified polystyrenes have been designed for different interactions and modes of immobilization such as ionic and hydrophilic, ionic, hydrophobic and aminated, covalent attachment of DNA via reaction between NH_2 and NOS groups, sulphydryl binding surfaces, surfaces prepared for covalent binding via hydrazide groups, and surfaces designed for UV crosslinking via extractable hydrogen with the biomolecules (marketed by Corning, Inc., Tewksbury, MA) for assay purposes [226], In addition to the different polystyrene surfaces designed for assay purposes, functionalized polystyrene surfaces for use in cell culture are also marketed by Corning. Epoxide coated glass slides with a uniform coating of 3-glycidoxypropyltrimethoxysilane epoxide or amine terminated surfaces prepared from a γ-aminopropylsilane coating are also available from the same company for microarray based studies. Nunc (Rochester, NY) also supplies modified surfaces for cell culture, immunology and molecular biology [227]. Polystyrene, glass, plastic and polycarbonate surfaces are modified for the purpose of covalent binding with the secondary amines on the surface, hydrophobic or hydrophilic interactions (Covalink, Rochester, NY) [228]. When polystyrene is used as a substrate for protein

immobilization, significant background or noise is observed in assays, due to the hydrophobicity of the surface and nonspecific adsorption. Carbohydrate modified beads are known for significant reduction of nonspecific adsorption of proteins, due to the hydrophilic nature of the surface [229]. Membrane based systems for immunoassays are fairly popular and have some advantages due to their higher surface area and porosity. Protein binding to these surfaces is mainly due to hydrophobic interactions and in some cases due to hydrophilic interactions. Some of the most widely used materials are cellulose nitrate ester (nitrocellulose), Nylon and polyvinylidene difluoride (PVDF).

Methods of detection in bioassays using these surfaces, are mostly optical measurements (either absorbance based or fluorescence measurement). Optical measurements have certain shortcomings when it comes to measurement of colored and turbid samples that scatter light. An alternative and highly sensitive set of measurements in ELISA are the electrochemical techniques, which have certain advantages over the absorbance based techniques as electrochemical techniques are less affected by interference from the color of the solution, turbidity and non-electroactive matrices [230]. Electrochemical measurements can potentially be miniaturized to develop portable detection devices [231]. With the development of nanotechnology, these electrochemical methods have boomed and several composite electrodes based on nanostructures have been shown to improve sensitivity and detection range of assays, compared to those of the traditional methods [232].

1.21 Nanoparticles, electrochemical immunoassays and signal enhancement

Historically, potentiometric and amperometric methods were the most favored electrochemical methods applied for the electrochemical detection of antibody-antigen

binding events. Pioneering studies on the application of electrochemical methods, for the study of antibody-antigen binding, were reported by Rechnitz et al. [233] Their potentiometric study was based on the trimethylphenyl ammonium ($TMPA^+$) ion selective electrode, and sheep erythrocyte ghosts containing $TMPA^+$ having a binding site for the Fossmann antigen, which can bind specifically to the hemolytic antibody. Complement then recognizes the complex of antigen and the hemolytic antibody causes cell lysis via a series of enzymatic reactions. Complement system consist of more than 30 serum proteins and cell surface receptors involved in several functions including cell lysis and enhancement of B and T cell responses [234]. The release of $TMPA^+$ after cell lysis was monitored by the potentiometric method and correlated to the amount of the antibody and complement present in the system, with the rest of the other components kept constant. This system was shown to respond to the amount of antibody and of the complement as analytes [235, 236]. In an another study, Rechnitz et al. reported synthesis of a membrane electrode for potentiometric studies for the development of an immunosensor, and they developed two types of membranes, one with dinitrophenol conjugated to the polyvinyl chloride membrane, and another with triacetyl cellulose for BSA immobilization. Using antibodies specific for BSA and dinitrophenol, these electrodes were shown to be specific for the respective antibodies (dinitrophenol-anti dinitrophenol antibody and BSA-anti BSA antibody), and potential application of the principle for other systems was also pointed out [235]. There are several other reports on the change in potential of the immunoelectrode after antibody-antigen reaction [237-239]. Janata et al. reported that the change in potential with proteins immobilized on the electrode surface after binding with its complementary protein, was due to the changes in

charge distribution [240]. As proteins are polyelectrolytes, when in solution they have certain charges; when bound to another protein, which also is charged, the charge ratio changes on the surface which causes a change in potential. Thus, the change in potential can be related to the amount of protein analyte in solution, which is in equilibrium with the bound protein on the electrode surface [241]. A potentiometric immunoassay was reported for the determination of α-fetoprotein (AFP) based on the composite nanostructure consisting of $CoFe_2O_4$-mercaptopropyl trimethoxy silane [242]. Au-nps were self-assembled on the modified $CoFe_2O_4$ surface, through the Au-S interaction, and the anti-AFP antibody was then immobilized by adsorption on the Au-nps. This composite consisting of magnetic core-(Au-np)-anti AFP antibody was then deposited onto carbon paste electrodes by magnetic interaction between a permanent magnet and the magnetic nanoparticles. Heinman et al. reported application of amperometry as a method for the detection of NADH in enzyme coupled immunoassay in flow injection analysis, using phenytoin as an analyte [243]. A non-enzymatic detection method for the immunoreaction of estriol and antibody, based on the redox label mercuric acetate, was reported using differential pulse polarography [244]. More recent approaches for the detection of immunoreaction have been diverse, and different electrochemical techniques have utilized including potentiometry, amperometry, differential pulse voltammetry, square wave voltammetry, anodic stripping voltammetry, electrochemical impedance spectroscopy and cyclic voltammetry [245-248]. The following discussion will focus on the enzyme linked immunosorbant assay with electrochemical detection techniques. The enzyme label is the important component of ELISA. The choice of the enzyme label in electrochemical ELISA depends upon several factors including the availability of a

suitable electrochemical substrate, simplicity of the enzymatic reactions, no interference from the sample matrix in electrochemical analysis, high catalytic activity, stable enzyme substrate and product etc. [249, 250] In this respect, alkaline phosphatase (ALP) and horseradish peroxidase (HRP) are the two most common enzyme labels in electrochemical immunoassays [230, 251]. Alkaline phosphatase is an attractive enzyme because of its high reaction rate (turnover number), robustness, and wide range of available substrates for different modes of detection [230]. Most of the substrates of alkaline phosphatase are electroinactive but the products are electroactive, which reduces interferences from the substrate as current is specifically due to the product of the enzymatic reaction [252]. Several electrode materials have been utilized for the electrochemical detection of the reaction product of the enzyme-linked immunosorbant assays. Some of the electrode surfaces commonly used for electrochemical detection in ELISA include gold, glassy carbon, indium tin oxide, platinum, graphite, or carbon paste electrodes [253, 254]. Colloidal and nanoparticles are most often applied to the electrode surface in order to increase surface area and increase sensitivity of assays [232]. A label-free immunoassay for hCG was developed based on a gold nanoparticle sol/gel composite, a conjugate of anti-hCG antibody-HRP was adsorbed to the gold nanoparticle and HRP-anti-hCG/nanogold was encapsulated into the titania sol-gel matrix composite membrane [255]. The principle of this measurement was based on the decrease in DPV peak current due to the hindrance in electron transfer between HRP and the electrode surface after antigen binding to the antibody. In another report, thiolated DNA conjugated gold nanoparticles were used in a sandwich type immunoassay for signal amplification in an immunoassay for alpha fetoprotein and heart fatty acid binding protein. In this

strategy, the increased sensitivity was achieved by signal amplification and the multiplexing behavior of the DNA molecules on the nanoparticle surface [256]. A Faradaic impedance spectroscopy based label-free immunoassay for CEA was reported by immobilizing antibody on glutathione modified gold nanoparticles, which were later immobilized on the Au electrode by electrocopolymerization with o-aminophenol. The antigen-antibody interaction between CEA and anti-CEA antibody was reported to increase the charge transfer resistance at the gold electrode. This strategy was reported to give a linear range of determination of 0.5-20 ng mL^{-1}, and a detection limit of 0.1 ng mL^{-1} [257]. Another electrochemical label-free technique based on a similar principle was reported for the detection of human IgG in which the gold surface was modified by electropolymerization of methionine and methylene blue, followed by the attachment of gold nanoparticles and antibody immobilization. After blocking nonspecific sites with BSA, an immunoassay was performed for human IgG. This immunoassay was reported to have a detection limit of 3 ng mL^{-1}, and showed a linear range of determination of 10 to 10^4 ng mL^{-1} [258]. A working electrode for the electrochemical detection of AFP was prepared by entrapping thionine in a Nafion film through electrostatic interaction, which provided amino functional groups for the self-assembly of gold nanoparticles. The presence of thionine in the Nafion membrane served to generate current in cyclic voltammetry. The amount of current was reported to drop with an increase in amount of AFP. This method had a detection limit of 2.4 ng mL^{-1} AFP, and a linear range of 5.0 to 200 ng mL^{-1} [259]. Another electrochemical immunoassay based on the layer by layer assembly of graphene-Nafion composite-methylene blue-Au-np-anti-CEA antibody/BSA was developed on a glassy carbon electrode surface. The differential pulse voltammetric

peak current was reported to be a linear function of antigen concentration in the range of 0.5-120 ng mL^{-1} with a detection limit of 0.17 ng mL^{-1} [260]. Nanoparticles immobilized on 5,2':5',2"-terthiophene-3'-carboxylic acid polymer via electrodeposition were also reported; anti-osteoproteogerin antibody immobilized to this composite electrode was then used for the determination of osteoproteogerin, based on the competitive assay of HRP-labeled osteoproteogerin and unlabeled osteoproteogerin. This assay had a detection limit of 2.0 pg mL^{-1} osteoproteogerin and a dynamic range of 2.5 to 25 pg mL^{-1} [261]. A sensing surface developed by incorporating toluidine blue and hemoglobin on multiwall carbon nanotube-chitosan modified glassy carbon electrode was applied for the sensitive detection of human chorionic gonadotrophin. The electrode had a sensitivity of 0.3 mIU mL^{-1} and a linear range of 0.8 to 500 mIU mL^{-1}. One international unit of hCG is defined as the activity present on 0.001279 mg of the second international standard for hCG [262]. Presumably hCG binding partly hindered the catalytic site of hemoglobin and hence caused a decrease in catalytic activity of hemoglobin for oxidation of immobilized toluidine blue by H_2O_2 [263]. Ding et al. reported a highly sensitive electrochemical immunoassay for alpha fetoprotein using three different nanoparticles. Magnetic nanoparticles were coated with streptavidin, followed by the attachment of biotinylated anti-AFP antibody. On the later step of this immunoassay, CdS nanoparticles were modified with bio barcode DNA and incubated with the magnetic nanoparticles with the anti-AFP-AFP immunocomplex. Cd^{2+} ions were released in solution by dissolving in HNO_3, which was then determined by anodic stripping voltammetry. This immunoassay had a detection limit of 9.6 pg mL^{-1}, and a linear range of 0.02 to 3.5 ng mL^{-1} [264]. Wu et al. reported a competitive immunoassay for the determination of CA125, based on

colloidal gold nanoparticles immobilized on cellulose acetate stabilized gold nanoparticles, on a glassy carbon electrode. CA125 antigen was immobilized on the gold nanoparticle surface and allowed to compete for the HRP labeled anti-CA125 antibody and o-phenylenediamine was used as a tracer and H_2O_2 as an enzyme substrate [265]. Another immunoassay for hCG was reported based on a similar principle with gold nanoparticles immobilized on a chitosan membrane on a glassy carbon electrode, with detection by differential pulse voltammetry (DPV) measurement of the redox behavior of o-phenylenediamine [266]. A signal amplified DPV electrochemical immunoassay, based on using gold nanoparticles containing multiple HRP conjugated anti-hepatitis B surface antigen antibodies was reported by Ding et al. [58] Anti-hepatitis B surface antigen antibody was immobilized on a nanoporous gold (NPG) electrode, followed by antigen binding and finally nanoparticles containing multiple conjugates were allowed to bind to the antigen immobilized on the surface. This strategy using nanoparticles for immobilization of multiple labels per antigen is a highly attractive strategy for signal amplification in immunoassays. Horseradish peroxidase encapsulated inside nanogold microspheres, coated on the surface with secondary anti-CEA antibody, was used in another approach reported for multiple label loading for signal amplification in an immunoassay for CEA [267]. The electrode surface was prepared by electropolymerization of thionine on the gold surface with several amino groups on the base of the polymer layer, in contact with the gold surface. Colloidal gold was deposited onto the gold surface by dipping the electrode into the gold particle solution followed by the immobilization of protein A, onto the colloidal gold surface. Anti-CEA antibody was immobilized due to its interaction with the protein A molecule on the surface. After

incubation of the immunosensor with the CEA solution, it was then incubated with the gold nanoshell containing HRP and anti-CEA antibody, and amperometric measurements were then done by CV after adding hydrogen peroxide. This immunoassay had a sensitivity limit of 1.5 pg mL^{-1} and a linear range of 0.01 to 200 ng mL^{-1}. An et al. reported an immunoassay for α-synuclein based on dual signal amplification by dendrimer-gold nanoparticle composites and multiple enzyme loaded nanoparticles [268]. In this assay, α-synuclein was immobilized on the dendrimers followed by the binding of an antibody for α-synuclein and then detection of surface attached α-synuclein by gold nanoparticles loaded with multiple HRP-antibody conjugates. Using HRP as an enzyme label, cyclic voltammetric measurements showed a drop in current with increase in antigen concentration, presumably due to the formation of immunocomplexes and subsequent blockage of the reaction between HRP and H_2O_2. Lin et al. reported an immunoassay for CEA based on gold nanoparticles immobilized on a chitosan membrane on an ITO (indium tin oxide) surface. The DPV based competitive assay constituted immobilized CEA on the electrode surface competing with the CEA in solution, and for the HRP labeled antibody in solution, was reported to show linear response from 2 to 20 ng mL^{-1}, with a detection limit of 1 ng mL^{-1} [269]. Yuan et al. reported a different approach for the development of an immunoassay based on Au-nps immobilized on the glassy carbon electrode, then nickel hexacyanoferrate nanoparticles, followed by another layer of gold nanoparticles for immobilization of anti-CEA antibody [270]. This immunoassay was based on the decrease in cyclic voltammetric peak current with the increase in CEA antigen concentration, as formation of immunocomplexes on the electrode surface was believed to create resistance to electron transfer across the

interface. This immunoassay was reported to show two linear ranges of determination from 0.5 to 10 ng mL^{-1} and 10 to 160 ng mL^{-1}. Zhou et al. reported a strategy for the simultaneous detection of two cardiac biomarkers on the microfluidic chip by immobilizing two antibodies on the gold nanoparticles immobilized on the PDMS surface followed by antigen binding and finally binding of an antibody-quantum dot label (two different quantum dots for each of the two antibodies) to the antigen which was finally detected by dissolution of the quantum dots and by AS SWV (anodic sweep square wave voltammetry) [271]. A multiplexed immunoassay for human and mouse IgG was developed by Lai et al. [272] Two working electrodes prepared by covalent immobilization of antibodies on screen printed carbon electrodes modified with chitosan. After antigen binding to the antibody on the electrode surface, antibody-ALP conjugate immobilized Au-nps were allowed to bind to the antigen. Enzymatic reaction of ALP with 3-indoxyl phosphate generated the indoxyl intermediate which helped to reduce Ag^{+} ions, which were deposited onto the electrode surface, and later determined by linear stripping voltammetry in aqueous KCl solution. This strategy was reported to reduce crosstalk between electrodes and could potentially be applied for the development of multiplexed array immunoassays. Wilson et al. reported a multiplexed immunoassay based on the sandwich type immunoassay by immobilizing four analytes on eight iridium oxide electrodes (IrOX) [273]. Each electrode was spatially separated to reduce crosstalk between electrodes. This assay utilized alkaline phosphatase labeled detection antibodies and hydroquinone diphosphate (HQDP) as an enzyme substrate; the hydroquinone generated by the enzymatic reaction was measured amperometrically. The same group later applied a similar approach to detect seven different antigens, using immobilized

antigens on the multiarray electrodes and incubating them with the antigen, followed by the detection of antibody using secondary antibodies conjugated to ALP. HQDP was used as an enzyme substrate for electrochemical detection [274]. A multiplex label free immunoassay based on a silicon nanowire field effect device was reported by Zheng et al. for free PSA, PSA- α-1 antichymotrypsin and mucin-1 [275]. Wu et al. reported an alternative approach for the multiplexed enzyme immunoassay, based on immobilized toluidine blue on the electrode surface, which served as a mediator in the electrochemical process, and crosstalk between electrodes was minimized [276]. This immunoassay was successfully applied for the simultaneous determination of four tumor markers: CEA, α-AFP, CA125 and β-hCG. Tang et al. reported an immunoassay for CA125 based on the immobilization of gold nanoparticles on thionine modified carbon paste electrode. Anti-CA125 antibody was immobilized on the gold nanoparticles. Binding of antigen to the antibody produced a decrease in peak current in DPV, proportional to the antigen concentration in solution [277]. Zhuo et al. reported development of a multienzyme immunoassay based on glucose oxidase and HRP immobilized on the three layer magnetic nanoparticle prepared from Au-np-Prussian blue-Fe_3O_4 [278]. The gold working electrode surface was modified with chitosan/nano-Au composite followed by the covalent attachment of anti-CEA antibody, antigen binding to the electrode and then binding of bienzyme nanocomposite. This assay approach was reported to have pg mL^{-1} sensitivity for CEA and for α-fetoprotein. Gold nanoparticles have also been employed as a label, for the detection of antibody-antigen binding, in multiplex immunoassays, and have been reported to reduce crosstalk between electrodes. Another signal amplification strategy commonly applied in immunoassays is enzyme channeling and substrate

regeneration by attaching two enzymes on the electrode surface. Ivnitski et al. developed a bienzyme system for the sandwich immunoassay using HRP labeled secondary antibody and glucose oxidase immobilized at the polyethylineimine polymer membrane surface [279]. Signal amplification was achieved via continued generation of enzyme substrate for HRP, due to the reaction of excess glucose with glucose oxidase for generating H_2O_2, as a substrate for HRP, and accumulation of the redox mediator, I_2/I^- at the electrode surface. Several other signal amplification strategies are reported in the literature such as electrochemical redox recycling of the product, chemical recycling by adding certain chemicals to the system, that will regenerate the initial substance, and electrochemical and chemical recycling of products [280].

Immunoassays are the gold standard for the detection of biomarkers, food contaminants, toxins, environmental pollutants etc. Since the discovery of immunoassays, there have been continued efforts to improve the performance of immunoassays in terms of sensitivity, selectivity, reliability, regeneration, speed and convenience of operation procedures. Some of the notable successes in this direction includes development of lateral flow assays [281], immunoassay cartridges such as iSTAT® cartridges for cardiac troponin [282], and other point of care diagnostic methods [283, 284]. Lateral flow assays are designed for point of care testing or home use, in non-laboratory settings. The principle of lateral flow assays is based on the immobilization of a labeled antibody in a compartment next to the sample application compartment of the immunochromatographic pad. This reacts with the detection analyte in the sample, and the signal is generated at a detection point, by reacting with another antibody immobilized on this compartment [285]. A schematic representation of the different components of the lateral flow assay is

given in **Figure 1.6.** Though LFA are simple and rapid assays, they are either qualitative or semi-quantitative tests, and are applicable only for yes or no type analysis. One of the most successful applications of this technology is the pregnancy test kit, which gives result within a few minutes [281]. The detection particles in the LFA are most often colloidal gold, latex nanoparticles, liposomes or enzyme substrate reaction products [285].

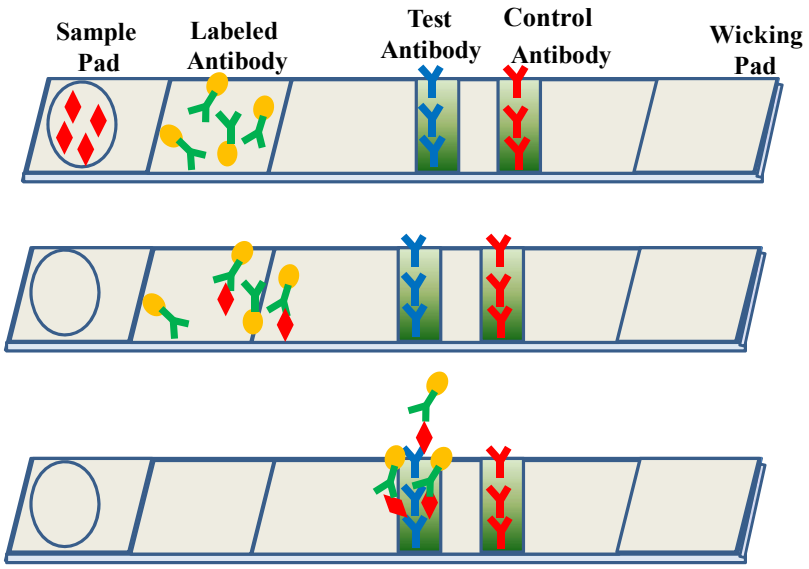

Figure 1.6. Schematic representation of the lateral flow assay. Different stages of the lateral flow assay are shown. The top panel shows different compartments for sample, labeled antibody, target antibody, control antibody and wicking pad; the middle panel shows antigen binding to the labeled antibody as it passes along the immunochromatographic strip; the lower panel shows the final visualization step of the assay.

iSTAT® cartridges are clinical testing devices designed for the fast and easy monitoring of blood analytes in point of care testing or bedside testing in doctor's offices

and clinics [286]. These iSTAT® cartridges can detect blood gases, blood pH, metabolites, lactate, coagulation and hematology and cardiac biomarkers. Analysis of cardiac biomarkers by these cartridges is based on immunoassay principles more or less similar to that of the lateral flow assays. Alkaline phosphatase tagged anti-cTnI antibody is placed at one point of the sensor surface. Once blood is applied to the spotting point it flows through the enzyme antibody conjugate. cTnI present in the blood sample binds to the antibody and flows with the liquid until it finds another antibody where it is immobilized, for electrochemical detection. During the washing step, p-aminophenyl phosphate, a substrate for ALP, is applied, which reacts with ALP to generate p-aminophenol, which is detected amperometrically [287].

The immunoassay principle has also been applied for the detection of whole cells for pathogen detection. An immunosensor for the detection of E. coli 0157:H7 was developed by Lin et al. [288] using gold nanoparticle–screen printed carbon strip electrodes for the immobilization of antibodies to E. Coli O157:H7. Using secondary antibodies conjugated to HRP a detection limits of 6 CFU and 50 CFU were obtained in PBS buffer and milk samples, respectively. Electrochemical detection of the reaction between HRP and hydrogen peroxide was mediated by ferrocene dicarboxylic acid. An anodic stripping voltammetry based immunoassay for E. coli determination was reported by Zhang et al.; their assay strategy was based on the immobilization of *E. coli* to polystyrene modified ITO surface, followed by the detection of bound *E. coli* by antibodies to *E. coli* coated on Cu-Au bimetallic nanoparticles [289].

1.22 Presence and significance of carbohydrates in biological system

Cell surfaces are heavily glycosylated, and act as the initial recognition element for most of the processes involving cell interactions such as, cell-cell communication, cell adhesion, antibody, hormones, toxins, intracellular trafficking of proteins, development of neural network, bacteria, viruses and host pathogen interactions [290-292]. Differential glycosylation has been observed in different stages of cell growth, cell differentiation, fertilization, and during malignancies as well [293-295]. Carbohydrates are also involved in pathological conditions such as inflammation, metastasis and host-pathogen interactions [296, 297]. Protein glycosylation is one of the most prominent post translational modifications, with almost 50% of all proteins and 80% of membrane proteins being glycosylated [298]. Based on the scaffolds to which monosaccharides are bound, glycoconjugates can be classified into four categories as glycoproteins (N-and O-linked), glycosaminoglycans, glycosylphosphatidylinositol (GPI) anchored proteins, and glycolipids [299]. Protein glycosylation has an important impact on protein conformation, protein folding, protein function, protein-protein interaction and protein-cell interactions [123, 300]. Thirteen different monosaccharides and eight amino acids are found to be conjugated in glycoproteins, via 41 bonds, due to the actions of 16 known glycosyl transferase enzymes [299]. The most common glycosidic linkages are N-glycosidic and O-glycosidic and other glycosidic linkages include C-mannosyl, phosphoglycosyl and glypiated linkages [301]. N-glycosidic linkages involve asparagine (Asn to Glc, GlcNAc, GalNAc, Rha) and arginine (Arg to Glc). O-Glycosidic linkages involve amino acids with hydroxyl groups such as Ser, Thr, Tyr, Hyl, and Hyp. C-Mannosyl (Trp to mannose), phosphoglycosyl–Ser, and glypiated bonds are formed in the following sequence

mannose-phosphoethanolamine-carboxyl group of the protein. All N-linked glycoproteins have a common pentasaccharide core consisting of a Manα1-6(Manα1-3)Manαβ1-4GlcNacβ1-4GlcNac unit. Oligomannose (high mannose, having only α-mannose units attached to a trimannosyl core), complex (branched with N-acetylglucosamine attached at the reducing end, to the mannose core), hybrid (containing both high mannose and complex type structures), and poly N-acetyl lactosamine (having repeated units of Galβ1-4GlcNacβ1-3 attached to the core glycan units), are four types of oligosaccharides added to the trimannosyl units. Classification is based on their location and glycan structure [299]. O-linked glycoproteins are more complex than the N-linked glycoproteins as they do not have common core units and six units have been identified so far [302]. Since carbohydrates are involved in diverse physiological processes they are potential targets for drug discovery, diagnostics, antibiotics etc. Carbohydrate-protein interaction is usually weak, which is overcome in nature by the presence of glycoclusters. In order to understand the detailed mechanism of protein-carbohydrate interaction and for high throughput screening of carbohydrate epitopes in glycoproteins, it is essential to immobilize carbohydrates on solid surfaces. With the advance of protein and DNA microarrays for proteomics and genomics, there have been a significant number of studies towards the development of glycan and lectin arrays for glycan profiling in glycomics [303, 304].

Different methods have been developed for the immobilization of carbohydrates on surfaces such as physisorption, covalent immobilization and biochemical immobilization [305, 306]. Physisorption of carbohydrate to surfaces is very weak so they are usually conjugated to some other molecules such as lipids, peptides,

neoglycoconjugates etc. [307] Different reaction schemes can be applied for the attachment of underivatized carbohydrates to the surface, which requires activation of carbohydrates by suitable activating groups such as CNBr, CNCl, divinylsulphone and isocyanate. Carbohydrates can be attached to the surface containing amine functionality via reductive amination of the reducing end of the sugar and the amine on the surface. Carbohydrates are oxidized under mild conditions to generate aldehydes or ketones, followed by the reaction with the amines on the surface to form Schiff's bases, which are ultimately reduced by hydrides to amides. Carbohydrates can also be immobilized to the surface via functional aglycones such as thiols or disulfide linkers attached to the carbohydrate, and another strategy involved modification of both surface and carbohydrate generating functional aglycone for reaction between these two functional groups. Immobilization via thiols and disulfides is by far the easiest and most favored approach for the immobilization of carbohydrates on gold surfaces. Finally, carbohydrates can be immobilized on the surface based on the affinity interaction between molecules such as biotin and streptavidin and or DNA mediated immobilization [307].

CHAPTER II

MATERIALS AND METHODS

2.1 Materials

Gold wire (0.2 mm diameter, 99.99%) was obtained from Electron Microscopy Sciences (Fort Washington, PA). PSA, CEA, anti-PSA monoclonal antibody, PSA (free) antigen, CEA antigen and anti-CEA monoclonal antibody were obtained from Fitzgerald (North Acton, MA). Alkaline phosphatase labeling kits were obtained from Dojindo Molecular Technologies Inc. (Rockville, Maryland). Concanavalin A, soybean agglutinin, peanut agglutinin, streptavidin-gold labeled (10 nm), Con A (biotinylated, 5 mole/mole Con A) were obtained from Sigma Aldrich (St. Louis, MO). P-aminophenyl phosphate (p-APP) was obtained from Gold Biochem (St. Louis, MO). Sodium carbonate (enzyme grade, >99%), N-hydroxysuccinimide (NHS) (≥ 97%), sodium phosphate (certified ACS grade), potassium phosphate (99.6%), sulfuric acid (certified ACS plus), nitric acid (trace metal grade), hydrogen peroxide (50%), and sodium bicarbonate (certified ACS) were all from Fisher Scientific (Pittsburg, PA). Potassium dicyanoargentate ($K[Ag(CN)_2]$) (99.96%) and potassium dicyanoaurate ($K[Au(CN)_2]$) (99.98%), ethanol (HPLC/spectrophotometric grade), acetonitrile (HPLC grade), lipoic acid, N-(3-Dimethylaminopropyl)-N′-ethylcarbodiimide hydrochloride (EDC) (>99%), Butanethiol (99%), hexanethiol (95%), octanethiol (98.5%), decanethiol (96%), dodecanethiol (98%), tetradecanethiol (98%), octadecanethiol (98%), mercaptododecanoic acid (99%) and mercaptoundecanol (97%) glycine (99%), sodium bicinchoninate (≥ 98%), sodium tartrate (> 99%), sodium hydroxide (99.99%), cupric

sulfate (≥ 99%), zinc chloride (≥ 98%), magnesium chloride (99%), and sodium chloride (99%) were obtained from Sigma–Aldrich (St. Louis, MO). All reagents were used without further purification. Milli-Q water (18.2 MΩ) was used for preparation of all aqueous solutions. Thiolated glycosides (α-D-Gal-(1→4)-β-D-Gal-(1→4)-D-Glc1-O-mercaptooctane (Gb3-C_8-SH) and 8-Mercaptooctyl α-D-mannopyranoside (Man-C_8-SH)) and 8-mercapto-3,6-dioxaoctanol (HO-PEG_2-SH) were obtained from Professor Alexei Demchenko's lab.

2.2 Preparation of nanoporous gold

2.2.1 Preparation of alloy of gold and silver

An alloy of gold and silver was electrodeposited on the gold wire surfaces of 0.2 mm diameter and 0.5 cm length. The solution used for electrodeposition was prepared by combining 4.9 mL of 50 mM $K[Ag(CN)_2]$ and 2.1 mL of 50 mM $K[Au(CN)_2]$ (each in 0.25 M sodium carbonate) to give a composition of 70% Ag and 30% Au in the 7.0 mL deposition solution used in the electrochemical cell. Deposition solution was degassed with Ar for 10 min and deposition was carried out at a potential of -1.0 V (versus Ag|AgCl) for 10 min. Electrodeposition was carried out in three electrode cell arrangement with gold wire as a working electrode, platinum wire as a counter-electrode and Ag|AgCl|KCl (saturated) as a reference electrode using a PARSTAT 2273 potentiostat and the Powersuite software.

2.2.2 Dealloying

Thus prepared alloys were dealloyed by submerging alloy coated gold wires into concentrated nitric acid solution (trace metal grade) for 24 hours in a sealed container.

These dealloyed wires were rinsed several times with Milli-Q water (18.2 MΩ) and then stored in Milli-Q water for at least 30 min, to get rid of any HNO_3 trapped into the pores, and then rinsed again. These wires were dipped into the ethanol for 30 min to reduce any gold oxide on the surface before further use. Gold wires were cleaned by dipping them in piranha solution (H_2SO_4 : H_2O_2 (30%), 4:1 for 10 minutes and rinsed with plenty of water and then with HPLC grade ethanol (*Caution: Piranha solution reacts vigorously with organic substances so caution should be taken while preparing and handling*).

2.2.3 Characterization of NPG

Surface morphology and general structure of NPG was studied by Scanning Electron Microscopy (JEOL JSM-6320F field emission SEM). Electrochemical surface area was determined by the gold oxide stripping method by scanning between 0 and 1.5 V at a scan rate of 100 mV sec^{-1}. The charge under the oxide reduction peak was integrated to estimate the surface area of the gold wires used in this study, using the reported conversion factor of 450 μC cm^{-2} for reduction of gold oxide in strong acid [308]. Presumably, a monolayer of gold oxide is formed on the positive scan, which reduces back to the metallic gold in negative scan. Gold oxide formation and reduction reactions are as follows [309],

$$Au_2O_3 + 6H^+ + 6e^- \rightarrow 2Au + 3H_2O \ (in\ strong\ acid\ solution)$$

$$Au(OH)_3 + 3H^+ + 3e^- \rightarrow Au + 3H_2O \ (in\ weak\ acid\ solution)$$

Electrochemical behavior of the NPG surface was also studied by electrochemical impedance spectroscopy.

2.3 Preparation of self-assembled monolayers for SAM characterization on NPG/GW

SAM preparation on NPG and gold wire surfaces were done by following well established standard protocol. These gold surfaces were immersed in 10 mM ethanolic solution of alkanethiols for 24 hours at room temperature. The resulting SAMs on the gold surfaces were copiously rinsed with ethanol, water and PBS buffer before performing any electrochemical measurements. Once gold wires were removed from the SAM solution and rinsed properly, it was connected to a copper wire and stored dipped into the PBS buffer solution.

2.4 Preparation of self-assembled monolayers for protein immobilization

Lipoic acid SAMs were prepared by immersing 10 wires at a time into a 10 mM lipoic acid solution, in ethanol, of 10 mL total volume. The wires were left for approximately 17 hours and then rinsed with ethanol twice followed by rinsing with acetonitrile. NPG coated wires modified with lipoic acid SAMs were immersed into the solution of EDC (5 mM) and NHS (5 mM) in acetonitrile for 5 hrs. After 5 hours, the wires were rinsed with acetonitrile and then twice with 10 mM phosphate buffered saline (pH 7.4) and immersed into the ALP-antibody conjugate solution (containing 25 μg of conjugate), in 10 mM PBS buffer (100 μL) of pH 7.4 in a small glass vial at 4 ^{o}C for 24 hours followed by rinsing with PBS buffer. For the competitive immunoassay, NPG coated gold wires with NHS activated –COOH groups were prepared as above and then these wires were incubated with 10 μg of antigen in 100 μl of PBS buffer for 2 hours at 4 ^{o}C in Eppendorf tubes.

2.5 Electrochemical impedance spectroscopic measurement

Electrochemical impedance spectroscopy is a powerful electroanalytical technique for the study of interfacial phenomenon. Unlike other electrochemical techniques, such as, chronoamperometry, chronopotentiometry and chronocoulometry, EIS gives sensitive, complete and detailed information about the system, in a single experiment [310]. If other electrochemical methods are chosen for the study of the interfacial processes several sets of experiments are required to get complete answer for the interfacial processes. The basic principle of EIS is based on the application of a small sinusoidal ac potential perturbation, to a system at equilibrium, followed by the measurement of the response current [311]. Application of small sinusoidal potential perturbation maintains the cell's response in the linear/pseudolinear regime and hence the response of the system is a sinusoidal current, at the same frequency but with a different phase. If a potential oscillation $E(t) = E_0\sin(\omega t)$ is applied to a system then the response current is $I(t) = I_0\sin(\omega t-\phi)$, where ϕ is the difference in phase angle between current and potential and E_0 and I_0 are the amplitudes of potential and current, respectively [312]. Thus, impedance of the system is defined as, [313].

$$Z_t = \frac{E_t}{I_t} = \frac{E_0\, Sin(\omega t)}{I_0\, Sin(\omega t+\emptyset)} = Z_0 \frac{Sin(\omega t)}{Sin(\omega t+\emptyset)} \tag{2.1}$$

From Euler's theorem,

$$Z(\omega) = \frac{E}{I} = |Z|e^{j\emptyset} = Z_0(Cos\emptyset + jSin\emptyset) = Z_{re} + jZ_{im} \tag{2.2}$$

where $j = (-1)^{1/2}$, Z_{re} and Z_{im} are real and imaginary impedance, respectively

Four principle criteria have to be fulfilled in order to get valid EIS data: the system should be at equilibrium, the response should be linear, the system should be stable and the response should be specific for the system or causality [314]. Due to the

widespread use and development of frequency response analyzers, EIS measurements are mostly performed in the frequency domain. EIS measurements can be done for a range of frequencies within a short period of time. The most common ways for representation of frequency data are the Nyquist plot and the Bode plot [315]. In the Nyquist plot, each data point represents the real and imaginary parts of the impedance as measured at one of the chosen measurement frequencies. The values at the highest frequencies are found closest to the origin. Once the impedance data is generated, the next step is the analysis of data based on the electrical equivalent circuit model, which helps in the measurement and complete description of the electrical interface. Circuit elements used in the model equivalent circuit for EIS data analysis are the common electrical circuit elements such as capacitors, resistors, inductors etc. Series and or parallel combinations of these circuit elements are designed to represent the electrochemical interface.

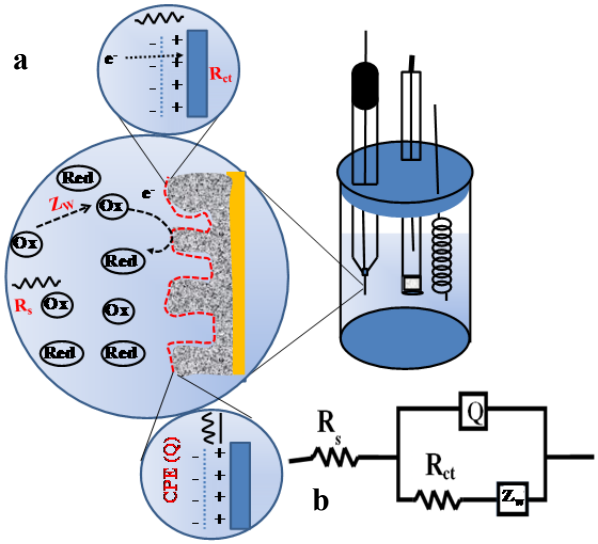

Figure 2.1. Schematic representation of the electrical interface and different electrochemical processes at the interface. a) Electrode electrolyte interface at the working electrode, and b) a modified Randle's circuit for modeling the electrified interface in an EIS experiment.

Let us consider an electrochemical redox reaction at the interface,

$$Ox + ne^{-} \rightarrow Red$$

Where, Ox is the oxidized form of the probe molecule, and n is the number of electrons involved in redox reaction to form reduced form (Red). The different components of the electrochemical interface are represented in **Figure 2.1**, in which the electrical double layer is represented by the Helmholtz model of the interface. There are both Faradaic and non-Faradaic processes taking place at the interface. A Faradaic process involves charge transfer across the interface, which takes place by overcoming the activation barrier, the polarization resistance (R_p), along with the uncompensated resistance (R_s). Charging of the double layer at the interface involves a non-Faradaic process i. e. no charge transfer takes place, and only involves redistribution of ions in solution and near the surface. Another component of the impedance of the electrified interface is the Warburg impedance (Z_w), associated with the diffusion of oxidized and reduced molecules to and from the interface, which is determined by the rate of charge transfer at the interface, i.e. the rate of conversion of Ox to Red at the interface. **Figure 2.1b**, shows the electrical equivalent circuit used for modeling the interface. Three different types of Nyquist plots are also shown in **Figure 2.2** for the interface, depending upon the nature of the electrochemical process taking place at the interface: a) kinetically controlled process, b) diffusion controlled process, and c) a mixed diffusion and kinetic controlled process. The total impedance of a system consists of real and imaginary parts; when the real part of the impedance is plotted on x-axis and imaginary part on the y-axis, the plot is called a Nyquist plot. Each point in the Nyquist plot is a representation of impedance at a certain frequency. Depending upon the nature of the system, a Nyquist plot could have one

semicircle, multiple semicircles or a combination of semicircle and straight lines with slopes of 45º. The semicircle intersects x-axis at two points, at higher frequency the intersection point gives a measure of the solution resistance (R_s) and the intersection at the lower frequency (if observed) gives the sum of solution resistance and charge transfer resistance (R_s+R_{ct}). In the Bode plot, the log of frequency is plotted on the x-axis and phase and the absolute value of impedance are plotted on the y-axis.

Different components of the equivalent circuit shown in **Figure 2.1** are explained as follows:

a) Solution resistance (R_s): Solution resistance between a reference electrode and the working electrode is an important component of the electrochemical system. Solution resistance depends upon several factors such as concentration, nature of the electrolyte, temperature and cell geometry.

Solution resistance is given by, $R_s = \rho \frac{l}{A}$ (2.3)

Where, ρ is the solution resistance, l and A are the characteristic of the cell geometry.

b) Double layer capacitance (C_{dl}): In an ideally polarizable electrode, the interface between electrode and the electrolyte consists of adsorbed ions (at a certain distance, in Å) on the electrode and equal but oppositely charged ions in the solution. There is an electrostatic equilibrium at the interface. Electrical double layer capacitance depends upon the nature of the electrode surface, electrolytes, temperature, electrode potential etc. Double layer capacitance for a bare metal electrode surface is in the range of 10-60 μF cm^{-2}. Impedance of the double layer capacitance is given by:

$$Z = \frac{1}{j\omega C} \quad (2.4)$$

Usually the metal surface is not an ideal capacitor and it behaves as a constant phase element.

Impedance of the constant phase element is given by,

$$Z_{CPE} = \frac{1}{(j\omega)^n C} \tag{2.5}$$

where, n is an empirical constant with no physical meaning. Its value ranges from 0 to 1, depending upon the nature of the interface. For an ideal capacitor $n = 1$ and for an ideal resistor $n = 0$.

c) Charge transfer resistance: After application of certain overpotential, electrochemical redox reaction takes place at the interface and charge is transferred from an ion to the electrode. Charge transfer occurs after overcoming a certain activation barrier commonly referred to as the polarization resistance and at formal potential of the redox probe it is known as charge transfer resistance. At a certain applied overpotential ($\eta = E_{app}$-E_{oc}), the difference of applied potential and the open circuit potential, the current potential relationship at the interface is given by Butler Volmer equation as,

$$i = i_0(e^{\left(\alpha\eta\frac{nF}{RT}\right)} - i_0(e^{-(1-\alpha)\eta\frac{nF}{RT}}) \tag{2.6}$$

This is the Butler-Volmer equation when concentrations of oxidized and reduced form of the molecules are equal at the interface and in the bulk of the solution. Here, i_0 is the exchange current density, α is the charge transfer coefficient and other terms have their usual meanings. At a very small applied overpotential, to the system at equilibrium, charge transfer resistance can be represented as,

$$R_{ct} = \frac{RT}{nFi_0} \tag{2.7}$$

Thus, the exchange current density can be calculated from R_{ct}.

d) Warburg impedance: Diffusion of ions at the interface also contributes to the total impedance of the system, which is referred to as the Warburg impedance. Warburg impedance is fairly small at higher frequencies and at smaller frequencies Warburg impedance becomes prominent. Warburg impedance in the Nyquist plot appears as a straight line with slope of 45°.

Warburg impedance is given by,

$$Z_\omega = \sigma(\omega)^{\frac{1}{2}}(1-j) \tag{2.8}$$

Where, σ is the Warburg coefficient given by,

$$\sigma = \frac{RT}{nFA\sqrt{2}}\left(\frac{1}{C_O D_0^{\frac{1}{2}}} + \frac{1}{C_R D_R^{\frac{1}{2}}}\right) \tag{2.9}$$

Where, D_O and D_R are the diffusion coefficients of oxidized and reduced form of the probe.

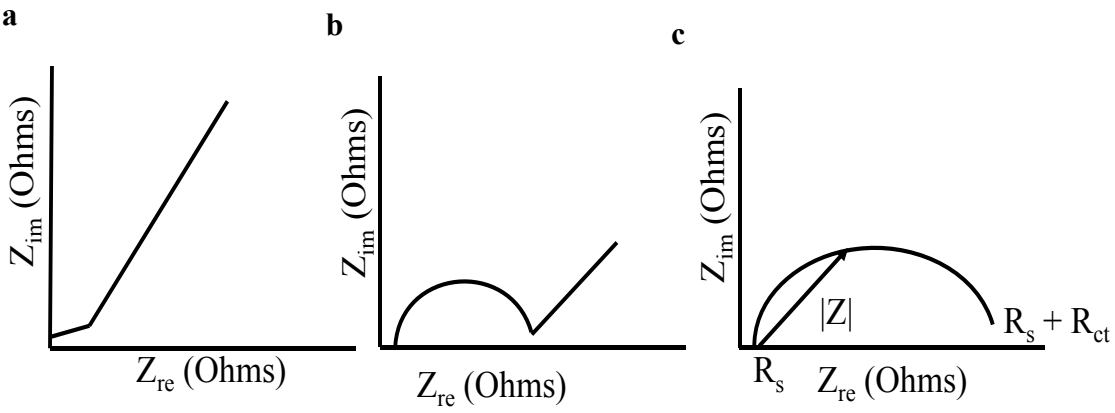

Figure 2.2. Nyquist plots for the different electrochemical processes at the interface. a) Diffusion controlled charge transfer process, b) mixed kinetic and diffusion controlled, and c) kinetic controlled process.

EIS measurements were done in a three-electrode cell of 3 mL solution volume containing 5 mM $K_3[Fe(CN)_6]$ and 5 mM$K_4[Fe(CN)_6]$ at frequencies from 10^5 Hz to 100 mHz, at 12 points per decade. A PARSTAT2273 potentiostat/galvanostat/FRA was used for the EIS measurement and the Powersine software was used for data collection. Data collection time was approximately 7 minutes for each data set of impedance as a function of frequency. Data analysis was done by using Zsimpwin 3.21 software (Princeton Applied Research, Oak Ridge, TN), by fitting to the modified Randles equivalent circuit shown in **Figure 2.1b**, in which the double layer capacitor has been replaced by the constant phase element (Q) to account for the non-ideal behavior associated with the roughness of the electrode. This circuit has been applied for fitting EIS data obtained on both modified NPG and gold wire surfaces. Charge transfer resistance was used as a measure of the resistance at the interface created by the addition of a layer of molecules because of lectin-carbohydrate binding. EIS measurements to assess binding kinetics were performed by incubating the electrode in the protein solution for the desired time followed by removal and acquisition of EIS data in the $Fe(CN)_6^{3-/4-}$ redox probe solution.

2.8 Cyclic voltammetry

Cyclic voltammetry is one of the most favorite electroanalytical techniques, mostly used for the study of redox processes and for understanding of the reaction intermediates and stability of the reaction products [316, 317]. The electron transfer rate constant of an electrochemical reaction can be estimated by studying the changes in peak separations as a function of scan rate. It is a potential sweep technique where potential of the working electrode is varied linearly between two operating potentials, at a certain scan rate. Once the final potential is reached it is scanned back to the initial potential, and

since the potential is cycled back to the same starting potential it is called cyclic voltammetry. **Figure 2.3** shows the typical potential scan scheme and a theoretical CV for a completely reversible electrochemical reaction. One of the disadvantages of the linear scan technique is the contribution of the charging current, which becomes more prominent at higher scan rates. Some of the important information that can be obtained from CV data includes reversibility of a reaction, formal potential, rate constant, number of electrons involved in the redox reaction, reaction mechanism, diffusion coefficients etc. Important parameters obtained by CV analysis include peak potentials (anodic (E_{pa}) and cathodic (E_{pc})) and peak currents (anodic ((I_{pa}) and cathodic (I_{pc})). Ideally, peak separation in a reversible reaction is, $\Delta E_p=|E_{pa}-E_{pc}| = 2.303RT/nF$, but usually there is some deviation from this value due to the cell resistance. For irreversible or quasireversible processes peak separation can be quite large. The formal potential of a redox reaction is given by, $E^0 = \frac{E_{pa}+E_{pc}}{2}$.

The relation between concentration and the peak current for a reversible reaction is given by the Randles-Sevick equation as follows,

$$i_p = 2.686 \times 10^5 n^{3/2} A C_0 D^{1/2} v^{1/2} \qquad (2.10)$$

Where, i_p is the peak current in amperes, A is the electrode surface area in cm^2, C_0 is the concentration of the redox molecules In mol/cm^3, D is the diffusion coefficient in cm^2/sec and v is the scan rate in V/sec. Self-assembled monolayers on the surface were characterized by cyclic voltammetry. It was also applied for the determination of the surface area of Au electrodes by the gold oxide stripping method as discussed above. Determination of surface area was performed by cyclic voltammetry (CV) scans between

0 V and 1.5 V (vs. Ag|AgCl), at a scan rate of 100 mV sec^{-1} in 0.5 M H_2SO_4, that was degassed with argon.

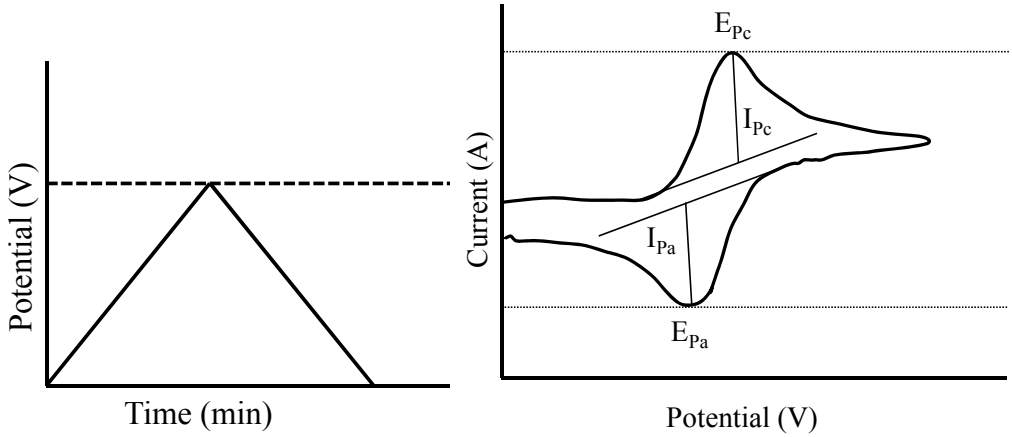

Figure 2.3. Cyclic voltammetry. Potential scan scheme in CV (a) and a representative CV for the reversible redox reaction (b).

This experiment with the SAM modified surfaces was used for estimation of the fractional coverage of the surface by the SAM. Additional CV scans to probe SAM integrity on gold wires and on NPG coated gold wire electrodes were conducted between 0 and 0.5 V (vs. Ag|AgCl) in 10 mM $K_3[Fe(CN)_6]$ at a scan rate of 100 mV sec^{-1}. The integrity is assessed by the ability of the SAM to block electron transfer to/from the metal complex $Fe(CN)_6^{3-/4-}$. Each determination of surface area was repeated ten times. Each CV measurement on SAM modified surfaces in sulfuric acid or in the presence of $K_3[Fe(CN)_6]$ was repeated for three different electrodes, and representative curves are shown in each case.

2.9 Reductive desorption of lipoic acid SAM

Reductive desorption of SAM was carried out in a 0.5 M NaOH solution, argon degassed for 30 minutes. CV scans were performed in 3 mL of solution in a three

electrode cell arrangement as mentioned before for other CV measurements. The CV scan was performed between 0 and -1.5 V (vs. Ag|AgCl) at a scan rate of 20 mV sec^{-1} on NPG; for gold wires, CV scans were performed at 500 mV sec^{-1}.

The process of reductive desorption of alkanethiol on the gold surface can be represented as [318],

$$R{-}S{-}Au{+}\ e^{-}{\rightarrow}R{-}\ S^{-}{+}\ Au \qquad (2.11)$$

The desorbed molecules either diffuse away from the surface or remain in vicinity of the surface, depending upon the solubility and hydrophobicity of the adsorbed molecules. In a study by Hobara et al., it has been reported that mercaptopropionic acid diffused away from the surface whereas 1-hexadecanethiol and 1-propanethiol remained close to the surface. The partial appearance of the readsorption peak on positive scans also supports the hypothesis that molecules remain close to the surface after reductive desorption [319].

2.10 Lectin-carbohydrate interaction studies on SAM modified surfaces

Gold surfaces with appropriate self-assembled monolayers, either pure αMan-C_8-SH, Gb3-C_8-SH or mixed SAM of αMan-C_8-SH/OCT, αMan-C_8-SH/HO-PEG_2-SH, Gb3-C_8-SH/OCT and Gb3-C_8-SH/HO-PEG_2-SH were prepared on NPG and gold wire surfaces and impedance spectra were recorded on these wires. After rinsing with copious amounts of PBS buffer the same wires were incubated with Con A or SBA solution in PBS buffer supplemented with 1.0 mM Ca^{2+} and 0.5 mM Mn^{2+}. These wires were then removed from the incubation solution and rinsed with copious amounts of PBS buffer and EIS measurement was performed.

2.11 Preparation of monoclonal antibody alkaline phosphatase (MAb-ALP) conjugate

200 µg of the antibody was labeled with the pre-activated alkaline phosphatase (NH_2 reactive ALP) provided in the Dojindo labeling kit (LK12-10) following the instructions provided with the kit. Briefly, 200 µg IgG was added to the microcentrifuge filter provided with the kit, washed twice with washing buffer and then 10 µL of ALP dissolved in reaction buffer was added to the tube and incubated at 37 ºC for 2 hours. 190 µL of storage buffer was added to the tube, mixed well and then the ALP-antibody conjugate was stored at -20 °C until use. All protein concentrations were determined by BCA assay.

2.12 Chronoamperometry

Chronoamperometry is a potential step technique where a sufficiently large potential step, large enough to cause an electrochemical reaction, is applied at the working electrode and current response is measured as a function of time. Thus, this technique records current as a function of time and is generally known as chronoamperometry (CA).

2.13 Square wave voltammetry

SWV is a pulse voltammetric technique, where a potential pulse of magnitude E_{SW} is applied to the working electrode and the current response is recorded with respect to the applied potential. Square wave voltammetry was developed by Barker et al. in the 1950s; however, the most commonly used technique is the one developed by Ramaley and Krause in 1969 [320]. **Figure 2.4** shows the potential pulse scheme of the

Osteryoung SWV. In this technique a symmetrical square wave potential pulse (E_{SW}) is superimposed in the staircase waveform with the step height of ΔE. Current is sampled twice, once at the start of the pulse and once at the end of the pulse or once at the forward pulse and once at the reverse pulse. Three types of current potential curves can be generated by this method: forward current vs. potential, reverse current vs. potential and difference in current vs. potential. Some of the advantages of SWV compared to the cyclic voltammogram include [321-323],

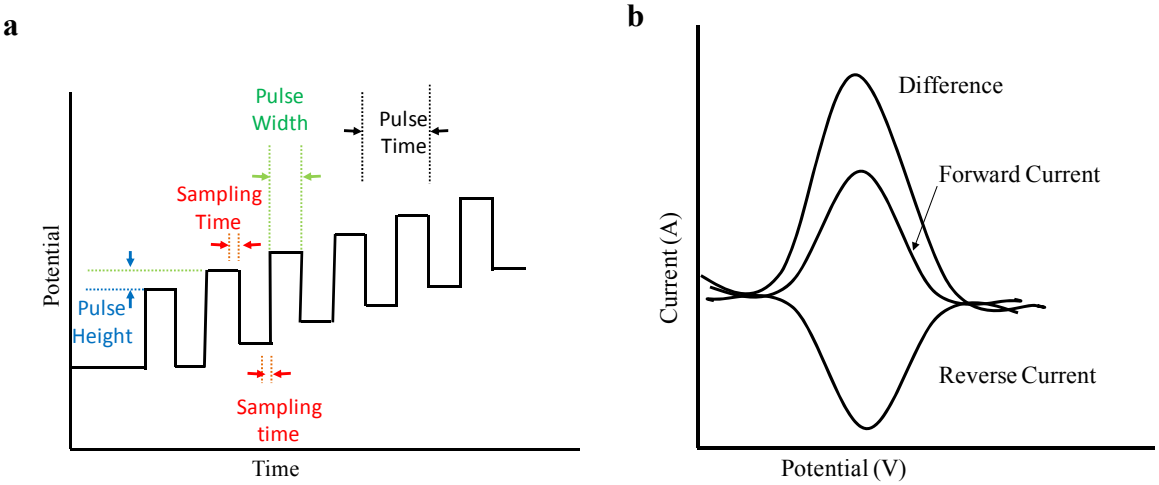

Figure 2.4. Square wave voltammetry. Potential pulse scheme for an Osteryoung square-wave voltammetry scan, (a) representative SWV for the forward, reverse and the difference in forward and the reverse current for a redox reaction.

A) No charging current: The effect of the charging current in SWV is minimal, as a result potential scan can be performed at higher scan rate and hence increases speed of the measurements. This makes measurement of faster reactions feasible by SWV.

B) Sensitivity: SWV is almost 1000 times more sensitive than cyclic voltammetry. Thus, this method can be a valuable tool for the measurement of trace metals and biological samples.

C) Broader dynamic range: Due to the small effect of the background or charging current SWV has a broader dynamic range of electrochemical determination.

2.14 Electrochemical immunoassays

Square-wave voltammetric (SWV) measurements were done using a PARSTAT 2273 (Princeton Applied Research, Oak Ridge, TN). The optimal parameters for the SWV were obtained from a series of experiments conducted by varying pulse width, pulse height and step height used in the square wave voltammetric analysis of a p-aminophenol standard solution. The best parameters determined for the square-wave voltammetric measurement of the oxidation of p-aminophenol were: pulse height 50 mV, pulse width 0.2 sec, and step height 2 mV. The potential was scanned from -0.1 V to 0.4 V at a rate of 5.0 mV sec^{-1}.

A Michaelis-Menten kinetics study was performed by incubating conjugate modified NPG wires with several concentrations of p-aminophenyl phosphate, and measuring the square wave voltammetric peak current at each concentrations of substrate. In the direct immunoassay, the peak current for p-aminophenol oxidation on each wire was measured before incubating with antigen and again after incubating with antigen. The incubation period with antigen used was 2 hours and was carried out in glycine buffer (pH 9, 100 mM). The substrate, p-aminophenyl phosphate (p-APP) was introduced via micropipette into the stirred solution (argon degassed) containing the MAb-ALP conjugate modified NPG covered Au wires and allowed to react for a period of 30 minutes prior to conducting the potential scan. Each measurement on each wire was repeated three times. The difference in peak current (i_p (before incubation) – i_p (after

incubation)) was plotted vs. the antigen concentration to obtain the response plots for PSA and CEA.

For the competitive immunoassay, the NPG covered gold wire electrodes modified with immobilized PSA or CEA antigens were allowed to compete for the MAb-ALP conjugate in solution with variable concentrations of free antigen in solution for 24 hours in PBS buffer (10 mM, pH 7.4). The concentration of MAb-ALP conjugate used was 100 ng mL^{-1}. After incubation with conjugate, the NPG coated wires with bound conjugate were incubated in 0.25 mM p-APP in glycine buffer (pH 9.0, 100 mM) for 30 minutes and then a square wave voltammetry scan was conducted. MAb-ALP conjugate solution of concentration 100 ng mL^{-1} was chosen, because a much less significant signal was obtained using 50 ng mL^{-1}, and 200 ng mL^{-1} did not produce a significantly different result than 100 ng mL^{-1}. p-APP concentrations less than 100 nM were not enough to obtain satisfactory currents, and thus 250 μM was chose as a working substrate concentration for the immunoassay.

2.15 Enzyme-linked lectinsorbant assay

Enzyme-linked lectinsorbant assays were performed in three different formats. In the direct kinetic lectinsorbant assay, Con A-ALP conjugate was immobilized on the LPA modified NPG surface. Enzyme activity was determined as above by studying Michaelis-Menten kinetics at different substrate concentrations. Traditional type ELLSA was performed by immobilization of glycoprotein on the NPG surface and allowing it to bind to the ConA-ALP conjugate. Amount of conjugate bound to the surface was determined by enzymatic activity of ALP with 1 mM p-APP. Kinetic ELLSA was performed by determining enzymatic activity of ALP before and after glycoprotein

binding to the Con A. As in the immunoassay, initial and final peak currents in SWV were determined and plotted against the glycoprotein concentrations. Competitive ELLSA was analogous to the traditional type ELLSA except surface bound glycoprotein was allowed to compete for the conjugate with free glycoprotein in solution. Inhibition studies with Me-D-Man were performed by incubating Con A-ALP conjugate immobilized on NPG with fixed concentration of glycoproteins and a variable concentration of Me-D-Man. IC_{50} values were determined by fitting data to the competitive model equation using the Graphpad prism software.

2.16 BCA Assay

The concentration of the MAb-ALP conjugate solution before and after incubation with the NHS-activated lipoic acid modified NPG wires was determined using the BCA (bicinchoninic acid) assay. Reagent A: 1 g sodium bicinchoninate (BCA), 2 g sodium carbonate, 0.16 g sodium tartrate, 0.4 g sodium hydroxide, and 0.95 g sodium bicarbonate were dissolved into 100 mL Milli-Q water and the pH was then adjusted to 11.25 with 10 M sodium hydroxide. Reagent B: 0.4 g cupric sulfate was dissolved in 10 mL Milli-Q water. A standard working solution was prepared by mixing 100 mL of reagent A and 2 mL of reagent B. Standard BSA or Con A samples containing 0.2 to 50 μg protein were prepared. 2500 μL of standard working reagent was combined with 500 μL protein and incubated at 60 ºC for 30 min. Samples were cooled and absorbance measurement was done at 562 nm using a Cary-50 uv-visible spectrophotometer. A similar procedure was applied for the sample proteins (PSA/CEA conjugates and antigens alone) as well.

2.17 Determination of molecular footprint on the NPG surface

Surface coverage of protein on the NPG surface was estimated based on the size of the protein, i. e. the maximum and minimum possible surface area of the proteins. Protein molecules were confined in a bound box in JMOL and the dimensions of each bound box was obtained. Maximum surface area was determined from the larger dimensions of the box and lowest possible surface area was estimated from the smaller values of the dimensions of the box. Comparison of the theoretical and the observed molecules per cm^2 gave the percentage coverage of protein on the NPG surface.

CHAPTER III

ELECTROCHEMICAL CHARATERIZATION OF SELF-ASSEMBLED MONOLAYERS OF ALKANETHIOLS ON NPG

3.1 Introduction

Gold nanostructures are at the center of research in nanoscience and nanotechnology. Gold nanostructures with increased surface area, excellent thermal and electrical conductivity and plasmonic properties have enormous potential applications in sensitive bioanalytical devices, nanoelectronics, catalysis, etc.[324, 325] Functionalized gold nanostructures are particularly interesting for these and many other applications. Gold surfaces are easy to functionalize because the moderately strong gold-sulfur interaction provides an convenient way to prepare desired functional interfaces using alkanethiols bearing the needed terminal groups [326]. Even though there have been studies describing the application of gold nanostructures to immobilize proteins by conjugation to activated alkanethiol molecules, information on the electrochemical and structural properties of SAMs on such rough surfaces is limited [35, 58].

Nanoporous gold (NPG) is a nanostructured material with a very high surface to volume ratio which could potentially increase the sensitivity of chemical and biological sensors, and is useful also for many electrocatalytic applications. It has been reported that alkanethiol SAMs on a surface comprised of Au columns of 20-30 nm diameter and 400-500 nm in height were stable for many more weeks than on standard mostly Au (111) surfaces due to strong gold-sulfur interactions at kinks and defects [327]. Nanoporous

gold surfaces display regions of both positive and negative curvature that very likely can affect the organization and stability of alkanethiol SAMs relative to what it would be on a relatively smooth polycrystalline gold surface. Most of the molecules in an SAM on NPG will be present on regions of positive curvature, and thus it is possible that additional stabilization may be gained. The NPG ligament surfaces will have regions of both positive and negative curvature (near where the ligaments are interconnected, or where they may randomly bend) and hence are intrinsically more complex than the surfaces of gold nanoparticles or nanorods, which only possess regions of positive curvature. Surface curvature creates a significant difference in the properties of adsorbates on the surface. Literature reports show pKa, redox potential and other properties of immobilized molecules being affected due to the curved surfaces of gold nanoparticles [328, 329]. On a positive surface curvature region, molecules are closer near the surface and separated at the top as a result the available surface for the tail group is larger compared to that of the head group [329]. On the other hand, molecular orientation on the negative surface curvature is opposite, tail groups are brought closer together and the head groups are spaced further apart. Structural effects due to curvature will become more prevalent as the ligament diameter decreases. Generally, for NPG, the average ligament diameter and average pore dimensions are equivalent [330]. The structure of SAMs on NPG could be closely related to that of SAMs on gold nanoparticles or nanorods, except that the curvature of NPG is more varied across the structure. The surface curvature may affect the orientation of thiols and especially the spacing between terminal functional groups [329]. Thus, the arrangement of alkanethiol molecules on the NPG surface can be imagined as being different from that on either flat gold or gold nanoparticle surfaces.

Thus, characterization of the properties of SAMs on NPG is crucial for applications in electroanalytical chemistry. Herein, we have applied the simple methodology of NPG preparation based on the electrodeposition of an alloy of gold and silver and then dealloying it by selective leaching of silver from the alloy in concentrated acid. The NPG is then utilized for the formation of self-assembled monolayers of different chain length alkanethiols and their effect on the interfacial properties is studied by electrochemical impedance spectroscopy (EIS) and cyclic voltammetry (CV). The effects of using alkanethiols with different terminal functional groups are also studied. Porous electrodes with their high surface to volume ratio are at the center of electrocatalysis because the increase in surface area decreases the reaction overpotential and also increases the intrinsic electrocatalytic activity [331]. Nanoporous materials reach the highest practically attainable surface areas and are important materials for supercapacitors for energy storage [332]. NPG is a nanomaterial with bicontinuous channels of interconnected pores and ligaments. Pores and ligaments are generally between ten nanometers and a few hundreds of nanometers in diameter [333]. Surface features and pore sizes of NPG can be tuned by changing the dealloying conditions or by applying thermal annealing treatments [330, 334, 335]. Fujita et al. have proposed that the three-dimensional surface of nanoporous gold is quasi-periodic and has been shown to have on average a zero surface curvature, even though the local curvature has both positive and negative values [336]. NPG with high surface to volume ratio, inertness to general laboratory conditions, and capability of serving as a support for the formation of SAMs of alkanethiols has made it an interesting material for life science research [337]. NPG has been applied in the development of chemical sensors [39, 52], biosensors [54, 55], for

the immobilization of proteins [79], immunoassays [6, 58, 338], catalysis [50, 339], fuel cells [340] etc. NPG is generally prepared by selectively leaching less noble metals either electrochemically [28] or by dealloying in nitric acid solution [3, 22], from an alloy of gold and other metals such as silver, copper, zinc, or others. The current trend of research shows that NPG is being highly utilized for immobilization of biomolecules either by direct adsorption [79, 341, 342] or via covalent attachment to the SAM [35, 343]. Covalent attachment to the SAM is more attractive because it reduces protein leaching from the surface [344].

SAMS of alkanethiols on flat gold have been extensively characterized [8, 326, 345-347]. They are found to form well-packed molecular assemblies [85]. The structural integrity of SAMs on gold surfaces of varying but limited roughness has also been studied [348]. Even though alkanethiol molecules form well-packed monolayers, the defects in SAMs are universal because of the defects in the underlying surface or those produced during SAM formation and handling [308, 347, 349]. These defects have been classified into two types: pinhole defects, i.e. small disc shaped electroactive spots on the surface uniformly scattered throughout the SAM, and collapsed sites, which are formed at the grain boundaries, kinks and edges and at the defect sites on the surface of gold crystals [350]. Creager et al. have found that the microscopic surface roughness, i.e. the roughness on the scale of the adsorbate, is critical in creating defects in the SAM, and that the macroscopic surface roughness is less important [351]. NPG with its ligaments and pores almost all being greater than 10 nm is highly rough on the macroscopic scale, and the distribution and nature of microscopic defects may be different than on macroscopically flat gold surfaces. Even though there have been some studies on the

formation of SAMs on NPG, the process has not been fully characterized and much remains to be learned [352]. NPG is reported to retain the initial crystallographic orientation as that of the alloy and has been reported to be mostly the Au(111) crystal structure, but with smaller contributions from other faces such as Au(200), Au(220), Au(222), and Au(311) [39, 353-355]. The characteristics of SAMs formed on different gold surfaces with varying roughness such as bulk gold, Au on mica, Au on annealed mica, flat gold, Au on glass with a Ti adhesion layer, and Au on 3-mercaptopropyltrimethoxysilane modified glass were studied by STM and electrochemical studies. STM is a widely applied tool for the microscopic characterization of SAMs on gold surface, and gives information about the molecular packing patterns on the surface and features associated with vacancies and defects in the SAM. Despite being a widely employed technique to assess the structure of SAMs on the surfaces, Goodding et al. have shown that STM is less sensitive to predict the differences in SAMs formed by microcontact printing and solution self-assembly [356]. Electrochemical methods are highly appropriate for characterizing macroscopic properties and integrities of SAMs. The studies on the selected gold surfaces showed differences in SAM formation depending on the defects and grain sizes of the gold. Atomically flat surfaces and those with less defects were found to support more ordered and intact SAMs, compared to those surfaces with a larger number of defects and smaller grains [356]. There are various reports on the domain sizes of alkanethiols on gold, as an example the domain sizes of as prepared dodecanethiol on Au(111) is reported to be 6.5 nm, thus the sizes of NPG ligaments are big enough for the formation of stable domains [357]. It is reasonable to assume a difference in orientation of alkanethiols at the edges of

the ligaments but most of the ligament surfaces are not curved sharply and are parts of a single grain, as a result continuous domain formation along ligaments should also be possible. There are several controversial reports on the grain sizes of NPG. In one report, it has been shown that the crystal lattice orientation of the original alloy is retained even after dealloying with a very small amount of high angle grain boundaries of 50 μm-100 μm grain size [49]. But in another TEM study, electrochemically formed gold foams have been shown to contain 40% of the surface with multiple grain boundaries [358]. HRTEM studies of the 100 nm ligaments of a compressed foam showed average grains of 5 nm in diameter [359].

The objectives of the present study are to electrochemically characterize the integrity of alkanethiol SAMs on NPG and compare the results with those for SAMs on flat gold. One recent study concerning EIS studies of alkanethiol SAMs alone on NPG from octanethiol to tetradecanethiol (C8, C10, C12, and C14 chain lengths) reported that the charge transfer resistance changed little with chain length on NPG but showed a steady increase on flat gold [360]. In the reported study, the EIS measurements were conducted in 0.1 M sulfuric acid using a single redox state of ferricyanide as probe ($Fe(CN)_6^{3-}$). In the present study, we examine SAMs on NPG in phosphate buffered saline (pH 7.4) for even chain length alkanethiols from butanethiol to octadecanethiol and also examine a number of SAMs presenting polar terminal groups. The electrochemical behavior of SAMs on gold surfaces has been reported to be dependent on the chain length of the alkanethiols as well as on the nature of the **ω**-functional groups. The integrity and defects in these SAM are studied by electrochemical impedance spectroscopy as well as by cyclic voltammetry. 8-Mercapto-1-octanol and 11-mercapto-1-undecanol were chosen

as molecules with a smaller but polar terminal group, and mercaptoundecanoic acid was chosen as an example of a molecule with a relatively larger polar terminal group, in order to study the effect of functional groups on the behavior of SAM on rough surface. As stated earlier the surface curvature of the NPG has a significant impact on the molecular orientation which increases as the size of the head group is increased. The negative surface curvature brings two ends of the molecules closer whereas the positive curvature brings head groups closer with the opposite effect on the other end. These polar molecules with the terminal bulky functional groups most probably form a disordered SAM on the NPG surface due to similar reasons.

3.2 Results and discussions

3.2.1 Surface and electrochemical characterization of bare NPG and bare gold wire

Surface characterization of the NPG and gold wires was done by scanning electron microscopy. SEM micrographs of flat and nanoporous gold wires are shown in **Figure 3.1**. NPG coated Au wire shows a random distribution of nanometer sized ligaments and nanopores, as is characteristic of a nanoporous gold surface. Even though the size range of these pores varies from ten to a few hundreds of nanometers, the majority of the pores are >10 nm and very few pores are >100 nm or <10 nm. Most of the ligaments are fairly large and at least greater than 10 nm. Most of pores and ligaments are 30-50 nm in diameter.

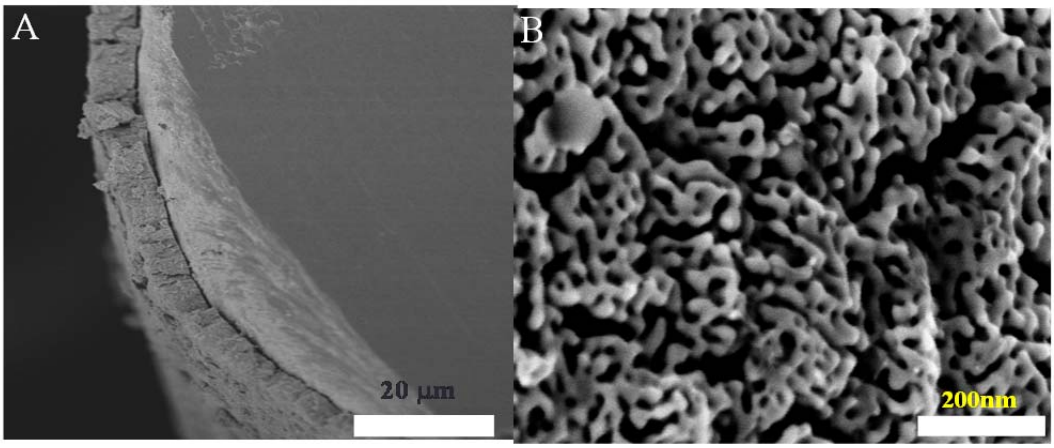

Figure 3.1. Scanning electron micrograph of NPG thin film on a gold wire. a) Cross sectional view of the nanoporous gold covered gold wires (magnification 1 kX) and b) topographic view of the nanoporous gold at higher magnification (100 kx).

Electrochemical characterization of NPG and gold wire surfaces was done by cyclic voltammetry and electrochemical impedance spectroscopy (EIS). Surface area estimation was done by the gold oxide stripping method in 0.5 M H_2SO_4. **Figure 3.2** shows the cyclic voltammogram for NPG coated Au wire and for Au wire alone recorded in 0.5 M H_2SO_4 at a scan rate of 100 mV sec^{-1}. The charge passed during the gold oxide reduction was measured by integrating the oxide reduction peak and the charge in μC was then divided by the conversion factor 450 μC cm^{-2} [308, 361, 362]. The surface area of a typical NPG coated Au wire by this method was found to be 12±1.3 cm^2 and that of a gold wire alone was found to be 0.040 cm^2; thus, the NPG coated Au wires have about 300 times higher surface area. The geometric surface area of gold wire and the surface area of the underlying gold in NPG coated wire is 0.032 cm^2, corresponding to a roughness factor of 1.25.

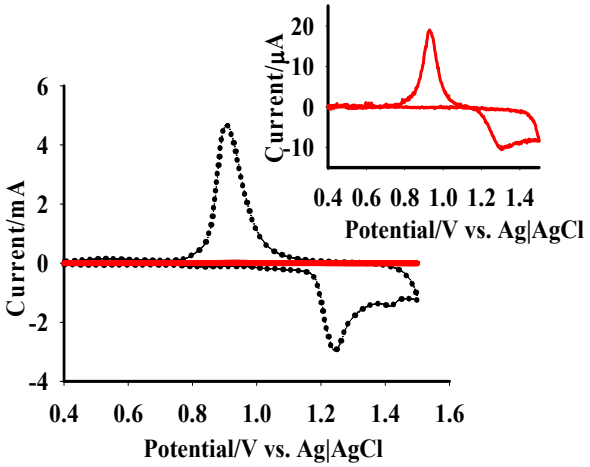

Figure 3.2. CV data for NPG and gold wire. Cyclic voltammograms of bare nanoporous gold (dotted line) and bared gold wire (solid line) electrodes. CV scans were performed in 0.5 M H_2SO_4 at a scan rate of 100 mV sec^{-1} and surface area was determined by integrating oxide reduction peak.

Bare NPG and bare gold wires were characterized by electrochemical impedance spectroscopy. Electrochemical impedance spectroscopy is a sensitive technique where a small sinusoidal potential perturbation is applied to the system at equilibrium and the response current is measured. The physical characteristic of the interface is then modeled to an equivalent circuit and respective values for the characteristic parameters are obtained [50]. A Nyquist plot for the bare gold wire **(Figure 3.3a)** shows a small semicircle at higher frequencies followed by a straight line at the lower frequency region, characteristic of the bare gold surface having a small value of charge transfer resistance, as reported in the literature [363]. The Nyquist plot of NPG **(Figure 3.3a**) on the other hand doesn't show a clear semicircle, and instead shows a depressed semicircle that

smoothly evolves to an almost straight line with a 45º slope versus the x-axis attributed to the Warburg impedance. This is the characteristic of a porous electrode and similar behavior has been reported for NPG prepared by other methods [331]. The pore geometry, pore size and distribution in the porous electrode have a significant impact on the EIS data [364, 365]. Various mathematical models have been developed for modeling impedance data of porous electrodes [366-368]. The model developed by De Levie, commonly known as transmission line model, is the most frequently used model for EIS data [369]. Most of the porous electrodes have heterogeneous pore distribution with the wide variation in pore sizes and shapes and continuous models are frequently applied for these porous electrode. The application of the theoretical models in the EIS studies demands information on the complete picture of pore geometry, size and distribution which is not always available, and as a result average information is obtained from the simplified models [364]. The equivalent circuit applied in this study is shown in **Figure 2.1b.** This simplified model has been applied for the porous electrode in several studies. This is the modified Randles equivalent circuit which consists of solution resistance (Rs), double layer capacitance replaced by the constant phase element (CPE), charge transfer resistance (Rct) and the Warburg impedance (W). The accurate estimation of R_{ct} on the bare NPG surface was not done because the semicircle on the Nyquist plot that characterizes R_{ct} is not well defined.

The Bode phase angle plots (**Figure 3.3b**) also show distinct differences between NPG and flat gold. When an interface behaves more like a pure capacitor, the phase angle is near 90^{o}; whereas, the phase angle of a purely resistive interface will be 0^{o}. For unmodified flat gold, a broad peak in phase angle is seen with a maximum of about 36.5^{o}

near a frequency of 3.16 kHz followed by a gradual increase at lower frequencies. The Bode plot found for these unmodified Au electrodes resembles that reported by Pillay and co-workers, although their peak phase angle was near 47^{o} at a frequency closer to 1000 Hz [370]. The result is also similar to that reported by Mashazi [371]. Bode plots reported for bare gold have a range of variability in features, in that some reports show a higher frequency peak, and others do not. In the low frequency limit of 0.01 – 1.0 Hz, values reported include 52^{o} at 1 Hz [370], and near 80^{o} at 1 Hz [372], as compared to our value of near 29^{o} at 1 Hz. The presence of a peak at a higher frequency is attributed to a relaxation process occurring at the electrode-electrolyte interface [373]. The Bode phase plot appears to be highly sensitive to the conditions of the Au surface and the nature of the contacting electrolyte solution. For the NPG electrodes, the Bode phase plot shows a low phase angle at high frequencies that does not begin to increase significantly until around 100 Hz, and then reaches a maximum value of 58.3º near 582 mHz. In the low frequency limit, the NPG electrode has a much higher phase angle than flat gold which is consistent with the capacitive behavior associated with its porosity [374]. At higher frequency, the impedance is dominated by the solution resistance and the Bode phase plot shows phase angles closer to zero degrees, while at the intermediated frequencies, the contribution of the capacitive component and charge transfer resistance becomes prominent.

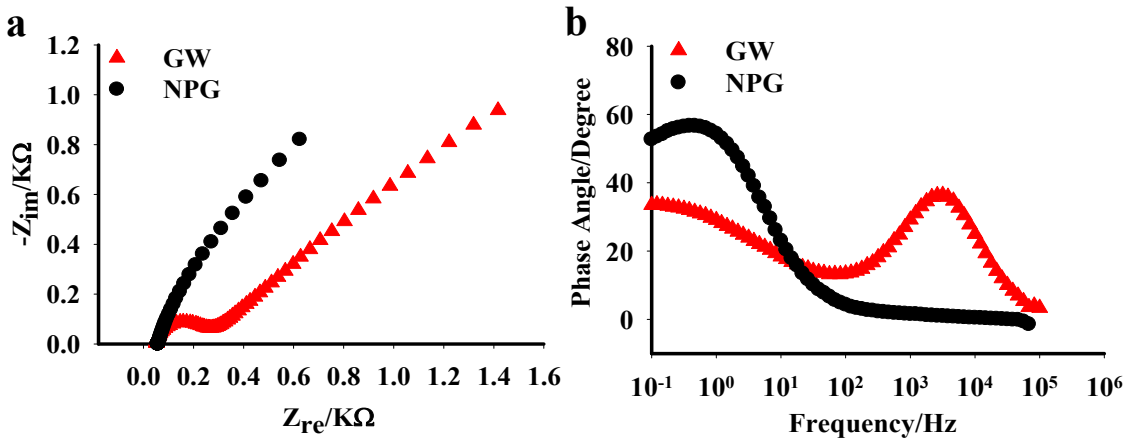

Figure 3.3. EIS characterization of NPG and gold wire electrodes. a) Nyquist plot for the bare gold wire (triangles) and NPG (circles). b) Bode phase plot for the gold wire (triangles) and NPG (circles).

3.2.2 Electrochemical characterization of the self-assembled monolayer of alkanethiols on NPG

3.2.2a Charge transfer resistance across different chain length alkanethiols on NPG and flat gold wires

Several other surface characterization techniques have been applied to characterize self-assembled monolayers, including ellipsometry for thickness [8], and infrared reflection absorption spectroscopy (IRRAS) for information on the orientation and crystallinity of the SAM [356]. Electrochemical techniques are well suited for the characterization of the microscopic properties of the interface and for the characterization of the extent of defects in SAM [363]. Given the rough and curved nature of the NPG surface, we used electrochemical techniques to characterize the structure of SAMs on NPG. The integrity and packing of the SAM on the substrate surface affects the electrochemical properties at the interface which is reflected in the double layer

capacitance and the heterogeneous electron transfer rate across the SAM in EIS studies. The extent of defects in SAM can easily be estimated by the relative ability of the SAM to hinder electron transfer across the interface. EIS has been widely used to characterized SAMs on the gold surface and is more sensitive and informative compared to other techniques such as CV or chronoamperometry because it is less affected by charging and background currents [310, 363]. Charge transfer resistance is a measure of the resistive behavior of the interface for the transfer of electrons to the metal surface from the metal solution interface. It has been reported for alkanethiol SAMs on polycrystalline gold surfaces that an increase in chain length increases the charge transfer resistance [363, 375]. NPG, with its high extent of surface curvature (both convex and concave), appears different in structure than either flat gold surfaces or the surfaces of electrodes modified with gold nanoparticles. Thus, it is interesting to determine how the charge transfer resistance varies with chain length on NPG versus on a flat gold surface; also, R_{ct} is an important parameter to compare the relative packing integrity and extent of defects in SAMs.

Figure 3.4 shows the representative Nyquist plots on NPG and GW for different chain length alkanethiols. We found that both the NPG and the gold wire surfaces showed an increase in charge transfer resistance, as manifested by an increase in the diameter of the observed semicircle, with the increase in chain length. The diameter of the semicircle increases with the increase in chain length for both the surfaces. For the smallest chain length alkanethiol in this study, butanethiol and hexanethiol, the low frequency linear region is prominent along with the semicircle on flat gold.

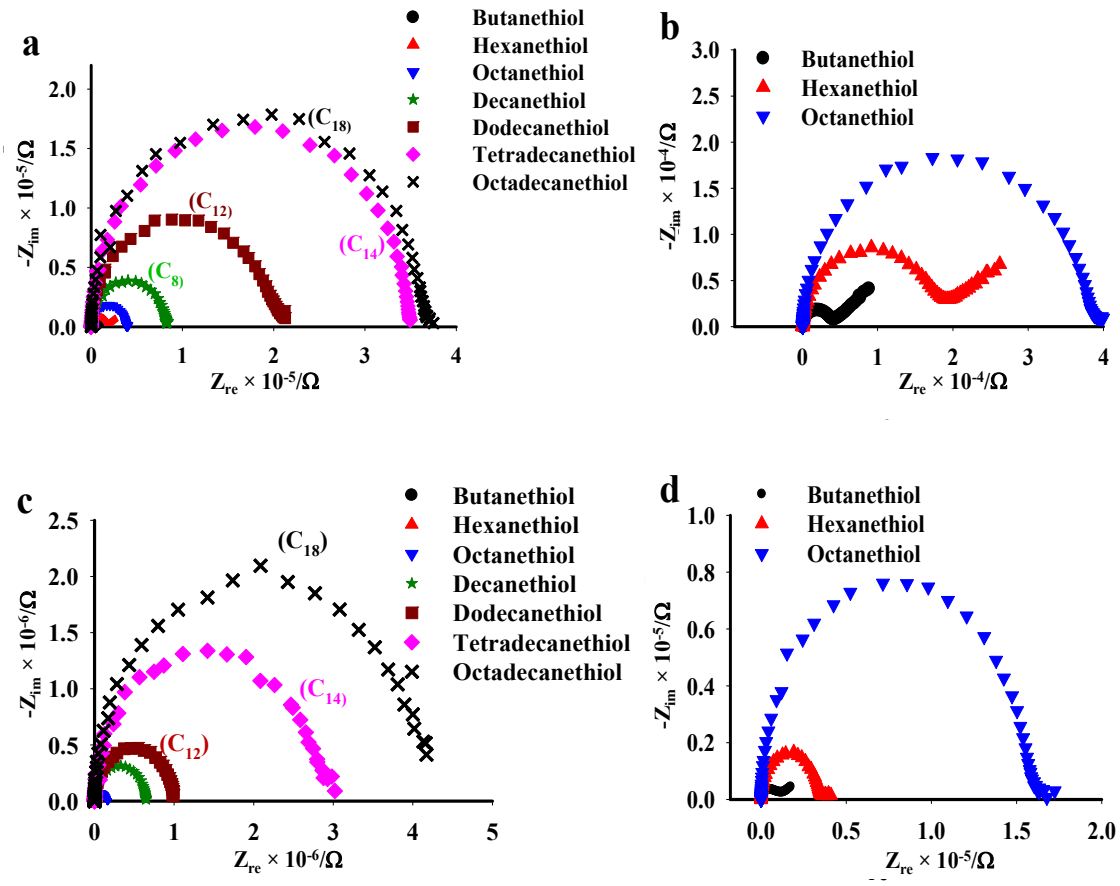

Figure 3.4. Nyquist plots for the SAM modified NPG and gold wires. a) Nyquist plot for alkanethiols ranging from 4 to 18 carbon chain length on gold wire. Butanethiol, hexanethiol and octanethiol SAM modified wires are shown in 3.4b for clarity. 3.4c and 3.4d are Nyquist plots for the alkanethiol modified NPG. Alkanethiols SAMs ranging from 4 to 18 carbon chains were prepared on NPG (3.4c). Butanethiol, hexanethiol and octanethiol modified wires are shown in 3.4d for clarity.

This straight line is a characteristic of Warburg impedance, representing diffusion of ions across the interface and hence provides evidence that the electron transfer process at the interface is not completely kinetically controlled, rather it is a mixed kinetic and diffusion controlled. This is an indication of a loosely packed SAM possible with defect

sites for efficient electron transfer. As the chain length increases, the straight line at lower frequency becomes less obvious and the overall Nyquist plot is dominated by the semicircle, characterizing a kinetically controlled electrochemical process at the interface. Hence a completely blocking interface with a SAM of greater integrity and blocking ability is created. In contrast, the low frequency linear region is much less evident for these SAMs on NPG, possibly attributed to restricted diffusion within pores [376].

Figure 3.5a shows the variation of R_{ct} with chain length for different alkanethiols on NPG and on flat gold. The R_{ct} value increases much more steeply with chain length on NPG than on flat gold. For the case of SAMs studied on flat or microscopically rough gold surfaces, the electrochemical properties and integrity of the SAM on the gold surface is dependent on the topography of the underlying surface, chain length related phenomenon like chain interlocking and van der Waals interactions, which increases with the increase in chain length, and the method of preparation [85]. Charge transfer resistance is the measure of the electrode kinetics and depends on the electrochemically active surface area of the electrode material and hence is a direct measurement of the defects and integrity of the SAM on the surface. The magnitude of R_{ct} is affected by the extent of defects like pinholes and collapsed sites as well as solvents trapped within the SAM [377, 378]. The SAMs formed on either surface display an increase in R_{ct} with increasing chain length of the alkanethiol. Values of R_{ct} for the different chain length alkanethiols SAMs on NPG are listed in **Table 3.1,** and values for the SAMs on flat gold are listed in **Table 3.2**. The observation that R_{ct} is much greater on the NPG electrode than on the flat gold electrode for the same alkanethiol chain length, and that this

difference appears to grow with chain length, suggests that effects of porosity and the increase in SAM ordering with chain length are both influencing the chain length dependence of R_{ct} for these SAMs on NPG. With the progressive decrease in the number of sites at which electron transfer can occur, as the SAM ordering increases with the chain length, the distance between such sites should increase. Within a porous structure, diffusion to these sites is restricted or anomalous, and this may result in a stronger increase in the R_{ct} values with chain length in an NPG electrode than on a flat Au surface towards which diffusion occurs in the normal linear manner.

Charge transfer resistance is related to electron transfer across the interface and hence calculation of the heterogeneous electron transfer rate constant by EIS has been widely applied. The standard procedures involve, fitting impedance data to an equivalent circuit model that represent the physical interface, in order to obtain R_{ct} from which apparent electron transfer rate constant can be calculated using equation (1). The apparent electron transfer rate constant for the SAM modified electrode has been calculated and used for the estimation of the extent of defects in the SAM [379-381].

Heterogeneous electron transfer rate constant across the interface can be obtained from the charge transfer resistance as follows,

$$R_{ct} = \frac{RT}{nFi_0} \tag{3.1}$$

$$i_0 = (1-\theta)Fk^0C \tag{3.2}$$

$$i_0 = Fk_{app}C \tag{3.3}$$

$$k_{app} = k^0(1-\theta) \tag{3.4}$$

$$k_{app} = \frac{RT}{n^2F^2R_{ct}C} \quad (3.5)$$

In the above equations, k^0 is the electron transfer rate constant across the bare metal surface and k_{app} is the electron transfer rate constant at the modified electrode surface, and other terms have their usual meanings.

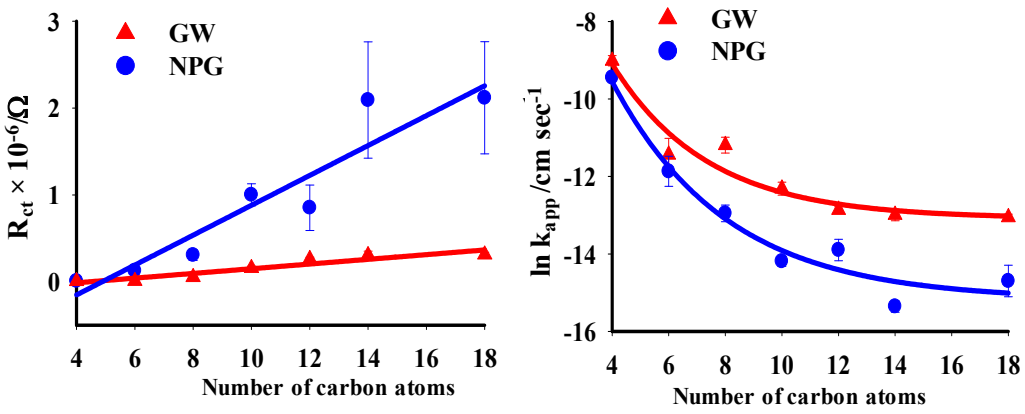

Figure 3.5. Electron transfer resistance at the interface. a) Charge transfer resistance vs. chain length on alkanethiols on NPG (circles) and on gold wires (triangles). Apparent electron transfer rate constant on the SAM modified NPG surface (circles) and gold wire (triangles).

Electron transfer across the blocking interface takes place through three major processes including non-adiabatic electron tunneling through the SAM, electron transfer across the pinhole defects where the electron transfer process is similar to that of the bare metallic surface and electron transfer across collapsed sites [378]. The heterogeneous electron transfer rate constant is a measure of the electron transfer kinetics across the interface and it increases with the increase in the number of defects in SAM. Several factors such as defects in the underlying substrate, kink edges, grain boundaries, trapped

solvents etc. cause such an increase in the electron transfer rate constant at SAM modified surfaces [350, 382].

The values of the apparent electron transfer rate constant for a polycrystalline flat gold wire modified with different alkanethiol length SAM are given in **Table 3.2,** these values are similar to the values reported in the literature [379, 383]. There is a huge drop in electron transfer rate constant at the polycrystalline gold electrode after formation of SAMs, from 0.03 cm sec^{-1} to the 10^{-6} range [384]. The magnitude of the drop in charge transfer resistance between butanethiol and hexanethiol is almost tenfold for both NPG and for the flat gold surface, while after hexanethiol the decrease with chain length is more gradual. As reported in the literature, the magnitude of the electron transfer rate constant decreases with the increase in chain length and magnitudes of R_{ct}. These values are close to the values reported in the literature for alkanethiol SAMs on polycrystalline gold surface [363, 375]. The values of the electron transfer rate constant decrease nonlinearly with chain length as if they are approaching limiting values when examined for the octadecanethiol SAMs, on either substrate. The decrease in electron transfer rate constant with chain length is due to the formation of progressively better ordered SAMs. The increased length of the alkanethiol increases the interaction between neighboring molecules and hence stabilizes the SAM [85]. Octadecanethiol, which has been reported in the literature to form pinhole-free SAMs, shows the lowest apparent rate constant on either surface and the dependence appears to be approaching a limiting value [385]. Shorter chain length alkanethiol SAMs have a relatively larger fraction of defects and thus much higher apparent electron transfer rate constants. The magnitude of the apparent

electron transfer rate constants for the SAM modified NPG electrodes (**Table 3.1**) are lower than those on the flat gold electrode.

Table 3.1. Summary of EIS data for SAM modified NPG electrodes

Alkanethiols (NPG)	CPE (FS^{n-1})	Exponent (n)	C_{dl} (F)	R_{ct} (Ω)	k_{app} ($cm\ sec^{-1}$)
Bare NPG	1.2×10^{-4}	0.81	1.33×10^{-4}	2192	---------
Butanethiol	3.17×10^{-7}	0.92	3.51×10^{-7}	8553	7.98×10^{-5}
Hexanethiol	7.91×10^{-8}	0.98	8.21×10^{-8}	126140	9.26×10^{-6}
Octanethiol	5.30×10^{-8}	0.99	5.47×10^{-8}	307200	2.60×10^{-6}
Decanethiol	4.62×10^{-8}	0.99	4.77×10^{-8}	1000800	7.11×10^{-7}
Dodecanethiol	3.69×10^{-8}	0.98	3.85×10^{-8}	852000	1.05×10^{-6}
Tetradecanethiol	3.42×10^{-8}	0.99	3.52×10^{-8}	2092000	2.21×10^{-7}
Octadecanethiol	2.44×10^{-8}	0.99	2.35×10^{-8}	2117200	5.84×10^{-7}

Table 3.2. Summary of EIS data for SAM modified gold wire electrode

Alkanethiols (FG)	CPE (FS^{n-1})	Exponent (n)	C_{dl} (F)	R_{ct} (Ω)	k_{app} ($cm\ sec^{-1}$)
Bare GW	2.3×10^{-6}	0.88	2.42×10^{-6}	242.7	---------
Butanethiol	2.40×10^{-7}	0.97	2.52×10^{-7}	5657	1.26×10^{-4}
Hexanethiol	1.36×10^{-7}	0.98	1.43×10^{-7}	7434	1.21×10^{-5}
Octanethiol	1.07×10^{-7}	0.98	1.11×10^{-7}	52140	1.51×10^{-5}
Decanethiol	7.13×10^{-8}	0.99	7.41×10^{-8}	156140	4.76×10^{-6}
Dodecanethiol	5.32×10^{-8}	0.99	5.51×10^{-8}	261000	2.63×10^{-6}
Tetradecanethiol	4.79×10^{-8}	0.99	4.94×10^{-8}	306000	2.38×10^{-6}
Octadecanethiol	3.80×10^{-8}	0.99	3.92×10^{-8}	313000	2.15×10^{-6}

Figure 3.6 shows the plot of $\ln(k_{app})$ vs. chain length for different chain length alkanethiols on NPG and on gold wire. The exponential decrease in electron transfer rate constant towards a limiting value with the increase in chain length has been observed for the alkanethiol SAM on gold surfaces [375]. The trend versus chain length is similar for

both NPG and gold wire. The overall lower values of the rate constants on NPG versus flat gold are related to the higher values of R_{ct} for the longer chain length SAMs on NPG, and should also be related to the combined effects of improved SAM integrity and diffusional restrictions, as accounted for by the employed circuit model.

3.2.2b Double layer capacitance for different chain length alkanethiols on NPG and gold wires

Even though NPG has been reported to behave to some extent as an ideal capacitor under potential sweep and potential step conditions, NPG under study shows frequency dispersion and hence the ideal double layer capacitor in the equivalent circuit model has been replaced by the constant phase element [386]. A constant phase element is universally present when working with solid and rough electrodes. This behavior is observed for ideally polarized electrodes in the presence of a Faradaic reaction [387]. There are basically two types of explanations for this capacitive dispersion, the most accepted explanation is due to the microscopic roughness of the electrode which causes variation in solution resistance along the surface and the capacitive and resistive terms become inseparable. Another explanation assumes capacitive dispersion to be purely interfacial and unrelated to the solution resistance [388]. EIS data in our study fit better to the use of the constant phase element rather than to a parallel plate capacitor. Impedance of a constant phase element is given in equation 1.

$$Z(\omega) = \frac{1}{Q}(j\omega)^{-n} \qquad (3.6)$$

Where, $j = \sqrt{-1}$, $0<n<1$ and Q is the quantity related to double layer capacitance with unit of FS^{n-1}. When n = 1, it is purely capacitive and when n = 0, it is a pure resistor. Usually for a rough electrode, the value of n is less than 1 but there is no correlation

between the exponent and the roughness of the surface [389]. Capacitance was calculated from CPE values using the relation given in equation (3.2) [390, 391] , where R_s, n and R_{ct} have their usual meanings.

$$Q = C_{dl}^{n} [R_s^{-1} + R_{ct}^{-1}]^{1-n} \quad (3.7)$$

Even though the characteristic of the bare NPG is somehow different from that of the bare gold surface there is a significant similarity after surface modification with the SAM. It has been reported that the interfacial CPE can be regarded as a double layer capacitance when the value of n is greater than 0.98 [392]. For all the SAMs with greater than six carbons in the alkanethiol, both for NPG and gold wire the value of n is always more than 0.98. Thus, the behavior of the interface will be considered as a double layer capacitor for the following discussions and for the estimation of the effective thickness of alkanethiol molecules at the interface. Double layer capacitance provides valuable information on the interface and the thickness of the interface which can be estimated from the capacitance obtained from EIS studies as discussed below. The Helmoltz electrical double layer model has been widely applied to SAM modified gold surfaces for the characterization of the interface and for the calculation of effective thickness of the monolayers at the interface, assuming the electrical interface can be represented as a parallel plate capacitor separated at a certain distance by the alkanethiols on the metal surface. Thus, alkanethiol molecules with the appropriate chain length at the interface behave as a dielectric material with the dielectric constant similar to that of polyethylene [382]. EIS provides a more sensitive and accurate estimation of the double layer parameters compared to those obtained from CV or chronoamperometry data [85].

Double layer capacitance values for a flat gold surface and nanoporous gold surface of similar geometric area, but different true surface area, are given in **Table 3.2 and Table 3.1,** respectively. The capacitance value for a bare gold surface is comparable with the literature reports, but the capacitance for NPG is slightly higher than that of the flat surface, but within the limit of values reported for a metal surface. Higher values of capacitance have been reported for the gold surface and the adsorption of hydroxide ions leads to increased capacitance at the interface. Double layer capacitance of the NPG electrodes before and after modification with SAMs was also compared for both flat gold and NPG. Double layer capacitance was found to decrease after SAM formation and this drop is similar to the values reported for SAMs on polycrystalline gold surfaces [382].

Figure 3.6a shows the plot of the reciprocal of double layer capacitance vs. chain length for NPG and also for flat gold wire electrodes. Double layer capacitance was converted from the CPE value obtained by fitting EIS data to the equivalent circuit mentioned above. Even though the value of C_{dl} is not directly comparable, the approximate estimation and relative comparison can be made having both the constant phase element exponent and CPE value on hand.

The CPE exponent values for the modified electrodes are given in **Table 3.1** and in **Table 3.2**. The interesting observation is that the n value for the same electrode increased after SAM formation compared to the value for the bare electrode. The magnitude of n is close to 1; hence, the interface looks more like an ideal capacitor after surface modification. The plot shows that there is a significant difference in the interfacial capacitance and the magnitude of CPE exponent for small chain alkanethiols ($n<6$) but with the increase in chain length ($n>6$) the interface becomes more ideal and

the effect of the roughness of the interface is mitigated to some extent. For the longer alkanethiols modified NPG and gold wires, the CPE value is fairly similar which is an indication that the amount of bare and exposed metal surface drops after SAM formation with a longer chain alkanethiols but it is still significant for the short chain alkanethiols. For alkanethiols longer than octanethiol, the n value is close to that of an ideal capacitor (n=1).

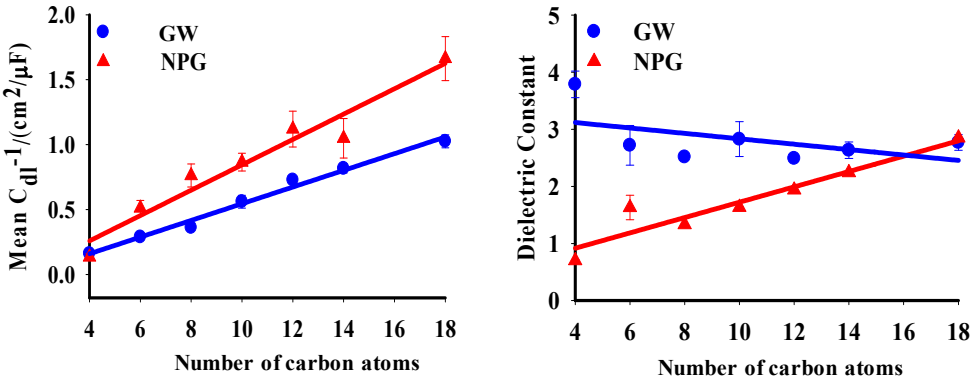

Figure 3.6. Double layer capacitance vs. chain length of SAM on NPG and gold wire. EIS measurements were done on SAM modified NPG (triangles) and gold wire (circles) with 5 mM each of $K_3[Fe(CN)_6]$ and $K_4[Fe(CN)_6]$. Dielectric constant vs. chain length for the same wires as in 3.6a.

It has been reported that when the value of n = 0.98, the interface can be represented as an ideal capacitor and the CPE value can be accepted as C_{dl}. For the smallest alkanethiol in this study, butanethiol, the CPE exponent n is lowest on NPG and suddenly rises after hexanethiol so the effect of two carbons is also dramatic to create a more regular interface and ordered SAM of alkanethiols on the highly rough interface. Even though the value of C_{dl} is slightly higher for SAM modified NPG, compared to that

of SAM modified gold wire, at a particular chain length of alkanethiols, the inverse of the C_{dl} vs. chain length plot shows a similar linearly increasing trend for both NPG and on GW. The slope of the plot on NPG is 0.098 and for on flat gold it is 0.06, which is close to the value reported in the literature for Au(111) surfaces [382]. The intercept of the plots are -0.13 and -0.097 for the data on NPG and on flat gold, respectively. There are reports showing the intercept variation depending upon the electrolyte so our data for the gold wire is in agreement with the reports for polycrystalline gold surfaces [382].

An approximate determination of the dielectric constant of the monolayer can be made by assuming the total capacitance to be a sum of the monolayer capacitance and the double layer capacitance at the bare spots [393, 394].

$$C_{tot} = C_m + C_{dl} = C_m(\theta) + C_{Au}(1-\theta) \quad (3.8)$$

In the above equation, C_{tot} is the measured capacitance at SAM modified electrode, C_m the capacitance of the SAM, C_{dl} the double layer capacitance at the bare spots, i.e. at pinholes and on any solvent exposed gold surface, and C_{Au} is the capacitance at the bare gold surface. When the surface coverage is very high and close to 100% as with the longer chain length alkanethiols, the total capacitance can be assumed to be equal to the capacitance of the monolayer [382]. The dielectric permittivity of the monolayer can be calculated from the monolayer capacitance by using the relation,

$$C_m = \frac{\varepsilon_m \varepsilon_0}{d} \quad (3.9)$$

Here in equation (3.4), ε_m is the permittivity of the SAM, $\varepsilon_0 = 8.85 \times 10^{-12}$ C^2 N^{-1} m^{-2} is the permittivity of the free space, and 'd' the thickness of the monolayer. In this study,

the thickness is assumed to be equal to the length of alkanethiol molecules and the effective thickness of the molecules reported on polycrystalline gold surfaces [363]. The literature reported value of ε_m for alkanethiols is 2- 3 [382]. **Figure 3.6b** shows a plot of the dielectric constant of the interface for different chain lengths of alkanethiols on NPG and on flat gold. The value of the dielectric constant (ε_m) for SAMs on gold wire is consistent with the literature report for the alkanethiols SAMs on polycrystalline gold [382]. The higher value of the ε_m for the butanethiol SAM on flat gold might be because of the short chain length of the thiol which doesn't form a very well ordered and completely resistive monolayer and hence the presence of relatively larger solvent accessible surface makes the overall SAM more hydrophilic. Hence, this approximation of the dielectric permittivity might not be completely true for the loosely packed SAMs. However, for alkanethiols longer than hexanethiol, the ε_m value is almost constant. On the other hand, the ε_m value is smaller for shorter chain length alkanethiols on NPG and reaches a value equal to that on the gold wire, for longer chain length alkanethiols. The ε_m value smaller than 1 might be because of the error associated with the approximation of chain length of alkanethiols and the presence of a larger surface exposed to the solution. The effective thickness of the double layer might be less than the chain length of the alkanethiol especially in case of NPG. This type of behavior of SAM has been reported in the literature by Rubinstein et al. where they found that the ε_m of Au-ATP was 0.52; they interpreted this due to the error associated with the estimated effective thickness of SAM on the surface [393]. With the increase in thickness of the interface, the double layer is more uniform and the Helmholtz model of a parallel plate capacitor for the interface is applicable for NPG as well. The value of ε_m for longer chain length

alkanethiols is close to the value for ε_m reported for these SAMs on polycrystalline gold [375].

3.2.3 Bode plots for the different chain length alkanethiols on NPG and GW

Nyquist plots are the most common and favorite methods of electrochemical impedance spectroscopic data presentation but they do not provide a complete picture of the experiment as no information on the phase angle as a function of the frequencies of the measurements are presented. Bode plots, either as Bode phase plots or as plots of |Z| versus log (ω), are alternate representations of the EIS data. **Figure 3.7** shows Bode phase plots for different chain length alkanethiol SAM modified NPG. At high frequencies, the phase angle is smaller and starts to rise, and at intermediate frequency, the phase angle reaches a maximum and again starts to fall again. The smallest phase angle was observed for the smallest chain length alkanethiol, which starts to increase with the increase in chain length of the alkanethiols. At higher chain length of the alkanethiols, the phase angle starts to reach 90^0 (C18= 88^0). A similar Bode phase plot for the gold wire electrodes is given in **Figure 3.8**. Trend of phase angle vs. the chain length of alkanethiols is similar to that on NPG, but the magnitude of phase angle is smaller than for every chain length of alkanethiols on GW. One other difference in the nature of these plots on NPG and GW is that the phase angle plateau is relatively broader on the NPG surface compared to that of the GW. The general dependence of the phase angle with frequency shown in these figures resembles that reported in Faradaic EIS studies of alkanethiol related SAMs on flat gold surface [395]. In the frequency range where the phase angle is closest to 90^o, the SAM is behaving like a capacitor, and as the angle becomes closer to 0^o, it is behaving more like a resistor.

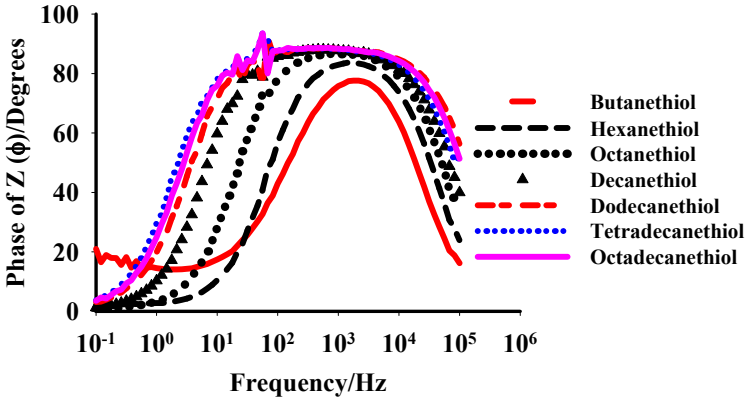

Figure 3.7. Bode phase plots for alkanethiol SAM modified NPG electrodes. NPG wires were modified with alkanethiols of varying even chain length from butanethiol (C4) to octadecanethiol (C18).

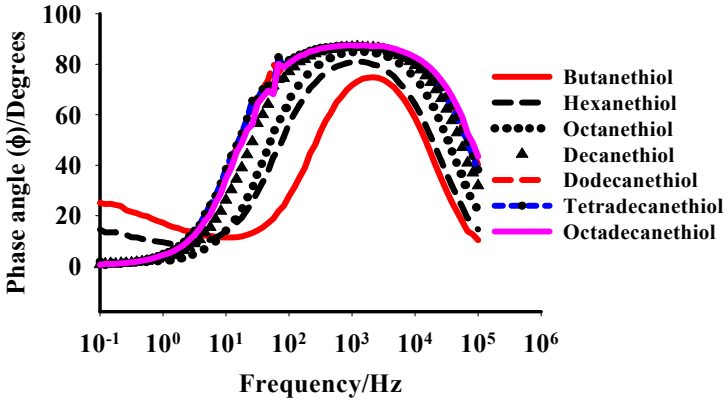

Figure 3.8. Bode phase plots for alkanethiol SAM modified GW electrodes. GWs were modified with alkanethiols of varying even chain length from butanethiol (C4) to octadecanethiol (C18).

3.2.4 Reductive desorption and surface coverage of the SAM on NPG and gold wires

Figure 3.9 shows the cyclic voltammogram for the reductive desorption of different chain length of alkanethiols on NPG and on GW, only selected curves are shown for clarity purpose. The reductive desorption studies were carried out to calculate the surface coverage of thiols on NPG and on GW. The reductive desorption curves show the increase in desorption potential with the increase in chain length for both NPG and for the GW.

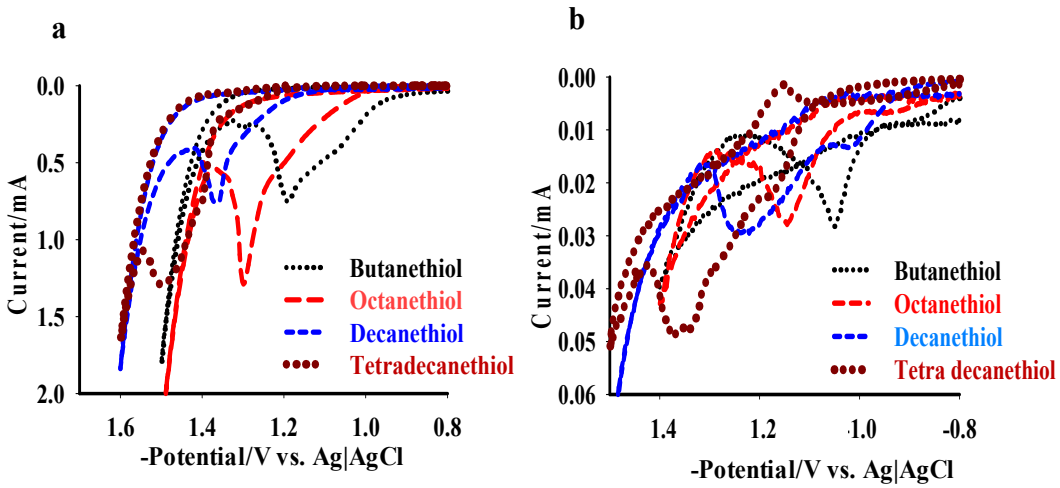

Figure 3.9. Reductive desorption of different alkanethiols on NPG and gold wire. Cyclic voltammogram for the reductive desorption of alkanethiols on a) NPG and b) gold wire. CV scans were performed in 0.5 M KOH solution at a scan rate of 500 mV sec^{-1} for gold wire, and at 20 mV sec^{-1} for NPG.

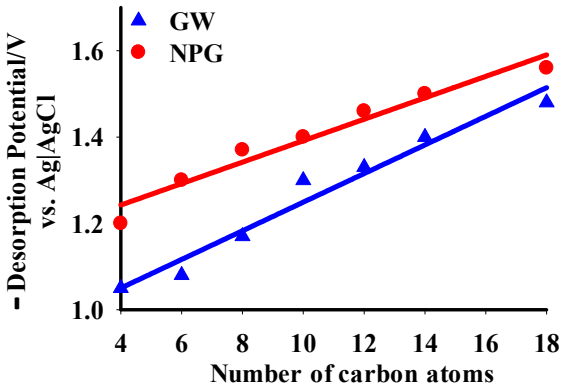

Figure 3.10. Chain length dependence of desorption potential of SAMs on NPG and gold wire. Chain length vs. desorption potential are plotted for the NPG (circles) and gold wires (triangles). The most negative peak potential was taken for thiols showing multiple desorption peaks.

The desorption potential is always more negative for the SAMs on the NPG surface compared to that of those on the gold wire surfaces, and that might be because of the increased stability of the SAM on NPG as reported or because of the difference in solvent accessibility at different surfaces, i.e. at pores of the NPG and ligament surfaces in immediate vicinity of the solution. Cortes et al. also reported a more negative desorption potential for SAMs on NPG compared to on the flat gold surface, but their study was not complete for all chain length alkanethiols and no information on the surface coverage was provided. They also presented linear scan voltammograms which do not show the oxidative readsorption part of the associated phenomenon [327]. An additional interesting feature observed during the reductive desorption studies is that the oxidative readsorption is observed even for lower chain length alkanethiols, such as for octanethiol at higher scan rate (**Figure 3.11**), whereas in previous studies on

polycrystalline gold it has been reported only for higher chain length alkanethiols. The reason for the observed readsorption peaks for only higher chain length alkanethiols was attributed to the easier diffusibility of shorter alkanethiols because of their size compared to the longer alkanethiols. The observed readsorption of alkanethiols can be explained based on the restricted diffusion of desorbed SAMs from the NPG surface from the pores and hence also explains the observation of re-adsorption peaks for relatively smaller alkanethiols. The oxidative readsorption peaks weren't observed for shorter alkanethiols on the flat gold wires, possibly because of the smaller surface area of the electrodes used in this study and hence lower amount of charge passed under the readsorption process. The other possible reason for this is that the desorbed thiols can easily diffuse away from the surface before they can be oxidatively readsorbed on the gold wire [396]. The reductive desorption curves were acquired at different scan rates for NPG and GW. At 20 mV sec^{-1} employed for NPG no reductive desorption peaks were observed on GW but at 500 mV sec^{-1} employed for gold wires reductive desorption peaks were obscured in NPG (**Figures 3.9**). At higher scan rate, only the oxidative readsorption peaks were observed for NPG (**Figure 3.9**). For all the SAMs on gold wires, a small shoulder was followed by the reductive desorption peak. The different peaks in reductive desorption has been attributed to the different crystal faces on polycrystalline gold [397, 398]. Two peaks are reported for long chain alkanethiols (n>10) but a single peak is observed for smaller alkanethiols [397]. In case of NPG, there was mostly one peak for shorter alkanethiols but for longer chain alkanethiols (n>10), multiple peaks were observed. Three peaks are observed for octadecanethiol SAMs on NPG.

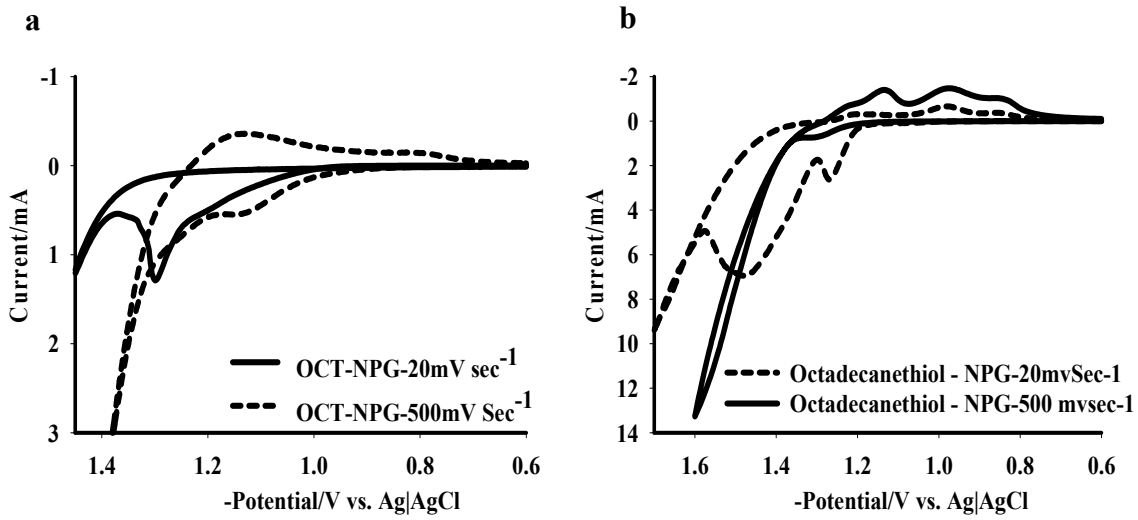

Figure 3.11. Reductive desorption of SAMs on NPG and gold wire surfaces. a) reductive desorption of octanethiol SAM on NPG at 20 mV sec^{-1} (dotted line) and 500 mV sec^{-1} (solid line) b) reductive desorption of octadecanethiol SAM on NPG at 20 mV sec^{-1} (dotted line) and 500 mV sec^{-1} (solid line).

This observation might be because of the different crystal faces as suggested in the literature or could also be cause of the different desorption profiles at the kinks, edges and pore walls compared to the flat surface of the ligaments on immediate vicinity of the solution or desorption of thiols from different domains of SAMs [398]. Reductive desorption of polar SAMs on NPG shows clear peaks, separated by almost 0.3-0.4 V. Two peaks were observed for all the other SAMs with polar head groups (lipoic acid, HO-PEG_2-SH and the Man-C_8-SH, data not shown). The surface coverage determined by reductive desorption studies in shown in **Table 3.3**, the surface coverages on flat gold, for all SAMs, are consistent with the literature reports, close to the 7.6×10^{-10} mol cm^{-2}. The relatively higher value of surface coverage obtained for SAMs on NPG must be because

of the large charging current which has been found to increase the calculated surface coverage on polycrystalline gold surfaces.

Table 3.3. Reductive desorption of SAMs on NPG and on Gold Wire.

Alkanethiols	Gold Wire		NPG Surface	
	Desorption Potential (V)	Surface Coverage (Mol cm^{-2})	Desorption Potential (V)	Surface Coverage (Mol cm^{-2})
Butanethiol	1.05	1.02×10^{-9}	1.20	2.62×10^{-9}
Hexanethiol	1.08	7.3×10^{-10}	1.25	3.10×10^{-9}
Octanethiol	1.20	8.33×10^{-10}	1.36	2.61×10^{-9}
Decanethiol	1.30	7.43×10^{-10}	1.38	1.02×10^{-9}
Dodecanethiol	1.32	8.41×10^{-10}	1.46	1.31×10^{-9}
Tetradecanethiol	1.37	8.31×10^{-10}	1.50*	9.89×10^{-10}
Octadecanethiol	1.48	1.15×10^{-9}	-------	----------
Mercaptooctanol	1.20	6.20×10^{-10}	(0.9, 1.2)	6.60×10^{-10}
Mercaptododecanoicacid	1.22	8.00×10^{-10}	(1.04,1.14,1.22)	4.00×10^{-10}

*For multiple desorption peaks, all peaks were integrated and sum of areas was taken for calculation of surface coverage. (Hydrogen evolution overlapped with the reductive desorption peak so surface coverage was not calculated)

It has been reported that the error associated with the charging current is almost close to the value of charge associated with the reductive desorption of SAM. Thus the relatively large background current associated with the large surface area of NPG explains the larger values of surface coverages [98]. Another possible reason for the high surface coverage on NPG could be associated with the restricted diffusion of desorbed thiols from the surface inside the pores which might readsorb and hence increase the overall charge associated with the reductive desorption of SAM. Surface coverage for polar SAMs on gold wire is close to the monolayer coverage whereas it is less than monolayer coverage on the NPG surface where it is almost 50 %.

3.2.5 EIS studies of SAMs with different ω-functional groups on NPG and on flat gold.

Structural organization and electrochemical behavior of SAMs on smooth gold surfaces has been well studied [326, 345]. Properties of the terminal functional groups of SAMs such as, bulkiness, hydrophobicity and tendency to form hydrogen bonding greatly influence the interfacial behavior of SAMs on the metal surface [347, 399]. Study of the effect of ω-functional groups on SAM formation and electrochemical behavior was carried out by comparing the characteristics of octanethiol and mercapto-1-octanol (comparison of $–CH_3$ vs. -OH functional group), similarly dodecanethiol and mercaptododecanoic acid were compared (comparison of $–CH_3$ vs -COOH functional group). **Figure 3.12a** shows the Nyquist plot overlays for the octanethiol, mercapto-1-octanol and mercaptoundecanol SAMs on NPG and on gold wire. Both mercapto-1-octanol and mercaptoundecanol form a fairly well ordered SAMs, with significant charge transfer resistance on the gold wire as indicated by their well defined semicircles in the Nyquist plots; the charge transfer resistance of SAMs with –OH terminal group is less than that of the $–CH_3$ terminated SAMs. There are some distinct differences in the Nyquist plot of these polar SAMs on NPG and on flat gold, the difference in the shape of the Nyquist plot indicates the difference in the organization of SAM on the NPG surface compared to that on flat gold. Octanethiol SAMs on NPG show a clear semicircle and smaller Warburg impedance, whereas the semicircle portion of the Nyquist plot is not well formed for mercaptooctanol SAMs, and instead it is a very small depressed semicircle followed by the Warburg impedance (**Figure 3.12a**).

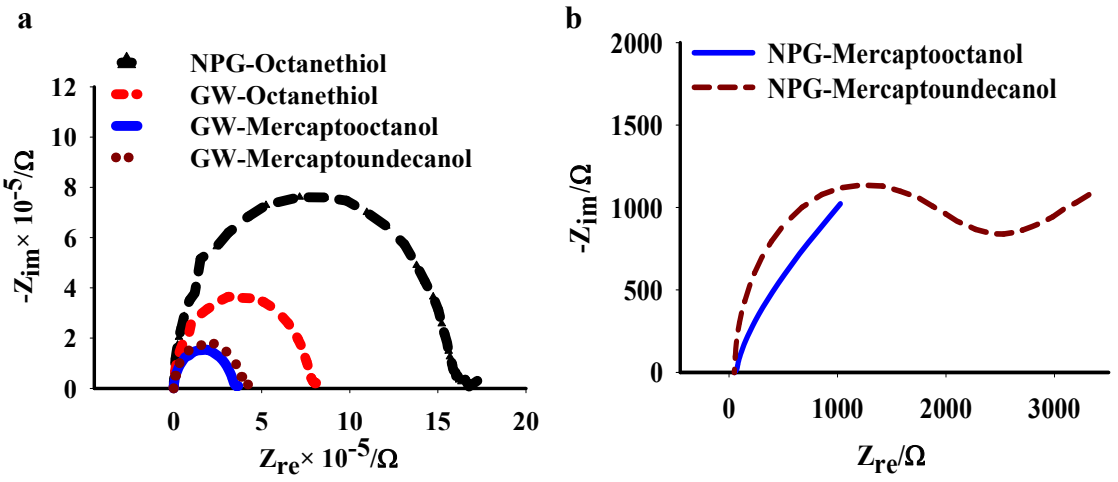

Figure 3.12. Nyquist plots for polar and nonpolar SAMs on NPG and gold wire. a) Comparisons are made between 8 carbon chains with –OH and $–CH_3$ tail groups. Mercaptooctanol and mercaptoundecanol SAM on NPG are shown in (b).

This is an indication of the fairly ion permissive and less ordered SAM of mercapto-1-octanol. Similarly, comparison of the Nyquist plot for SAMs of dodecanethiol vs. that for mercaptododecanoic acid SAMs also shows clear differences on NPG (**Figure 3.13**). Mercaptododecanoic acid with the negatively charged terminal carboxyl group and with the longer chain length is expected to from a repellent monolayer for ferro/ferricyanide ions, and as expected, a monolayer of mercaptododecanoic acid SAM on flat gold appears well-ordered, whereas SAMs on NPG are relatively less resistive to ion transfer across the interface. One interesting observation is that the charge transfer resistance of MDDA SAM on gold wire is higher than that of the dodecanethiol SAM, whereas it is opposite on the NPG surface. The lower charge transfer resistance of the MDDA SAM on NPG compared to that of the dodecanethiol SAM despite the presence of a negatively charged terminal group is a result of the loose packing of the SAM with the bulkier and polar functional groups. This

observation shows some striking differences in the organization of SAM on NPG and on flat gold, which is a subject of further characterization. Similarly comparison was made between two different chain length alkanethiols with terminal –OH groups **(Figure 3.12a and Figure 3.12b)**, results show that the increase in chain length of the alkanethiol with polar head group also start to form a better organized and resistive interface. The preliminary result of our EIS study shows that the molecules with polar head groups, both –OH and –COOH, are more permissible to ions across the interface compared to the similar chain length SAM with a $–CH_3$ terminal group.

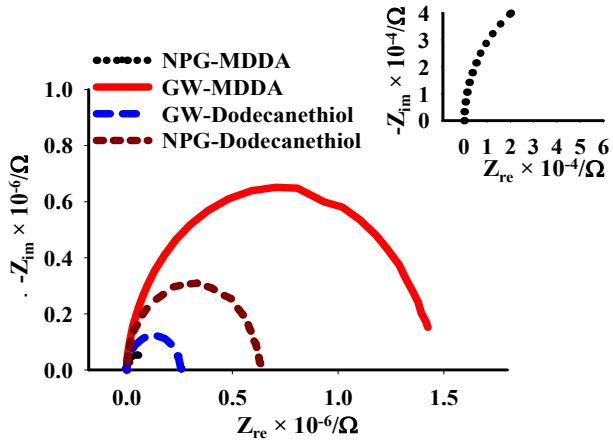

Figure 3.13. Nyquist plots for meraptododecanoic acid (MDDA) and dodecanethiol SAM on NPG. Comparison of $–CH_3$ tail group and –COOH, nonpolar, and polar negatively charged tail groups. MDDA SAM on NPG is shown in inset for clarity.

A summary of results from EIS experiments on polar SAMs on NPG and flat gold is given in **Table 3.4**. Studies have shown that the extent of hydrophobicity or hydrophilicity is not the sole reason for the formation of a charge transfer barrier in SAMs [400]. Thus, the difference in the behavior of two different SAMs on NPG

corresponds to the difference in the packing of SAM on NPG surface and on the gold wire. Robinson et al. also reported that the formation of a less organized SAM of polar molecules on NPG and they interpreted it as due to crowding of head-groups at the concave surface of the pore wall that might be the responsible factor for the formation of a defective SAM [352]. As mentioned earlier, for the NPG surface with the a large fraction of ligaments and pores, it is possible that the effective barrier thickness of the SAM, at the edge of the pores, is reduced and ion penetration is increased; this decrease in thickness on the NPG surface must be higher than on the flat gold surface thus increasing electron transfer across the interface. Comparison of the capacitance of the –OH SAM and $–CH_3$ SAM shows that the capacitance of $–CH_3$ terminated SAM is lower than that of the –OH terminated SAM, hence the effective thickness of the SAM is reduced with polar head groups, which supports our arguments of reduced thickness of the SAM and the increased charge transfer across the interface. A similar observation was made for the –COOH terminated SAM as compared with the $–CH_3$ terminated SAM.

Table 3.4. EIS data summary for polar SAMs on NPG and on gold wire.

SAM	Surface	CPE (FS^{n-1})	n	R_{ct} (Ω)
Mercaptooctanol	GW	2.1×10^{-7}	0.97	28334
	NPG	7.0×10^{-4}	0.74	---*
Mercaptoundecanol	GW	8.2×10^{-8}	0.98	410000
	NPG	1.8×10^{-5}	0.98	2116
Mercaptododecanoic acid	GW	1.0×10^{-7}	0.97	1966667
	NPG	1.8×10^{-5}	0.99	30750

*R_{ct} value for mercapto octanol on NPG was not calculated because the semicircle on Nyquist plot was poorly formed. (Surface areas: GW= 0.040 cm^2 and NPG= 12 cm^2)

3.3 Conclusions

NPG surface with approximately 300 times higher surface area was prepared by simple alloying and dealloying process and this was characterized for the formation of SAM. The behavior of SAM on the rough and curved NPG surface shows some similarities and differences compared to the SAM on GW surface. Shorter chain length alkanethiols are less ordered and less packed in NPG as in the GW surface and hence double layer capacitance, charge transfer resistance and heterogeneous electron transfer resistance are as expected. The longer chain length alkanethiols are more organized and behave similarly to the SAM on the gold wire surface. Even though NPG is expected to have a large amount of defects and is potentially the SAM is expected to be disordered but hydrophobic SAM with same chain length is similar to that of the SAM on gold wire. Hydrophilic SAMs on the other hand are dramatically different on these two surfaces, SAMs with –OH and –COOH functional groups used in this study are relatively less organized and more permeable to ions across the interface. The effect of the terminal charge on the –COOH functional groups in mercatododecanoic acid SAM on the GW surface is overcome by the less organization effect on the NPG surface.

CHAPTER IV

CARBOHYDRATE-LECTIN INTERACTION STUDIES ON NANOPOROUS GOLD AND FLAT GOLD SURFACES

4.1 Introduction

Carbohydrates are one of the most complex and prevalent biomolecules in biological systems. Different glycoconjugates such as glycolipids, glycoproteins, glycosaminoglycans and proteoglycans extensively decorate cell surfaces, and are the part of frontiers of cell related biological interactions [401]. Variation in glycosylation patterns occurs according to cell type, stage of cell development, growth, and differentiation [402]. Abnormal patterns of glycosylation are observed during the malignancy and metastasis of cancer cells [403]. Carbohydrates are an important element of several biological processes such as cell-cell communication, cell recognition, cell adhesion in inflammation and metastasis, recognition in bacterial and viral infections, immune response, fertilization, and also the conformation and stability of proteins are affected by the changes in glycosylation [295, 404]. Carbohydrates are being studied as potential biomarkers due to changes in glycotopes (carbohydrate epitopes) during malignant transformation of cells, which has made carbohydrates valuable targets for diagnostics and therapeutics [405]. Lectins bind to mono- or oligosaccharides with high specificity, and are proteins of non-enzymatic and non-immune origin [161]. Due to the multiple carbohydrate binding sites present in lectins, when they interact with cell surface carbohydrates they interact with multiple cells and hence can cause cell precipitation, as it occurs when lectins are used in the haemagglutination assay [159]. The scarcity of high

affinity carbohydrate antibodies and the high specificity of lectins towards carbohydrates has made them an important component of the glycan target based studies such as, the study of structural and functional roles of complex carbohydrates, cell surface carbohydrates [156], cell sorting [406], the study of protein glycosylation patterns [407], and other applications that rely on advances in glycobiology for biomedical and biotechnological applications [160, 408]. One of the predicaments to the studies of carbohydrate-protein interactions is the lower affinity between carbohydrates and proteins, and that current common biochemical techniques have not yet been perfected to fulfill all the requirements for such studies. The issues with the weak affinity of carbohydrate protein interaction have been partially overcome by the attachment of carbohydrates on solid surfaces, polymer surfaces, or dendrimers. These surface immobilization techniques result in a significant increase in the binding affinity most probably due to the cluster glycoside effect, which facilitates multivalent interactions [409, 410].

Carbohydrate arrays are still in the early phases of development and there is much to be done for them to be comparable to the advancement made in proteomic and genomic technologies, through their arrayed immobilization on solid surfaces. Solid phase assays via immobilized biomolecules simplify the steps needed for the isolation and characterization of biomolecules. Solid surface modification with carbohydrates and their successive application in carbohydrate based interaction studies can be taken as a simplified model for the cell-cell interactions often involving binding of a protein from one cell to the carbohydrates on an adjacent cell. Controlled immobilization at a desired level of functional display of carbohydrates on solid surfaces will be a great achievement

in this direction [303, 411]. The display of carbohydrate ligands on the solid surface at appropriate density can favor the multivalent interactions of carbohydrates with lectins, and hence increase the affinity [409]. Due to the several advantages of gold for the biomolecule immobilization, as discussed in earlier chapters, and its spontaneous interaction with sulfur atoms makes it an attractive substrate in carbohydrate immobilization and related studies [8]. The interfacial properties of self-assembled monolayers (SAMs) can be controlled by varying composition and functionality of SAMs on the surface [89, 412]. Earlier studies have shown that the affinity of carbohydrate lectin interaction can vary with the fraction of carbohydrates in the mixed self assembled monolayer, also the affinity of carbohydrate for a lectin on surface can be different from the affinity of lectin for carbohydrate in solution [413].

Highly sensitive label-free techniques for studying molecular interactions are highly desirable because of the inherent greater complexity such as fluorescent and radio-labeling techniques associated with labeling techniques [414]. Electrochemical impedance spectroscopy (EIS) is a label-free and sensitive technique for characterizing redox behavior at the electrode-electrolyte interface, which has been applied for the study of the changes in this behavior occurring as a result of biomolecular interactions at the interface [415]. In this chapter, we report and discuss the application of EIS to study carbohydrate-lectin interactions on NPG and on gold wire surfaces, and comparison of the response to lectin binding on these surfaces modified with mannose presenting SAMs. Several approaches have been developed for the immobilization of carbohydrates to solid surfaces, including biotin-streptavidin based affinity attachment [416], incorporation into SAMs formed on gold surfaces [417], and click chemistry reactions

onto appropriately functionalized surfaces [418]. The SAM based immobilization strategy has been favorite and straightforward technique for obtaining carbohydrate modified surfaces using thiolated glycosides. Thus, we fabricated carbohydrate modified electrodes by the self-assembly of thiolated glycosides either from a pure or from a mixed ethanolic solution. OCT and HO-PEG_2-SH were used as diluting molecules in mixed SAM preparation along with αMan-C_8-SH, in the desired ratios, in order to determine the optimal ratio of mixed SAM for the maximum increase in charge transfer resistance, due to Con A binding to mannose. Even though there are reports of utilization of mixed SAMs for carbohydrate-lectin binding studies, to our knowledge, there has not been a comparison over a full range of composition to determine the optimal SAM mixture for binding. Most of the prior studies, with the exception of those utilizing Au nanoparticles [419, 420], were conducted on flat gold surfaces [409, 421]. The present study provides a comparison of lectin carbohydrate interactions on SAMs modified rough and porous NPG to that on relatively smooth gold wire surfaces. The SAM composition was varied on each surface to elucidate the optimal binding of Con A to mannose, chosen as the carbohydrate target due to its well-known binding behavior and biological relevance, such as its association with the virulence of pathogens [422].

Use of monosaccharide presenting SAMs simplifies the model system for carbohydrate-lectin/protein interaction studies but they don't truly mimic the behavior of complex carbohydrate units on the cell surface or on a glycoprotein. A limited number of studies have been performed by incorporating complex carbohydrates into the SAM [423-425]. Gb3 presenting SAMs were chosen as an effort to mimic the real and complex carbohydrate-lectin interaction studies. Globotriosylceramide is a P^k blood

group antigen also known as CD77 antigen with the terminal glycan unit consisting of unique Galα1-4Gal moieties [426]. It is expressed in high density in kidney and brain endothelial cells, and in human erythrocytes [427]. It is an important recognition element in the attachment of shiga toxins, shiga like toxins or verotoxins to the host cells [428]. These toxins are the important cytotoxins that cause diarrhoeal disease and hemolytic uremic syndrome. Shiga toxin is produced by the pathogenic bacteria *Shigella dysenteriae* and certain enterohemorrhagic *Escherichia coli* produce shiga like toxins [429]. Galα1-4Gal unit of the globo series of glycolipid is the recognition unit of most of the uropathogenic bacteria [430]. *Burkholderia cepacia*, an opportunistic bacteria found in the sput of cystic fibrosis patient has been found to bind to the unsubstituted terminal Galα1-4Gal unit of digalactosylceramide and globotriosylceramide [431]. Higher expression of Gb3 has been reported in human colorectal tumors and their metastases [432]. Keyhole limpet hemocyanin (KLH) contains the trisaccharide portion of Gb3 linked by a MUC5AC peptide epitope, which has been prepared for use as a vaccine for treating ovarian cancer [433]. Gb3 is overexpressed in colorectal adenoma cells, in Burkitt's lymphoma cells, in breast and ovarian cancer and some other cancers [434-437]. There is an increasing interest to mimic the cell surface and present carbohydrates in self-assembled monolayers or in bilayers. A very limited number of derivatives of globotriose have been synthesized for various studies in this direction. Synthesis of P^k antigen linked to the mercaptohexadecanol was reported by Bundle et al. for the application in amperometric sensor for verotoxin [438]. Self assembled monolayers of globotriose terminated alkanethiols or of oligoethylene glycol terminated species were prepared on gold surfaces and their properties including, wetting, surface interaction and surfactant

adsorption were studied [439]. This study reported that the lateral interaction between globotriose groups was dependent on the surface density and this interaction, primarily hydrogen bonding, which could be either direct or water mediated. Svedhem et al. reported synthesis of globotriose coupled to the bis(16-hydroxy hexadecanyl) disulfide or with the tetra or diethylene glycol spacer and SAMs of the molecules were prepared on gold. Antibody binding studies were performed on this SAM and binding of the highest amount of the antibody occurred at 1-10% carbohydrate coverage on the surface in mixed SAMs [440]. Based on infrared spectroscopy studies with this large spacer they reported that the carbohydrate SAM on the gold surface was highly ordered and showed crystallinity, characteristic of SAM on the gold surface but no electrochemical characterization has been reported so far. Globotriose encapsulated gold nanoparticles were synthesized and employed for the inhibition of toxicity of shiga toxin [441]. Gold nanoparticles encapsulated with globotriose showed size dependent effects in the inhibition of shiga toxin, Au-nps of 20 nm size was reported to be good enough for the multivalent binding of Stx B and globotriose, since ligament size of the NPG are in the similar range and hence can be assumed as an optimal surface for such binding studies [442]. A large portion of the reports in the literature, concerning carbohydrate-lectin interactions, have predominantly utilized mannose and Concanavalin A pairs as a model systems for such studies [409, 443]. Complex carbohydrates have also been used but the information is limited [306, 423]. The self assembly of complex carbohydrates might be different from the self assembly of the simple monosaccharide bearing molecules. Earlier studies have predominantly utilized flat gold surfaces or some gold nanostructures as a model substrate [419, 423, 444]. Carbohydrate orientation in cell and organelle is not as

in the perfectly flat surfaces which lack curvature and fluidity, thus we used NPG with ligaments dimension close to that of the vesicles and cell organelle which we believe could be a better model for the study of carbohydrate-protein interaction. At least NPG with its curvature and the ligament sizes which are close to the size of microdomains of the membrane, caveolae (55 nm diameter), nanodomains (20-30 nm) and transient lipid localization region or confinement zone (100-300 nm) of the membrane, which has been reported to have high content of glycosphingolipids, can be a better substrate for mimicking membrane properties [445, 446]. Here we report for the first time the synthesis, characterization of SAM of Gb3-C_8-SH on NPG surface and compared that with the SAM on the well characterized substrate, gold wire, and employed them to study of globotriose soybean agglutinin binding studies on NPG and gold wire surfaces.

4.2 Results and discussions

4.2.1 Electrochemical characterization of the carbohydrate presenting SAMs on NPG and on gold wire

Self-assembled monolayers were prepared on the gold surfaces by immersing the wires into a solution of thiols in ethanol for the given period of time. SAMs on the gold surfaces were characterized by cyclic voltammetry (CV) as well as by electrochemical impedance spectroscopy. **Figure 4.1** shows the CV scans for gold oxide stripping on both bare and modified NPG and gold wires. CV scans of bare as well as αMan-C_8-SH and mixed SAM of αMan-C_8-SH and OCT modified electrodes were performed in 0.5 M H_2SO_4, in order to assess the ability of the SAM to hinder the process of gold oxide formation and reduction, and thereby provide a measure of the integrity of the monolayer. CV scans were performed in 0.5 M H_2SO_4 at 100 mV sec^{-1}. The CVs on gold wire

showed one oxidation peak starting at 1.3 V and extending up to 1.5 V as a flat plateau, on the positive scan, characteristics of gold oxide formation on the surface (all potentials are noted versus the Ag|AgCl reference electrode). A reduction peak at around 0.93 V was observed for the reduction of gold oxide on the reverse scan. Peak position of the αMan-C_8-SH modified wire extended in the range of 1.48 - 1.50 V, at a relatively larger overpotential, but of greater current. The enhanced current on the modified electrode represents a contribution from oxidation of the αMan-C_8-SH species, and that the higher overpotential results from the monolayer, which results in hindrance on the onset of gold oxide formation. The oxide reduction peak was observed at around 0.96 V.

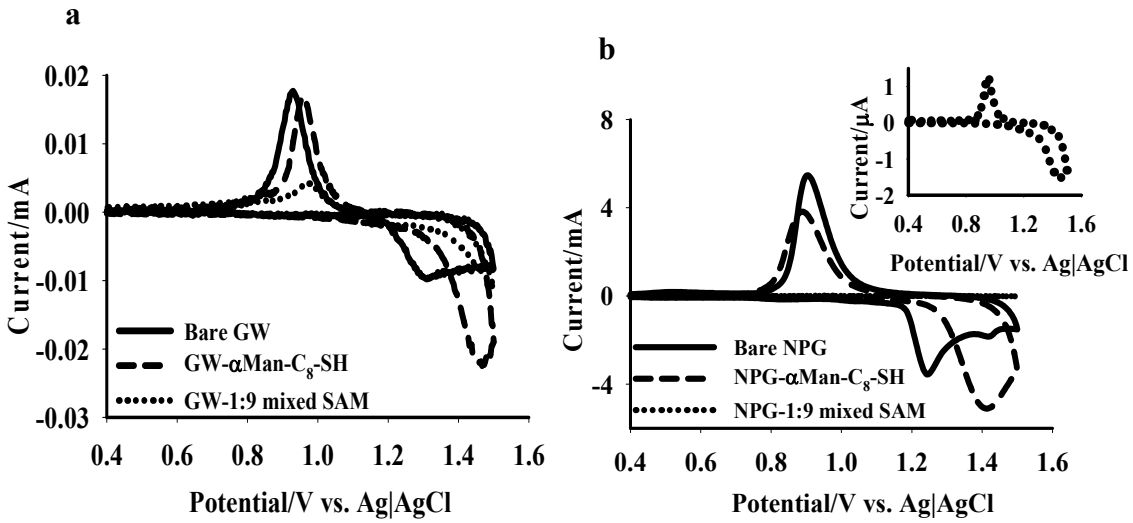

Figure 4.1. CV scans for gold oxide stripping of bare and modified surfaces of mannoside presenting SAMs. CV scan of the modified GW (a) and NPG (b) for the study of integrity of SAM on potential scans. CV scan of modified wires were performed in 0.5 M H_2SO_4.

The mixed SAM (1:9 molar ratio) of αMan-C_8-SH and OCT modified gold wires shows reduced current and onset at an even higher overpotential, suggesting that this monolayer is more compact and robust, more resistant to oxidation itself, and that it is also hindering the formation of gold oxide. The reduction peak is slightly positively shifted in potential and appears near 0.98 V. Only a modest decrease in oxide reduction peak was observed for the αMan-C_8-SH modified gold wire (20 - 23%) whereas around a 78 - 83% drop in charge passed under the oxide reduction peak was observed for mixed SAM modified gold wire.

The CV scan on bare NPG in 0.5 M H_2SO_4 is characterized by two peaks at around 1.25 V and 1.42 V prior to the scan reversal peak at 1.5 V. The gold oxide reduction peak appeared near 0.91 - 0.93 V. αMan-C_8-SH modified NPG shows one broad peak at around 1.4 V with larger currents than those observed on the bare NPG. The reduction peak was observed around 0.88 - 0.90 V. The mixed SAM modified NPG shows a peak at around 1.47 V and the onset of oxidation is shifted here to higher overpotentials as was observed on gold wire modified with the mixed SAM. The gold oxide reduction peak was observed near 0.96-0.98 V. Relatively a modest, around 11 - 15% ,decrease in charge passed under the oxide reduction peak was observed for the pure αMan-C_8-SH modified NPG compared to that on the bare NPG. In contrast, almost 99.0-99.9% drop in charge passed was observed for mixed SAM modified NPG. This significant drop in charge passed for the mixed SAM modified NPG compared to the mixed SAM modified gold wire could be partly attributed to the porosity of NPG. For the objective of monitoring gold oxide formation and stripping, scans on SAM modified NPG were done to assess the robustness and packing of the pure αMan-C_8-SH thiol SAM

vs. the mixed SAM of αMan-C_8-SH and OCT. It is clear from the data acquired on both gold wire and NPG surfaces that mixed monolayers are more effective at hindering the process of gold oxide formation. This observation suggests that the mixed monolayers are better ordered.

Figure 4.2 shows similar studies performed on the globotriose containing SAMs. Globotriose is relatively a larger molecule and hence its organization on surface is expected to be different from that of the mannose containing SAM. The trend of gold oxide formation and reduction peaks on Gb3 modified surfaces are similar to that of the mannose containing SAM. As in mannose containing SAM on gold wire, Gb3-C_8-SH modified surfaces showed a slight decrease in oxide reduction peak height, but after the formation of a mixed SAM with OCT there was a significant drop in the charge under the oxide reduction peak. Globotriose modified NPG surface shows one significant difference as the oxide reduction peak in the globotriose SAM is more negatively shifted than on gold wire. This is most possibly because of the restrictions on diffusion of ions inside pores or possible hydrogen bonding in the carbohydrate presenting SAMs [444]. As on gold wire, there was a drop in oxide reduction peak after formation of mixed SAM and only a small change was observed with the pure Gb3-C_8-SH SAM.

Given that the gold oxide formation and stripping approaches probes a process taking place on the internal surfaces of NPG, it was pursued as a complementary approach to the more common strategy of measuring the ability of SAMs to block the redox potential of a diffusing probe. CV scans in electrolyte solutions containing redox probes like $Fe(CN)_6^{3-/4-}$ or $[Ru(NH_3)_6]^{2+/3+}$ are commonly employed for the assessment of

the integrity of the SAM on surfaces since well-ordered SAMs will create barrier for the electron transfer across the interface thus greatly reducing the peak current [400, 447].

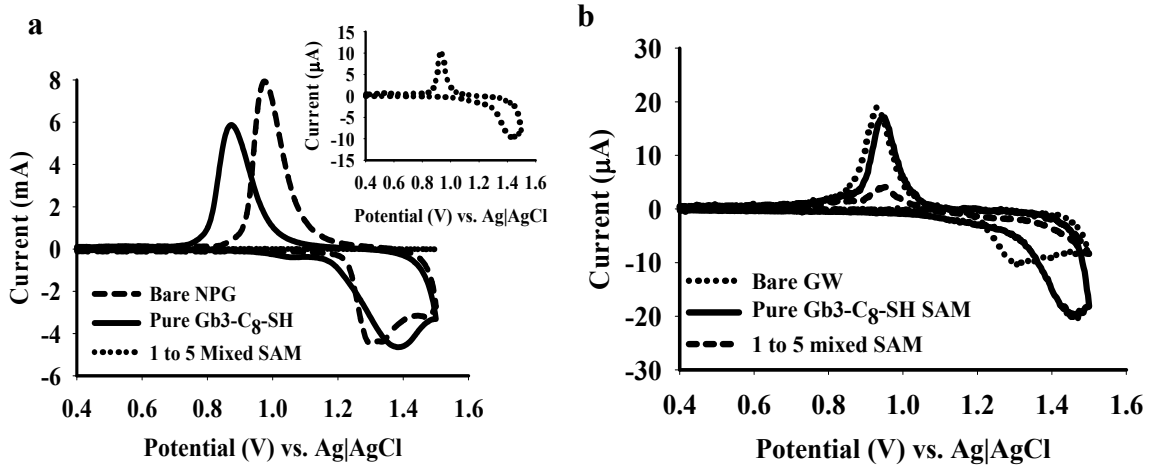

Figure 4.2. Gold oxide stripping for the bare and globotriose presenting SAMs on NPG and gold wire. CV scans were performed in 0.5 M H_2SO_4 for the determination of surface coverage and robustness of pure Gb3-C_8-SH SAMs and mixed SAMs of Gb3-C_8-SH with OCT or HO-PEG_2-SH on NPG (a) and on gold wire (b). CV of bare NPG and gold wires are also shown for comparison. CV scans were performed as in **Figure 4.1.**

Thus, the integrity of the SAMs was also assessed by performing CV scans in the presence of the widely used redox probe $Fe(CN)_6^{3-/4-}$ [356, 448]. **Figure 4.3a** shows the cyclic voltammograms for three different electrodes: bare gold wire, gold wire with αMan-C_8-SH and gold wire with the 1:9 mixed SAM of Man-C_8-SH and OCT measured in 10 mM $K_3[Fe(CN)_6]$. There are two clear and distinct characteristic peaks for the oxidation and reduction of $Fe(CN)_6^{3-/4-}$ on gold wire, whereas these peaks completely disappear on both αMan-C_8-SH and on mixed SAM modified wires (**Figure 4.3b (gold wire)** and **Figure 4.3d (NPG)**).

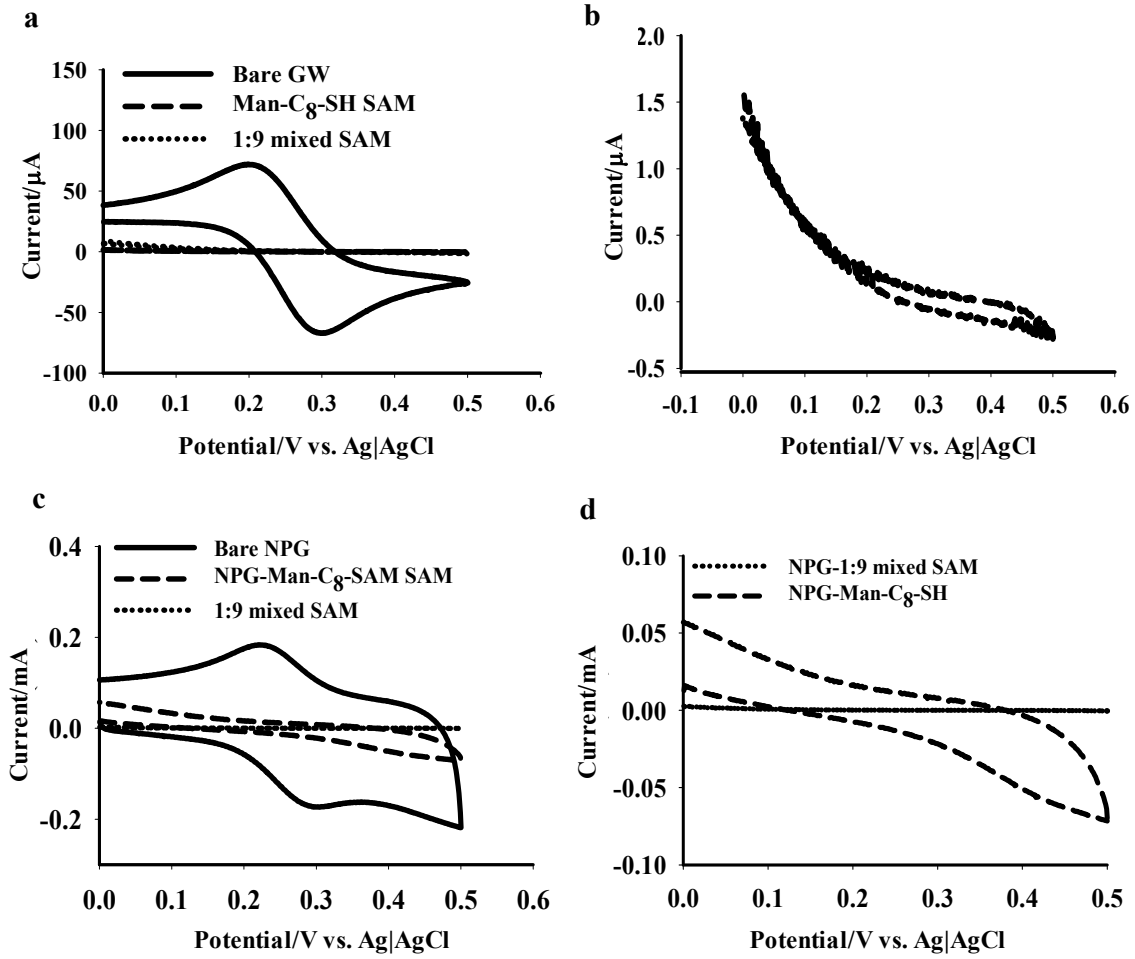

Figure 4.3. Cyclic voltammograms of bare and modified surfaces in 10 mM $K_3[Fe(CN)_6]$. CV scans for the pure Man-C_8-SH and mixed SAM of αMan-C_8-SH and OCT modified gold wire (a and b) and NPG (c and d) surface with 10 mM $K_3[Fe(CN)_6]$. CV scans were performed between 0 and 0.5 V at a scan rate of 100 mV sec^{-1}.

A very small charging current was observed in CV scans on these SAM modified wires, which indicated effective blocking behavior on both modified surfaces towards electron transfer to or from $Fe(CN)_6^{3-/4-}$. Similar results were obtained for CV scans on bare NPG, as on bare gold wire, except a much larger charging current was observed for the NPG wire, because of the comparatively higher surface area of NPG. A nearly 30

times larger peak current was observed on NPG, and the electrode capacitance was also much larger. Slightly different behavior was observed on the NPG electrodes when modified with pure αMan-C_8-SH or a mixed SAM. The αMan-C_8-SH modified wires still shows some charging current, in the CV scan, indicating presence of some bare areas on the electrode. A characteristic S-shaped CV curve was observed with the mixed SAM modified NPG, indicating a completely resistive interface with very little redox current passed. These data are complementary to the data on oxide stripping in the presence of the SAM and support the conclusion that the mixed SAM is much better packed and ordered than the SAM of the pure αMan-C_8-SH.

Figure 4.4a and **Figure 4.4b** shows the cyclic voltammograms for five different electrodes: bare gold wire, gold wire with Gb3-C_8-SH, gold wire with the 1:5 mixed SAM of Gb3-C_8-SH:OCT and 1:5 mixed SAM of Gb3-C_8-SH:HO-PEG_2-SH, measured in 10 mM $K_3[Fe(CN)_6]$. The effective blocking behavior of the pure Gb3-C_8-SH, 1:5 molar ratio mixed SAM of Gb3-C_8-SH:OCT and 1:5 molar ratio mixed SAM of Gb3-C_8-SH:HO-PEG_2-SH modified surfaces, for the charge transfer across the interface is indicated by the complete disappearance of the redox peaks of the probe. The amount of charging current is very low for pure Gb3-C_8-SH SAM and mixed SAM with OCT modified electrodes, whereas the charging current is relatively larger for the mixed SAM of Gb3-C_8-SH and HO-PEG_2-SH. SAMs of polyethylene glycol has been reported to be disordered due to the hydration of the terminal hydroxyl groups and solvent penetration into the oligoethylene unit, this accounts for the increased permeability of the HO-PEG_2-SH and Gb3-C_8-SH mixed SAM compared to the other two SAMs on the GW [449].

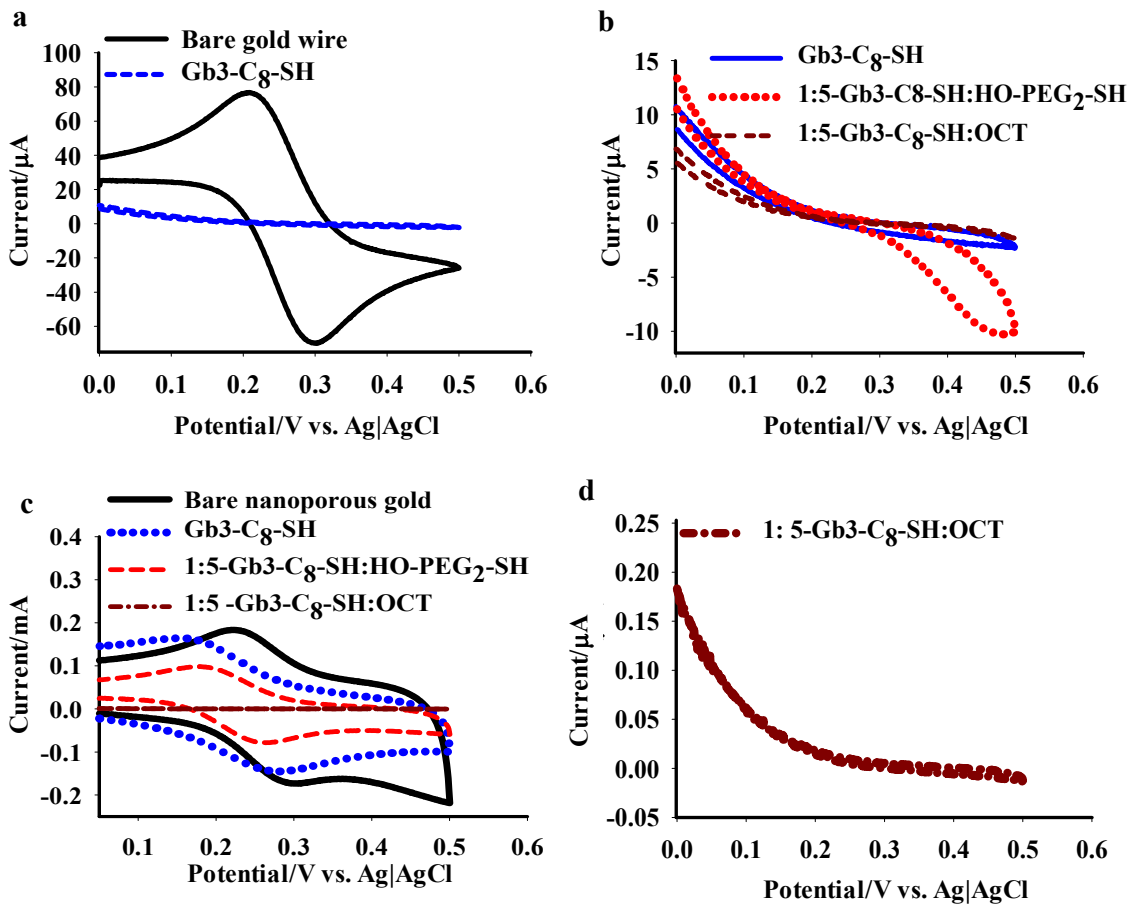

Figure 4.4. Cyclic voltammograms of bare and globotrioside presenting SAMs on NPG and on gold wire. CV scans on gold wire GW (a and b) and on NPG (c and d) electrodes, with and without modifications. CV scans were performed in 10 mM $K_3[Fe(CN)_6]$ at a scan rate of 100 mV sec^{-1}.

Figure 4.4c and **Figure 4.4d** shows CV scan of similarly modified NPG surfaces. CV scan of the bare NPG shows fairly large charging current compared to that of the gold wire, because of the large surface area of NPG, otherwise it is fairly similar to that of the CV on gold wire, showing both redox peaks. CV scans on modified NPG show slightly different behavior when modified with pure Gb3-C_8-SH, a mixed SAM of Gb3-C_8-SH and OCT, or a mixed SAM of Gb3-C_8-SH and HO-PEG_2-SH. Oxidation and reduction

peaks of $Fe(CN)_6^{3-/4-}$ are clearly seen for both the pure Gb3-C_8-SH and mixed SAMs of Gb3-C_8-SH and HO-PEG_2-SH modified surface. The OCT mixed SAM modified NPG has a characteristic S-shaped CV curve, this indicated completely resistive interface with very little redox current passed. Gb3-C_8-SH modified NPG surface is fairly similar to the bare gold surface even though the magnitude of the redox currents is significantly decreased. The magnitude of the reduction of the redox current increases with the formation of the mixed SAM of HO-PEG_2-SH and Gb3-C_8-SH, still redox peaks are seen and this is characteristic of a significantly permeable interface. The magnitude of the residual charging current for mixed SAMs of OCT and Gb3-C_8-SH modified gold wire is slightly larger than the charging current on similarly modified NPG; this might be because of the increased hydrophobicity of the SAMs on the gold nanostructure compared to those on the flat gold surface and for the reasons as discussed earlier for the mannose presenting SAMs [35].

4.2.2 Reductive desorption of SAMs, and surface coverage

CV scans for the reductive desorption of αMan-C_8-SH and mixed SAM of αMan-C_8-SH and OCT are shown in **Figure 4.5.** Surface coverage for alkanethiol on gold wire is consistent with the similar studies reported, a slightly lower surface coverage for SAMs with polar and bulkier ω-functional groups has been reported in the literature and these molecules are reported to form disordered SAM. Reductive desorption of SAMs on NPG on the other hand shows fairly different behavior, surface coverage for octanethiol and mixed SAM with octanethiol is fairly large (almost twice) compared to the monolayer coverage on the flat and polycrystalline gold surface (**Table 4.1**).

Table 4.1. Summary of the results of reductive desorption of SAMs on NPG and gold wire surfaces.

	Gold wire		NPG	
SAM	**Des. potential (V)**	**Surface coverage (mol/cm^2)**	**Des. potential (V)**	**Surface coverage (mol/cm^2)**
OCT	1.14	8.7×10^{-10}	1.38	2.9×10^{-9}
Gb3-C$_8$-SH	1.13	5.6×10^{-10}	1.17	2.4×10^{-10}
HO-PEG$_2$-SH	1.07	6.1×10^{-10}	1.18	2.3×10^{-10}
1:9-Man-C$_8$-SH:OCT	1.16	9.7×10^{-10}	1.30	2.1×10^{-9}
1:19-Man-C$_8$-SH:OCT	1.15	8.3×10^{-10}	1.30	1.9×10^{-9}
1:5-Gb3:HO-PEG$_2$-SH	1.10	6.3×10^{-10}	1.05	3.0×10^{-10}
1:5-Gb3:HO-PEG$_2$-SH	1.16	8.1×10^{-10}	1.35	2.4×10^{-9}

This higher value of charge under the reductive desorption peak, and hence the higher surface coverage is most likely because of the large charge associated with the charging current. Depending upon the magnitude of the potential at zero charge and the integrity or defects in the SAM, the charging current can contribute up to 100 μC cm^{-2} which is almost equal to the charge passed during reductive desorption of SAM, considering desorption as a one electron process [98]. Thus, almost 300 times higher surface area of NPG and inherently increased charging current adds to the charging current during reductive desorption. A similar observation was reported for the higher surface coverage of SAM on gold surface with almost 1.5 times larger value, compared to the estimated value for ($\sqrt{3}\times\sqrt{3}$)R30 surface coverage, on the gold surface [450]. The detailed discussion on this has been already presented in an earlier chapter. The broader desorption peak on NPG compared to that of the gold wire also supports the assumption that desorption over the large potential range also incorporates a large background. A similar observation, almost twice the amount of charge under the thiol reduction peak, was reported for hexanedithiols on gold surface [451]. The surface coverage calculated

from reductive desorption of SAMs with polar tail group is almost one third of the monolayer coverage. Even though there is a slightly higher coverage for the mixed SAM of HO-PEG_2-SH, it is almost 30% of monolayer coverage. This is consistent with the observation in the CV scans in 10 mM $K_3[Fe(CN)_6]$ and indicates that these SAMs are less organized on the NPG surface, and needs further characterization in order to understand the conformation, orientation and organization of polar molecules on NPG surface. Another striking feature seen for desorption of αMan-C_8-SH, Gb3-C_8-SH and HO-PEG_2-SH SAMs on NPG, is the observation of two peaks separated by approximately 0.30 V-0.4 V. This type of peak splitting or multiple desorption peaks for a single component SAM has been observed for alkanethiols SAMs on gold surface and has been attributed to the thiols adsorbed at different sites on the surface, desorption of phase separated domains etc.[397, 452]

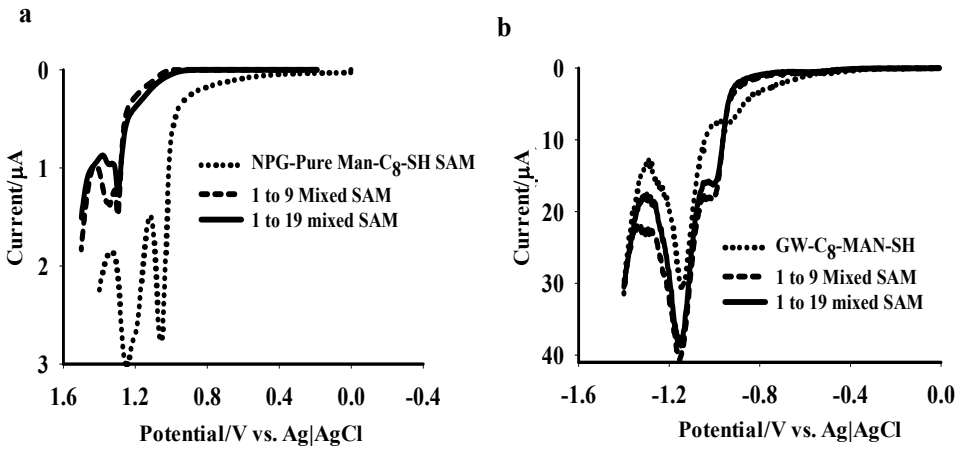

Figure 4.5. Reductive desorption of SAM on pure αMan-C_8-SH and mixed SAM of Man-C_8-SH and OCT modified NPG and on god wire. CV scans were performed in 0.5 M KOH at a scan rate of 20 mV sec^{-1} for NPG and at 500 mV sec^{-1} for gold wire.

Cyclic voltammograms for the reductive desorption of globotriose containing SAMs are given in **Figure 4.6**. As in mannose containing SAMs both Gb3-C_8-SH and HO-PEG_2-SH containing SAMs showed multiple desorption peaks. Both of the peaks are prominent in the CV and are separated by approximately 30 mV. Surface coverages determined for all the surfaces containing pure or mixed monolayers of carbohydrate and diluting molecules are shown in **Table 4.1**.

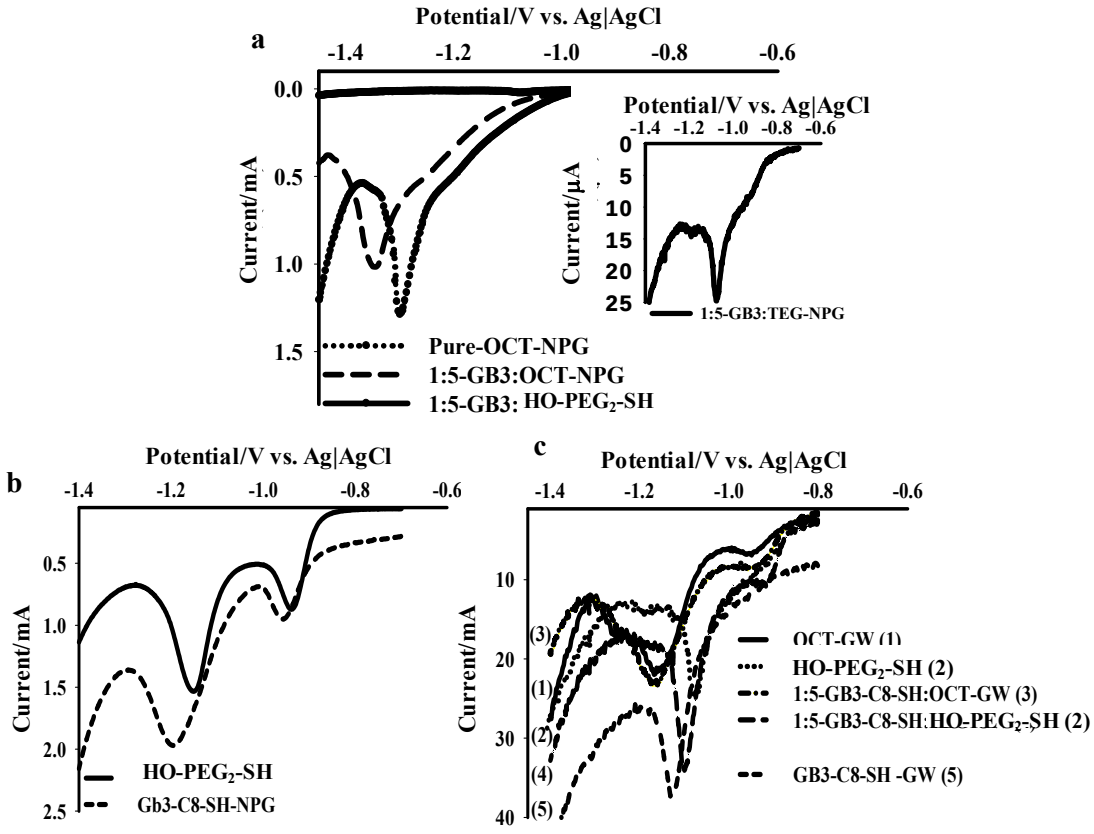

Figure 4.6. Reductive desorption of globotriose containing SAM on NPG and gold wire. CV scans were performed in 0.5 M KOH solution at a scan rate of 20 mV sec^{-1} for NPG (a and b) and at a scan rate of 500 mV sec^{-1} for gold wire (c).

4.2.3 Electrochemical impedance spectroscopic studies of lectin-carbohydrate interaction on surfaces

A Nyquist plot for a αMan-C_8-SH SAM on a gold wire surface (**Figure 4.7a**) shows a well-defined semicircle**,** representing charge transfer resistance and a small straight line, characteristic of the Warburg diffusion. The αMan-C_8-SH SAM on NPG, on the other hand, is characterized by a very small semicircle and a straight line (**Figure 4.7b**) characteristic of a dominantly diffusion controlled redox process at the NPG/electrolyte interface. Thus, the αMan-C_8-SH SAM shows a distinct difference in characteristic behavior on NPG versus on gold wire surfaces. Molecules with polar and bulkier end-groups such as αMan-C_8-SH are less likely to form well packed and resistive monolayers on the surfaces of NPG, although it appears that they can assemble and pack better on the flatter gold wire surface. NPG and gold wires with the pure mannoside monolayer were then incubated with Con A in the presence of 1 mM Ca^{2+} and 0.5 mM Mn^{2+}, which are both required as cofactors. The EIS measurements after Con A binding to pure mannoside monolayers on the gold wire surfaces showed only a small increase in charge transfer resistance whereas the change in charge transfer resistance on NPG was negligible. One possible reason for this small change in R_{ct} could be that the mannose density on the gold surface was too high and populated with random and laying down orientations of αMan-C_8-SH creating steric hindrance to the binding of Con A to mannose. Another possibility is that even though a small amount of Con A could access and bind to mannose on the surface, it was not enough to create an increase in the charge transfer resistance because of the random and laying down orientations of αMan-C_8-SH on the NPG surface. Both the NPG and the gold wire surfaces did not show a significant

increase in R_{ct} upon Con A binding to pure αMan-C_8-SH SAMs. Carbohydrate density dependent enzymatic activity of N-glycosyltransferase enzyme was reported by Mrksich et al. and their study showed that the activity of the enzyme was very low on high density N-acetyl glucosamine terminated SAMs. When the surface density was diluted at the interface by preparing a mixed SAM of the N-acetylglucosamine terminated species and alkanethiolates bearing triethylene glycol terminal groups, an increase in enzymatic activity was seen [453].

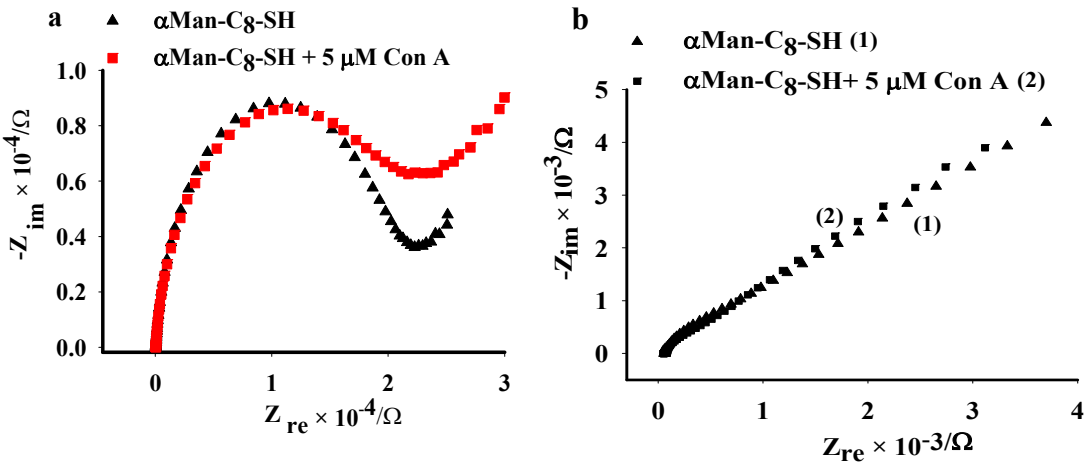

Figure 4.7. Nyquist plots for pure αMan-C8-SH modified gold wires in the presence and absence of Con A. a) Pure αMan-C8-SH modified GW before (triangles) and after (Squares) incubation with 5 μM Con A, and b) Pure αMan-C8-SH modified NPG before (triangles) and after (Squares) incubation with 5 μM Con A.

Van Duyne et al. reported a SPR study of mannose-Con A binding on gold using only 5% mannose in the mixed SAM [417]. Loaiza et al. also reported an EIS study showing carbohydrate density dependent effect on carbohydrate-lectin interaction. Their study of a thiolated mannoside with a five carbon chain linker, immobilized on gold

nanoparticles assembled on screen printed electrodes, showed a response comparable to the background using the pure mannoside SAM, but a large response was observed after lectin binding in a mixed SAMs with mercaptopropane sulfonate [419].

Alkanethiols with terminal methyl groups can assemble and form well-packed resistive monolayers on both NPG and gold wire surfaces. We sought to create a mixed monolayer of OCT and αMan-C_8-SH for carbohydrate-protein binding studies. A 1:9 molar ratio mixture of Man-C_8-SH to OCT was prepared on both NPG and gold wire surfaces. When these wires were incubated with a solution of the lectin Con A, there was a significant increase in charge transfer resistance as indicated by the increase in diameter of the semicircle in the Nyquist plot (**Figure 4.8**). This result showed that there was lectin-carbohydrate binding, and an additional layer of molecules being added at the interface. In accordance with the literature reports, we also saw better response for carbohydrate-lectin binding with the dilution of ligand density on the metal surface [419].

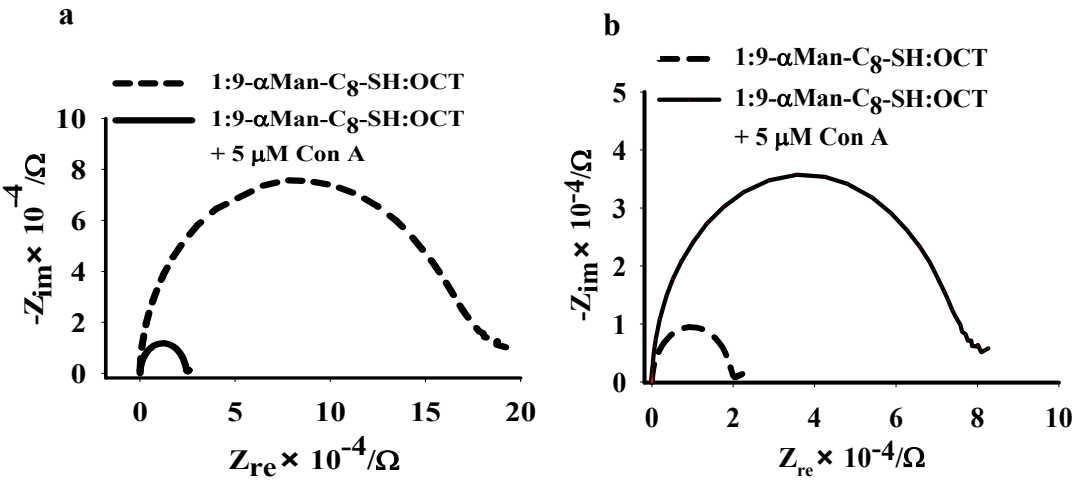

Figure 4.8. Nyquist plots for the Man-C_8-SH and OCT mixed SAM modified surfaces for Con A - mannose interaction studies. Nyquist plots for modified gold wire (a) and NPG (b), with and without Con A.

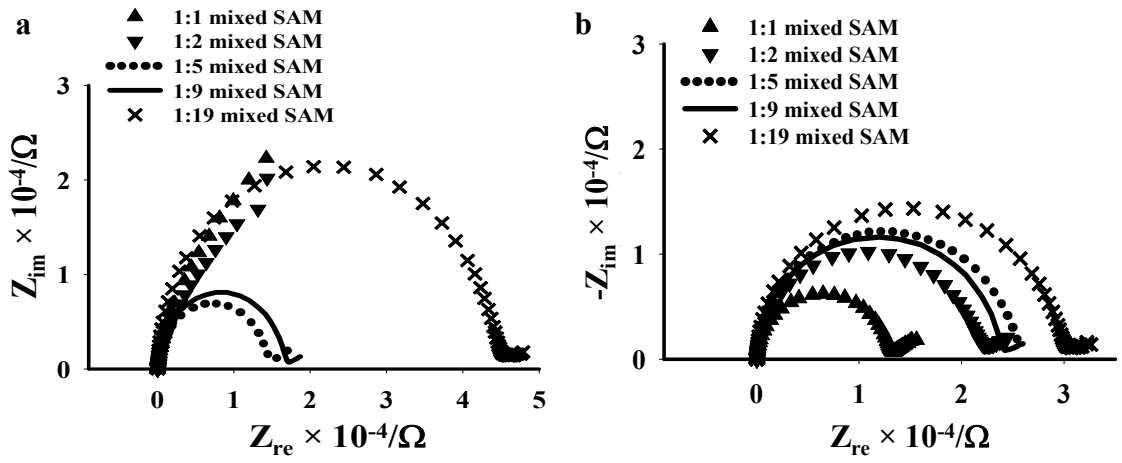

Figure 4.9. Nyquist plots for the different ratio mixed SAMs on Man-C_8-SH and OCT on NPG (a) and gold wire (b).

Increase in charge transfer resistance was observed after lectin binding on both the relatively smooth gold wire surfaces as well as the NPG surface. Nyquist plots for the modified NPG and gold wire, at different ratios of mixed SAMs of Man-C_8-SH and OCT are shown in **Figure 4.9a** and **Figure 4.9b,** respectively. **Figure 4.10a** shows a plot of percentage change in R_{ct} resulting from incubation with Con A on both NPG and gold wire for SAMs prepared from different ratios of the αMan-C_8-SH and OCT in solution. The highest response to Con A binding was obtained near 1:9 molar ratio of Man-C_8-SH to OCT on gold wire. In the case of NPG, a clear semicircle was observed on SAM formed from solution molar ratios of Man-C_8-SH: OCT of 1:4 or less. Approximately a 1:19 molar ratio of αMan-C_8-SH to OCT in the SAM solution gave the highest response to Con A binding on NPG (**Figure 4.10b**). This difference in optimal ratio could be attributed to the difference in the nature of the surface and in the ligand display associated with the surface curvature of the NPG. Molecules with polar and bulkier ω-functional groups are believed to create a larger hindrance to the adjacent molecules and

hence such molecules form more disordered monolayers. EIS data alone are not sufficient to rule out any possibility of phase segregation and formation of separate domains of αMan-C_8-SH and OCT. At lower mole ratios of mannoside, a well-mixed SAM is more likely with mannose units spaced further apart, *i.e.* highly dispersed mannose units with OCT molecules between them. Polyethylene glycol SAMs are well studied and accepted as protein resistant surfaces. In this study, HO-PEG_2-SH was also used as a diluting molecule to study effect of the polar molecules with unfavorable nonspecific adsorption. **Figure 4.10b** shows the plot of different molar ratio of the αMan-C_8-SH and HO-PEG_2-SH SAMs, and the response obtained after Con A binding.

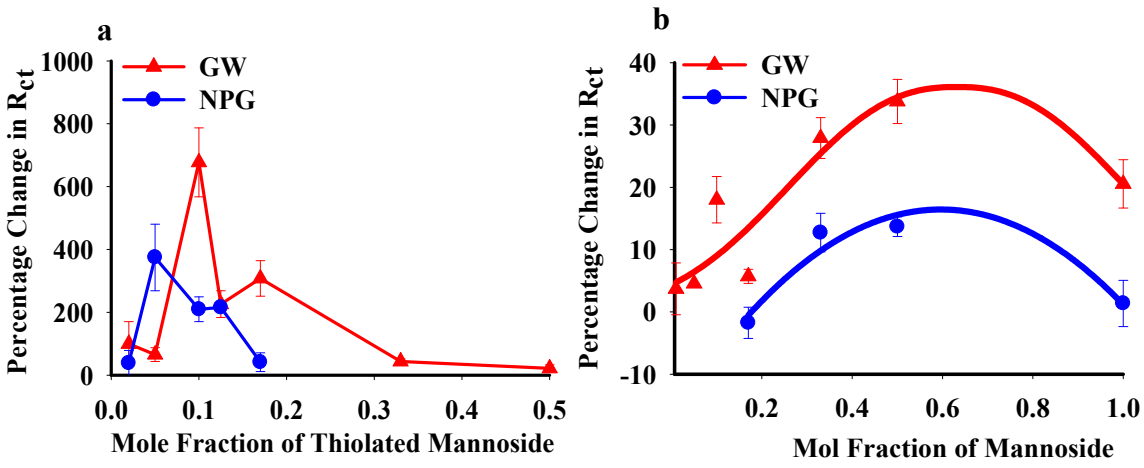

Figure 4.10. Optimal ratio of mixed SAM for Con A-mannose interaction. Mixed SAMs of αMan-C_8-SH and OCT (a) or HO-PEG_2-SH (b) mixed SAMS for Con A binding to mannose on the surface. a) Mixed SAMs of αMan-C_8-SH and OCT on gold wire (triangles) and NPG (circles) b) mixed SAMs of αMan-C_8-SH and HO-PEG_2-SH on gold wire (triangles) and on NPG (circles).

A striking observation here is that the optimal response was observed at much higher ratio of mannose in the SAM solution. The maximum response was observed at a 1:1 solution molar ratio of αMan-C_8-SH and HO-PEG_2-SH on gold wire surfaces, whereas a maximum response was observed at 1:2 molar ratios on the NPG surface.

The Nyquist plot, for the pure Gb3-C_8-SH SAM on a flat gold wire surface shows a well-defined semicircle (**Figure 4.11a**), representing charge transfer resistance and a small straight line, characteristic of the Warburg diffusion. In contrast, the Nyquist plot of Gb3-C_8-SH SAM on NPG (**Fig 4.11b** (inset)) is characterized by a very small and depressed semicircle and a dominant straight line. As for the mannoside SAM, this is a distinct difference in characteristic behavior of the carbohydrate SAM on NPG versus that on gold wire. The absence of the semicircle in NPG is because of the very large surface area and roughness of the NPG compared to that of the gold wire. A semicircle was observed for NPG either with the pure OCT SAM or the mixed SAM of OCT and Gb3-C_8-SH; no semicircle was clearly observed for the pure HO-PEG_2-SH and mixed SAM of Gb3-C_8-SH and HO-PEG_2-SH. Consistent with the CV studies EIS also shows that molecules with polar and bulkier end-groups such as Gb3-C_8-SH and HO-PEG_2-SH form relatively loosely packed and permeable monolayers on the surfaces of NPG, although similar studies show more closely packed and resistive monolayer of these molecules on the gold wire surface. These carbohydrate modified surfaces were then used for the study of carbohydrate lectin interaction (**Figure 4.11a, 4.11b, 4.11c and 4.12**). Soybean agglutinin is a lectin from *Glycine max* and binds to the NAcGal/Gal carbohydrate moiety, even though the affinity of SBA to galactose in solution phase has been found to be less compared to its affinity for NAc-Gal. Manimala et al. reported a

very low detection limit of SBA on the globotriose-modified surface which was even lower than that reported for the NAcGal [454]. Thus, the binding of carbohydrate to lectin on the surface in an SAM is different than that in the solution. SBA was chosen as a model lectin for Gb3-C_8-SH lectin interaction in our study.

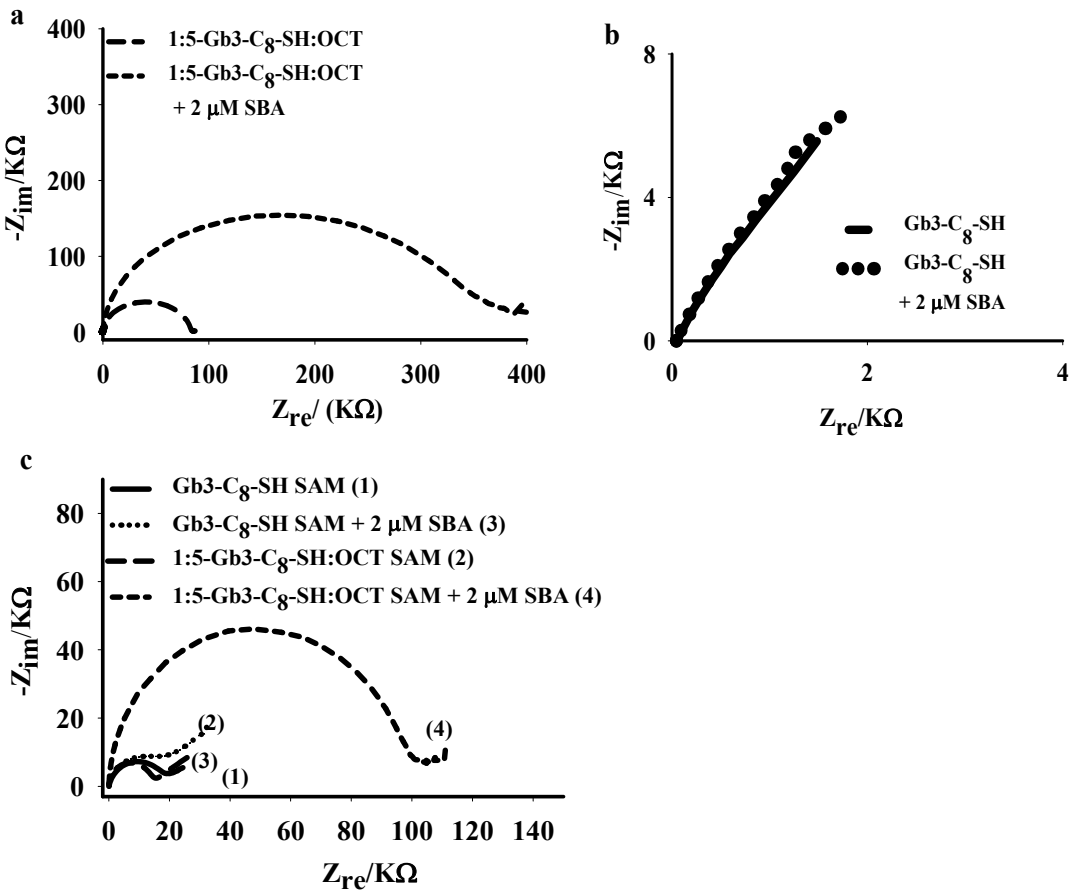

Figure 4.11. Nyquist plots for the EIS studies of the globotriose-SBA interactions on globotriose presenting SAMs. Mixed SAMs of Gb3-C_8-SH and OCT on NPG (a) Pure SAMs of Gb3-C_8-SH on NPG (b) and pure and mixed SAM of globotriose with OCT on NPG (c).

The change in charge transfer resistance after incubation with SBA for the pure Gb3-C_8-SH modified surfaces was very low for both the NPG and the gold wire surfaces (**Figures 4.12b, 4.12c**). As mentioned earlier for the mannoside presenting SAMs, this lower affinity of lectins or biomolecules at high ligand density is reported in literature and has been attributed to the sterically unfavorable interactions, because of the crowding of neighboring carbohydrate groups [453].

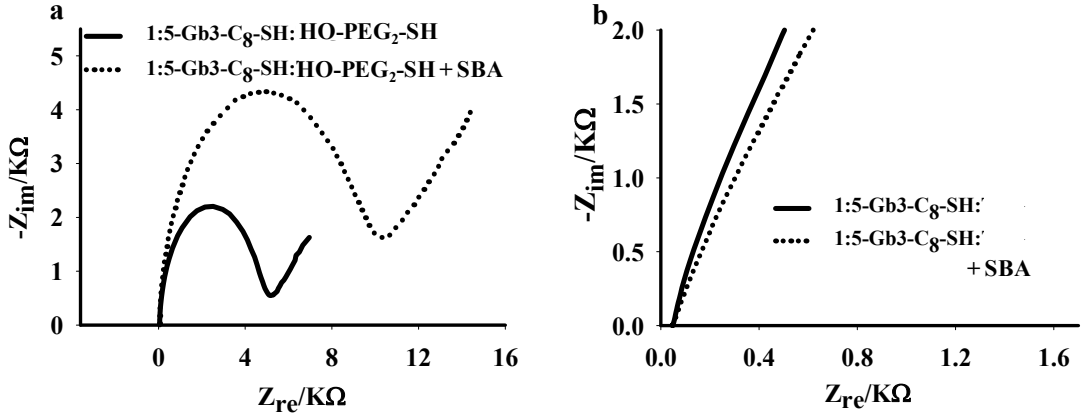

Figure 4.12. Nyquist plots for 1:5 mixed SAM of Gb3-C_8-SH and HO-PEG_2-SH. Gold wire modified with 1:5 mixed SAM of Gb3-C_8-SH and HO-PEG_2-SH before incubation with SBA, and after incubation with SBA (a), and similarly modified NPG (b).

In order to overcome this lower affinity of the lectins for high density of carbohydrates on the surface, carbohydrates on the surface are often diluted with other molecules. Polyethylene glycols are polar molecules and are the molecules of choice for the creation of protein resistant surfaces; these molecules are reported to reduce nonspecific protein adsorption to insignificant levels [455]. The increase in diameter of the semicircle of the Nyquist plot, for the OCT SAM on gold wire (**Figure 4.13a**),

showed that there is a huge increase in charge transfer resistance after incubation with 0.5 μM SBA; whereas, the increase was significantly lower for the NPG surface (**Figure 4.13b**). Increase in hydrophobicity of the SAM on NPG, relative to a gold wire surface, along with the reduced contact surface of protein in this rough architecture may be responsible for the loss of non-specifically surface adsorbed protein during washing, which is consistent with literature reports on loss of adsorbed proteins on nanoscale rough surfaces during washing [456, 457].

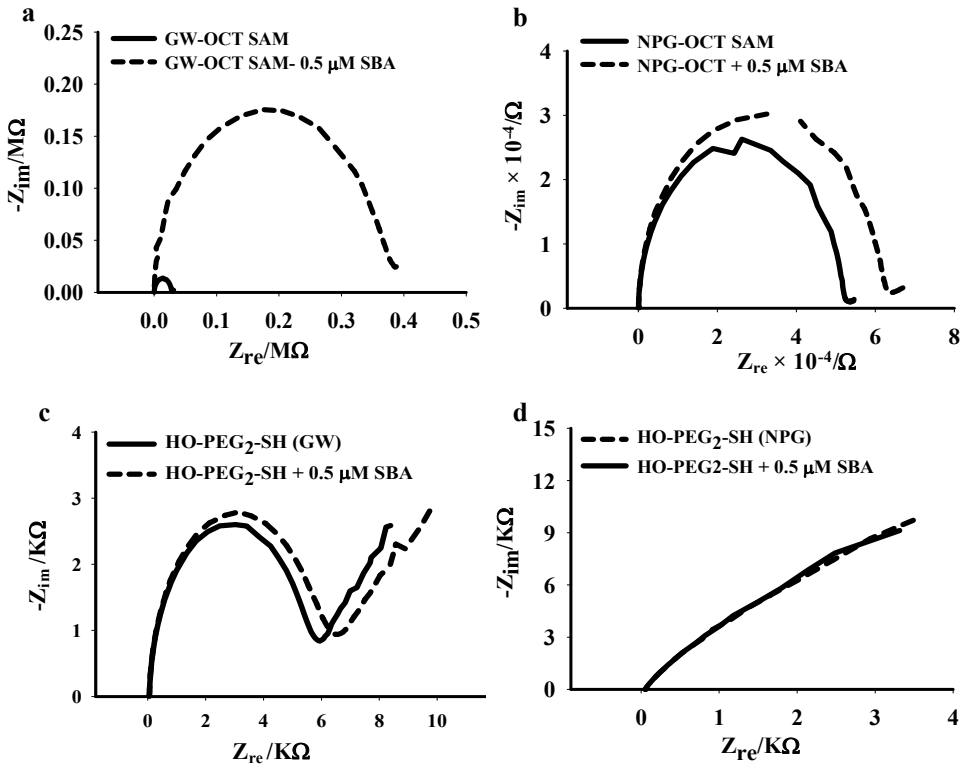

Figure 4.13. Study of the non-specific adsorption of SBA on OCT and on HO-PEG$_2$-SH on NPG and on gold wire. (a) OCT modified gold wire with and without SBA, (b) OCT modified NPG with and without SBA, (c) HO-PEG$_2$-SH modified gold wire with and without SBA (c), and HO-PEG$_2$-SH modified NPG with and without SBA in (d).

Similar studies for the nonspecific adsorption of protein were also performed using HO-PEG_2-SH modified surfaces, and no significant change in charge transfer resistance was observed after incubation with SBA on either surfaces ((**Figure 4.13c and 4.13d**).

Interestingly, the extent of increase in the size of the semicircle for OCT modified NPG was comparatively low even at 10 times higher concentrations of SBA (5 μM), indicates that the low protein attachment on the NPG surface must be either because of the low protein adsorption or because of the detachment of protein during washing.

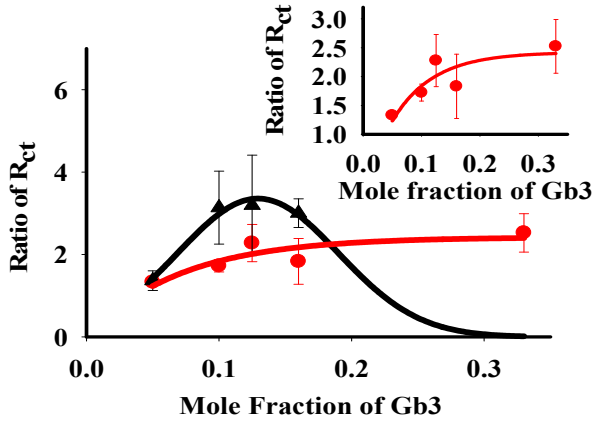

Figure 4.14. Optimal ratio of mixed SAM of Gb3-C_8-SH and OCT for SBA-globotriose interaction studies. Ratio of R_{ct} on NPG (circles) and on gold wire (triangles) is plotted for the various mole fractions of Gb3-C_8-SH and OCT in SAM solution. NPG and gold wire were incubated with different ratio mixtures of Gb3-C_8-SH and OCT followed by EIS measurement, each wire was then incubated with SBA solution for 2 h and EIS measurements were done again. Ratio of R_{ct} was obtained by dividing $(R_{ct})_{final}$ by the $(R_{ct})_{initial}$.

Figure 4.14 shows EIS studies for the various ratios of octanethiol and Gb3-C_8-SH in SAMs. The highest change in R_{ct} was observed at around 1:5 molar ratio of Gb3-C_8-SH and OCT. The length of the tail group has been found to affect the organization of the SAM on the surface and the larger tail group in Gb3 compared to that of the mannose might be responsible for the observed variation in the optimal ratio for lectin binding.

4.2.4 Comparison of Concanavalin A binding kinetics on flat gold and on NPG surfaces

Nanoporous gold with such a complex network of pores might be expected to create restricted diffusion of Con A within the network of pores and ligaments. Thus, all of the mannose molecules at the interfaces might not be equally accessible, and the lectin-carbohydrate binding kinetics might be affected by the nature of the surface resulting in the difference in kinetics compared to that on the gold wire surface. To test this hypothesis, we studied the change in charge transfer resistance as a function of Con A incubation time for NPG and gold wire surfaces. Con A to mannose binding kinetics data are shown in **Figure 4.15** at 1:9 and 1:19 solution molar ratios of αMan-C_8-SH and OCT mixed SAMs on both NPG and gold wire. Charge transfer resistance increased with the increase in incubation period, indicating an increase in surface coverage of Con A, bound to mannose at the interface. The k_{obs} value was obtained by fitting data to the equation for an exponential rise to a maximum. The k_{obs} value was dependent both on the nature of the surface as well as on the composition of SAM. **Table 4.2** shows the k_{obs} values for different composition SAMs on the NPG and gold wire surface. At 1:19 molar ratio, the binding kinetics on gold wire was faster and reached saturation more quickly than on NPG. It took about twice as long for saturation to be achieved on the NPG

surface, which can certainly be partly attributed to the longer incubation times required for Con A to diffuse into the NPG pores, and bind to the mannose units on the interior surfaces. Whereas at 1:9 molar ratio, which gives the optimal response for gold wire as the surface, no significant difference in binding kinetics was observed on NPG and gold wire surfaces. The difference in binding kinetics on these surfaces and its dependence upon the composition of the diluting molecule can be attributed to the curvature of the NPG surfaces, which results different molecular organization and ligand presentation that affect the binding kinetics at the local molecular level.

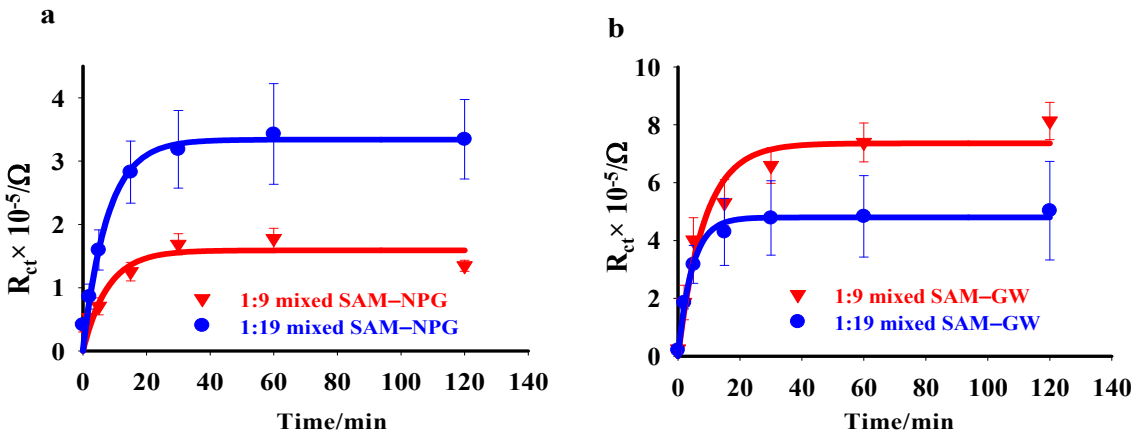

Figure 4.15. Con A-mannose binding kinetics. NPG (a) and on gold wire (b) surfaces modified with 1:9 and 1:19 mixed SAMs of Man-C8-SH and OCT were incubated with 2 μM Con A for various period of time and EIS measurements were done.

The difference in the nature of SAM on surfaces, 2D (gold wire) vs. 3D (NPG), creates differences in the rate of intermolecular interaction and hence affect the kinetics of biomolecular interactions [32, 458]. In the porous structure, this is also affected by the dimension of the molecule and the accessibility of the target molecules inside pores. Gb3-

C_8-SH is significantly larger than the diluting octanethiol molecules and αMan-C_8-SH, which might have some effect in intermolecular interaction and binding kinetics.

Table 4.2. Data summary of the binding kinetics on NPG and gold wire with different SAMs.

SAM	k_{obs} (min^{-1}) GW	k_{obs} (min^{-1}) NPG
1:9-Man-C_8-SH:OCT	0.120	0.128
1:19-Man-C_8-SH:OCT	0.220	0.130
1:5-Gb3-C_8-SH:OCT	0.135	0.063
1:5-Gb3-C_8-SH:HO-PEG_2-SH	0.093	0.113

Figure 4.16 shows the binding kinetics of Gb3-C_8-SH and SBA on the gold wire and NPG surfaces; kinetics of interaction is dependent on the nature of the diluting molecules in the SAM as well as on the nature of the surfaces. The kinetics is faster on gold wire surface compared to on NPG for both OCT and HO-PEG_2-SH mixed SAMs with Gb3-C_8-SH. Slower kinetics was observed for the mixed SAMs with OCT compared to that of the mixed SAM with HO-PEG_2-SH. The time required for saturation on NPG was 1.5 times longer than the time required on gold wire. This is similar to the observation reported for the binding of Con A to mannose on the NPG surface [21]. The slower binding kinetics in the porous three-dimensional NPG compared to that of the two-dimensional flat gold surface can be attributed to the restricted diffusion of protein through the pores [458]. Even though a clear semicircle wasn't observed for NPG with Gb3-C_8-SH or a mixed SAM with HO-PEG_2-SH, EIS data could be fit satisfactorilyto the given equivalent circuit and charge transfer resistance was extracted. Non linear least square fitting of the experimental data and the model was judged by the χ^2 values (less

than 10^{-4}) and standard error (less than 20% which is the minimum acceptable value for fitting according to Zsimpwin software supplier) both indicated that the chosen equivalent circuit represented the physical interface. The magnitude of the increase in R_{ct} with protein binding on the surface was very high on the surfaces modified with OCT and Gb3-C_8-SH SAM whereas the magnitude of R_{ct} was fairly low on the mixed SAM with HO-PEG_2-SH. As stated earlier, this higher value of R_{ct} with the mixed SAM of hydrophobic octanethiol molecules is due to the hydrophobicity assisted binding of SBA with Gb3-C_8-SH onto this SAM alone. The other reason for this higher charge transfer resistance is due to the hydrophobicity of alkanethiols SAM which creates better blocking interface compared to other SAMs in this study.

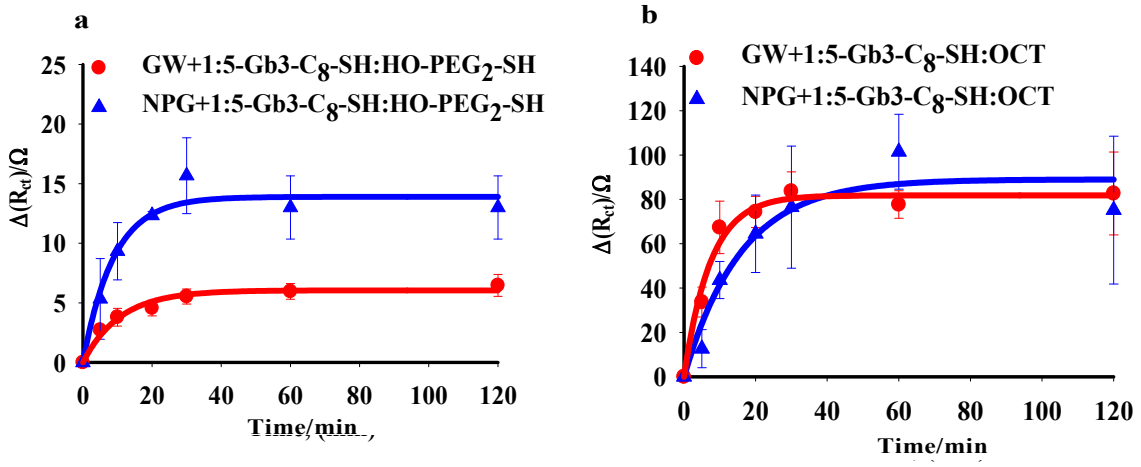

Figure 4.16. SBA-Gb3 binding kinetics on modified surfaces. Binding kinetics on Gb3-C_8-SH-SBA on 1:5 molar ratio mixed SAM on Gb3-C_8-SH and HO-PEG_2-SH (a) and OCT (b) presenting SAM. Mixed SAM of HO-PEG_2-SH on NPG ((a), triangles) and gold wire ((a), circles). Similarly, mixed SAM of Gb3-C_8-SH and OCT on NPG ((b), triangles) and gold wire ((b), circles).

4.2.5 Binding studies of Concanavalin A to mannose on gold wire and on NPG surfaces

Binding isotherms for Con A to mannose on both NPG and gold wire at 1:9 and 1:19 molar ratio of Man-C_8-SH to OCT mixed SAMs is shown in **Figure 4.17**. The binding isotherm was obtained by plotting the difference in charge transfer resistance ($\Delta R_{ct} = R_{ct,(protein)} - R_{ct,(SAM)}$) versus the Con A concentration. Stronger affinity of Con A to mannose was observed on the gold wire surface for both ratios of mixed SAM, the binding affinities calculated from this study by fitting data to a one site ligand binding model are 15 ± 4 nM and 13 ± 7 nM for the 1:9 and 1:19 molar ratios, respectively. It should also be noted that magnitude of R_{ct} achieved at saturation is different for these two different ratios of mixed SAM. Gold wires with the 1:9 molar ratio mixed SAM have almost a two-fold higher R_{ct} value at saturation compared to the R_{ct} value for the 1:19 molar ratio. There have been different reports for the binding affinity of Con A to mannose depending upon the method of study and surface composition.

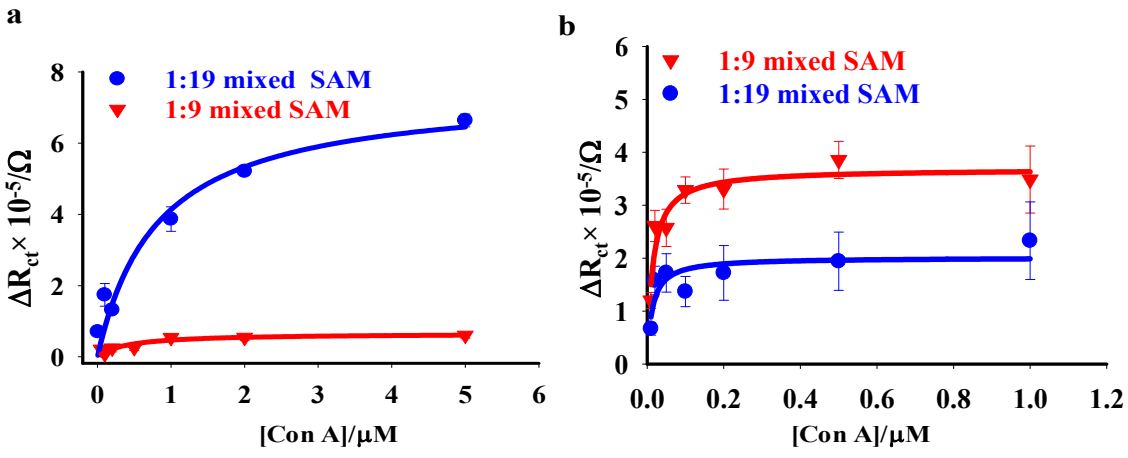

Figure 4.17. Binding affinity of Con A to mannose on mixed SAM modified NPG and gold wire surfaces. NPG with 1:9 and 1:19 mixed SAM of Man-C_8-SH and OCT

on NPG (a) and on gold wire (b) were incubated with different concentrations of Con A for 2 h and EIS measurements were done. Difference in $R_{ct} = (R_{ct})_{Con\ A}-(R_{ct})_{SAM}$.

Table 4.3. Summary of the binding affinity of Con A-mannose on different SAMs.

SAM	K_d -GW	K_d - NPG
1:9-Man-C_8-SH:OCT	15±4 nM	400±190 nM
1:19-Man-C_8-SH:OCT	13±7 nM	815±280 nM
1:2-Man-C_8-SH:OCT	244±47 nM	ND
1:2-Gb3-C_8-SH:OCT	470±0.18 nM	1.87±0.44 nM
1:5-Gb3-C_8-SH:OCT	240±0.06 nM	1.33±0.64 mM
1:5-Gb3-C_8-SH:HO-PEG_2-SH	1.57±0.340 mM	270±0.15 nM

A dissociation constant (K_d) of 178 nM was reported in a SPR imaging study of Con A - mannose interaction on a gold surface, with 50% mannose mixed SAM diluted with pyridyl groups at the interface. Even though this report showed a fairly constant K_d for different mole fractions of mannose at the interface, the difference in the nature of the diluting molecules (other molecules of the mixed SAM) and hence the nature of the interface might be one responsible factor for the observed variation in binding affinity in our case Liang et al. reported a variation in surface dissociation constant of Con A to mannoside modified glass slides depending upon the printing concentrations of mannoside on N-hydroxysuccinimide activated glass slides. An average surface dissociation constant of 83 nM was reported in this study [459]. Nahalkova et al. reported a relatively high binding affinity (K_d = 4.3 nM) of Con A to p-aminophenyl α-D-mannopyranoside immobilized on the dextran modified sensor chip (CM5) [460]. Con A - mannose interaction studies were also performed at the higher mannose concentration in the SAM. Changes in R_{ct}, after Con A binding was observed at a 1:2 mole ratio of Man-

C_8-SH and OCT on gold wire, but for NPG we did not observe any change in R_{ct}. The dissociation constant of Con A to mannoside on gold wire, at this ratio, was 244 nM (**Figure 4.18**). This is fairly similar to the literature report of Con A mannoside binding affinity, at similar ratio of mixed SAM, of 178 nM [409].

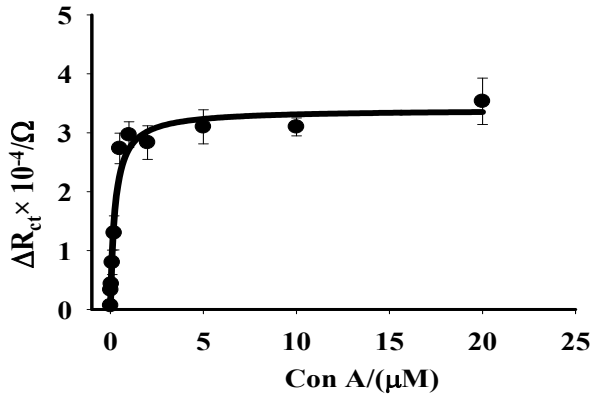

Figure 4.18. Binding isotherm for 1:2 molar ratio mixed SAM of Man-C_8-SH and OCT on gold wire.

The binding affinity of Con A mannose interaction is significantly affected by the the fraction of mannose in the mixed SAM solution used to immobilize onto surface, the binding affinity of Con A to mannose on NPG gives K_d = 400 ± 190 nM and K_d = 815 ± 280 nM at 1:9 and 1:19 molar ratio of Man-C_8-SH and OCT, respectively. Difference in ligand display at the NPG and gold wire surfaces is one of the reasons for this difference in K_d, compared to that of the gold wire, and between different ratios of mixed SAM on NPG. Another possibility is the multivalent interactions at clustered domains of mannose which might be different on the rough and curved areas of NPG and on gold wire. Apparent binding affinity could also be affected by the difference in the accessibility of ligand to the Con A molecules at NPG and gold wire surfaces. The limited ligand

accessibility for Con A molecules in the relatively constricted and narrow pores of NPG can create diffusional limitations to Con A accessing the inner parts of the nanoporous structure. The decreased on-rate of biomolecular interaction in a porous matrix because of the diffusion controlled interaction inside the pores might be another possible reason for the observed lower affinity of Con A to mannose on NPG [461, 462].

Binding studies were also conducted in a mixed SAM on αMan-C_8-SH and HO-PEG_2-SH (**figure 4.19**). As stated earlier no clear semicircle was observed with the polar HO-PEG_2-SH molecule so bias potential in EIS was decreased, and at 0.2 V applied bias potential a semicircle was observed. So, for the SAMs with HO-PEG_2-SH a bias potential of 0.2 V was applied in contrast to the formal potential applied for rest of the studies. As in the case of mixed SAM with OCT, binding affinities were higher on gold wire compared to the affinity found on the NPG surface.

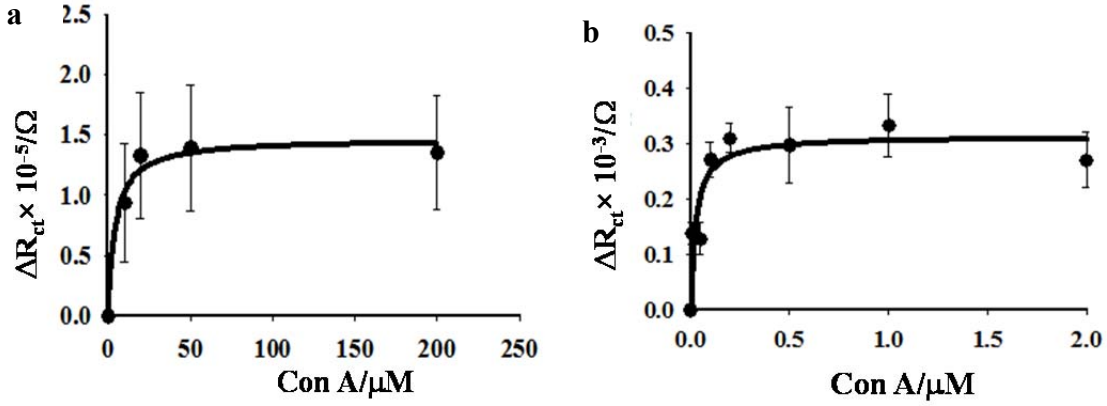

Figure 4.19. Binding isotherm of Con A mannose on 1:2 and 1:1 mixed SAM on NPG (a) and on gold wire (b) surfaces.

Binding affinity measurements were also performed for the chosen ratio of mixed SAM on NPG and GW with both OCT and HO-PEG_2-SH as diluting molecules for globotriose presenting SAMs (**Figure 4.20a and 4.20b**). **Figure 4.20a**, shows the binding isotherm for SBA binding to Gb3 on 1:5 mixed SAM of Gb3-C_8-SH and OCT on gold wire and NPG surface. The dissociation constant for adsorption of SBA to the 1:5 mixed SAMs of Gb3-C_8-SH and OCT on gold wire is K_d = 0.24 μM whereas, it is 1.33 μM on NPG. Similar results for the mixed SAMs with HO-PEG_2-SH are shown in **Figure 4.20b**, the value of K_d is 1.57 μM on gold wire and 0.27 μM on NPG for the mixed SAM of HO-PEG_2-SH and Gb3-C_8-SH. The higher affinity of the SBA on mixed SAM with OCT on gold wire can be attributed to the effect of hydrophobicity of the underlying surface that might increase the affinity by hydrophobic interaction with the lectin hydrophobic patches. The lower affinity of SBA to the mixed SAM with OCT on NPG could possibly be taken as an advantage of the NPG surface in reducing the contribution from non-specific protein adsorption, which is consistent with our prior results on binding of Concanavalin A to SAMs of OCT and a thiolated mannoside [21]. The opposite result was observed on the rough NPG surface. Because of the flat nature of the gold wire which might assist in binding of SBA to Gb3 and stabilize the complex and hence lower the K_d value. The opposite effect would be expected on the mixed SAM with HO-PEG_2-SH and hence an increase in K_d value is expected. The observed higher affinity for SBA to the HO-PEG_2-SH containing mixed SAMs on NPG than to those on flat Au suggests that NPG may have the advantage of presenting mixed SAMs with higher lectin affinity and fully resistant to non-specific protein adsorption. There are no reports for the binding affinity of SBA to Gb3 but based on the very low detection limit of SBA on the Gb3

modified surface and compared to that of the detection limit for GalNAc the value determined here seems reasonable.

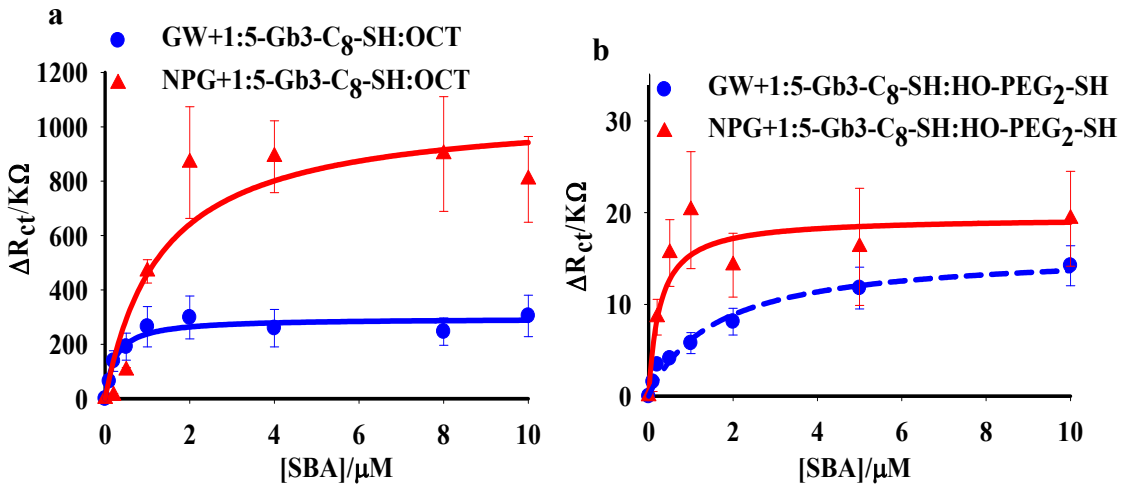

Figure 4.20. Binding isotherm for the 1:5 molar ratio mixed SAMs of Gb3-C8-SH and SBA. 1:5 molar ratio mixed SAM of Gb3-C_8-SH and OCT on gold wire ((a), circles), NPG ((a), triangles) and 1:5 mixed SAM of Gb3-C_8-SH and HO-PEG_2-SH on gold wire ((b), circles) and NPG ((b), triangles).

Table 4.4. Summary of binding affinities (K_d values) for soybean agglutinin to mixed self-assembled monolayers containing α-D-Gal-(1→4)-β-D-Gal-(1→4)-D-Glc-mercaptooctane (Gb3-C_8-SH) and either 8-mercapto-3,6-dioxaoctanol (HO-PEG_2-SH) or octanethiol (OCT).

Substrate	1:5 Gb3-C_8-SH/HO-PEG_2-SH	1:5 Gb3-C_8-SH/OCT
Flat gold	1.57 μM	0.24 μM
Nanoporous Gold	0.21 μM	1.33 μM

The overall structure and orientation of the carbohydrate presenting molecules in a mixed SAM is likely influenced by the nature of the second component in the SAM

which affects the presentation of carbohydrate group to the lectin. In a mixed SAM with OCT as a second component, is expected to promote van der Waals interaction with the octanethiol chains of carbohydrate presenting molecules and in principle lead to a more regular orientation and presentation of the carbohydrates at the interface. Similar to the longer chain alkanethiols, smaller chain alkanethiols also adopt all trans configuration on the flat gold surface [463]. In addition to the specific binding of lectin to the carbohydrates, the use of OCT in the mixed SAM will result in some measure of non-specific lectin adsorption to the surface. HO-PEG_2-SH molecules on the other hand will have a weaker interaction with the alkyl chain regions of Gb3-C_8-SH, and should result in a less well defined presentation of the carbohydrate units at the interface. However, the advantage of using HO-PEG_2-SH is that it strongly limits non-specific lectin binding to the SAM. The presence of curvature on the NPG surface in comparison with flat gold is expected to create some additional space between neighboring OCT chains, an increase in the number of gauche defects, and hence form a less ordered presentation than expected on flat gold [464]. In this study the vibrational spectroscopic data have shown that alkanethiol SAMs on nanoparticle surfaces of greater curvature present a higher fraction of gauche defects in SAM. Studies have shown that the helical or amorphous forms of polyethylene glycol chains resist protein adsorption, while an all trans configuration is not as effective [465]. Solvent penetration results in the formation of disordered HO-PEG_2-SH units [449]. The curved nature of the nanoporous gold surface should promote more effective solvent penetration amongst the HO-PEG_2-SH units and the amorphous form is more favorable on NPG than on the flat gold surface. The detailed

structural differences of these species on NPG and on flat gold surface can be obtained via spectroscopic studies of chain order and configuration on these surfaces.

4.2.6 SEM imaging of carbohydrate lectin interaction using streptavidin coated Au-np and biotinylated Con A

Protein molecules on metal surfaces cannot be imaged directly by SEM, and their imaging requires appropriate labeling of the molecules with some metals of different contrast from the supporting metal surface. Imaging becomes even more difficult on the NPG surface because of the variation in surface heights, which sometimes creates same contrast as that of the metal used for molecules on the surface. In order to study the distribution of mannose molecules, their possible orientations and their effect on mannose-Con A interaction, various SAMs were prepared on both the NPG and flat gold surface and allowed to bind to the biotinylated Con A, which was finally incubated with streptavidin coated gold nanoparticles, and imaged by SEM. Au-nps (10 nm) were expected to diffuse through the pores of NPG and provide information on the location and possible differences in molecular affinity, if any, at the pores and at the outer ligament surface of NPG. **Figure 4.21** shows the SEM images of nanoparticle immobilized on the pure SAM modified NPG and flat gold surfaces. Large numbers of Au-np were clearly seen on the flat gold surface modified with Man-C_8-SH SAM and relatively small numbers of particles were observed on the OCT modified flat gold surface. No nanoparticles were observed on the pure HO-PEG_2-SH modified flat gold surface. On the other hand, nanoparticles were not observed on any HO-PEG_2-SH, Man-C_8-SH or OCT SAM modified NPG surface. At this point it was not clear whether it was

because of the similarity in contrast of the NPG surface and Au-np or because no nanoparticles were attached to the surface.

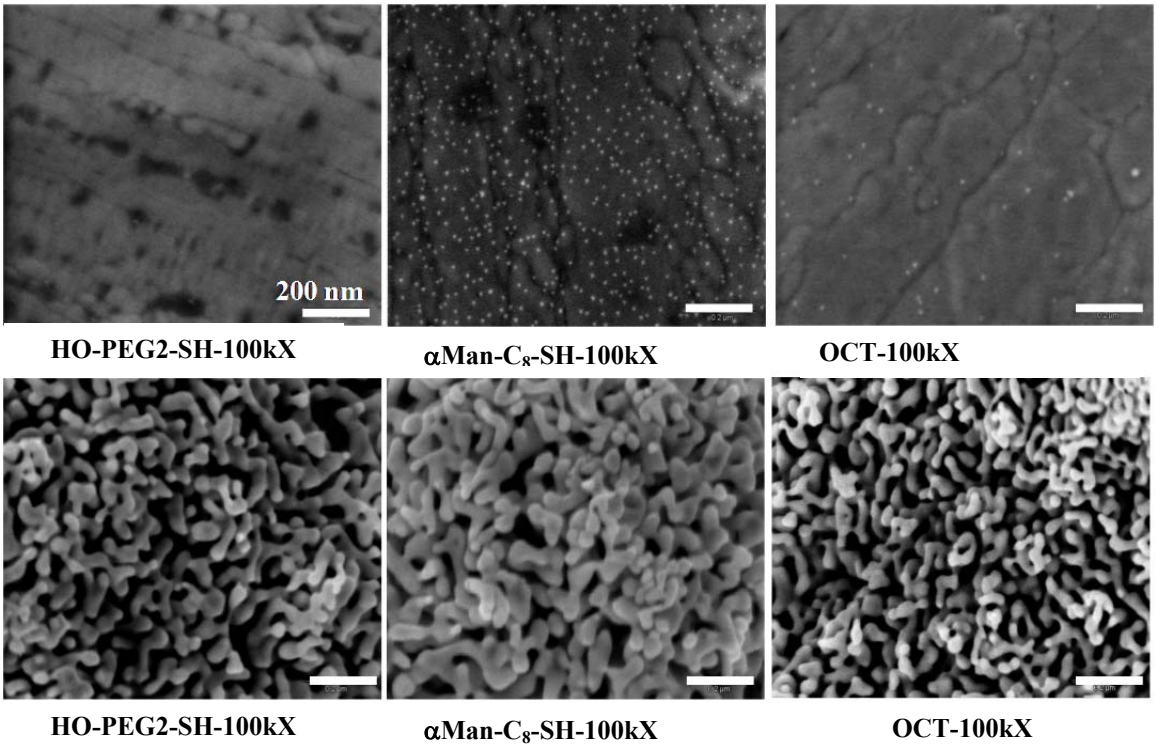

Figure 4.21. SEM images of Au nanoparticles on the single component SAMs on flat gold surfaces (upper panel) and NPG (lower panels). Surfaces were modified with various SAMs as indicated and allowed to bind to biotinylated Con A followed by incubation with streptavidin labeled Au-np. (Scale bar = 200 nm)

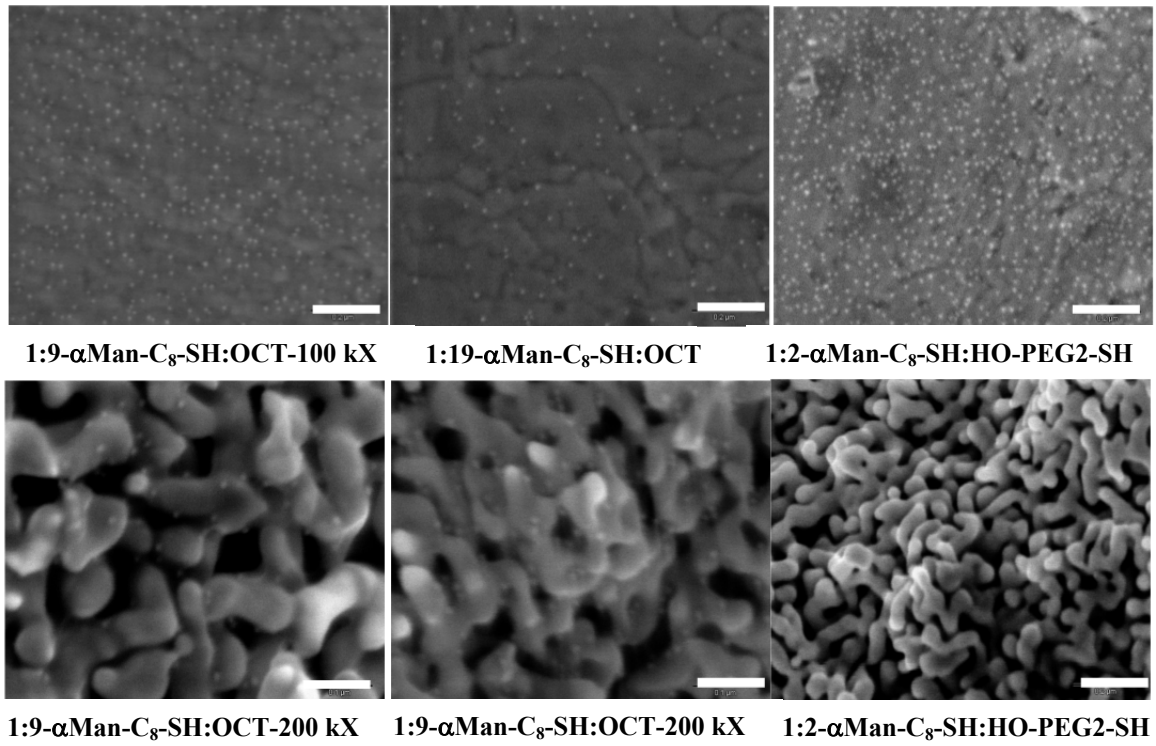

Figure 4.22. SEM images for the different mixed SAM modified NPG and flat gold surfaces. 1:9 and 1:19 molar ratio of Man-C_8-SH and OCT were chosen based on the highest response obtained for Con A binding on flat gold (upper panels) and NPG (lower panels) respectively. 1:2 molar ratio of αMan-C_8-SH:HO-PEG_2-SH has shown better response in EIS studies on NPG surface, which was chosen as the optimal ratio for Con A-mannose interaction on surface. NPG surfaces are shown at higher magnification, as Au-nps were hard to visualize at lower magnifications. (scale 200 nm for upper panel and lower right (100 kX) and 100 nm for two images on the lower left panels (200 kX)).

Figure 4.22 shows the SEM images of Au-nps immobilized on the mixed SAM modified gold wire and NPG surfaces. Consistent with the EIS studies, relatively large number of the Au-nps were seen on the 1:9 ratio mixed SAM modified flat gold surface

and almost similar number of Au-nps were observed on the NPG surface for both 1:9 and 1:19 molar ratio mixed SAMs with OCT. Mixed SAMs with HO-PEG_2-SH, on the other hand show different behavior on the NPG and the flat gold surface. No Au-nps were observed on the 1:2 molar ratio of Man-C_8-SH:HO-PEG_2-SH mixed SAM modified NPG surface but significantly large number of particles were observed on the flat gold surface. Even though there was some change in the charge transfer resistance on the EIS studies with 1:2 molar ratio mixed SAM modified NPG surface there was no nanoparticles seen on the surface, which indicates relatively small number of Au-np must have been obscured on the NPG surface due to the similar contrast of the supporting surface and the Au-np [466]. Some other methods are required for the detail understanding of the difference in molecular adsorption on these surfaces but the nanometer dimension of the NPG ligaments might be creating similar ripples as reported in literature for the gold nanoparticles. These ripples formed in mixed SAMs with polar and nonpolar tail groups and have been reported to reduce protein adsorption on the surface.

4.3 Conclusions

A number of both similarities and differences are observed in the behavior of SAMs containing a glycoside-terminated alkanethiol, either as a pure component or together with some diluting molecules. The variation in nature of the surface, i.e. gold wire surface vs. the surfaces of nanoporous gold which are curved, irregular, present a rough topography, and for which most of the surface is internal from the immediate boundary with the solution has been found to affect both the kinetics and affinity of biomolecular interactions. On both flat gold and NPG, the addition of an appropriate diluting molecule improves monolayer integrity and degree of packing order. The mixed

SAM with octanethiol presents a more effective interface for mannose binding of Con A, presumably due to improved orientation in the presentation of mannose units and a lower surface density of mannose units that allows for the multivalent binding of Con A. On the other hand the mixed SAM with polar and protein resistant HO-PEG_2-SH molecule on NPG was not as conducive as OCT molecule. Nonspecific protein adsorption is significant on the OCT modified gold wire surface, whereas it was significantly smaller on the NPG surface. However, the optimal mole fraction of mannose for Con A binding is lower on NPG than on flat gold, with the mixed SAMs of Man-C_8-SH and OCT at 1:19 molar ratio providing the optimal response on NPG as compared with a ratio of 1:9 providing an optimal response on flat gold. The binding affinity of Con A to mannose presented in SAMs on NPG is reduced, most probably due to the diffusion time required for proteins to access mannose units on the interior surfaces, which will reduce the on-rate and hence increase the value of K_d. Similar studies were performed on the globotriose presenting SAMs on NPG and on gold wire as well. The ratio of mixed SAM solution that gave maximum response after SBA incubation was different from that of the mannose presenting SAM and is attributed to the longer tail and different solubility of these molecules, which ultimately creates a different organization of SAMs on the surface. Binding affinities were stronger on the gold wire surface than on the NPG surface.

The differences in lectin – carbohydrate binding on flat Au versus on NPG are significant, and some potential advantages of NPG for use of EIS as a label-free screening method. The mixed SAMs of thiol modified carbohydrates with the hydrophobic OCT diluent show a reduced contribution from non-specific binding on

NPG, which is a potential advantage for use of NPG as a surface for such studies. The mixed SAMs containing HO-PEG_2-SH shows different effects in binding affinity for carbohydrate and lectin compared to that of the mixed SAM with OCT. The difference in affinity also depends on the nature of the carbohydrate units used in the study. EIS is highly sensitive to the variations in nature of the surface and monolayer structure and their combined effects on protein binding affinity. Detailed characterization of the organization of SAMs on NPG and on flat Au by vibrational spectroscopic methods could help understand differences in conformational order. NPG in an electrode array format could potentially prove to be of future interest for lectin-carbohydrate interactions.

CHAPTER V

DEVELOPMENT OF SQUAREWAVE VOLTAMMETRIC IMMUNOASSAYS ON NPG

5.1 Introduction

Current analytical techniques for protein biomarker detection involve methods based on radioactive labeling [467], fluorescent labeling [468], chemiluminescent labeling of either antigen or antibody to probe antibody-antigen binding [469], mass spectrometry [470], electrophoretic analysis [471] and changes in surface properties as a result of biomolecular interaction [472]. Gold nanostructures are very attractive and actively studied substrates for immunoassay development. A sensitive method for free prostate specific antigen (fPSA) detection based on antibody immobilization on gold coated cantilevers was reported by Majumdar et al. [473] Choi et al. reported an SPR based assay for PSA based on formation of a sandwich complex between antibodies immobilized on the gold surface, PSA, and gold nanoparticles labeled with polyclonal antibodies for PSA [474]. Garcia et al. reported a dual sensor for the detection of both free and total PSA based on nanogold modified screen printed electrodes and the voltammetric detection of silver deposited on their surface from Ag^{+} in solution. Deposition of Ag on the surface was assisted by indoxyl generated from the enzymatic reaction of alkaline phosphatase conjugated to the anti PSA antibody on indoxyl phosphate [475]. Rusling et al. immobilized anti-PSA antibody on a film of gold nanoparticles and developed an immunoassay based on multiple horseradish peroxidase labeled magnetic beads attached to the secondary antibody [476]. An immunoassay for carcinoembryonic antigen (CEA) captured in an antibody sandwich on nanoporous gold

leaf electrodes was reported in which the secondary antibody was conjugated to CdTe quantum dots and a 5.5 fold increase in electrochemiluminescence intensity over that on a bare gold electrode was observed [338]. An immunoassay for PSA based on the quartz crystal microbalance and gold nanoparticle amplification was reported by Tothill et al. [477] A SPR based immunosensor for CEA was reported by Nishimura et al. [25] Gao et al. reported an amperometric immunoassay for CEA on glassy carbon electrodes modified by the layer by layer assembly of carbon nanotubes onto which gold nanoclusters were electrodeposited, followed by immobilization of anti-CEA antibody, and with detection achieved by measuring the reduction in current due to oxidation of $Fe(CN)_6^{3-}$ as a result of CEA binding [478]. A competitive immunoassay for CEA was reported based on CEA|colloidal gold|chitosan membranes on screen printed carbon electrodes [479]. Electrochemical immunoassays are highly attractive because electrochemical methods can be applied to highly absorbing samples for which spectrophotometric methods are less useful**.** In addition, electrochemical devices are relatively cheap, sensitive and can be miniaturized and do not require high energy power sources [249]. A label free amperometric immunosensor for human serum chorionic gonadotrophin using hydroquinone as a redox marker and based on glassy carbon electrodes modified by both graphene sheets and nanoporous gold was reported [83]. A square wave voltammetric method based immunoassay for the detection of polychlorinated biphenyls in water samples was reported using horseradish peroxidase and o-aminophenol-H_2O_2 as a substrate [480].

Alkaline phosphatase (ALP) is a widely used enzyme label for immunoassays because of its high activity, relatively low cost, and activity against a range of possible

substrates [481]. ALP hydrolyses orthophosphoric esters to alcohols, and substrates are available whose products can be monitored using uv-visible spectrophometry [482], fluorimetry [483], chemiluminescence measurement [484] and amperometry [485]. Cyclic or linear scan voltammetry, pulse and differential pulse voltammetry and square wave voltammetry are the most popular voltammetric techniques for electroanalytical measurements [486]. The advantage of square wave voltammetry over cyclic voltammetry is listed in materials and methods. Briefly the sensitivity of SWV is higher compared to that of CV due to the rejection of background current from double layer charging in SWV [487, 488]. A competitive electrochemical immunoassay based on antibody modified gold coated nylon membrane was reported in which the competition was between antigen and glucose oxidase labeled antigen with the extent of binding detected by oxidation of the hydrogen peroxide product [489]. A competitive flow-injection immunoassay for CEA with the CEA antigen immobilized on a chitosan/gold nanoparticle composite on glassy carbon electrode surfaces, and an antibody for CEA conjugated to horseradish peroxidase competing for antigen in solution has also been reported [479].

Here we demonstrate the application of nanoporous gold as a solid electrode support for an electrochemical immunoassay for CEA or PSA using square wave voltammetry. The assay method makes use of alkaline phosphatase- antibody conjugates covalently coupled to lipoic acid SAMs on NPG. Unlike other traditional sandwich type immunoassays using multiple antibodies, the direct kinetic assay described uses a single antibody present in the conjugate with ALP. The assay was performed in both a direct and competitive format. The direct assay is based on the inhibition of the rate of

conversion of the ALP substrate p-aminophenylphosphate to product p-aminophenol due to antigen binding, which is then detected by its oxidation in a square wave voltammetric sweep. The competitive assay is based on competition for the antibody-enzyme conjugate in solution between antigen immobilized on NPG and free antigen in solution. PSA and CEA were chosen as representative protein biomarkers, readily accessible for experimentation. PSA is a biomarker for prostate cancer, in normal healthy person PSA level is less than 4 ng mL^{-1} but depending upon the age, race and family history of prostate cancer this value can vary [167]. Estimations of the surface coverage of antibody-enzyme conjugate on the NPG based on solution depletion and protein concentration assays are also presented.

5.2 Results and discussions

5.2.1 Michaelis-Menten analysis of the immobilized MAb-ALP conjugate

Enzyme immobilization has significant impact on the enzymatic activity. In order to test the biocompatibility and activity of enzyme-antibody conjugate immobilized on NPG, Michaelis-Menten kinetics studies were performed. As described in materials and methods, conjugate immobilization on NPG involved modification of surface with lipoic acid SAMs followed by the activation of carboxyl group using the EDS/NHS reaction, and finally coupling to the monoclonal antibody-alkaline phosphatase conjugate (MAb-ALP), where the MAb is either the monoclonal antibody for the PSA antigen or for the CEA antigen. Square-wave voltammetric sweeps were conducted using these modified NPG covered gold wires as working electrodes. The sweeps were conducted after incubation for 30 minutes with different concentrations of p-APP, the substrate for ALP. The incubation period allows time for the ALP enzyme to generate the p-aminophenol

product which is then oxidized to p-quinoneimine during the SWV sweep. These SWV sweeps resulted in a prominent peak for the oxidation of p-aminophenol in this concentration range. Due to the high background currents arising from charging of the electric double layer of NPG, attempts to measure the current peak due to oxidation of p-aminophenol by linear sweep voltammetry were much less successful. The 30 minute period was found to be the shortest period needed to maximize the current response arising from oxidation of the p-aminophenol ALP reaction product to p-quinoneimine, which occurs near or less than 0.1 V (vs. Ag|AgCl). The negative shift in oxidation potential of p-AP on NPG surface relative to flat gold occurs because of the better electrocatalytic activity of NPG compared to the smooth gold surface [490]. The oxidation potential of p-AP was found to be higher on gold wire surfaces compared to that on NPG. Concentrations of p-APP of 0.05 mM to 2.0 mM were studied, and a set of SWV sweeps are shown in **Figure 5.1a** for an NPG electrode modified by the MAb-ALP conjugate, where the MAb is the anti-PSA MAb. A plot of the maximum p-aminophenol oxidation peak current versus initial p-APP concentration is shown in **Figure 5.1b**. The peak current has been reported as proportional to the velocity of the reaction and can be used to create a Michaelis Menten plot. The rate of a reaction on the electrode surface can be obtained by dividing peak current by the product of nF, where, 'n' is the number of electron involved in the redox processes and 'F' is the Faraday's constant [488]. From this plot, the K_m value for the immobilized conjugate was found to be 290 μM. A K_m value of 56 ± 5 μM was reported for free alkaline phosphatase in solution using p-APP as the substrate [252]. In an earlier study using the MAb-ALP conjugate where the MAb binds free PSA, and the substrate used was p-nitrophenyl phosphate with UV-visible

detection of the p-nitrophenolate product at 410 nm, an increase in K_m from 210 μM to 300 μM was observed upon immobilization using EDC activated lipoic acid monolayers on NPG covered gold wires. The conjugation of the MAb to the antibody itself in solution was found to increase the measured value of K_m from 40 μM to 210 μM [6]. A further analysis of the Michaelis-Menten fit to these data is presented further below.

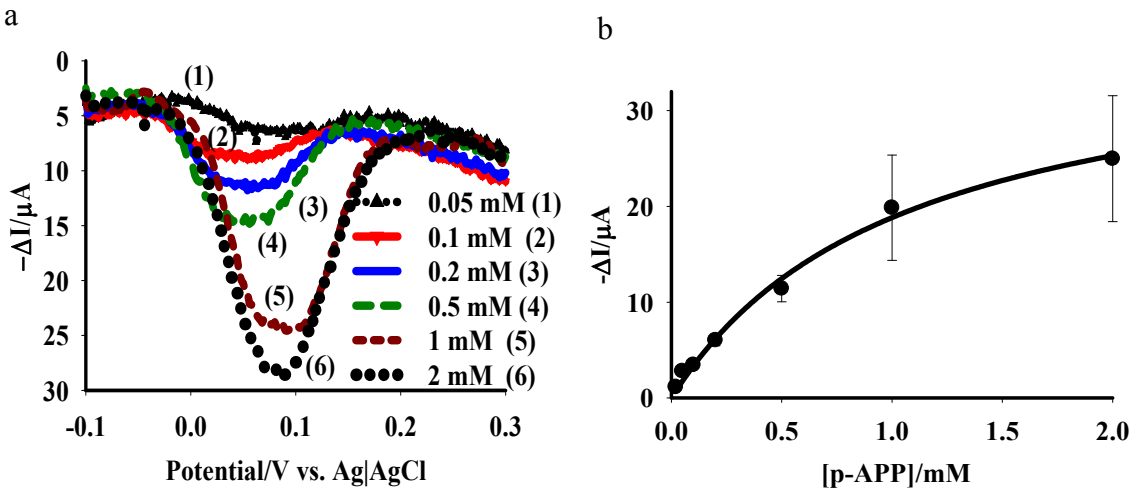

Figure 5.1. Michaelis Menten Kinetics of the IgG-ALP conjugate immobilized on the lipoic acid modified NPG surface. (a) SWV of different concentrations of p-APP incubated with anti PSA antibody-ALP conjugate immobilized NPG for 30 mins. (b) p-APP concentration vs. peak current for the estimation of K_m value of immobilized conjugate on NPG.

An increase in K_m is anticipated for enzyme immobilization inside a porous support, and there are ample literature reports showing such an increase in K_m of an enzyme after immobilization. A K_m value of 410 μM was reported by Lorenzo et al. for alkaline phosphatase covalently attached to nylon mesh using BSA and glutaraldehyde as cross linkers [491]. An approximately three-fold increase in the K_m value for type III

adenosine deaminase and a five-fold increase for type V enzyme immobilized by BSA glutaraldehyde crosslinking onto the Teflon® membrane of an ammonia sensor was reported by Rechnitz et al. [492]. A drop in V_{max} was also reported when the enzyme was immobilized onto the surface. A ten-fold increase in K_m of alkaline phosphatase to p-nitrophenyl phosphate and p-aminophenyl phosphate substrates was reported for enzyme immobilized on Nylon mesh [491]. An increase in K_m for acetylcholinesterase physisorbed on nanoporous gold surface was reported by Shulga et al. [79] A similar increase in K_m for ALP with hydroquinone diphosphate as the substrate was reported by Wilson et al. [493] Conjugation of an enzyme with some other molecule also causes some loss in enzymatic activity, a decrease in turnover number was reported when the enzyme was conjugated to IgG [494]. Enzymatic activity is dependent upon the pore sizes of the porous materials, a pore size dependent variation in enzymatic activity and K_m values were reported for 'gigaporous' (314 nm), macroporous (104 nm) and mesoporous (14.7 nm) polystyrene microspheres for the lipase from *Burkholderia cepacia* immobilized by strong hydrophobic interactions [495]. Brinker et al. showed that the change in enzymatic activity and affinity for the corresponding substrate, on immobilization, can be enzyme dependent. Their study on glucose-6-phosphate dehydrogenase and horseradish peroxidase (HRP) showed 36 % and 73% retention of enzymatic activity of the free enzyme in solution. Significant increase in K_m value was reported for both of these enzymes [496]. Enzymatic activity of immobilized glutathione-S-transferase immobilized on the porous silica was 4 times lower than the homogeneous enzyme activity of glutathione-S-transferase in solution, Miller et al. [497] Stevenson et

al. also reported an increase in K_m and decrease in enzymatic activity of HRP immobilized on glass coverslips [488].

5.2.2 Immunoassay using square-wave voltammetry and immobilized conjugates

The principle of the direct kinetic immunoassay is based on the inhibition of the access of the p-APP substrate to the active site of ALP in the MAb-ALP conjugate upon binding of the antigen, in this case either PSA or CEA and hence a drop in reaction rate of the enzyme after immunocomplex formation.

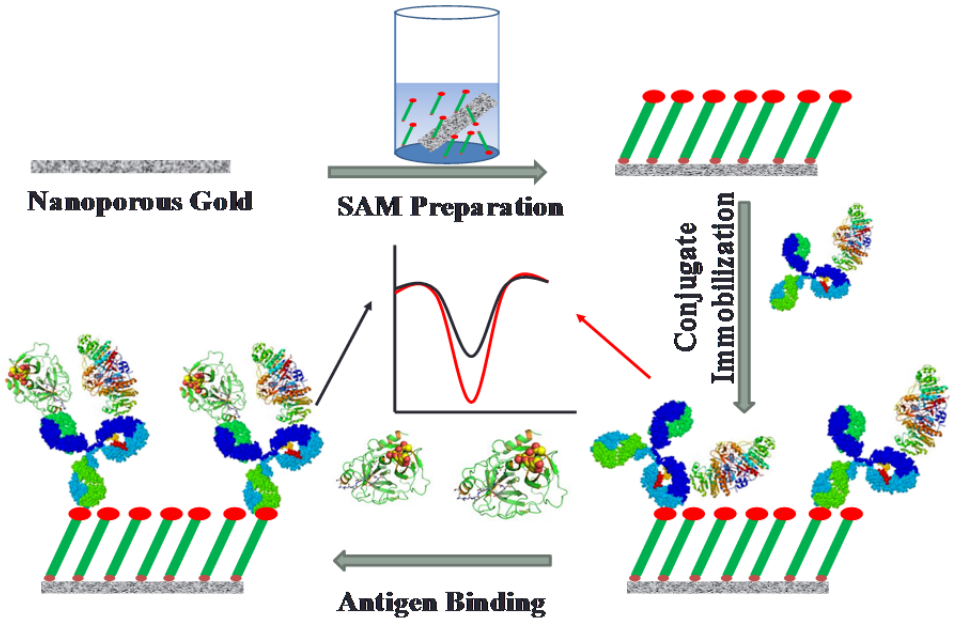

Figure 5.2. Schematic representation of the direct kinetic enzyme linked immunoassay on NPG surface.

A schematic representation of the working concept for the assay is shown in **Figure 5.2.** The binding of the antigen is expected to reduce the rate at which p-APP substrate is converted to the oxidizable p-aminophenol product. The enzyme reaction rate is assumed to be proportional to the peak current in the square wave voltammogram. The

difference in peak current before and after antigen binding is the response for the calibration plot of the immunoassay. A 250 μM substrate concentration was chosen because this is close to the K_m value and falls at the pseudolinear range of substrate enzyme kinetics. Concentrations of p-APP less than 100 μM did not produce sufficient current peaks in the SWV scans. The results obtained for the differences in peak current as a function of antigen concentration are shown in **Figure 5.3a** and **5.3b**, for PSA and in **Figure 5.3c** and **Figure 5.3d** for CEA.

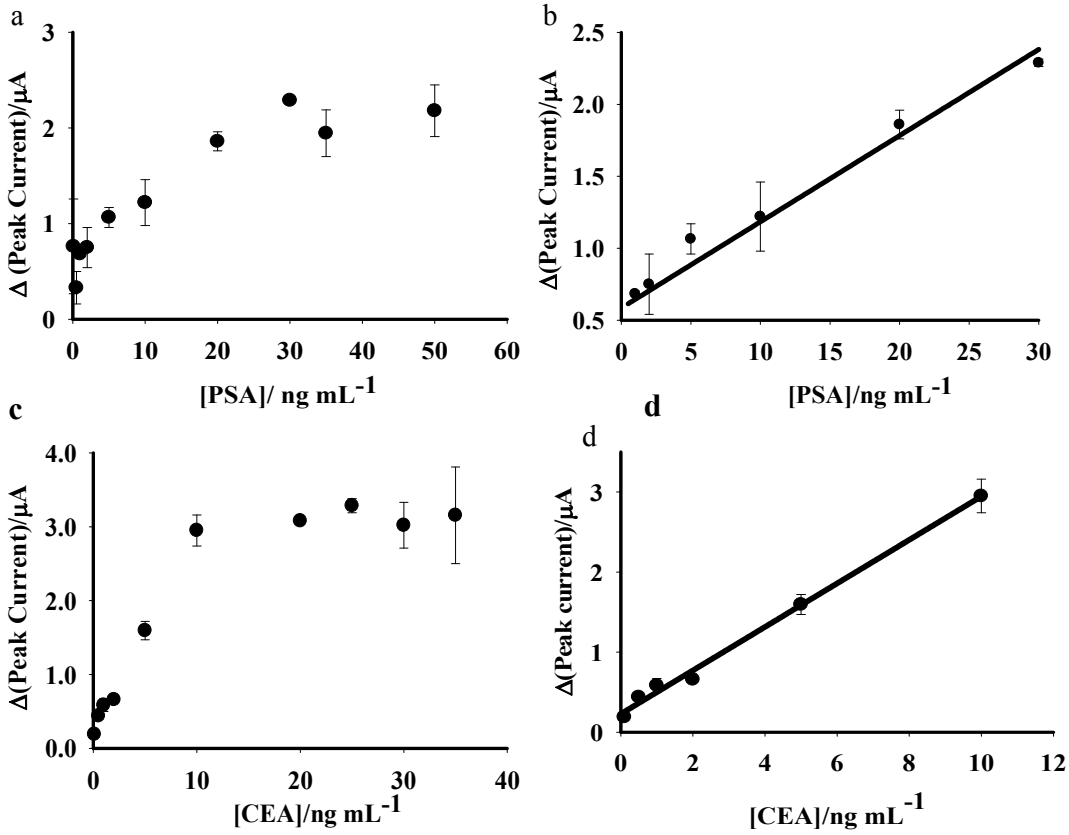

Figure 5.3. Calibration plots for the kinetic enzyme immunoassay for PSA and CEA on NPG.

The response does show a trend towards saturation at higher antigen concentration in each case. The linear range for the PSA response plot extends up to 30 ng mL^{-1} and that for the CEA response plot extends up to 10 ng mL^{-1}. The detection limit for the assay was found to be 0.75 ng mL^{-1} for PSA and 0.015 ng mL^{-1} for CEA, taking 3×SD of the lowest limit of the linear range of determination. A small finite intercept is observed in each plot, although it is more evident for the response to PSA than to CEA. We attribute this small finite positive intercept to some small loss of enzyme activity that may incur while moving the modified NPG wires back and forth between the glycine and PBS buffer solutions.

Effect of the interfering protein matrix was studied using 5.0 mg mL^{-1} of bovine serum albumin into the PBS buffer along with antigen, conjugate immobilized NPG electrodes were incubates with it and SWV measurements were performed. This was the largest amount that could be successfully dissolved. A calibration plot for the immunoassay in presence of BSA is shown in **Figure 5.4**. The presence of this amount of BSA had little effect on the response plot and the performance of the assay for PSA. The concentration of human serum albumin in serum is as high as 40 mg mL^{-1}, although we could not dissolve this amount in either buffer [498]. There was a slight increase in the intercept of the calibration plot, which might be due to the adsorption of BSA to the bare NPG surface which ultimately decreasing the redox current. New born calf serum was also used as a substitute for the human serum matrix, to study effect of interfering proteins in immunoassay. A linear response was observed even in the presence of the serum matrix but the slope and intercept both were found to change. An increased intercept is because of the adsorption of some of the component proteins or lipids onto

the NPG surface whereas the increase in slope of the calibration plot indicates some nonspecific interactions or formation of a complex between PSA and some proteins in serum.

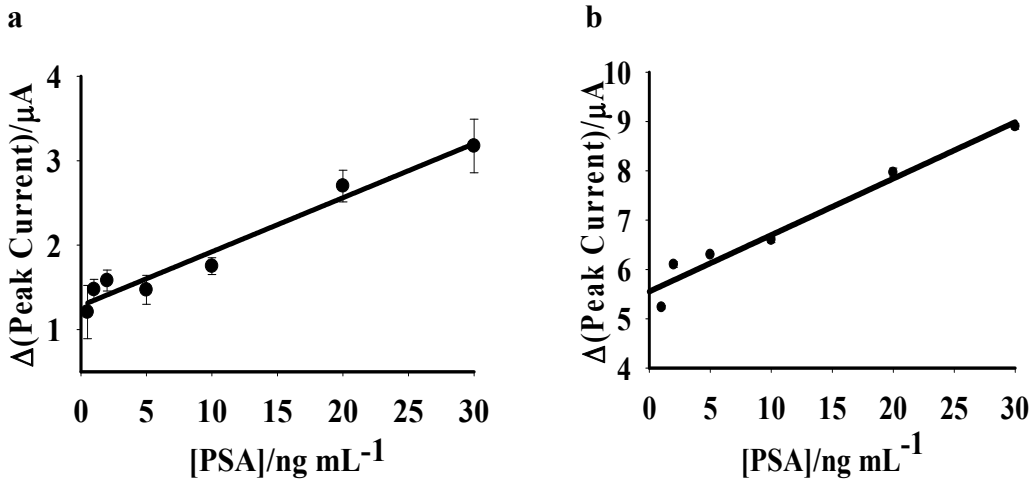

Figure 5.4. Effect on interfering proteins in kinetic immunoassay. a) Effect of 5 mg mL^{-1} BSA spiked into the incubation buffer. b) Effect of new born calf serum in the kinetic immunoassay.

5.2.3 Competitive immunoassay using square-wave voltammetry and immobilized antigen

Electrochemical immunoassay was also performed in the competitive format using immobilized antigen on NPG. A schematic representation of the working principle for the competitive assay is shown in **Figure 5.5**. The NPG surface was modified by lipoic acid SAMs followed by EDC/NHS activation of the terminal –COOH group, as noted. The activated lipoic acid esters were then coupled to either the CEA or PSA antigen.

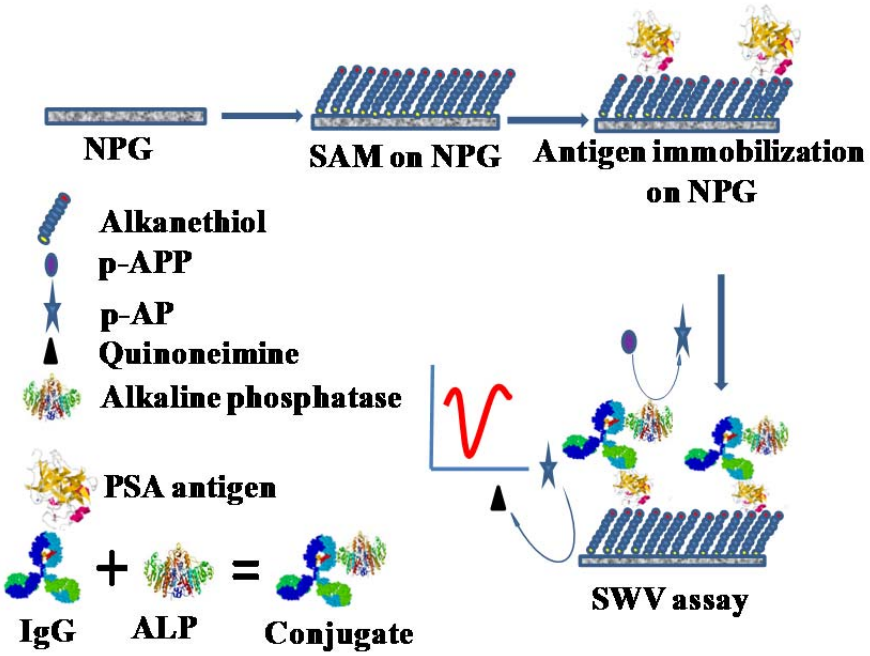

Figure 5.5. Schematic representation of the competitive immunoassay on NPG.

The concentration of MAb-ALP conjugate used in solution was chosen as 100 ng mL^{-1} after a series of experiments with different concentrations of conjugate in solution. A very small signal was obtained with conjugate concentrations of 50 ng mL^{-1} and higher concentrations did not enhance the response beyond that obtained using 100 ng mL^{-1}. The results for the competitive assay for PSA and CEA are shown in **Figure 5.6**. The addition of 5.0 mg mL^{-1} BSA to the PBS or glycine buffers did not show any effect in the response (**Figure 5.7**). The competitive assay is sensitive at lower concentrations of antigen, below about 4 ng mL^{-1} and is somewhat complimentary in response to the direct assay presented above. The amount of conjugate bound to antigen on the NPG surface, measured from the activity of ALP, was proportional to the amount of antigens in solution and showed an exponential decay with concentration. At higher antigen concentrations, a residual and nearly constant peak current is observed, which we

attribute to some non-specific adsorption of the MAb-ALP conjugate onto the gold surface.

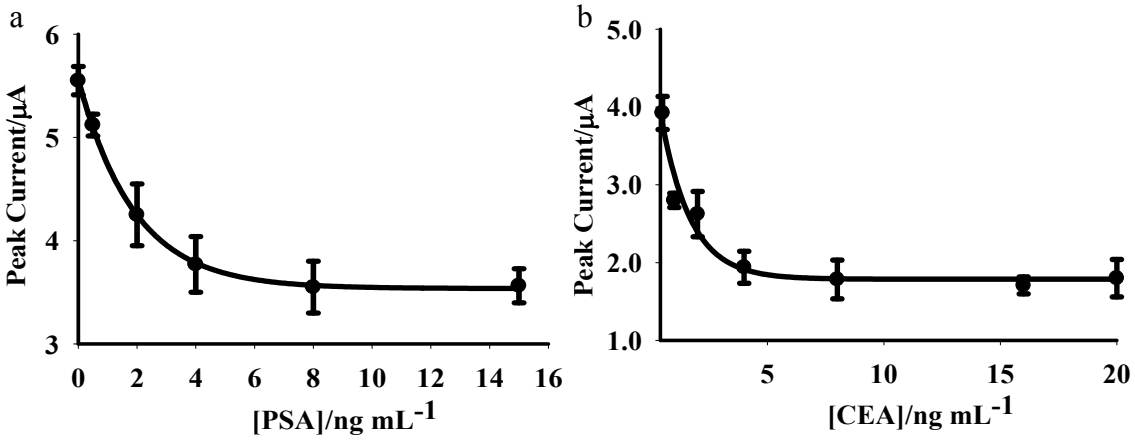

Figure 5.6. Calibration plots for the competitive immunoassays for PSA (a) and CEA (b).

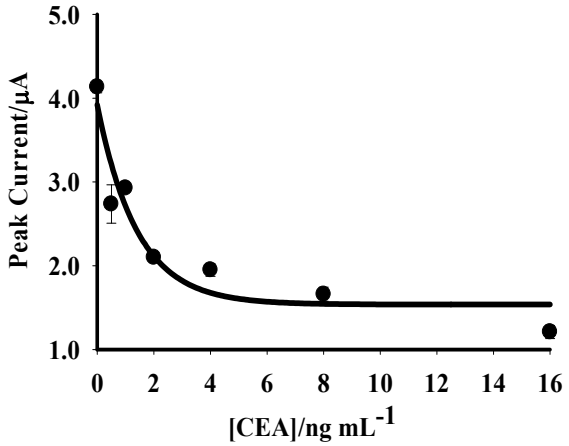

Figure 5.7. Effect of 5 mg mL^{-1} BSA in competitive assay. Standard CEA solution was added to the incubation buffer containing 5 mg mL^{-1} BSA for a given period of time and immunoassay was performed .

5.2.4 Estimation of surface coverage of MAb-ALP conjugate on NPG

Since the NPG surface is modified with LPA before protein immobilization, the surface coverage of lipoic acid on the NPG electrodes was estimated by reductive desorption of the SAMs in 0.5 M NaOH solution. Two reductive desorption peaks were observed for LPA SAM modified NPG. Each peak was integrated independently and the sum of the charge under the two peaks was taken for the estimation of surface coverage. The average (n =5) surface coverage for lipoic acid SAMs was found to be 2.42×10^{-10} mol cm^{-2}. The gold surface area was taken as the 12.5 cm^2, which was determined from the oxide stripping experiments. The surface coverage of thiol atoms of straight chain alkanethiols SAMs on flat gold surfaces has been reported to be 7.6×10^{-10} mol cm^{-2}. Similarly, the surface coverage of lipoic acid is reported to be 7.1×10^{-10} mol (of thiols) cm^{-2}, which is equivalent to 3.5×10^{-10} mol cm^{-2} of lipoic acid molecules cm^{-2}, assuming two thiol groups per lipoic acid molecule [499, 500]. These results show that the surface coverage of lipoic acid on NPG surface was less than monolayer coverage and only 70% of the surface was occupied by these molecules. Thus the monolayer of the lipoic acid molecules on the NPG surface is disordered. Surface coverage of protein molecules on the lipoic acid modified NPG surface was determined by solution depletion studies and by BCA protein concentration assay. 10 NPG wires modified with a lipoic acid SAM, and terminal –COOH group activated by EDC/NHS chemistry, were added to the 25 µg of MAb-ALP conjugate or to 10 µg of the antigen in 100 µL PBS buffer. Wires were incubated for 24 hours at 4 ºC. Wires were then removed from the incubation solution and rinsed with 100 µL of PBS buffer three times. The PBS buffer used for rinsing was collected and the amount of protein in it was determined by the BCA assay. The amount

of protein remaining in the incubation solution was determined independently and added to the amount of protein leached during washing. The difference between the amount of protein initially present in solution and the final amount gave the estimated amount of protein attached to the NPG wires. The amount of these biomolecules immobilized on the NPG surface, as determined by BCA assay, is given in **Table 5.1**. Given the surface coverage of lipoic acid, equivalent to 2.42 $x10^{-10}$ mole cm^{-2} and the surface coverage in mole cm^{-2} of either the MAb-ALP conjugate (1.9×10^{-13}) or of the PSA (9.7×10^{-13}) or CEA (3×10^{-13}) antigens, it is evident that a small fraction of the lipoic acid molecules are conjugated to protein in either case.

Due to the range of possible orientations of these molecules on the surface, the occupied area per molecule of these antigens or the conjugate is subject to variability. Hence, any estimate of surface coverage is approximate in the absence of orientational information. However, estimations can be made based on the dimensions of these proteins. Maximum and minimum possible surface area estimation was done using the structures found in the Protein Data Bank. Individual protein molecules were confined in a bound box and the dimension of the bound box is regarded as the possible dimension of the protein molecule. For example, the structures of PSA in the Protein Data Bank (2PSA), the dimensions of the PSA antigen are 4.1 nm x 4.5 nm x 5.1 nm. The footprint on the surface for the PSA antigen is thus estimated as ranging from 18.5 (4.1 x 4.5) nm^2 – 23.0 (5.1 x 4.5) nm^2. The corresponding dimensions for the CEA antigen (1E07) are 28 nm x 3.4 nm x 3.7 nm, those for ALP (1B8J) are 7.8 nm x 8.6 nm x 10 nm, and those for a typical IgG (1HZH) are 11.4 nm x 10.5 nm x 16 nm. The information on the dimensions of these proteins is summarized in **Table 5.1**, along with the ranges of their

possible surface footprint areas. Approximate dimensions of the MAb-ALP conjugate can be estimated assuming that there is one enzyme added per antibody. The labeling process is expected to add 1-3 ALP enzymes per IgG [501].

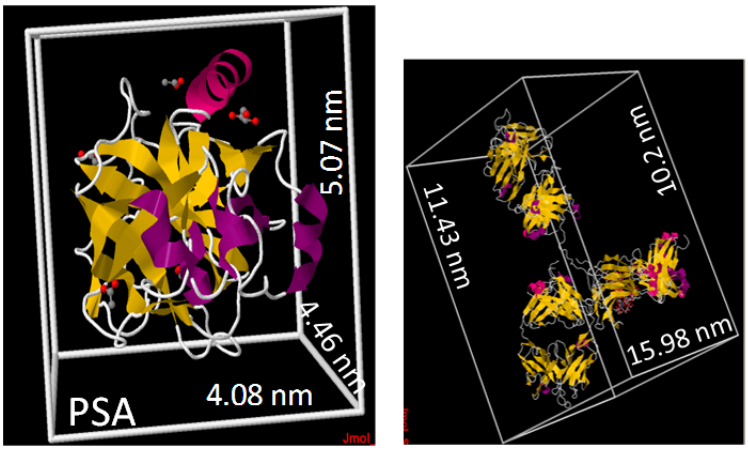

Figure 5.8. Bound box for the estimation of the protein footprint on NPG surface.

Using these dimensions, the maximum theoretical surface coverage would be in the range of (0.355 - 1.16) x 10^{12} molecules cm^{-2}. The surface coverage that resulted from the protein concentration assay solution depletion measurements for the MAb-ALP conjugate is 0.115 x 10^{12} molecules cm^{-2}, which corresponds to the fractional surface coverage of 10 – 32%. For the PSA antigen, the range of estimated maximum theoretical surface coverage is (4.35 – 5.41) x 10^{12} molecules cm^{-2} compared to the coverage estimated from solution depletion measurements of 0.588 x 10^{12} molecules cm^{-2} suggesting a fractional coverage of 11-42%. For the CEA antigen, the range of estimated maximum theoretical surface coverage is (1.03 – 0.97) x 10^{12} molecules cm^{-2} compared to the coverage estimated from solution depletion measurements of 0.1 x 10^{12} molecules cm^{-2}, suggesting an approximate fractional coverage of 10 % or less. The estimated ranges for surface coverages are summarized in **Table 5.2.**

Table 5.1. Summary of surface coverage for different proteins on NPG, calculated by solution depletion studies (BCA assay).

Protein	Mol wt. kDa	Surface Coverage		
		Mass $\mu g\ cm^{-2}$	mol cm^{-2}	Molecules cm^{-2} (mol $m^{-2} \times N_{avo}$)
PSA Antigen	34	0.033	$9.7x10^{-13}$	$5.8\ x10^{11}$
Conjugate (IgG+ALP)	146+69	0.041	$1.9x10^{-13}$	$1.1\ x10^{11}$
CEA Antigen	180	0.054	$3x10^{-13}$	$1.0\ x10^{11}$

Table 5.2. Theoretical and experimental surface coverage of proteins on NPG.

Proteins	Max[a]		Min[b]		Surface Coverage (calculated) (molec/cm^2)
	Surface area(cm^2)	Surface Coverage (molec/cm^2)	Surface area (cm^2)	Surface coverage (molec/cm^2)	
PSA antigen	57.4210^{-14}	1.44×10^{12}	18.5×10^{-14}	5.4×10^{12}	5.8×10^{11}
IgG-ALP conjugate	$282\ 10^{-14}$	3.55×10^{11}	86×10^{-14}	1.16×10^{12}	1.1×10^{11}
CEA antigen	$103.6\ 10^{-14}$	9.65×10^{11}	$12.6\ 10^{-14}$	7.94×10^{12}	1.0×10^{11}

[a]Theoretically possible maximum surface areas were calculated by confining molecules inside a bound box and maximum combination of dimensions were takes to obtain maximum surface areas. [b]Minimum surface area was calculated from minimum values of dimensions.

5.3 Conclusions

The high surface area of NPG and its ability to be used as an electrode for SWV detection of an oxidizable enzyme product, in this case p-aminophenol, was successfully

applied for the development of electrochemical immunoassays. The use of SWV is required to overcome the large double layer charging effect on the NPG electrode. The assay approach can be applied to a wide range of protein antigens. In the present study, PSA and CEA are used as readily available and widely studied biomarkers for testing the strategy of using SWV and a NPG electrode. The use of other enzymes in the MAb-enyzme conjugate, such as horseradish peroxidase, could also be considered. Even though there might be relatively lower specificity of the current assay approach compared to the sandwich immunoassays utilizing multiple antibodies, it reduces the cost and complexity of the assay. Linear range and the detection limit of PSA immunoassay extend across the so called diagnostic gray zone of 4-10 ng mL^{-1} [476] and the analytical characteristics mentioned for some of the commercial kits such as PSA watch TM, BS-0011 (Mediwatch USA Inc, West Palm Beach, FL,USA) [502] and Human PSA Elisa Kit (cat.No. EL10005) (Abazyme LLC, Needham, MA, USA) [503] and literature reports on immunoassay for PSA [257, 476, 504]. Our results on the immunoassay for CEA are in reasonably good agreement with the other reports in similar studies such as that of Lin et al., who reported an immunoassay for CEA with linear range of 1-25 ng mL^{-1} and detection limit of 0.5 ng mL^{-1} [505]. In another study, Tang et al. reported an impedimetric immunoassay for CEA with detection limit of 0.1 ng mL^{-1} and a linear range of 0.5-20 ng mL^{-1} [79].

The p-APP substrate is convenient due to its commercial availability; however, ALP can act against a number of other reported substrates that can be oxidized at an electrode surface. The product p-aminophenol is oxidized near 0.1 V (vs. Ag|AgCl). Other possible substrates include p-nitrophenyl phosphatate which is converted to p-

nitrophenol by alkaline phosphatase and undergoes electrooxidation at +1.0 V, at such a high potential substantial background due to electrooxidation of components in biological samples will reduce the bioanalytical applicability of the assay also at this high potential electrooxidation of gold might weaken Au-S bond and hence desorb SAM from the surface, phenyl phosphate is converted to phenol at +0.7 V vs. Ag|AgCl but it has been reported to form a passivating polymeric film on the electrode surface.[506] Naphthyl phosphate is converted to naphthol and undergoes electrooxidation at 0.4 V vs. Ag|AgCl [507], ascorbic acid phosphate is converted to ascorbic acid at 0.32 V vs. Ag|AgCl but no redox peak was observed in our study for this substrate, also, the presence of ascorbic acid in biological sample makes it a relatively less attractive substrate for biological assays [504]. Hydroquinone diphosphate is a relatively new substrate for alkaline phosphatase which gives hydroquinone under dephosphorylation by alkaline phosphatase. Hydroquinone undergoes electrooxidation at 21 mV on gold surfaces [493]. Hydroquinone diphosphate was not commercially available so p-aminophenyl phosphate was the substrate of choice, which is one of the most favored substrate for ALP in electrochemical assays [480, 507]. The product p-aminophenol is oxidized near 0.2 V (vs. Ag|AgCl) on glassy carbon electrode surface. Some of the advantages of p-APP over other substrates that make p-APP an attractive substrate include the low oxidation potential, less electrode fouling and electrochemical reversibility, also it is commercially available [507]. p-Aminophenyl phosphate was the substrate of choice, which is one of the most favored substrate for ALP in electrochemical assays [257, 480]. The product p-aminophenol is oxidized near 0.2 V (vs. Ag|AgCl). Some of the advantages of p-APP over other substrates that make p-aminophenyl phosphate an attractive substrate is

because of the low oxidation potential, less electrode fouling and electrochemical reversibility; also it is commercially available [505]. Therefore in our experiments, sweeps were conducted after incubation for 30 minutes with different concentrations of p-APP, a substrate for ALP. The incubation period allowed time for the ALP enzyme to generate sufficient p-aminophenol product that is then oxidized to p-quinoneimine during the SWV sweep.

A feature of this assay strategy that should be noted is that access of the p-AP product to the gold surface where it is oxidized must be possible, and as such perfect and well-packed monolayers with very high coverage of protein may not be conducive to the presented assay since they would block the oxidation of p-AP. As such, disordered monolayers presenting sites at which p-AP can be oxidized are actually a desired feature of this assay. The p-AP produced by the enzyme action during prior to the SWV sweep is likely building up inside the NPG pores and beginning to diffuse out into the bulk solution. Additional substrate will be diffusing into the NPG pores as p-APP is depleted within NPG by the action of the ALP enzyme. The oxidation current observed should arise from oxidation of p-AP within the NPG interior and also from p-AP located around the NPG electrode some distance into the bulk solution.

NPG electrodes can be prepared in a range of sizes and formats, with a range of pore sizes, and are suitable for miniaturization or use in flow-through electrochemical devices. The properties of NPG electrodes present opportunities for the development of new electrochemical assay formats. The greatly enhanced surface to volume ratio of NPG facilitates strategies such as the one described here which rely upon the enhancement in

peak current in a square wave voltammetry sweep following product formation within a nanoporous electrode.

CHAPTER VI

DEVELOPMENT OF SQUAREWAVE VOLTAMMETRIC ENZYME LINKED LECTIN ASSAYS ON NPG

6.1 Introduction

Protein glycosylation is one of the most common post-translational modifications and plays crucial roles in protein folding, biological activity and proper functioning of proteins [508]. Differential protein glycosylation has been found to be associated with different disease conditions and malignancies [509]. Since nearly 50 % of mammalian proteins and almost 80 % of membrane proteins are glycosylated, carbohydrate based biomarkers are attractive and are actively being researched [298, 510]. Cell surfaces are covered with a glycocalyx which performs many important functions, varies with cell type, and with different stages of cell growth and differentiation [511]. Cell surface carbohydrates are found to change during the course of malignancy and with cancerous state [403]. Data on the strength and selectivity of protein-carbohydrate interactions is important for improved understanding of carbohydrate associated biological processes.

Some of the most commonly used analytical techniques in glycoanalysis include mass spectrometry [512], nuclear magnetic resonance spectroscopy (NMR) [513], high performance liquid chromatography (HPLC) [514], and capillary electrophoresis (CE) [515]. Even though these techniques are highly sensitive and can provide detailed information about the structure of carbohydrate units, these techniques require high expertise, and expensive and complex instrumentations which is not feasible for many laboratories or for high throughput glycoprofiling. Also, some of these techniques are

destructive and most are not suitable for the cell surface glycan analysis in living cells. Thus development of array type analytical methods for the high throughput screening of glycoforms is gaining increasing interest among researchers in glycomics [117]. Even though array based methods do not provide detailed information about carbohydrate structure, often information on only the terminal or functional carbohydrate unit is enough for routine analysis and for the identification of active carbohydrate units on glycoproteins, on extracellular matrices of biofilms, etc. Several biosensors have been developed for the study of glycan-protein interactions based on optical transduction (surface plasmon resonance [516], localized surface plasmon resonance [417], fluorescence measurements [517]), piezoelectric (quartz crystal microbalance [518]), electrochemical[519] (cyclic voltammetry, electrochemical impedance spectroscopy [520], differential pulse voltammetry [521], square wave voltammetry, pulse amperometric detection), microcantilever deflection[522], flow cytometry [523], amongst other methods. Electrochemical methods for the analysis of cell surface glycans have been employed for glycan analysis on living cells [425]. As discussed in earlier section, the binding affinity of the carbohydrate and lectin is associated with the nature of the underlying surface and the density of the carbohydrate on the surface. Traditionally carbohydrate-protein interaction studies are predominantly performed on relatively flat surfaces such as on substrate supported gold films [425], glass [524] or polystyrene [525] with a limited but growing number of studies on nanoparticles [526]. Gold surfaces are highly attractive for protein immobilization because of the spontaneous interaction of gold and sulfur which makes functionalization of gold surfaces convenient, and the surface can then be modified by self-assembled monolayers presenting many different

terminal functional groups, which can be used in conjugation reactions for the attachment of biomolecules [85]. Of NPG to protein-carbohydrate interaction studies is the prospect that the rough and curved nature of the surfaces of NPG may prove to be a better mimic of carbohydrate display on cell surfaces. NPG is an excellent surface for signal amplification. Additionally NPG is superior to nanoparticle modified electrodes since it doesn't involve steps of nanoparticle purification and immobilization onto the electrode surface. Our electrochemical lectin assays on the NPG surface is simple, easy and an excellent technique for the high throughput screening of glycoforms of glycoproteins or any glycoconjugates.

Enzyme-linked immunosorbant assays (ELISA) represents a gold standard for assays, whereas similar assays based on lectins as the recognition element for glycans, enzyme linked lectin sorbent assays, are not as common [527]. Lectins are carbohydrate binding proteins of non-immune origin and without enzymatic activity [157]. Lectins are used as recognition elements in several glycoanalytical techniques including enzyme linked lectin assays, immunohistochemistry, affinity chromatography etc.[528] As a consequence of the poor immunogenicity of carbohydrates, antibodies specific for carbohydrates are not very common because the resulting antibodies are of low affinity; thus, lectins are the preferred recognition element in glycoanalysis [528]. Even though enzyme linked lectin assays are important techniques for the analysis of glycoforms, they have not been used routinely for glycoanalysis. This is partly because of the weaker carbohydrate-lectin affinity, the complexity of the carbohydrate distribution in biological systems, absence of a standard and easy to operate technique, and the high background in traditional ELLSA because of the nonspecific adsorption of proteins which are often

glycosylated and hence bind to the lectin. Studies have been performed to evaluate blocking agents and significant progress has been made to identify blocking agents that produce the least background in ELLSA [529]. The traditional approach of ELLSA involves immobilization of glycoproteins or glycoconjugates on the 96 well plates by physisorption followed by washing and then incubation with biotinylated lectins and then avidin or extravidin labeled alkaline phosphatase or horseradish peroxidase as an enzyme label, for the purpose of detection [530]. Enzyme linked lectin assays are important for studying the glycan binding of novel lectins or in the study of different glycosylation and identification of glycan biomarkers [531, 532]. The most common approach for the immobilization of carbohydrate and glycan conjugate is physisorption but this is not a very efficient process as there is always a possibility of loss of protein during washing, denaturation etc. The essential requirements for the development of high throughput screening of glycoform is efficient loading onto the surface and retention of activity as well as proper orientation of the recognition moiety on the surface. Thus, covalent coupling onto the surface would be a better approach than physisorption for immobilizing glycoproteins onto the surface. SAMs on gold are relatively easy to prepare and functionalize for subsequent coupling to lectins. A SAM based ELLSA was developed by adsorbing proteins on Ti/Au coated slides with detection performed by assembling biotinylated lectin and avidin/alkaline phosphatase (ALP) on the plates [533]. The amount of lectin bound to the surface was then correlated with the activity of ALP. Another approach involves the use of lectins covalently attached to enzymes. A majority of these assays are based on the absorbance measurements and are done by incubating the surface bound complexes for a significantly long period of time to produce an adequate

signal. The long incubation times can lead to complications as many of the enzymatic products are not always stable and errors are introduced due to substrate self-degradation.

The aim of the present study is to develop an electrochemical enzyme linked lectin assay on nanoporous gold. Proof of concept has been successfully applied to some of the biologically significant glycoproteins which are being studied as biomarkers for various diseases including transferrin, immunoglobulin G, carcinoembryonic antigen, and prostate specific antigen. Serum transferrin consists of two biantennary glycan units and glycosylation changes in transferrin have been reported for different diseased conditions including hepatocellular carcinoma, sepsis etc.[534, 535] Carbohydrate deficient transferrins are regarded as biomarkers for alcoholism [191]. Human IgG is the one of the most prominent proteins in human serum and different glycosylation is observed during diseased states [536]. Fetuin is regarded as a biomarker for vascular calcification and low levels of circulating fetuin has been found to be associated with the peripheral arterial disease in type 2 diabetes [537, 538]. Carcinoembryonic antigen is a 180 kDa glycoprotein which is involved in cell attachment and is a biomarker of colorectal cancer, almost 50 % of the total weight of CEA is associated with the glycan part [539]. Prostate specific antigen is a biomarker for prostate cancer; it is also heavily glycosylated and its different glycosylation patterns have been reported as related to tumorigenic conditions [540].

Electrochemical assays are attractive because they are not affected by turbidity or background absorbances, involve cheaper and relatively simple instrumentation, and potentially can be miniaturized and made quicker to operate [252]. We report here the application of NPG for development of an electrochemical ELLSA, both as a kinetic

assay as well as in the traditional ELLSA format using NPG as a solid substrate and self-assembled monolayers for the protein immobilization. Our traditional type ELLSA on the NPG surface simplifies the assay procedure by using direct electrochemical determination of product formed from the enzymatic reaction of alkaline phosphatase on the substrate p-aminphenylphosphate. This electrochemical assay is comparatively quick as no long incubation with the substrate is required and thus the possibility of degradation of the enzyme substrate or the reaction product is reduced. Concanavalin A is one of the most commonly used lectins in glycan analysis and pull down assays [541]. Concanavalin A is a lectin specific for α-D-mannopyranosides and α-D-glucopyranosides [542]. It has also been reported to bind to biantennary mannose units and with less affinity to the triantennary units of mannose in glycoproteins [543].

Electrochemical methods have been applied in a number of studies for the detection of carbohydrates presented on cell surfaces. A SAM based electrochemical method was developed by Wang et al. for the determination of cell surface carbohydrates. A 5-hydroxy-3-hexanedithiol-1,4-naphthoquinone SAM was used as a reporter and L-selectin binding to the aptamer or the L-selectin interaction with the cell surface carbohydrates was monitored by the change in DPV peaks of the probe molecules based on the interaction with the aptamer which is believed to block electron transfer to the electrode surface, when it is interacting with the SAM molecules [544]. Another lectin based electrochemical sensor was developed by Zhang et al. for the analysis of glycans on living cells. Their assay was based on lectin immobilization on a gold nanoparticle multi-walled carbon nanotube composite substrate, after cell binding to the lectin on the substrate surface another tag was allowed to incubate with it; this tag was prepared by

conjugating lectin-Au-thionine, then thionine was detected electrochemically by differential pulse voltammetry [545]. Similar study was reported by these authors but this time detection was performed based on the enzymatic catalytic reaction of HRP for the oxidation of thionine by H_2O_2 [546]. A cytosensor was developed by immobilizing cells on the arginine-glycine-aspartic acid-serine carbon nanotube nanocomposite and the Con A conjugated HRP was attached to the surface and electrochemical detection was performed [547]. Another electrochemical cytosensor was reported based by Ju et al. based on the competitive interaction between cell surface mannose units and the mannan units on the gold surface immobilized via self assembled monolayer [425].

A nanoparticle based sensor for lectin-carbohydrate interactions was reported by Wang et al. who immobilized lectin onto the mixed SAM modified gold surface and then a competitive assay was performed using CdS nanoparticle labeled and unlabeled sugars. Amount of nanoparticles attached to lectin was then determined by dissolution and then by stripping analysis [548]. Gold nanoparticles modified with Con A and immobilized in polyvinyl butyral were found to exhibit a response as determined by electrochemical impedance spectroscopy, to the sera of patients infected with dengue fever or dengue hemorrhagic fever [549]. Serotypes of dengue fever were distinguished using this detection scheme with *Cratylia morris* (CramoLL) lectin immobilized on iron oxide nanoparticles within the polymer film on a gold electrode. Immobilization of the *Bauhinia monandra* (BmoLL) lectin onto gold nanoparticles dispersed in polyaniline on a gold electrode surface was also able to detect dengue fever glycoproteins via electrochemical impedance spectroscopy. The same group also reported applying these

modified electrodes with gold nanoparticles modified with either Con A or CramoLL lectin to the detection of ovalbumin [550, 551].

Three different approaches in electrochemical glycobiosensing are most common i) EIS based methods, ii) immobilization of lectin followed by glycoconjugates and then finally labeling with the lectin enzyme conjugate or lectin redox agent conjugate, and iii) immobilization of cells onto the surface and then detecting with similar probes as in (ii) [425, 519, 546, 552]. Direct electrochemical determination of the enzymatic products on the traditional flat gold electrode surfaces is not feasible so, surface amplification which results in increased sensitivity is achieved through the use of nanoparticles.

6.2 Results and discussions

6.2.1 Direct electrochemical enzyme linked lectinsorbant assay (ELLSA) on NPG

A comparative study of NPG covered gold wire with uncoated gold wire for potential application as electrodes in enzyme assays was done by preparing a lipoic acid SAM on both surfaces followed by immobilization of the Con A-ALP conjugate onto the EDC/NHS activated SAMs. SWV studies were performed by incubating these modified electrodes with 1 mM p-APP in glycine buffer (pH 9.0) for 2 minutes. **Figure 6.1a** shows the SWVs of both of the modified electrodes; the SWV for the modified gold wire shows no discernible current peak after incubation with 1 mM p-APP, whereas a significant peak current was observed after incubation with 1 mM p-APP for the modified NPG covered Au wire electrode.

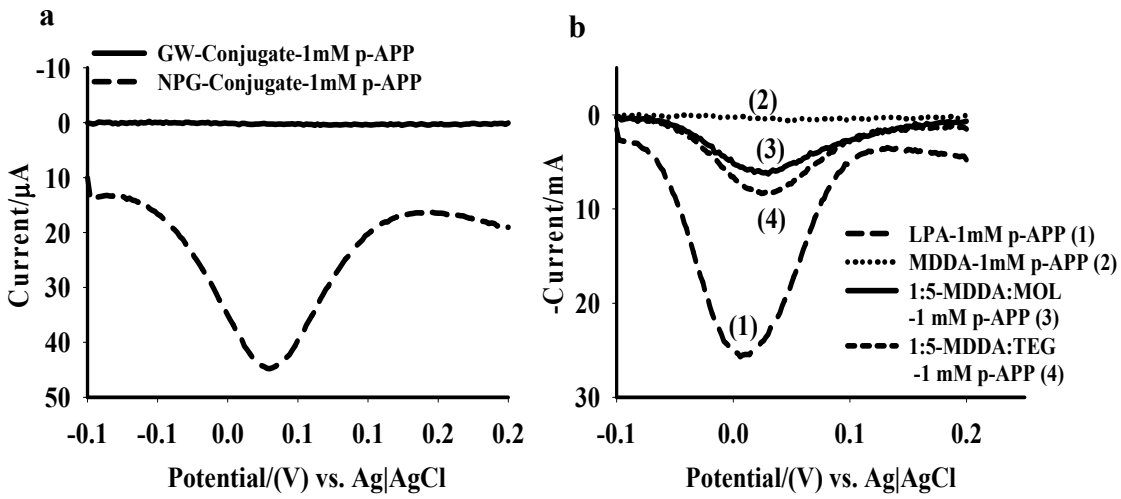

Figure 6.1. Identification of surfaces for ELLSA. A) SWV of Con A-ALP conjugate modified gold wire and NPG and b) different SAMs for conjugate immobilization, and for the product detection.

This observation shows the vastly increased sensitivity of the NPG covered Au wire electrode compared to that of the gold wire electrode alone for use in an electrochemical assay using the immobilized enzyme-lectin conjugate. A key property of lipoic acid is that it forms a relatively disordered SAM on the NPG surface with a significant presence of defects and exposed bare gold [553]. These defects provide sites for the electrooxidation of the p-aminophenol generated after the enzymatic reaction of alkaline phosphatase and p-aminophenyl phosphate. Several different SAMs were studied for possible application for protein immobilization and hence assay development. **Figure 6.1b** shows SWVs of Con A-ALP conjugate immobilized onto different SAMS on NPG. SAMs of mercaptododecanoic acid (MDDA), mercaptododecanoic acid + mercaptooctanol, and MDDA + triethylene glycol were studied for possible application in the electrochemical ELLSA. Among all of the SAMs studied, those of lipoic acid resulted in SWV peak currents that were much larger than those of the other SAMs studied. Since

MDDA forms relatively well organized and blocking SAMs, p-aminophenol can't easily access the NPG surface to undergo electrooxidation, and hence the peak current is reduced. Thus, LPA was chosen as a suitable molecule for SAM formation in the present assay approach.

Having identified SAMs of lipoic acid as attractive for NPG modification, lectin-carbohydrate interactions were studied both in the traditional ELLSA format, competitive format, and by using a kinetic assay approach based on the rate of enzymatic reaction before and after lectin- glycoprotein interaction. ELLSA are traditionally performed by immobilizing the glycoproteins of interest onto the surface and then allowing either lectins labeled with enzymes or fluorophores, or biotinylated lectins to bind. If a biotinylated lectin is allowed to bind, then it is subsequently reacted with a streptavidin or avidin labeled enzyme. The amount of lectin bound to the surface bound glycoprotein is then detected by enzymatic reaction with the product formation followed spectrophotometrically [527, 554, 555].

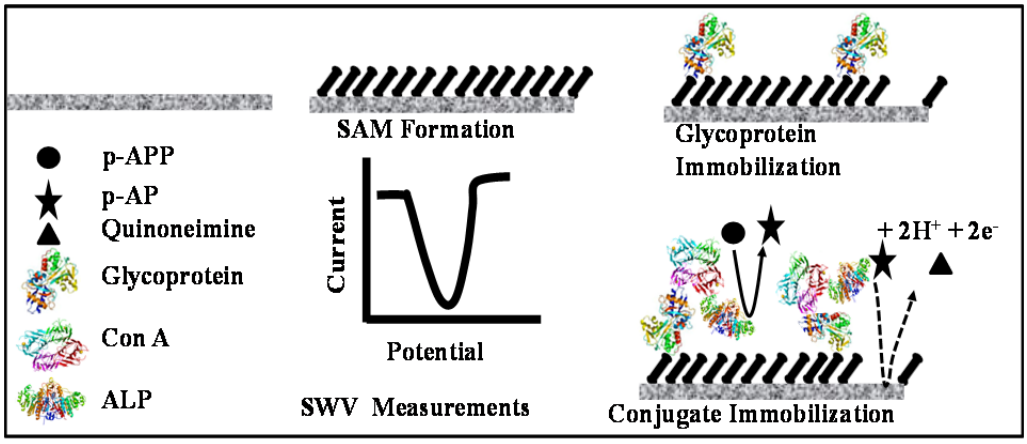

Figure 6.2. Schematic diagram of the traditional type ELLSA on NPG surface.

Electrochemical ELLSA was performed on NPG in the traditional format by immobilizing the glycoproteins onto the SAM modified NPG surfaces. Immobilization of glycoproteins via covalent tethering into SAMs has several advantages including increased stability and limited protein loss due to leaching during washing and handling, as compared to the more common physisorption approach. Additionally, this approach protects the protein from denaturing after adsorption onto the metal surface and hence increases its retention of binding specificity.

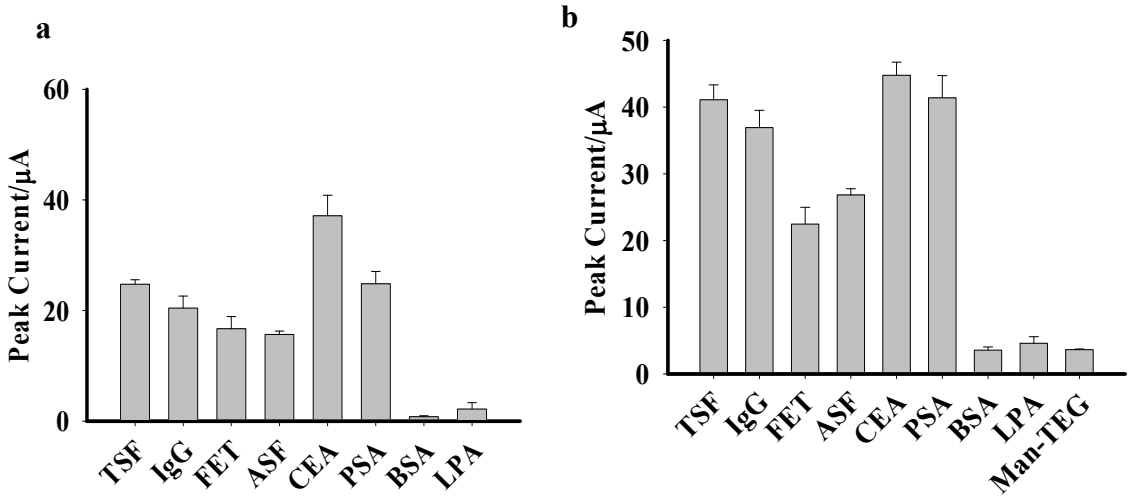

Figure 6.3. Bar plots for the traditional type ELLSA. Different glycoproteins were immobilized on the NPG surface and incubated with 50 μg mL^{-1} Con A-ALP conjugate for 2 hours (a) and 24 hours (b). SWV measurements were done with 1 mM p-APP. (TSF-Transferrin, IgG-Immunoglobulin G, FET-Fetuin, ASF-Asialofetuin, CEA-Carcinoembryonic antigen, PSA prostate Specific antigen, BSA-Bovine serum albumin, LPA-lipoic acid, Man = αMan-C_8-SH, TEG = HO-PEG_2-SH and Man-TEG is the 1:1 molar ratio of these two molecules).

Figure 6.2 shows a schematic diagram of the traditional ELLSA on NPG. Different glycoproteins (transferrin, IgG, fetuin, asialofetuin, PSA and CEA) were covalently immobilized onto the lipoic acid SAM on the gold surface by EDC/NHS coupling. Bovine serum albumin (BSA) and LPA modified NPG were used as a negative control. These protein modified wires after incubation with the Con A - ALP conjugate were then incubated with the ALP substrate p-APP and then SWV was performed.

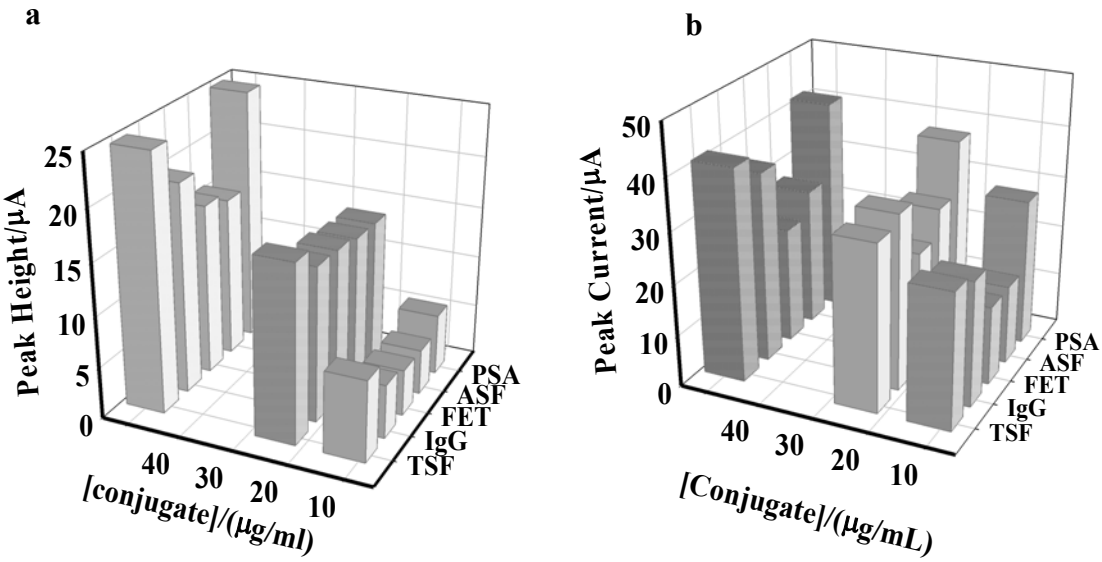

Figure 6.4. 3D bar plots for the traditional type ELLSA. ELLSA was performed as in figure 6.3 with different concentrations of Con A-ALP conjugate. Glycoprotein immobilized wires were incubated with conjugate for 2 hours (a) and 24 hours (b); SWV was performed with 1 mM p-APP.

Figure 6.3a and **Figure 6.3b** shows the bar plot for traditional ELLSA, plotting peak currents of the SWVs for the different glycoproteins. The glycoproteins immobilized on NPG covered Au wires were incubated with 50 μg mL^{-1} Con A-ALP conjugate in PBS (pH 7.4, 10 mM containing 1 mM each of Ca^{2+} and Mn^{2+}) for 2 hours

and then SWV scans were performed in the presence of 1 mM p-APP in pH 9.0 glycine buffer for 2 min. Different peak currents were observed depending on the amount of conjugate immobilized onto the NPG surface. The maximum peak current was obtained for CEA immobilized on NPG, intermediate peak currents were observed for PSA, TSF and IgG and the least peak current was observed with FET and ASF. BSA immobilized on NPG and the LPA SAM on NPG alone both showed only very small peak currents. Significantly larger peak currents were observed with the bare NPG incubated with the Con A-ALP conjugate due to the non-specific adsorption of protein on the NPG surface. This indicates that even though protein adsorbed onto the bare NPG surface there was significantly reduced adsorption of protein onto the LPA SAM modified surface. A αMan-C_8-SH modified NPG was also used for the study but no signal was obtained with either pure mannose SAM or the 1:5 mixed SAM of mannose and thiolated triethylene glycol. This could be because either the conjugate did not bind to the SAM or the p-aminophenol product could not diffuse through the SAM on the surface. It is possible that the ALP-Con A conjugate encounters some steric interference in its interaction with the surface that is not found for Con A alone. Con A is reported to bind to the mannose units of glycoproteins and its binding affinity is higher with biantennary glycoproteins as compared to triantennary glycan units [543]. TSF and IgG have biantennary mannose units in the majority of their glycan structure and have been reported to bind to Con A [556, 557]. CEA has also been shown to bind to Con A [558]. Comparable frequency changes for binding of fetuin, asialofetuin and transferrin were reported in a quartz crystal microbalance based study [559]. Safina et al. reported strong binding and relatively large SPR signals for Con A binding to TSF compared to its interaction with

fetuin and asialofetuin, thus the relative signal intensity and observed binding affinity and hence relative differentiation between two glycoproteins is also affected by the method of study [560]. We have also seen higher binding affinity and hence higher peak current for CEA and TSF. Incubation of wires with conjugate in PBS buffer at 4ºC for 24 hours did not significantly increase the signal, thus the SAM was stable enough for the duration of study. Different conjugate concentrations were used to study the binding of conjugate to the surface immobilized glycoproteins (**Figure 6.4a** and **Figure 6.4b**). Improved differentiation of the glycoproteins is seen for use of 50 μg mL^{-1} of conjugate in the incubation step. In the ELLSA developed here, based on covalent linkage of the glycoprotein to lipoic acid SAMs, differentiation of different glycoproteins was achieved. However, the present study has not pursued the goal of studying response as a function of glycoprotein concentration, a goal reserved for future studies. The immobilization of the glycoproteins to the SAMs provides a basis for the competitive assay presented here in this chapter.

6.2.2 Characterization of NPG surface after modification using electrochemical impedance spectroscopy

After each modification step, the NPG covered Au wire electrodes were characterized by electrochemical impedance spectroscopy (EIS). EIS is a sensitive technique for the characterization of the capacitive and resistive properties of electrochemical interfaces. A small sinusoidal ac perturbation potential applied to the system at equilibrium and the current response is monitored over a selected range of frequencies. **Figure 6.5a** and **Figure 6.5b** show the Nyquist plots of gold wire and NPG coated gold wires at different stages of modification. Quantitative determination of the

EIS parameters for the constant phase element (CPE) and charge transfer resistance (R_{ct}) are shown in **Figure 6.6**, these data were obtained by fitting EIS data to the equivalent circuit shown in **Figure 2.1b**. The charge transfer resistance for bare NPG was not determined because relative standard error of the parameter fitted to above equivalent circuit is more than 20 %, which is taken as the maximum acceptable standard error in fitting, all other parameters have less than 1 % standard error in fitting except charge transfer resistance for modified NPGs, which is less than 5 %. Formation of the SAM on the surface and protein immobilization is characterized by an increase in charge transfer resistance and a decrease in double layer capacitance. Changes in impedance behavior on the gold wire are obvious and with each modification there is a prominent increase in charge transfer resistance except for the formation of the activated esters after the EDC/NHS activation step. After the EDC/NHS activation step, there is a drop in charge transfer resistance and this is attributed to the formation of neutral ester with the bulkier head group, in place of the negatively charged carboxylate groups at the interface which are able to electrostatically hinder the charge transfer from the ferricyanide probe which is also negatively charged in both of its oxidation states. Similarly, the CPE value decreased as expected after formation of the LPA SAM and increased slightly after NHS ester formation and again decreased after protein immobilization and binding of IgG. The EIS data for the SAMs on NPG show a very small semicircle and a dominant slightly curved line in the Nyquist plot. After each modification step there is only a slight change in the Nyquist plot. Similarly, the charge transfer resistance increased after conjugate immobilization but after IgG binding it didn't increase, this might be because of the significantly exposed surface for electron transfer on NPG. The overall magnitudes of R_{ct}

are smaller on NPG due to the increase in surface area. The CPE, which is related to the double layer capacitance, has been used instead of double layer capacitance because of the rough nature of the electrode.

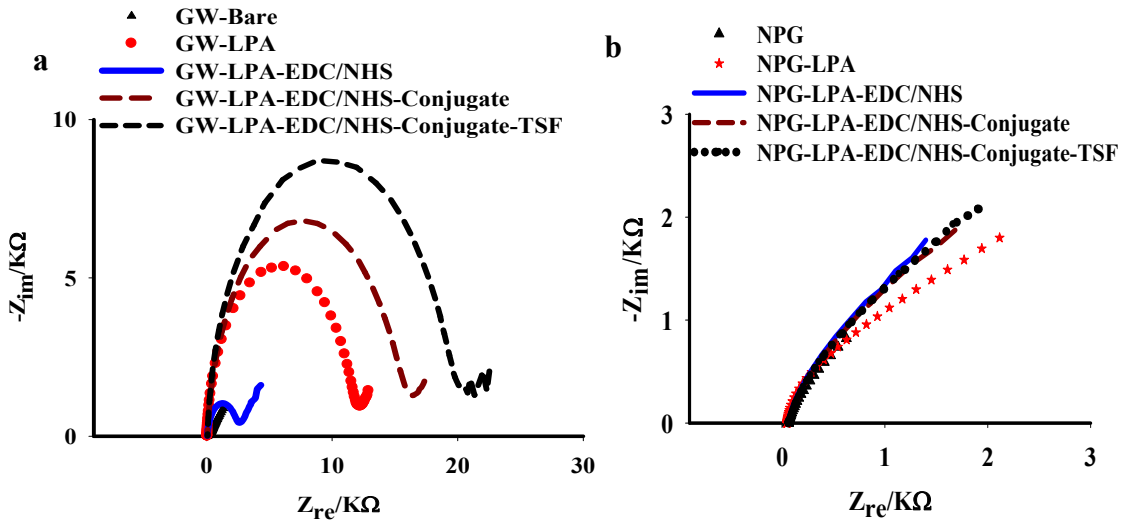

Figure 6.5. EIS studies of the modified NPG and gold wire for ELLSA. Gold wire (a) and NPG (b) electrodes were modified as indicated and EIS measurement was done with 5 mM each of $K_3[Fe(CN)_6]$ and $K_4[Fe(CN)_6]$.

The magnitude of CPE decreased significantly after SAM formation but increased after the formation of NHS activated ester head groups from the negatively charged carboxylate terminal groups. The CPE decreased after conjugate immobilization but only a very small drop in CPE value was then observed after IgG binding to the Con A-ALP conjugate on the surface.

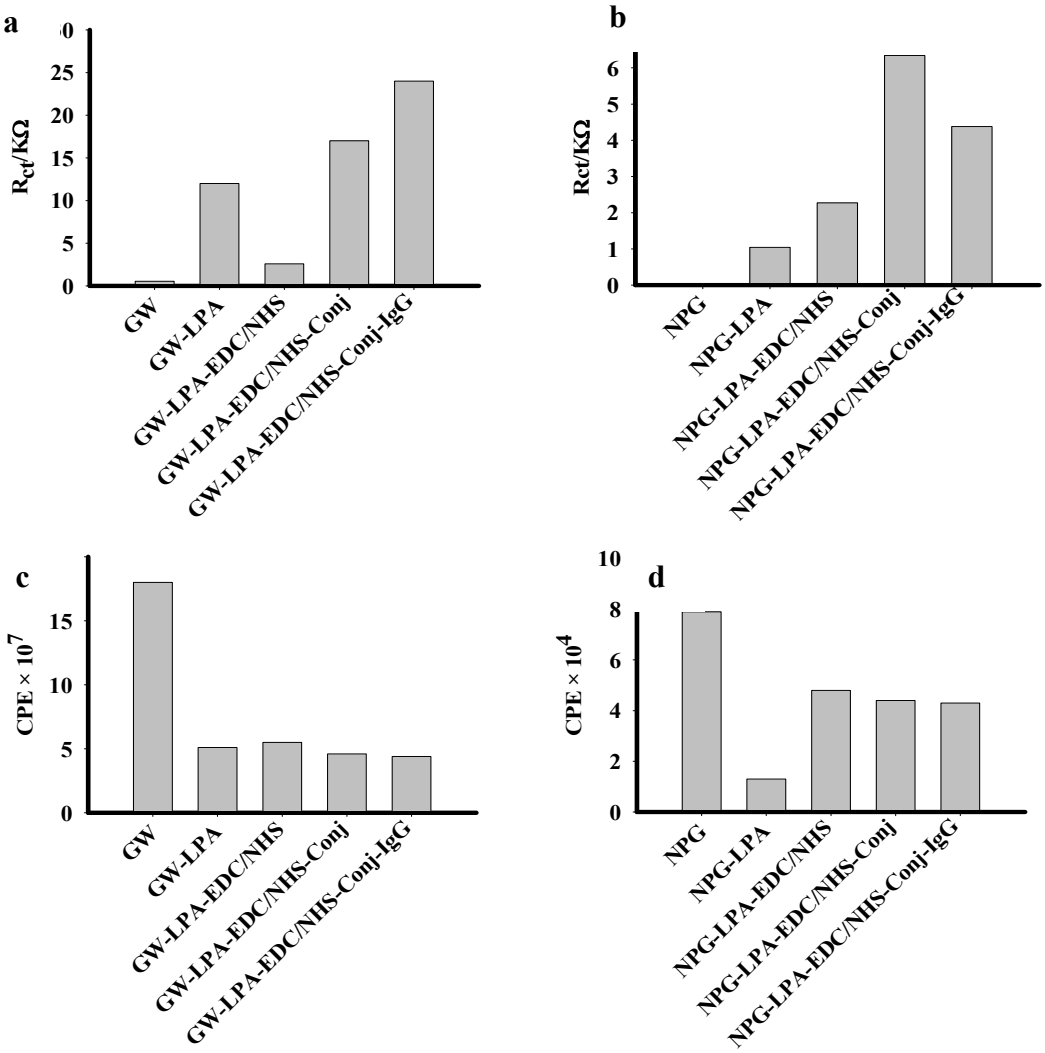

Figure 6.6. Data summary of the EIS analysis of modified electrodes. EIS data were fitted to the equivalent circuit mentioned above and several parameters were extracted.

6.2.3 Michaelis-Menten kinetics of Con A-ALP conjugate on NPG

The activity of the alkaline phosphatase conjugate immobilized on the SAM modified NPG was measured to further study the suitability of surface and conjugate immobilization for assay development. Michaelis-Menten kinetics on the NPG surface was studied by varying the concentration of substrate and recording peak current signals. p-APP concentrations of 0.01 mM to 1.0 mM were studied, and a set of SWV sweeps are

shown in **Figure 6.7** for an NPG electrode modified by the Con A-ALP conjugate exposed to these substrate concentrations for a period of 2 minutes each. There was an increase and trend towards saturation in the peak current with the increase in substrate concentration which finally reached plateau, characteristic of a Michaelis-Menten kinetics behavior. The peak current of the SWV measurement is related to the rate of a reaction and hence to the reaction kinetics [488]. The K_m value was determined by fitting the data to the Michaelis-Menten equation and it was found to be 200 μM (**Figure 6.8**). This was also important because most enzyme electrodes are operated near K_m values. Thus, we chose 200 μM for our kinetic assays, a concentration which falls in the pseudo-linear range. The SWV sweeps resulted in a prominent peak for the oxidation of p-aminophenol in this concentration range. In contrast, attempts to measure the current peak due to oxidation of p-aminophenol using linear sweep voltammetry were much less successful due to the high background currents arising from charging of the electric double layer of NPG. The oxidation of the p-aminophenol ALP reaction product to p-quinoneimine occurs near a potential close to 0 V (vs. Ag|AgCl). The surfaces of NPG are more electroactive than relatively smooth gold surfaces. Catalytic activity depends on nanostructure which leads to the oxidation potential depending upon the defects, curvature and roughness of the surface. The slightly lower oxidation potential observed for p-aminophenol in this study compared to the oxidation potential of p-aminophenol on relatively flat gold surfaces reported elsewhere might be related to the nanostructure of NPG [561]. A negative shift in oxidation potential of methanol on NPG has been reported by Zhang et al. [37] The peak current of the SWV has been reported as be proportional to the velocity of the reaction and can be used to create a Michaelis-Menten plot [488, 562].

The rate of a reaction on the electrode surface can be obtained by dividing the peak current by the product of nF, where, n is the number of electron involved in the redox process and F is Faraday's constant [488]. From this plot, the K_m value for the immobilized conjugate was found to be 200 µM. A K_m value of 56 ± 5 µM was reported for free alkaline phosphatase in solution using p-APP as the substrate [252]. In another similar study with the MAb-ALP conjugate on NPG we have found the K_m value to be 290 µM. In our prior study using the MAb-ALP conjugate where the MAb binds free PSA, and the substrate used was p-nitrophenyl phosphate with UV-visible detection of the p-nitrophenolate product at 410 nm, an increase in K_m from 210 µM to 300 µM was observed upon immobilization using EDC activated lipoic acid monolayers. The conjugation of the MAb to the antibody itself in solution was found to increase the measured value of K_m from 40 µM to 210 µM [6]. A further analysis of the Michaelis-Menten fit to these data is presented further below. This analogy can be applied for the Con A-ALP conjugate on NPG surface.

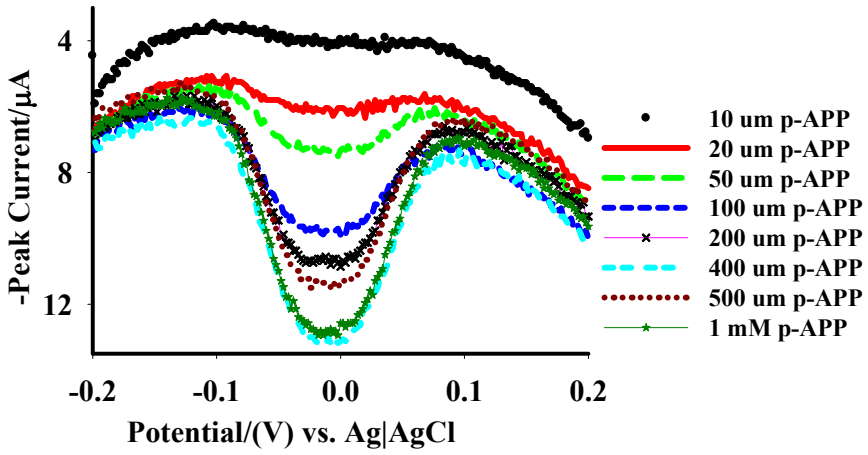

Figure 6.7. SWV for the Michaelis Menten kinetics studies on NPG.

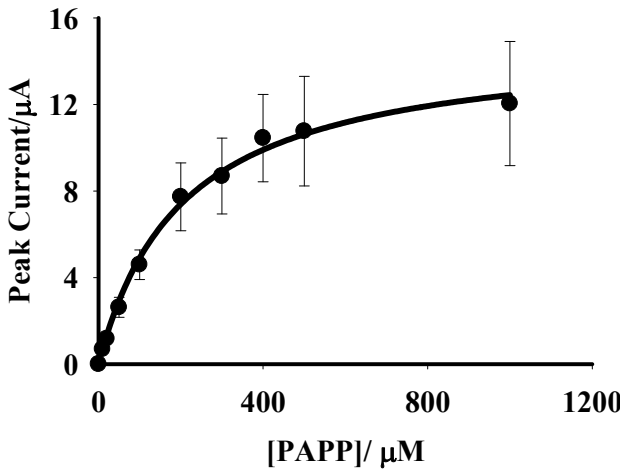

Figure 6.8. Michaelis-Menten plot for Con A-ALP conjugate immobilized on NPG.

An increase in K_m is anticipated for enzyme immobilization inside a porous support, and such increases have been previously reported. Lorenzo et al. reported a K_m value of 410 μM for alkaline phosphatase covalently attached to nylon mesh using BSA and glutaraldehyde as cross-linkers [491]. Rechnitz et al. reported an approximately three-fold increase in the K_m value for type III adenosine deaminase and a five-fold increase for type V enzyme immobilized by BSA glutaraldehyde crosslinking onto the Teflon® membrane of an ammonia sensor. They also reported a drop in V_{max} when the enzyme was immobilized onto the surface. A ten-fold increase in K_m was reported for alkaline phosphatase immobilized on nylon mesh using p-nitrophenyl phosphate and p-aminophenyl phosphate substrates. Shulga et al. reported an increase in K_m for acetylcholinesterase immobilized by physisorption on nanoporous gold surfaces [79]. A similar increase in K_m for ALP and hydroquinone diphosphate substrate was reported by Wilson et al. [493] A decrease in turnover number was reported when enzyme was

conjugated to IgG. A pore size dependent change in enzymatic activity and K_m values were reported for 'gigaporous' (314 nm), macroporous (104 nm) and mesoporous (14.7 nm) polystyrene microspheres for the lipase from *Burkholderia cepacia* immobilized by strong hydrophobic interactions [495]. Brinker et al. showed that the change in enzymatic activity and affinity for the corresponding substrate can be enzyme dependent; their study on glucose-6-phosphate dehydrogenase and horseradish peroxidase showed that enzymatic activity of immobilized glucose 6-phosphate was 36 % and the enzymatic activity of HRP was 73% of that of the free enzyme in solution. Miller et al. reported that the enzymatic activity of free glutathione-S-transferase was 4 times higher than the activity of glutathione-S-transferase immobilized in porous silica [497]. Stevenson et al. also reported an increase in K_m and decrease in enzymatic activity of HRP immobilized on glass coverslips [488].

6.2.4 Optimization of the kinetic ELLSA protocol

Optimal conditions for the activity of alkaline phosphatase enzyme on the NPG surface as well as for assay development were determined by varying buffer conditions, incubation time with substrate, and the glycoprotein. **Figure 6.9** shows the profile of enzymatic activity versus pH for the conjugate on the NPG surface, measured as peak current versus pH. As reported in the literature, the activity of alkaline phosphatase is maximum around pH 9.0 [563]. There was almost no activity observed in pH 7.4 PBS buffer. So glycine buffer at pH 9.0 was chosen as the optimal buffer for this study. Since alkanethiol SAMs are reported to be less stable at basic pH, PBS buffer at pH 7.4 was chosen for the incubation of electrodes with the conjugates and for longer storage.

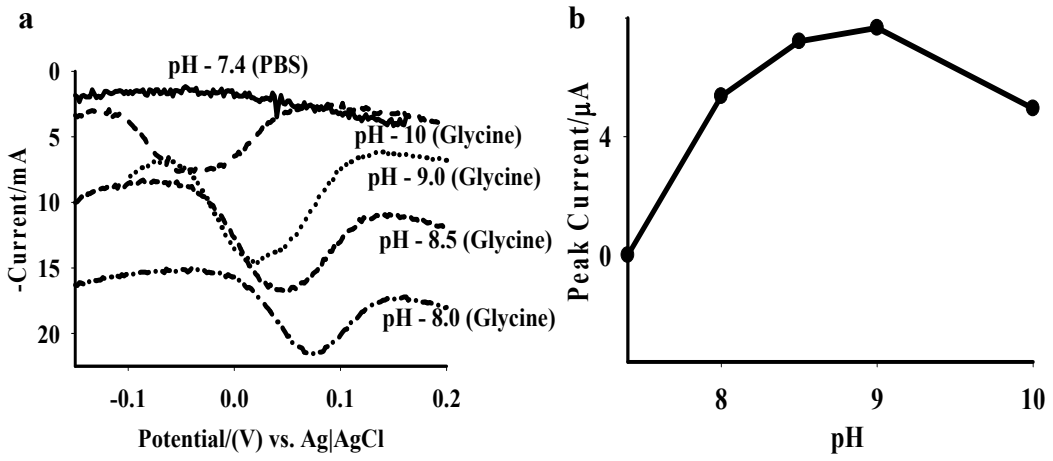

Figure 6.9. Optimal pH for the activity of conjugate on NPG. a) SWV data recorded in different pH buffers, b) peak current vs. pH for the plots in **Figure 6.8a**.

For the kinetic assay, the incubation time for conjugate and glycoproteins is important so a similar study was performed by varying incubation time with the glycoprotein and the conjugate immobilized NPG (**Figure 6.10a**). There was an almost constant peak current after 2 min of incubation (**Figure 6.10b**) with the substrate so 2 min was chosen as incubation time with the substrate. Saturation was reached within 2 hours and this was chosen for the incubation time. The same information was used for the incubation time for the competitive assay studies.

The use of other enzymes in the Con A-enzyme conjugate, such as horseradish peroxidase, could also be considered. Alkaline phosphatase was chosen as it is one of the most widely used enzymes which is robust and has lower substrate specificity as almost any phosphate group containing compound can act as a substrate for this enzyme.

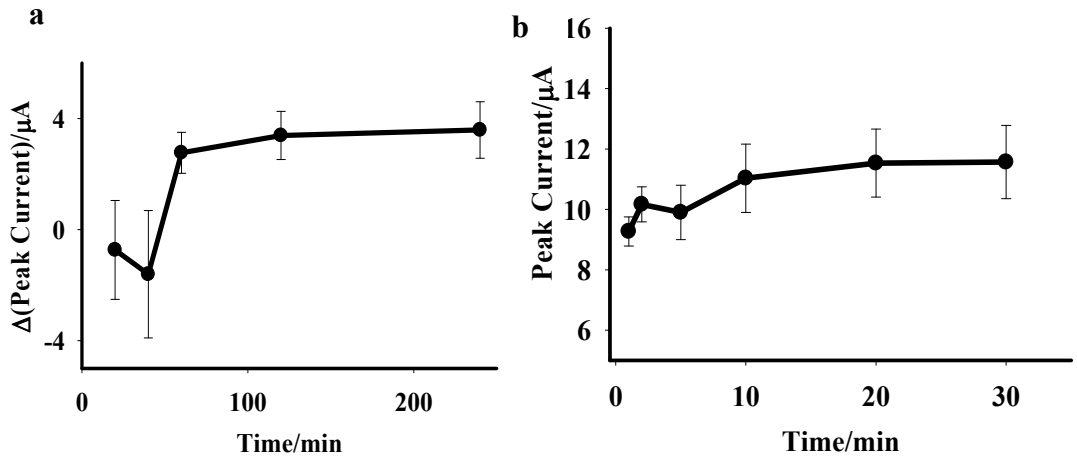

Figure 6.10. Optimal incubation times for the ELLSA. (a) Con A-ALP conjugate immobilized wires were incubated with glycoprotein for a different period of time and SWV measurements were done with 200 μM p-APP. (b) Con A-ALP conjugate immobilized wires were incubated with the substrate for different period of time and the SWV measurements were done.

6.2.5 Kinetic enzyme linked lectinsorbant assay on NPG

The kinetic lectinsorbant assay is based on the difference in the rate of enzymatic reaction of ALP conjugated to the Con A, before and after glycoprotein binding to the Con A. The presence of a large glycoprotein molecule bound to the lectin close to the ALP causes steric hindrance of the access of the p-APP substrate to the active site of ALP. A scheme depicting the working concept for the assay is shown in **Figure 6.11**. The binding of the glycoprotein will reduce the initial rate of enzymatic conversion of p-APP to the oxidizable p-aminophenol product.

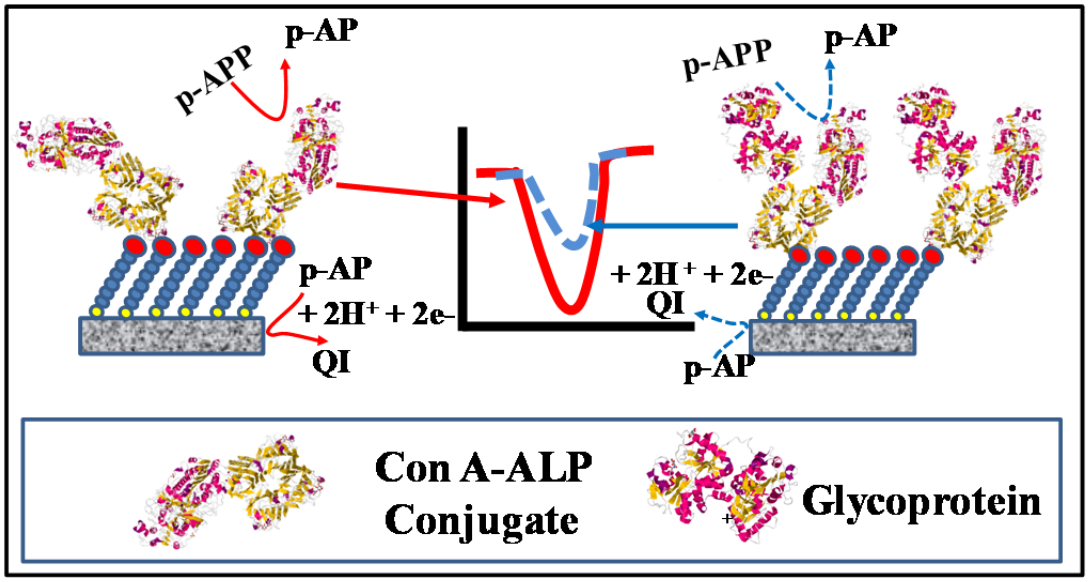

Figure 6.11. Schematic representation of the kinetic ELLSA on NPG.

The enzyme reaction rate is assumed to be proportional to the peak current in the square wave voltammogram. The difference in peak current before and after incubation is the response variable for the immunoassay. It was not possible to monitor product formation continuously using chronoamperometry, so instead we measure the peak current after a fixed incubation time which is assumed to be proportional to the relative rates of the enzymatic reaction of ALP before and after glycoprotein binding to the Con A. The concentration of p-APP used is 200 μM, this concentration was chosen because this is close to the K_m value and hence close to the pseudo linear range of substrate enzyme kinetics, and p-APP concentrations less than 100 μM did not produce sufficient current peaks in the SWV scans.

Enzyme kinetics and hence the rate of conversion of substrate to product depends on the access of the substrate to the active site of the enzyme. When relatively large and bulky molecules bind to the lectin conjugated to the enzyme access of the substrate to the active site is hindered and results in a decrease in activity and hence a decrease in initial

velocity of the reaction. Kinetic assays are not very common in the literature. As a proof of concept of this assay on NPG, we chose four different glycoproteins, transferrin (80 kDa), IgG (160 kDa), ASF (40 kDa) and FET (40 kDa), based on the binding of these proteins to Con A determined from traditional type ELLSA and literature reports. When these proteins bind to Con A conjugated to alkaline phosphatase, access of the p-APP is hindered and hence results in a decrease in the reaction velocity. **Figure 6.12a** and **Figure 6.12b** shows the binding isotherm determined for the binding of CEA and TSF to the immobilized Con A–ALP conjugate. Similar binding isotherm for IgG is shown in **Figure 6.13a**. As expected, there was a decrease in enzymatic activity with the increase in concentration of glycoprotein which is observed in terms of the increased difference in peak current. The binding affinity of Con A to CEA determined by this method was K_d = 17 nM, for TSF K_d= 650 nM and for the Con A to IgG was found to be K_d= 105 nM. The binding affinity of Con A to TSF in solution was reported to be 1-2 μM [564]. The literature reported studies and our measurements are in agreement. Similar binding studies of IgG and Con A was not found but it has been reported to bind to Con A [565]. Two other proteins ASF and FET were also studied for the kinetic assay but these proteins did not produce any significant change in the peak current, this we believe is because of the relatively lower binding affinity and especially the smaller sizes of these proteins.

The effect of an interfering protein was studied using bovine serum albumin (BSA) as a model major serum protein and 5 mg mL^{-1} BSA was added to the incubating solution along with 2μM IgG. The addition of BSA had no effect on the difference in peak current **(Figure 6.13b).** As a control experiment, 5 mg mL^{-1} BSA was used alone,

instead of glycoprotein, in the kinetic assay and no change in signal was observed; therefore, the drops seen in peak current are due to the binding of glycoprotein to Con A and then consequently reduced enzymatic reaction rate. A competitive type enzyme multiplied immunoassay (EMIT) for digoxin was reported by Chang et al. based on the difference in enzymatic activity of glucose-6-phosphate dehydrogenase (G6PDH) covalently attached to the digoxin. The enzymatic activity of G6PDH was reported to decrease when digoxin specific antibody bound to the digoxin and as more unlabeled digoxin were added more enzyme bound digoxin was released from the antibody and hence enzymatic activity increased [566]. Rosenthal et al. evaluated EMIT and compared with the standard radioimmunoassay for digoxin and has found excellent agreement between the two methods [217].

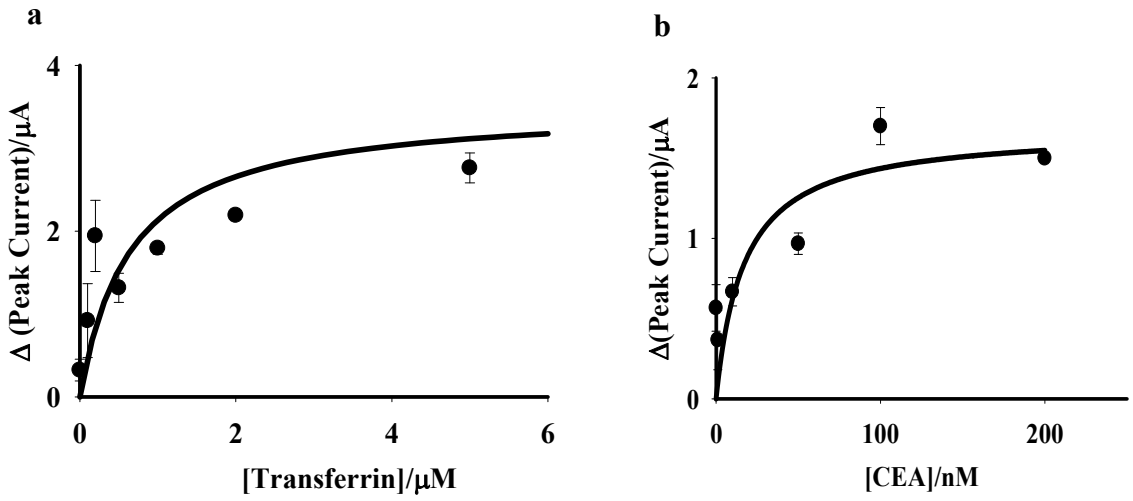

Figure 6.12. Calibration plot of kinetic ELLSA for carcinoembryonic antigen (a) and transferrin (b).

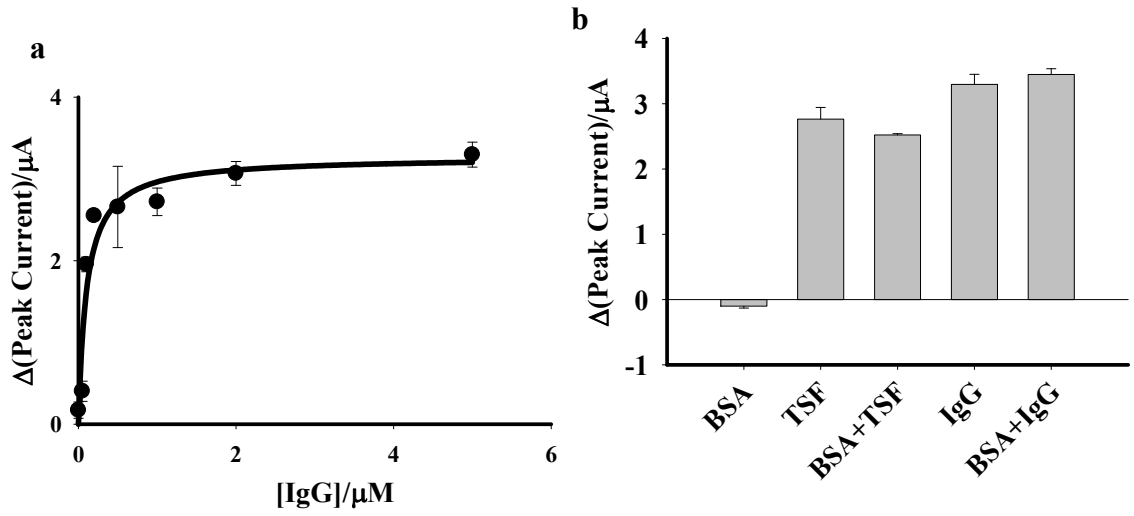

Figure 6.13. (a) Calibration plot for the kinetic ELLSA on NPG for IgG and (b) study of the effect of BSA on kinetic ELLSA. 5 mg mL^{-1} BSA was added to the incubation buffer along with the glycoprotein in solution, SWV measurements were done as before. (BSA-Bovine serum albumin, TSF-Transferrin, and IgG-Immunoglobulin G)

6.2.6 Competitive assay on NPG

Competitive ELLSA was also performed on the NPG surface using the two glycoproteins TSF and IgG. In principle, this assay should work for any sets of binding partners i.e. lectin- glycoprotein, antibody-antigen, or protein-protein pairs but as a proof of concept on NPG we chose these proteins for our study. **Figure 6.14** shows the schematic principle of the competitive ELLSA on the NPG surface. Glycoproteins were covalently immobilized on the NPG surface and allowed to compete for binding to Con A –ALP conjugate in solution with free glycoprotein in solution. There was a decrease in amount of the bound conjugate with an increase in amount of free glycoprotein in solution. A different response depending upon the binding affinity, and size of the

proteins and hence number of conjugates immobilized on the NPG surface was observed for the two different glycoproteins used in this study.

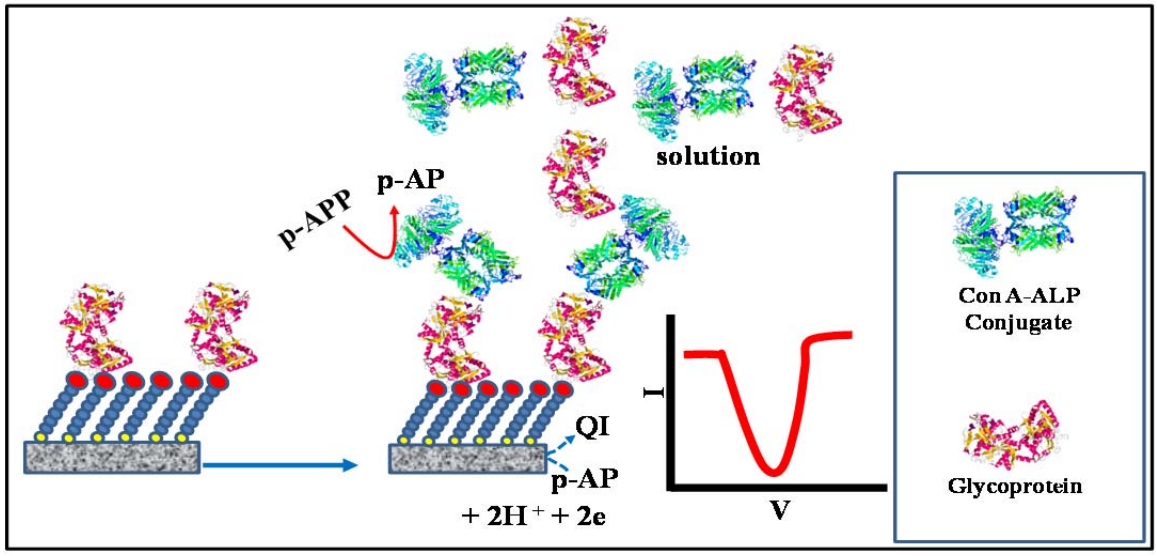

Figure 6.14. Schematic representation of the competitive ELLSA on NPG.

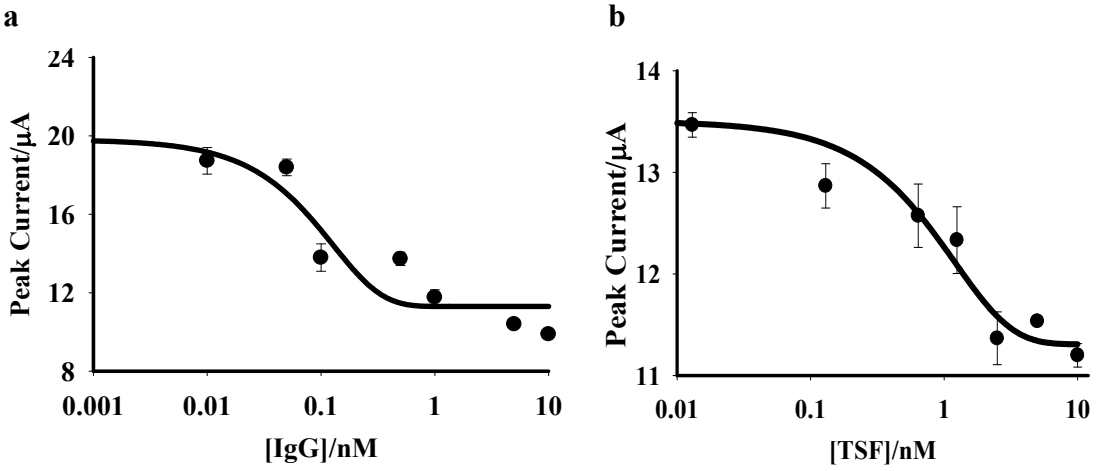

Figure 6.15. Calibration plots for competitive ELLSA. NPG wires were modified with IgG (a) and TSF (b) followed by the incubation with 50 mg μL^{-1} Con A-ALP conjugate, SWV measurements were done with 1 mM p-APP.

Figure 6.15 shows calibration plots for the competitive assays of TSF and IgG on NPG. Binding of conjugate to TSF and hence a significant signal was observed with 12 μg mL^{-1} of conjugate whereas, at this conjugate concentration, a relatively small signal was obtained for IgG on the NPG surface. Competitive response for TSF on NPG and in solution was obtained for 25 μg mL^{-1} conjugate and with 200 μM p-APP solution. Significant signal and competitive response was observed with 50 μg mL^{-1} conjugate with 1 mM p-APP for IgG immobilized on the NPG surface.

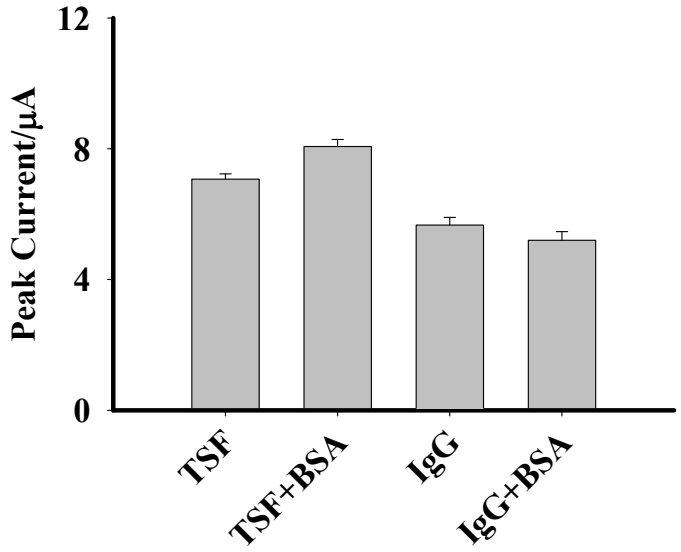

Figure 6.16. Effect of BSA on competitive ELLSA. 5 mg mL^{-1} BSA was spiked to the incubation buffer along with the Con A-ALP conjugate. SWV measurements were done as mentioned above.

The relatively lower peak current observed for IgG could be because of the larger size of IgG and smaller number of molecules cm^{-2} **(Table 6.1),** which leads to lesser number of conjugates cm^{-2} and hence a smaller peak current. The response will also

depend on the relative size of the protein, orientation on the surface and extent of glycosylation. Incubation time was also varied for the competitive assay between 2 hours and 17 hours incubation time showed highly increased signal at 17 hours incubation.

Similarly effect of BSA was also studied in the competitive assay as well and added BSA was found to have no real effect. The effect of BSA in the competitive assay was studied for both proteins TSF and IgG (**Figure 6.16b**).

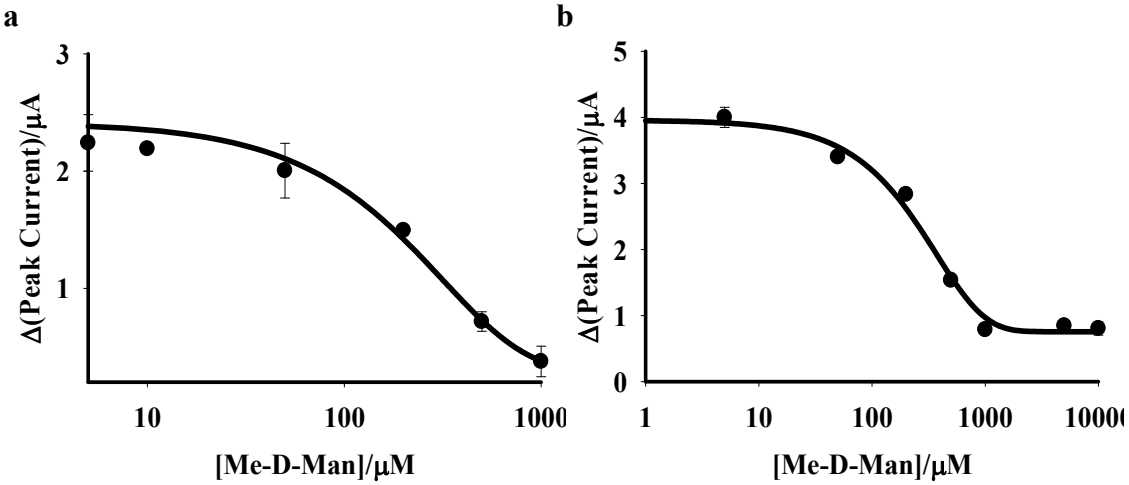

Figure 6.17. Inhibition studies with Me-D-man. IgG (a) and TSF (b) were immobilized on the NPG surface and incubated with 50 mg mL^{-1} Con A-ALP conjugate and different concentrations of Me-D-Man. Difference in peak current was calculated from the difference in peak current without Me-D-Man and with the different concentration of the inhibitor.

6.2.7 Inhibition studies by methyl D-mannose (Me-D-man)

Methyl D-mannose is a ligand for Con A, binding of Con A to other glycoproteins and glycoconjugates has been reported to be inhibited by Methyl D-man. So in order to test the binding specificity, inhibition studies were performed in the competitive format

assay. With the increase in amount of the Methyl D-man there was less conjugate bound to the surface and less enzymatic activity resulted into smaller peak current (**Figure 6.17**). Inhibition constants (IC_{50}) obtained by these methods for TSF and IgG are around 100 μM, inhibition constant of Methyl D-man to Con A has been reported to be 92±6 μM hence our result is in close agreement with the literature reports [567].

6.2.8 BCA assay and amount of protein immobilized on the NPG surface

The amount of protein immobilized on the NPG surface was determined by the BCA assay and solution depletion. **Table 6.1** summarizes the surface coverages of different proteins immobilized on NPG surface in moles cm^{-2}. A calibration plot was obtained using known concentrations of Con A and the amount of protein immobilized on NPG surface was determined from the difference in amount of protein initially present in solution and remaining in solution after immobilization onto the NPG surface. The surface coverage of lipoic acid on the NPG electrodes was estimated by reductive desorption of the SAMs in 0.5 M NaOH solution. Surface coverage of lipoic acid on NPG surface is approximately 70% and is thus less than a monolayer and is likely disordered. Estimation of the surface coverage of the conjugate on the lipoic acid modified SAMs was sought by solution depletion measurements. The amount of either Con A-ALP conjugate or glycoprotein (TSF or IgG) immobilized onto the surface was estimated by using a solution depletion measurement of protein concentration and the BCA protein concentration assay.

Table 6.1. Surface coverage of proteins on NPG

Proteins	*Wt. in (μg)	Mol Wt. (kDa)	Mol cm^{-2}	Molecules cm^{-2}
Con A-ALP (Conjugate)	10.04	104 + 69**	4.6×10^{-13}	2.8×10^{11}
TSF	7.1	80	7.1×10^{-13}	4.3×10^{11}
IgG	9.4	160	4.7×10^{-13}	2.6×10^{11}

*Surface coverage was determined by BCA assay based on the solution depletion studies. Amount of protein left in the incubation solution was subtracted from the amount initially present in the solution to obtain amount immobilized on the NPG surface, wt. represent protein immobilized in 10 NPG wires. ** Calculation is based on the assumption of one ALP per Con A molecule.

Ten NPG wires modified with a lipoic acid SAM, and a terminal –COOH group activated by EDC/NHS chemistry, were added to the 50 μg of Con A-ALP conjugate or to 50 μg of the glycoproteins dissolved in 100 μL PBS buffer. The wires were incubated for 24 hours at 4 ºC. The amount of protein remaining in the incubation solution was then determined. The difference between the amount of protein initially present in solution and the final amount left in solution gave the estimated amount of protein immobilized onto the NPG wires. **Table 6.1** presents the amounts of these biomolecules found on average immobilized on an NPG wire as determined from the BCA assay. Given the surface coverage of lipoic acid, equivalent to 2.42×10^{-10} mole cm^{-2} and the surface coverage in mole cm^{-2} of either the Con A-ALP conjugate (4.6×10^{-13}) or of the TSF (7.1×10^{-13}) or IgG (4.7×10^{-13}), one protein is estimated to be attached for approximately every 340-500 lipoic acid molecules. This shows that the conjugation of the amount of protein to the surface is dependent upon the type of protein, although association is most probably to the easily accessible lysine residues. TSF and IgG

conjugated to ALP are immobilized in larger amounts compared to IgG by itself. This is also consistent with the lower signal observed for IgG in the competitive assay. It is evident from these data that a small fraction of the lipoic acid molecules are conjugated to protein in either case. The area occupied by these glycoproteins or by the conjugate is subject to variability considering that they can occupy a range of orientations. Hence, any estimate of surface coverage is approximate in the absence of orientational information.

6.3 Conclusions

The assay strategy presented makes use of the high surface area of NPG and of its ability to be used as an electrode for SWV detection of an oxidizable enzyme product, in this case p-aminophenol. The use of SWV is required to overcome the large double layer charging effect in the NPG electrode. The assay approach can be applied to a wide range of proteins. In the present study, IgG, FET, ASF and TSF are used as readily available biologically significant glycoproteins and potential biomarkers. Enzyme linked lectin assays are important for the high throughput screening of glycoproteins. NPG electrodes can be prepared in a range of sizes and formats, and are suitable for miniaturization or use in flow-through electrochemical devices. The properties of NPG electrodes present opportunities for the development of new electrochemical assay formats. The greatly enhanced surface to volume ratio of NPG facilitates strategies such as the one described here which relies upon the enhancement in peak current in a square wave voltammetry sweep following production formation within a nanoporous electrode. The assay is potentially convenient to perform given its one-step electrochemical determination of glycoprotein, and if applied using arrays of NPG electrodes could be miniaturized and applied for use in high-throughput glycan analysis.

REFERENCES

[1] Forty AJ. Corrosion micromorphology of noble metal alloys and depletion gilding. Nature. 1979;282:597-8.

[2] Ding Y, Kim YJ, Erlebacher J. Nanoporous Gold Leaf: "Ancient Technology"/Advanced Material. Advanced Materials. 2004;16:1897-900.

[3] Dixon MC, Daniel TA, Hieda M, Smilgies DM, Chan MHW, Allara DL. Preparation, Structure, and Optical Properties of Nanoporous Gold Thin Films. Langmuir. 2007;23:2414-22.

[4] Zhang J, Ma H, Zhang D, Liu P, Tian F, Ding Y. Electrocatalytic activity of bimetallic platinum-gold catalysts fabricated based on nanoporous gold. Physical Chemistry Chemical Physics. 2008;10:3250-5.

[5] Yu F, Ahl S, Caminade A-M, Majoral J-P, Knoll W, Erlebacher J. Simultaneous Excitation of Propagating and Localized Surface Plasmon Resonance in Nanoporous Gold Membranes. Analytical Chemistry. 2006;78:7346-50.

[6] Shulga OV, Zhou D, Demchenko AV, Stine KJ. Detection of free prostate specific antigen (fPSA) on a nanoporous gold platform. Analyst. 2008;133:319-22.

[7] Stine KJ, Jefferson K, Shulga OV. Nanoporous Gold for Enzyme Immobilization Enzyme Stabilization and Immobilization. In: Minteer SD, editor.: Humana Press; 2011. p. 67-83.

[8] Strong L, Whitesides GM. Structures of self-assembled monolayer films of organosulfur compounds adsorbed on gold single crystals: electron diffraction studies. Langmuir. 1988;4:546-58.

[9] Sigal GB, Bamdad C, Barberis A, Strominger J, Whitesides GM. A Self-Assembled Monolayer for the Binding and Study of Histidine-Tagged Proteins by Surface Plasmon Resonance. Analytical Chemistry. 1996;68:490-7.

[10] Chrisey LA, Lee GU, O'Ferrall CE. Covalent Attachment of Synthetic DNA to Self-Assembled Monolayer Films. Nucleic Acids Research. 1996;24:3031-9.

[11] Elghanian R, Storhoff JJ, Mucic RC, Letsinger RL, Mirkin CA. Selective Colorimetric Detection of Polynucleotides Based on the Distance-Dependent Optical Properties of Gold Nanoparticles. Science. 1997;277:1078-81.

[12] Storhoff JJ, Elghanian R, Mucic RC, Mirkin CA, Letsinger RL. One-Pot Colorimetric Differentiation of Polynucleotides with Single Base Imperfections Using Gold Nanoparticle Probes. Journal of the American Chemical Society. 1998;120:1959-64.

[13] Gao J, Bender CM, Murphy CJ. Dependence of the Gold Nanorod Aspect Ratio on the Nature of the Directing Surfactant in Aqueous Solution. Langmuir. 2003;19:9065-70.

[14] Liao H, Hafner JH. Gold Nanorod Bioconjugates. Chemistry of Materials. 2005;17:4636-41.

[15] Huang C-J, Wang Y-H, Chiu P-H, Shih M-C, Meen T-H. Electrochemical synthesis of gold nanocubes. Materials Letters. 2006;60:1896-900.

[16] Kim F, Connor S, Song H, Kuykendall T, Yang P. Platonic Gold Nanocrystals. Angewandte Chemie. 2004;116:3759-63.

[17] Hao F, Nehl CL, Hafner JH, Nordlander P. Plasmon Resonances of a Gold Nanostar. Nano Letters. 2007;7:729-32.

[18] Pandian Senthil K, Isabel P-S, Benito R-G, Abajo FJGd, Luis ML-M. High-yield synthesis and optical response of gold nanostars. Nanotechnology. 2008;19:015606.
[19] Ji C, Searson PC. Synthesis and Characterization of Nanoporous Gold Nanowires. The Journal of Physical Chemistry B. 2003;107:4494-9.
[20] Pandey B, Demchenko A, Stine K. Nanoporous gold as a solid support for protein immobilization and development of an electrochemical immunoassay for prostate specific antigen and carcinoembryonic antigen. Microchimica Acta.1-11.
[21] Pandey B, Tan YH, Fujikawa K, Demchenko AV, Stine KJ. Comparative Study of the Binding of Concanavalin A to Self-Assembled Monolayers Containing a Thiolated α-Mannoside on Flat Gold and on Nanoporous Gold. Journal of Carbohydrate Chemistry. 2012;31:466-503.
[22] Ding Y, Erlebacher J. Nanoporous Metals with Controlled Multimodal Pore Size Distribution. Journal of the American Chemical Society. 2003;125:7772-3.
[23] Deng Y, Huang W, Chen X, Li Z. Facile fabrication of nanoporous gold film electrodes. Electrochemistry Communications. 2008;10:810-3.
[24] Biener J, Hodge AM, Hayes JR, Volkert CA, Zepeda-Ruiz LA, Hamza AV, et al. Size Effects on the Mechanical Behavior of Nanoporous Au. Nano Letters. 2006;6:2379-82.
[25] Sun Y, Balk TJ. A multi-step dealloying method to produce nanoporous gold with no volume change and minimal cracking. Scripta Materialia. 2008;58:727-30.
[26] Seker E, Gaskins JT, Bart-Smith H, Zhu J, Reed ML, Zangari G, et al. The effects of post-fabrication annealing on the mechanical properties of freestanding nanoporous gold structures. Acta Materialia. 2007;55:4593-602.
[27] Qian LH, Yan XQ, Fujita T, Inoue A, Chen MW. Surface enhanced Raman scattering of nanoporous gold: Smaller pore sizes stronger enhancements. Applied Physics Letters. 2007;90:153120.
[28] Jia F, Yu C, Ai Z, Zhang L. Fabrication of Nanoporous Gold Film Electrodes with Ultrahigh Surface Area and Electrochemical Activity. Chem Mater. 2007;19:3648-53.
[29] Lang X, Hirata A, Fujita T, Chen M. Nanoporous metal/oxide hybrid electrodes for electrochemical supercapacitors. Nat Nano. 2011;6:232-6.
[30] Simon P, Gogotsi Y. Materials for electrochemical capacitors. Nat Mater. 2008;7:845-54.
[31] Gopinath SCB, Awazu K, Fujimaki M, Sugimoto K, Ohki Y, Komatsubara T, et al. Influence of Nanometric Holes on the Sensitivity of a Waveguide-Mode Sensor: Label-Free Nanosensor for the Analysis of RNA Aptamer−Ligand Interactions. Analytical Chemistry. 2008;80:6602-9.
[32] Sikavitsas V, Nitsche JM, Mountziaris TJ. Transport and Kinetic Processes Underlying Biomolecular Interactions in the BIACORE Optical Biosensor. Biotechnology Progress. 2002;18:885-97.
[33] Bok H-M, Shuford KL, Kim S, Kim SK, Park S. Multiple Surface Plasmon Modes for a Colloidal Solution of Nanoporous Gold Nanorods and Their Comparison to Smooth Gold Nanorods. Nano Letters. 2008;8:2265-70.
[34] Kim D-K, Kerman K, Saito M, Sathuluri RR, Endo T, Yamamura S, et al. Label-Free DNA Biosensor Based on Localized Surface Plasmon Resonance Coupled with Interferometry. Analytical Chemistry. 2007;79:1855-64.

[35] Ciesielski PN, Scott AM, Faulkner CJ, Berron BJ, Cliffel DE, Jennings GK. Functionalized Nanoporous Gold Leaf Electrode Films for the Immobilization of Photosystem I. ACS Nano. 2008;2:2465-72.
[36] Lang X, Qian L, Guan P, Zi J, Chen M. Localized surface plasmon resonance of nanoporous gold. Applied Physics Letters. 2011;98:093701--3.
[37] Zhang J, Liu P, Ma H, Ding Y. Nanostructured Porous Gold for Methanol Electro-Oxidation. The Journal of Physical Chemistry C. 2007;111:10382-8.
[38] Seker E, Reed M, Begley M. Nanoporous Gold: Fabrication, Characterization, and Applications. Materials. 2009;2:2188-215.
[39] Huang JF, Sun IW. Fabrication and Surface Functionalization of Nanoporous Gold by Electrochemical Alloying/Dealloying of Au–Zn in an Ionic Liquid, and the Self-Assembly of L-Cysteine Monolayers. Advanced Functional Materials. 2005;15:989-94.
[40] Zhang Q, Wang X, Qi Z, Wang Y, Zhang Z. A benign route to fabricate nanoporous gold through electrochemical dealloying of Al–Au alloys in a neutral solution. Electrochimica Acta. 2009;54:6190-8.
[41] Rouya E, Reed ML, Kelly RG, Bart-Smith H, Begley M, Zangari G. Synthesis of Nanoporous Gold Structures via Dealloying of Electroplated Au-Ni Alloy Films. ECS Transactions. 2007;6:41-50.
[42] Snyder J, Asanithi P, Dalton AB, Erlebacher J. Stabilized Nanoporous Metals by Dealloying Ternary Alloy Precursors. Advanced Materials. 2008;20:4883-6.
[43] Lu X, Balk TJ, Spolenak R, Arzt E. Dealloying of Au–Ag thin films with a composition gradient: Influence on morphology of nanoporous Au. Thin Solid Films. 2007;515:7122-6.
[44] Lavrik NV, Tipple CA, Sepaniak MJ, Datskos PG. <i>Gold Nano-Structures for Transduction of Biomolecular Interactions into Micrometer Scale Movements</i&gt. Biomedical Microdevices. 2001;3:35-44.
[45] Qian LH, Chen MW. Ultrafine nanoporous gold by low-temperature dealloying and kinetics of nanopore formation. Applied Physics Letters. 2007;91:083105--3.
[46] Erlebacher J, Aziz MJ, Karma A, Dimitrov N, Sieradzki K. Evolution of nanoporosity in dealloying. Nature. 2001;410:450-3.
[47] Petegem SV, Brandstetter S, Maass R, Hodge AM, El-Dasher BS, Biener Jr, et al. On the Microstructure of Nanoporous Gold: An X-ray Diffraction Study. Nano Letters. 2009;9:1158-63.
[48] Rösner H, Parida S, Kramer D, Volkert CA, Weissmüller J. Reconstructing a Nanoporous Metal in Three Dimensions: An Electron Tomography Study of Dealloyed Gold Leaf. Advanced Engineering Materials. 2007;9:535-41.
[49] Parida S, Kramer D, Volkert CA, Rösner H, Erlebacher J, Weissmüller J. Volume Change during the Formation of Nanoporous Gold by Dealloying. Physical Review Letters. 2006;97:035504.
[50] Wittstock A, Zielasek V, Biener J, Friend CM, Bäumer M. Nanoporous Gold Catalysts for Selective Gas-Phase Oxidative Coupling of Methanol at Low Temperature. Science. 2010;327:319-22.
[51] Xu C, Su J, Xu X, Liu P, Zhao H, Tian F, et al. Low Temperature CO Oxidation over Unsupported Nanoporous Gold. Journal of the American Chemical Society. 2006;129:42-3.

[52] Liu Z, Searson PC. Single Nanoporous Gold Nanowire Sensors. The Journal of Physical Chemistry B. 2006;110:4318-22.
[53] Liu Z, Du J, Qiu C, Huang L, Ma H, Shen D, et al. Electrochemical sensor for detection of p-nitrophenol based on nanoporous gold. Electrochemistry Communications. 2009;11:1365-8.
[54] Zhu A, Tian Y, Liu H, Luo Y. Nanoporous gold film encapsulating cytochrome c for the fabrication of a H2O2 biosensor. Biomaterials. 2009;30:3183-8.
[55] Hu K, Lan D, Li X, Zhang S. Electrochemical DNA Biosensor Based on Nanoporous Gold Electrode and Multifunctional Encoded DNA−Au Bio Bar Codes. Analytical Chemistry. 2008;80:9124-30.
[56] Qiu H, Xue L, Ji G, Zhou G, Huang X, Qu Y, et al. Enzyme-modified nanoporous gold-based electrochemical biosensors. Biosensors and Bioelectronics. 2009;24:3014-8.
[57] Zeis R, Mathur A, Fritz G, Lee J, Erlebacher J. Platinum-plated nanoporous gold: An efficient, low Pt loading electrocatalyst for PEM fuel cells. Journal of Power Sources. 2007;165:65-72.
[58] Ding C, Li H, Hu K, Lin J-M. Electrochemical immunoassay of hepatitis B surface antigen by the amplification of gold nanoparticles based on the nanoporous gold electrode. Talanta. 2010;80:1385-91.
[59] Liu B, Lu L, Hua E, Jiang S, Xie G. Detection of the human prostate-specific antigen using an aptasensor with gold nanoparticles encapsulated by graphitized mesoporous carbon. Microchimica Acta. 2012;178:163-70.
[60] Zielasek V, Jürgens B, Schulz C, Biener J, Biener MM, Hamza AV, et al. Gold Catalysts: Nanoporous Gold Foams. Angewandte Chemie International Edition. 2006;45:8241-4.
[61] Seo B, Kim J. Electrooxidation of Glucose at Nanoporous Gold Surfaces: Structure Dependent Electrocatalysis and Its Application to Amperometric Detection. Electroanalysis. 2010;22:939-45.
[62] Zeis R, Lei T, Sieradzki K, Snyder J, Erlebacher J. Catalytic reduction of oxygen and hydrogen peroxide by nanoporous gold. Journal of Catalysis. 2008;253:132-8.
[63] Yin H, Zhou C, Xu C, Liu P, Xu X, Ding Y. Aerobic Oxidation of d-Glucose on Support-Free Nanoporous Gold. The Journal of Physical Chemistry C. 2008;112:9673-8.
[64] El-Said WA, Lee J-H, Oh B-K, Choi J-W. 3-D nanoporous gold thin film for the simultaneous electrochemical determination of dopamine and ascorbic acid. Electrochemistry Communications. 2010;12:1756-9.
[65] Willets KA, Van Duyne RP. Localized Surface Plasmon Resonance Spectroscopy and Sensing. Annual Review of Physical Chemistry. 2007;58:267-97.
[66] Sepúlveda B, Angelomé PC, Lechuga LM, Liz-Marzán LM. LSPR-based nanobiosensors. Nano Today. 2009;4:244-51.
[67] Anker JN, Hall WP, Lyandres O, Shah NC, Zhao J, Van Duyne RP. Biosensing with plasmonic nanosensors. Nat Mater. 2008;7:442-53.
[68] Kim HM, Jin SM, Lee SK, Kim M-G, Shin Y-B. Detection of Biomolecular Binding Through Enhancement of Localized Surface Plasmon Resonance (LSPR) by Gold Nanoparticles. Sensors. 2009;9:2334-44.
[69] Yang J, Ryckman JD, Liscidini M, Sipe JE, Ciesielski PN, Escobar CA, et al. Direct imprinted gratings on nanoporous gold as effective SERS substrates. Lasers and Electro-Optics (CLEO), 2011 Conference on2011. p. 1-2.

[70] Kucheyev SO, Hayes JR, Biener J, Huser T, Talley CE, Hamza AV. Surface-enhanced Raman scattering on nanoporous Au. Applied Physics Letters. 2006;89:053102--3.
[71] Zhang L, Lang X, Hirata A, Chen M. Wrinkled Nanoporous Gold Films with Ultrahigh Surface-Enhanced Raman Scattering Enhancement. ACS Nano. 2011;5:4407-13.
[72] Qian L, Das B, Li Y, Yang Z. Giant Raman enhancement on nanoporous gold film by conjugating with nanoparticles for single-molecule detection. Journal of Materials Chemistry. 2010;20:6891-5.
[73] Qiu H, Xu C, Huang X, Ding Y, Qu Y, Gao P. Immobilization of Laccase on Nanoporous Gold: Comparative Studies on the Immobilization Strategies and the Particle Size Effects. The Journal of Physical Chemistry C. 2009;113:2521-5.
[74] Chen LY, Fujita T, Chen MW. Biofunctionalized nanoporous gold for electrochemical biosensors. Electrochimica Acta. 2012;67:1-5.
[75] Scanlon MD, Salaj-Kosla U, Belochapkine S, MacAodha D, Leech D, Ding Y, et al. Characterization of Nanoporous Gold Electrodes for Bioelectrochemical Applications. Langmuir. 2011;28:2251-61.
[76] Kafi AKM, Ahmadalinezhad A, Wang J, Thomas DF, Chen A. Direct growth of nanoporous Au and its application in electrochemical biosensing. Biosensors and Bioelectronics. 2010;25:2458-63.
[77] Ahmadalinezhad A, Kafi AKM, Chen A. Glucose biosensing based on the highly efficient immobilization of glucose oxidase on a Prussian blue modified nanostructured Au surface. Electrochemistry Communications. 2009;11:2048-51.
[78] Qiu H, Li Y, Ji G, Zhou G, Huang X, Qu Y, et al. Immobilization of lignin peroxidase on nanoporous gold: Enzymatic properties and in situ release of H2O2 by co-immobilized glucose oxidase. Bioresource Technology. 2009;100:3837-42.
[79] Shulga OV, Jefferson K, Khan AR, D'Souza VT, Liu J, Demchenko AV, et al. Preparation and Characterization of Porous Gold and Its Application as a Platform for Immobilization of Acetylcholine Esterase. Chem Mater. 2007;19:3902-11.
[80] Yan X, Wang X, Zhao P, zhang Y, Xu P, Ding Y. Xylanase immobilized nanoporous gold as a highly active and stable biocatalyst. Microporous and Mesoporous Materials. 2012;161:1-6.
[81] Chen X, Wang Y, Zhou J, Yan W, Li X, Zhu J-J. Electrochemical Impedance Immunosensor Based on Three-Dimensionally Ordered Macroporous Gold Film. Analytical Chemistry. 2008;80:2133-40.
[82] Hu X, Wang R, Ding Y, Zhang X, Jin W. Electrochemiluminescence of CdTe quantum dots as labels at nanoporous gold leaf electrodes for ultrasensitive DNA analysis. Talanta. 2010;80:1737-43.
[83] Li R, Wu D, Li H, Xu C, Wang H, Zhao Y, et al. Label-free amperometric immunosensor for the detection of human serum chorionic gonadotropin based on nanoporous gold and graphene. Analytical Biochemistry. 2011;414:196-201.
[84] Wink T, J. van Zuilen S, Bult A, P. van Bennekom W. Self-assembled Monolayers for Biosensors. Analyst. 1997;122:43R-50R.
[85] Ulman A. Formation and Structure of Self-Assembled Monolayers. Chem Rev. 1996;96:1533-54.

[86] Matthiesen JE, Jose D, Sorensen CM, Klabunde KJ. Loss of Hydrogen upon Exposure of Thiol to Gold Clusters at Low Temperature. Journal of the American Chemical Society. 2012;134:9376-9.
[87] Tielens F, Santos E. AuS and SH Bond Formation/Breaking during the Formation of Alkanethiol SAMs on Au(111): A Theoretical Study. The Journal of Physical Chemistry C. 2010;114:9444-52.
[88] Poirier GE, Tarlov MJ. The c(4X2) Superlattice of n-Alkanethiol Monolayers Self-Assembled on Au(111). Langmuir. 1994;10:2853-6.
[89] Love JC, Estroff LA, Kriebel JK, Nuzzo RG, Whitesides GM. Self-Assembled Monolayers of Thiolates on Metals as a Form of Nanotechnology. Chemical Reviews. 2005;105:1103-70.
[90] Schwartz DK. Mechanisms and Kinetics of Self-Aassembled Monolayer Formation. Annual Review of Physical Chemistry. 2001;52:107-37.
[91] Poirier GE, Pylant ED. The Self-Assembly Mechanism of Alkanethiols on Au(111). Science. 1996;272:1145-8.
[92] Bain CD, Troughton EB, Tao YT, Evall J, Whitesides GM, Nuzzo RG. Formation of monolayer films by the spontaneous assembly of organic thiols from solution onto gold. Journal of the American Chemical Society. 1989;111:321-35.
[93] Camillone N, Leung TYB, Schwartz P, Eisenberger P, Scoles G. Chain Length Dependence of the Striped Phases of Alkanethiol Monolayers Self-Assembled on Au(111): An Atomic Beam Diffraction Study. Langmuir. 1996;12:2737-46.
[94] Haehner G, Woell C, Buck M, Grunze M. Investigation of intermediate steps in the self-assembly of n-alkanethiols on gold surfaces by soft x-ray spectroscopy. Langmuir. 1993;9:1955-8.
[95] Folkers JP, Laibinis PE, Whitesides GM. Self-assembled monolayers of alkanethiols on gold: comparisons of monolayers containing mixtures of short- and long-chain constituents with methyl and hydroxymethyl terminal groups. Langmuir. 1992;8:1330-41.
[96] Creager SE, Olsen KG. Self-assembled monolayers and enzyme electrodes: Progress, problems and prospects. Analytica Chimica Acta. 1995;307:277-89.
[97] Xu S, Liu G-y. Nanometer-Scale Fabrication by Simultaneous Nanoshaving and Molecular Self-Assembly. Langmuir. 1997;13:127-9.
[98] Schneider TW, Buttry DA. Electrochemical quartz crystal microbalance studies of adsorption and desorption of self-assembled monolayers of alkyl thiols on gold. Journal of the American Chemical Society. 1993;115:12391-7.
[99] Tan YH, Davis JA, Fujikawa K, Ganesh NV, Demchenko AV, Stine KJ. Surface area and pore size characteristics of nanoporous gold subjected to thermal, mechanical, or surface modification studied using gas adsorption isotherms, cyclic voltammetry, thermogravimetric analysis, and scanning electron microscopy. Journal of Materials Chemistry. 2012;22:6733-45.
[100] Li Y, Huang J, McIver RT, Hemminger JC. Characterization of thiol self-assembled films by laser desorption Fourier transform mass spectrometry. Journal of the American Chemical Society. 1992;114:2428-32.
[101] Badia A, Cuccia L, Demers L, Morin F, Lennox RB. Structure and Dynamics in Alkanethiolate Monolayers Self-Assembled on Gold Nanoparticles: A DSC, FT-IR,

and Deuterium NMR Study. Journal of the American Chemical Society. 1997;119:2682-92.
[102] Hostetler MJ, Murray RW. Colloids and self-assembled monolayers. Current Opinion in Colloid & Interface Science. 1997;2:42-50.
[103] Badia A, Singh S, Demers L, Cuccia L, Brown GR, Lennox RB. Self-Assembled Monolayers on Gold Nanoparticles. Chemistry – A European Journal. 1996;2:359-63.
[104] Homola J, Yee SS, Gauglitz G. Surface plasmon resonance sensors: review. Sensors and Actuators B: Chemical. 1999;54:3-15.
[105] Butler JE. Solid Supports in Enzyme-Linked Immunosorbent Assay and Other Solid-Phase Immunoassays. Methods. 2000;22:4-23.
[106] Miller JC, Zhou H, Kwekel J, Cavallo R, Burke J, Butler EB, et al. Antibody microarray profiling of human prostate cancer sera: Antibody screening and identification of potential biomarkers. Proteomics. 2003;3:56-63.
[107] Hartmann M, Roeraade J, Stoll D, Templin M, Joos T. Protein microarrays for diagnostic assays. Analytical and Bioanalytical Chemistry. 2009;393:1407-16.
[108] Sanghvi AB, Miller KPH, Belcher AM, Schmidt CE. Biomaterials functionalization using a novel peptide that selectively binds to a conducting polymer. Nat Mater. 2005;4:496-502.
[109] Kasemo B. Biological surface science. Surface Science. 2002;500:656-77.
[110] Shin H, Jo S, Mikos AG. Biomimetic materials for tissue engineering. Biomaterials. 2003;24:4353-64.
[111] Yeo DSY, Panicker RC, Tan LP, Yao SQ. Strategies for Immobilization of Biomolecules in a Microarray. Combinatorial Chemistry & High Throughput Screening.7:213-21.
[112] Albala JS. Array-based proteomics: the latest chip challenge. Expert Review of Molecular Diagnostics. 2001;1:145-52.
[113] Scouten WH, Luong JHT, Stephen Brown R. Enzyme or protein immobilization techniques for applications in biosensor design. Trends in Biotechnology. 1995;13:178-85.
[114] Templin MF, Stoll D, Schrenk M, Traub PC, Vöhringer CF, Joos TO. Protein microarray technology. Drug Discovery Today. 2002;7:815-22.
[115] Schena M, Shalon D, Davis RW, Brown PO. Quantitative Monitoring of Gene Expression Patterns with a Complementary DNA Microarray. Science. 1995;270:467-70.
[116] Wagner P. Immobilization strategies for biological scanning probe microscopy. FEBS Letters. 1998;430:112-5.
[117] Blixt O, Head S, Mondala T, Scanlan C, Huflejt ME, Alvarez R, et al. Printed covalent glycan array for ligand profiling of diverse glycan binding proteins. Proceedings of the National Academy of Sciences of the United States of America. 2004;101:17033-8.
[118] Rosenfeld R, Bangio H, Gerwig GJ, Rosenberg R, Aloni R, Cohen Y, et al. A lectin array-based methodology for the analysis of protein glycosylation. Journal of Biochemical and Biophysical Methods. 2007;70:415-26.
[119] MacBeath G. Protein microarrays and proteomics. Nat Genet. 2002;32:526-32.
[120] MacBeath G, Schreiber SL. Printing Proteins as Microarrays for High-Throughput Function Determination. Science. 2000;289:1760-3.
[121] Love KR, Seeberger PH. Carbohydrate Arrays as Tools for Glycomics. Angewandte Chemie International Edition. 2002;41:3583-6.

[122] Houseman BT, Mrksich M. Carbohydrate Arrays for the Evaluation of Protein Binding and Enzymatic Modification. Chemistry & Biology. 2002;9:443-54.
[123] Lee YC, Lee RT. Carbohydrate-Protein Interactions: Basis of Glycobiology. Accounts of Chemical Research. 1995;28:321-7.
[124] Jayaraman N. Multivalent ligand presentation as a central concept to study intricate carbohydrate-protein interactions. Chemical Society Reviews. 2009;38:3463-83.
[125] Rusmini F, Zhong Z, Feijen J. Protein Immobilization Strategies for Protein Biochips. Biomacromolecules. 2007;8:1775-89.
[126] Williams RA, Blanch HW. Covalent immobilization of protein monolayers for biosensor applications. Biosensors and Bioelectronics. 1994;9:159-67.
[127] Liu Y-C, Wang C-M, Hsiung K-P. Comparison of Different Protein Immobilization Methods on Quartz Crystal Microbalance Surface in Flow Injection Immunoassay. Analytical Biochemistry. 2001;299:130-5.
[128] Roach P, Farrar D, Perry CC. Interpretation of Protein Adsorption: Surface-Induced Conformational Changes. Journal of the American Chemical Society. 2005;127:8168-73.
[129] Wesslén B, Kober M, Freij-Larsson C, Ljungh Å, Paulsson M. Protein adsorption of poly(ether methane) surfaces modified by amphiphilic and hydrophilic polymers. Biomaterials. 1994;15:278-84.
[130] Park JH, Bae YH. Hydrogels based on poly(ethylene oxide) and poly(tetramethylene oxide) or poly(dimethyl siloxane): synthesis, characterization, in vitro protein adsorption and platelet adhesion. Biomaterials. 2002;23:1797-808.
[131] Wadu-Mesthrige K, Amro NA, Liu G-Y. Immobilization of proteins on self-assembled monolayers. Scanning. 2000;22:380-8.
[132] Rao SV, Anderson KW, Bachas LG. Oriented immobilization of proteins. Microchimica Acta. 1998;128:127-43.
[133] Lee JM, Park HK, Jung Y, Kim JK, Jung SO, Chung BH. Direct Immobilization of Protein G Variants with Various Numbers of Cysteine Residues on a Gold Surface. Analytical Chemistry. 2007;79:2680-7.
[134] Hong HG, Jiang M, Sligar SG, Bohn PW. Cysteine-specific surface tethering of genetically engineered cytochromes for fabrication of metalloprotein nanostructures. Langmuir. 1994;10:153-8.
[135] Morales-Sanfrutos J, Lopez-Jaramillo J, Ortega-Munoz M, Megia-Fernandez A, Perez-Balderas F, Hernandez-Mateo F, et al. Vinyl sulfone: a versatile function for simple bioconjugation and immobilization. Organic & Biomolecular Chemistry. 2010;8:667-75.
[136] Blawas AS, Reichert WM. Protein patterning. Biomaterials. 1998;19:595-609.
[137] Lutz J-F, Zarafshani Z. Efficient construction of therapeutics, bioconjugates, biomaterials and bioactive surfaces using azide–alkyne “click” chemistry. Advanced Drug Delivery Reviews. 2008;60:958-70.
[138] Watzke A, Köhn M, Gutierrez-Rodriguez M, Wacker R, Schröder H, Breinbauer R, et al. Site-Selective Protein Immobilization by Staudinger Ligation. Angewandte Chemie. 2006;118:1436-40.
[139] Khan F, He M, Taussig MJ. Double-Hexahistidine Tag with High-Affinity Binding for Protein Immobilization, Purification, and Detection on Ni−Nitrilotriacetic Acid Surfaces. Analytical Chemistry. 2006;78:3072-9.

[140] Boozer C, Ladd J, Chen S, Jiang S. DNA-Directed Protein Immobilization for Simultaneous Detection of Multiple Analytes by Surface Plasmon Resonance Biosensor. Analytical Chemistry. 2006;78:1515-9.
[141] Gauchet C, Labadie GR, Poulter CD. Regio- and Chemoselective Covalent Immobilization of Proteins through Unnatural Amino Acids. Journal of the American Chemical Society. 2006;128:9274-5.
[142] Camarero JA, Kwon Y, Coleman MA. Chemoselective Attachment of Biologically Active Proteins to Surfaces by Expressed Protein Ligation and Its Application for "Protein Chip" Fabrication. Journal of the American Chemical Society. 2004;126:14730-1.
[143] Kindermann M, George N, Johnsson N, Johnsson K. Covalent and Selective Immobilization of Fusion Proteins. Journal of the American Chemical Society. 2003;125:7810-1.
[144] Hodneland CD, Lee Y-S, Min D-H, Mrksich M. Selective immobilization of proteins to self-assembled monolayers presenting active site-directed capture ligands. Proceedings of the National Academy of Sciences. 2002;99:5048-52.
[145] MacBeath G. Protein microarrays and proteomics. Nat Genet.
[146] Huhn C, Selman MHJ, Ruhaak LR, Deelder AM, Wuhrer M. IgG glycosylation analysis. Proteomics. 2009;9:882-913.
[147] Amzel LM, Poljak RJ. Three-Dimensional Structure of Immunoglobulins. Annual Review of Biochemistry. 1979;48:961-97.
[148] Sundberg EJ. Structural Basis of Antibody–Antigen Interactions: Epitope Mapping Protocols. In: Schutkowski M, Reineke U, editors.: Humana Press; 2009. p. 23-36.
[149] Padlan EA. Anatomy of the antibody molecule. Molecular Immunology. 1994;31:169-217.
[150] Brinkmann V, Heusser CH. T Cell-Dependent Differentiation of Human B Cells into IgM, IgG, IgA, or IgE Plasma Cells: High Rate of Antibody Production by IgE Plasma Cells, but Limited Clonal Expansion of IgE Precursors. Cellular Immunology. 1993;152:323-32.
[151] Oxelius V-A. Immunoglobulin G (IgG) subclasses and human disease. The American Journal of Medicine. 1984;76:7-18.
[152] Bradbury A, Cattaneo A. The use of phage display in neurobiology. Trends in Neurosciences. 1995;18:243-9.
[153] Taylor RMR. Monoclonal and polyclonal antibodies: clinical aspects. Immunology Letters. 1991;29:113-6.
[154] Gardiner, Mackie, Machin. Simultaneous assay of free and total protein S by ELISA using monoclonal and polyclonal antibodies. Clinical & Laboratory Haematology. 1998;20:41-5.
[155] Goldstein IJ, Hayes CE. The Lectins: Carbohydrate-Binding Proteins of Plants and Animals. In: Tipson RS, Derek H, editors. Advances in Carbohydrate Chemistry and Biochemistry: Academic Press; 1978. p. 127-340.
[156] Sharon N, Lis H. Lectins as cell recognition molecules. Science. 1989;246:227-34.
[157] Sharon N, Lis H. Lectins: Cell-Agglutinating and Sugar-Specific Proteins. Science. 1972;177:949-59.
[158] Etzler ME. Plant Lectins: Molecular and Biological Aspects. Annual Review of Plant Physiology. 1985;36:209-34.

[159] Sharon N, Lis H. History of lectins: from hemagglutinins to biological recognition molecules. Glycobiology. 2004;14:53R-62R.
[160] Lis H, Sharon N. Lectins as Molecules and as Tools. Annual Review of Biochemistry. 1986;55:35-67.
[161] Sharon N. Lectins: Carbohydrate-specific Reagents and Biological Recognition Molecules. Journal of Biological Chemistry. 2007;282:2753-64.
[162] Weis WI, Drickamer K. Structural Basis of Lectin-Carbohydrate Recognition. Annual Review of Biochemistry. 1996;65:441-73.
[163] Sharon N, Lis H. The Structural Basis for Carbohydrate Recognition By Lectins The Molecular Immunology of Complex Carbohydrates —2. In: Wu AM, editor.: Springer US; 2001. p. 1-16.
[164] Bundle DR, Young NM. Carbohydrate-protein interactions in antibodies and lectins. Current Opinion in Structural Biology. 1992;2:666-73.
[165] Sharma V, Surolia A. Analyses of carbohydrate recognition by legume lectins: size of the combining site loops and their primary specificity. Journal of Molecular Biology. 1997;267:433-45.
[166] Rini JM. Lectin Structure. Annual Review of Biophysics and Biomolecular Structure. 1995;24:551-77.
[167] Stenman U-H, Leinonen J, Zhang W-M, Finne P. Prostate-specific antigen. Seminars in Cancer Biology. 1999;9:83-93.
[168] Lilja H, Ulmert D, Vickers AJ. Prostate-specific antigen and prostate cancer: prediction, detection and monitoring. Nat Rev Cancer. 2008;8:268-78.
[169] Nakashima J, Tachibana M, Horiguchi Y, Oya M, Ohigashi T, Asakura H, et al. Serum Interleukin 6 as a Prognostic Factor in Patients with Prostate Cancer. Clinical Cancer Research. 2000;6:2702-6.
[170] Brawer MK. Prostate-specific antigen. Seminars in Surgical Oncology. 2000;18:3-9.
[171] Djavan B, Zlotta AR, Byttebier G, Shariat S, Omar M, Schulman CC, et al. Prostate Specific Antigen Density of the Transition Zone for Early Detection of Prostate Cancer. The Journal of Urology. 1998;160:411-8.
[172] USPSTF. The USPSTF recommends against PSA-based screening for prostate cancer. http://wwwuspreventiveservicestaskforceorg/prostatecancerscreeninghtm. 2012.
[173] Catalona WJ. The United States Preventive Services Task Force Recommendation against Prostate-Specific Antigen Screening—Counterpoint. Cancer Epidemiology Biomarkers & Prevention. 2012.
[174] Payton S. Prostate cancer: PSA screening[mdash]more data, more debate. Nat Rev Urol. 2012;9:59-.
[175] Vickers AJ, Lilja H. Urological cancer: Time for another rethink on prostate cancer screening. Nat Rev Clin Oncol. 2012;9:7-8.
[176] Chen Y, Scher HI. Prostate cancer in 2011: Hitting old targets better and identifying new targets. Nat Rev Clin Oncol. 2012;9:70-2.
[177] Osborne JR, Akhtar NH, Vallabhajosula S, Anand A, Deh K, Tagawa ST. Prostate-specific membrane antigen-based imaging. Urologic Oncology: Seminars and Original Investigations.
[178] Jakob CG, Lewinski K, Kuciel R, Ostrowski W, Lebioda L. Crystal structure of human prostatic acid phosphatase. The Prostate. 2000;42:211-8.

[179] Quintero IB, Araujo CL, Pulkka AE, Wirkkala RS, Herrala AM, Eskelinen E-L, et al. Prostatic Acid Phosphatase Is Not a Prostate Specific Target. Cancer Research. 2007;67:6549-54.
[180] Taira A, Merrick G, Wallner K, Dattoli M. Reviving the Acid Phosphatase Test for Prostate Cancer. Oncology. 2007;21:1-2.
[181] Fair WR, Israeli RS, Heston WDW. Prostate-specific membrane antigen. The Prostate. 1997;32:140-8.
[182] Hammarström S. The carcinoembryonic antigen (CEA) family: structures, suggested functions and expression in normal and malignant tissues. Seminars in Cancer Biology. 1999;9:67-81.
[183] Benchimol S, Fuks A, Jothy S, Beauchemin N, Shirota K, Stanners CP. Carcinoembryonic antigen, a human tumor marker, functions as an intercellular adhesion molecule. Cell. 1989;57:327-34.
[184] Duffy MJ. Carcinoembryonic Antigen as a Marker for Colorectal Cancer: Is It Clinically Useful? Clinical Chemistry. 2001;47:624-30.
[185] Moertel CG, Fleming T. R., Macdonald J. S., Haller D. G., Laurie J. A., C. T. AN evaluation of the carcinoembryonic antigen (cea) test for monitoring patients with resected colon cancer. JAMA: The Journal of the American Medical Association. 1993;270:943-7.
[186] Vassalle C, Pratali L, Ndreu R, Battaglia D, Andreassi Maria G. Carcinoembryonic antigen concentrations in patients with acute coronary syndrome. Clinical Chemistry and Laboratory Medicine2010. p. 1339.
[187] Beard DB, Haskell CM. Carcinoembryonic antigen in breast cancer. Clinical review. The American Journal of Medicine. 1986;80:241-5.
[188] Vincent RG, Chu TM, Lane WW. The value of carcinoembryonic antigen in patients with carcinoma of the lung. Cancer. 1979;44:685-91.
[189] Gomme PT, McCann KB, Bertolini J. Transferrin: structure, function and potential therapeutic actions. Drug Discovery Today. 2005;10:267-73.
[190] Baker EN, Lindley PF. New perspectives on the structure and function of transferrins. Journal of Inorganic Biochemistry.47:147-60.
[191] Stibler H. Carbohydrate-deficient transferrin in serum: a new marker of potentially harmful alcohol consumption reviewed. Clinical Chemistry. 1991;37:2029-37.
[192] Bond A, Alavi A, Axford JS, Bourke BE, Bruckner FE, Kerr MA, et al. A Detailed Lectin Analysis of IgG Glycosylation, Demonstrating Disease Specific Changes in Terminal Galactose and N-acetylglucosamine. Journal of Autoimmunity. 1997;10:77-85.
[193] Parekh RB, Dwek RA, Sutton BJ, Fernandes DL, Leung A, Stanworth D, et al. Association of rheumatoid arthritis and primary osteoarthritis with changes in the glycosylation pattern of total serum IgG. Nature. 1985;316:452-7.
[194] Stenvinkel P, Wang K, Qureshi AR, Axelsson J, Pecoits-Filho R, Gao P, et al. Low fetuin-A levels are associated with cardiovascular death: Impact of variations in the gene encoding fetuin. 2005;67:2383-92.
[195] Mori K, Emoto M, Araki T, Yokoyama H, Teramura M, Lee E, et al. Association of serum fetuin-A with carotid arterial stiffness. Clinical Endocrinology. 2007;66:246-50.
[196] Stefan N, Fritsche A, Weikert C, Boeing H, Joost H-G, Häring H-U, et al. Plasma Fetuin-A Levels and the Risk of Type 2 Diabetes. Diabetes. 2008;57:2762-7.
[197] INc. NEB. http://www.neb.com/nebecomm/products/productm0290.asp. 2012.

[198] Cordell JL, Falini B, Erber WN, Ghosh AK, Abdulaziz Z, MacDonald S, et al. Immunoenzymatic labeling of monoclonal antibodies using immune complexes of alkaline phosphatase and monoclonal anti-alkaline phosphatase (APAAP complexes). Journal of Histochemistry & Cytochemistry. 1984;32:219-29.
[199] Engvall E, Perlmann P. Enzyme-Linked Immunosorbent Assay, Elisa. The Journal of Immunology. 1972;109:129-35.
[200] Krebs EG, Beavo JA. Phosphorylation-Dephosphorylation of Enzymes. Annual Review of Biochemistry. 1979;48:923-59.
[201] Yalow RS, Berson SA. Assay of Plasma Insulin in Human Subjects by Immunological Methods. Nature. 1959;184:1648-9.
[202] Engvall E, Jonsson K, Perlmann P. Enzyme-linked immunosorbent assay. II. Quantitative assay of protein antigen, immunoglobulin g, by means of enzyme-labelled antigen and antibody-coated tubes. Biochimica et Biophysica Acta (BBA) - Protein Structure. 1971;251:427-34.
[203] Catt K, Tregear GW. Solid-Phase Radioimmunoassay in Antibody-Coated Tubes. Science. 1967;158:1570-2.
[204] Ekins R. Immunoassay: recent developments and future directions. Nuclear Medicine and Biology. 1994;21:495-521.
[205] Gosling JP. A decade of development in immunoassay methodology. Clinical Chemistry. 1990;36:1408-27.
[206] Hosoda K, Eguchi H, Nakamoto T, Kubota T, Honda H, Jindai S, et al. Sandwich immunoassay for intact human osteocalcin. Clinical Chemistry. 1992;38:2233-8.
[207] Maiolini R, Ferrua B, Quaranta JF, Pinoteau A, Euller L, Ziegler G, et al. A sandwich method of enzyme-immunoassay. II. Quantification of rheumatoid factor. Journal of Immunological Methods. 1978;20:25-34.
[208] Jia M, Belyavskaya E, Deuster P, Sternberg EM. Development of a Sensitive Microarray Immunoassay for the Quantitative Analysis of Neuropeptide Y. Analytical Chemistry. 2012;84:6508-14.
[209] Larue C, Calzolari C, Bertinchant JP, Leclercq F, Grolleau R, Pau B. Cardiac-specific immunoenzymometric assay of troponin I in the early phase of acute myocardial infarction. Clinical Chemistry. 1993;39:972-9.
[210] Luborsky JL, Visintin I, Boyers S, Asari T, Caldwell B, Decherney A. Ovarian Antibodies Detected by Immobilized Antigen Immunoassay in Patients with Premature Ovarian Failure. Journal of Clinical Endocrinology & Metabolism. 1990;70:69-75.
[211] Rubenstein KE. Homogeneous Enzyme Immunoassay Today. Scandinavian Journal of Immunology. 1978;8:57-62.
[212] Rowley GL, Rubenstein KE, Huisjen J, Ullman EF. Mechanism by which antibodies inhibit hapten-malate dehydrogenase conjugates. An enzyme immunoassay for morphine. Journal of Biological Chemistry. 1975;250:3759-66.
[213] Ullman EF, Yoshida RA, Blakemore JI, Maggio E, Leute R. Mechanism of inhibition of malate dehydrogenase by thyroxine derivatives and reactivation by antibodies Homogeneous enzyme immunoassay for thryroxine. Biochimica et Biophysica Acta (BBA) - Enzymology. 1979;567:66-74.
[214] Chiu ML, Ytterberg AJ, Ogorzalek Loo RR, Loo JA, Monbouquette HG. Characterization of Morphine–Glucose-6-phosphate Dehydrogenase Conjugates by Mass Spectrometry. Bioconjugate Chemistry. 2011;22:1595-604.

[215] Rodgers R, Crowl CP, Eimstad WM, Hu MW, Kam JK, Ronald RC, et al. Homogeneous enzyme immunoassay for cannabinoids in urine. Clinical Chemistry. 1978;24:95-100.
[216] Ullman EF, Blakemore JI, Leute R, Eimstad WM, Jaklitsch A. Homogeneous Enzyme Immunoassay for Thyroxine. Clinical Chemistry. 1975;21:1011.
[217] Rosenthal AF, Vargas MG, Klass CS. Evaluation of enzyme-multiplied immunoassay technique (EMIT) for determination of serum digoxin. Clinical Chemistry. 1976;22:1899-902.
[218] Arvieux J, Darnige L, Caron C, Reber G, Bensa JC, Colomb MG. Development of an ELISA for autoantibodies to prothrombin showing their prevalence in patients with lupus anticoagulants. Thrombosis and haemostasis. 1995;74:1120-5.
[219] Malvano R, Boniolo A, Dovis M, Zannino M. Elisa for antibody measurement: Aspects related to data expression. Journal of Immunological Methods. 1982;48:51-60.
[220] Cho J-H, Han S-M, Paek E-H, Cho I-H, Paek S-H. Plastic ELISA-on-a-Chip Based on Sequential Cross-Flow Chromatography. Analytical Chemistry. 2006;78:793-800.
[221] Bora U, Sharma P, Kannan K, Nahar P. Photoreactive cellulose membrane—A novel matrix for covalent immobilization of biomolecules. Journal of Biotechnology. 2006;126:220-9.
[222] Janitschke K, Reinhold A, Bode L. Nitrocellulose dot-ELISA for serodiagnosis of schistosomiasis. Transactions of the Royal Society of Tropical Medicine and Hygiene. 1987;81:956-8.
[223] Böcher M, Giersch T, Schmid RD. Dextran, a hapten carrier in immunoassays for s-triazines a comparison with ELISAs based on hapten-protein conjugates. Journal of Immunological Methods. 1992;151:1-8.
[224] Eteshola E, Leckband D. Development and characterization of an ELISA assay in PDMS microfluidic channels. Sensors and Actuators B: Chemical. 2001;72:129-33.
[225] Stefan RI, van Staden JF, Aboul-Enein HY. Immunosensors in clinical analysis. Fresenius' Journal of Analytical Chemistry. 2000;366:659-68.
[226] Corning. http://www.corning.com/lifesciences/us_canada/en/technical_resources/surfaces/assay.aspx. 2012.
[227] http://www.nuncbrand.com/en/page.aspx?ID=1238.
[228] Thermo Scientific N. http://www.nuncbrand.com/en/page.aspx?ID=251. 2012.
[229] Luk Y-Y, Kato M, Mrksich M. Self-Assembled Monolayers of Alkanethiolates Presenting Mannitol Groups Are Inert to Protein Adsorption and Cell Attachment. Langmuir. 2000;16:9604-8.
[230] Ronkainen-Matsuno NJ, Thomas JH, Halsall HB, Heineman WR. Electrochemical immunoassay moving into the fast lane. TrAC Trends in Analytical Chemistry. 2002;21:213-25.
[231] Wang J, Ibáñez A, Chatrathi MP, Escarpa A. Electrochemical Enzyme Immunoassays on Microchip Platforms. Analytical Chemistry. 2001;73:5323-7.
[232] Pumera M, Sánchez S, Ichinose I, Tang J. Electrochemical nanobiosensors. Sensors and Actuators B: Chemical. 2007;123:1195-205.
[233] Keating MY, Rechnitz GA. Potentiometric digoxin antibody measurements with antigen-ionophore based membrane electrodes. Analytical Chemistry. 1984;56:801-6.

[234] Carroll MC. The complement system in regulation of adaptive immunity. Nat Immunol. 2004;5:981-6.
[235] Solsky RL, Rechnitz GA. Ion-Selective Electrodes in Biomedical Analysis. C R C Critical Reviews in Analytical Chemistry. 1982;14:1-52.
[236] D'Orazio P, Rechnitz GA. Ion electrode measurements of complement and antibody levels using marker-loaded sheep red blood cell ghosts. Analytical Chemistry. 1977;49:2083-6.
[237] Robinson GA, Cole VM, Rattle SJ, Forrest GC. Bioelectrochemical immunoassay for human chorionic gonadotrophin in serum using an electrode-immobilised capture antibody. Biosensors. 1986;2:45-57.
[238] Green MJ. Electrochemical Immunoassays. Philosophical Transactions of the Royal Society of London B, Biological Sciences. 1987;316:135-42.
[239] Lunte C, Heineman W. Electrochemical techniques in bioanalysis In: Steckhan E, editor. Electrochemistry II: Springer Berlin / Heidelberg; 1988. p. 1-48.
[240] Collins S, Janata J. A critical evaluation of the mechanism of potential response of antigen polymer membranes to the corresponding antiserum. Analytica Chimica Acta. 1982;136:93-9.
[241] Janata J. Immunoelectrode. Journal of the American Chemical Society. 1975;97:2914-6.
[242] Wang L, Gan X. Antibody-functionalized magnetic nanoparticles for electrochemical immunoassay of α-1-fetoprotein in human serum. Microchimica Acta. 2009;164:231-7.
[243] Eggers HM, Halsall HB, Heineman WR. Enzyme immunoassay with flow-amperometric detection of NADH. Clinical Chemistry. 1982;28:1848-51.
[244] Heineman W, Anderson C, Halsall H. Immunoassay by differential pulse polarography. Science. 1979;204:865-6.
[245] Díaz-González M, González-García MB, Costa-García A. Recent Advances in Electrochemical Enzyme Immunoassays. Electroanalysis. 2005;17:1901-18.
[246] Ghindilis AL, Atanasov P, Wilkins M, Wilkins E. Immunosensors: electrochemical sensing and other engineering approaches. Biosensors and Bioelectronics. 1998;13:113-31.
[247] Sitta Sittampalam G, Wilson GS. Enzyme immunoassays with electrochemical detection. TrAC Trends in Analytical Chemistry. 1984;3:96-9.
[248] Mehrvar M, Abdi M. Recent Developments, Characteristics, and Potential Applications of Electrochemical Biosensors. Analytical Sciences. 2004;20:1113-26.
[249] Warsinke A, Benkert A, Scheller FW. Electrochemical immunoassays. Fresenius' Journal of Analytical Chemistry. 2000;366:622-34.
[250] Li X-M, Yang X-Y, Zhang S-S. Electrochemical enzyme immunoassay using model labels. TrAC Trends in Analytical Chemistry. 2008;27:543-53.
[251] Tang D, Yuan R, Chai Y. Ultrasensitive Electrochemical Immunosensor for Clinical Immunoassay Using Thionine-Doped Magnetic Gold Nanospheres as Labels and Horseradish Peroxidase as Enhancer. Analytical Chemistry. 2008;80:1582-8.
[252] Thompson RQ, Barone Iii GC, Halsall HB, Heineman WR. Comparison of methods for following alkaline phosphatase catalysis: Spectrophotometric versus amperometric detection. Analytical Biochemistry. 1991;192:90-5.

[253] Wang J. Electrochemical biosensors: Towards point-of-care cancer diagnostics. Biosensors and Bioelectronics. 2006;21:1887-92.
[254] Murphy L. Biosensors and bioelectrochemistry. Current Opinion in Chemical Biology. 2006;10:177-84.
[255] Chen J, Tang J, Yan F, Ju H. A gold nanoparticles/sol–gel composite architecture for encapsulation of immunoconjugate for reagentless electrochemical immunoassay. Biomaterials. 2006;27:2313-21.
[256] Han K-C, Yang EG, Ahn D-R. A highly sensitive, multiplex immunoassay using gold nanoparticle-enhanced signal amplification. Chemical Communications. 2012;48:5895-7.
[257] Tang H, Chen J, Nie L, Kuang Y, Yao S. A label-free electrochemical immunoassay for carcinoembryonic antigen (CEA) based on gold nanoparticles (AuNPs) and nonconductive polymer film. Biosensors and Bioelectronics. 2007;22:1061-7.
[258] Qiu L-P, Wang C-C, Hu P, Wu Z-S, Shen G-L, Yu R-Q. A label-free electrochemical immunoassay for IgG detection based on the electron transfer. Talanta. 2010;83:42-7.
[259] Zhuo Y, Yuan R, Chai Y, Tang D, Zhang Y, Wang N, et al. A reagentless amperometric immunosensor based on gold nanoparticles/thionine/Nafion-membrane-modified gold electrode for determination of α-1-fetoprotein. Electrochemistry Communications. 2005;7:355-60.
[260] Li Y, Yang W-K, Fan M-Q, Liu A. A Sensitive Label-free Amperometric CEA Immunosensor Based on Graphene-Nafion Nanocomposite Film as an Enhanced Sensing Platform. Analytical Sciences. 2011;27:727-.
[261] Singh K, Rahman MA, Son JI, Kim KC, Shim Y-B. An amperometric immunosensor for osteoproteogerin based on gold nanoparticles deposited conducting polymer. Biosensors and Bioelectronics. 2008;23:1595-601.
[262] Bangham DR, Grab B. The Second International Standard for Chorionic Gonadotrophin. Bulletin of the World Health Organization. 1964;31:111-25.
[263] Li N, Yuan R, Chai Y, Chen S, An H. Sensitive immunoassay of human chorionic gonadotrophin based on multi-walled carbon nanotube–chitosan matrix. Bioprocess and Biosystems Engineering. 2008;31:551-8.
[264] Ding C, Zhang Q, Zhang S. An electrochemical immunoassay for protein based on bio bar code method. Biosensors and Bioelectronics. 2009;24:2434-40.
[265] Wu L, Chen J, Du D, Ju H. Electrochemical immunoassay for CA125 based on cellulose acetate stabilized antigen/colloidal gold nanoparticles membrane. Electrochimica Acta. 2006;51:1208-14.
[266] Chen J, Yan F, Du D, Wu J, Ju H. Electrochemical Immunoassay of Human Chorionic Gonadotrophin Based on Its Immobilization in Gold Nanoparticles-Chitosan Membrane. Electroanalysis. 2006;18:670-6.
[267] Tang D, Ren J. In Situ Amplified Electrochemical Immunoassay for Carcinoembryonic Antigen Using Horseradish Peroxidase-Encapsulated Nanogold Hollow Microspheres as Labels. Analytical Chemistry. 2008;80:8064-70.
[268] An Y, Jiang X, Bi W, Chen H, Jin L, Zhang S, et al. Sensitive electrochemical immunosensor for α-synuclein based on dual signal amplification using PAMAM dendrimer-encapsulated Au and enhanced gold nanoparticle labels. Biosensors and Bioelectronics. 2012;32:224-30.

[269] Lin J, Qu W, Zhang S. Electrochemical Immunosensor for Carcinoembryonic Antigen Based on Antigen Immobilization in Gold Nanoparticles Modified Chitosan Membrane. Analytical Sciences. 2007;23:1059-63.
[270] Yuan Y-R, Yuan R, Chai Y-Q, Zhuo Y, Miao X-M. Electrochemical amperometric immunoassay for carcinoembryonic antigen based on bi-layer nano-Au and nickel hexacyanoferrates nanoparticles modified glassy carbon electrode. Journal of Electroanalytical Chemistry. 2009;626:6-13.
[271] Zhou F, Lu M, Wang W, Bian Z-P, Zhang J-R, Zhu J-J. Electrochemical Immunosensor for Simultaneous Detection of Dual Cardiac Markers Based on a Poly(Dimethylsiloxane)-Gold Nanoparticles Composite Microfluidic Chip: A Proof of Principle. Clinical Chemistry. 2010;56:1701-7.
[272] Lai G, Yan F, Wu J, Leng C, Ju H. Ultrasensitive Multiplexed Immunoassay with Electrochemical Stripping Analysis of Silver Nanoparticles Catalytically Deposited by Gold Nanoparticles and Enzymatic Reaction. Analytical Chemistry. 2011;83:2726-32.
[273] Wilson MS, Nie W. Electrochemical Multianalyte Immunoassays Using an Array-Based Sensor. Analytical Chemistry. 2006;78:2507-13.
[274] Wilson MS, Nie W. Multiplex Measurement of Seven Tumor Markers Using an Electrochemical Protein Chip. Analytical Chemistry. 2006;78:6476-83.
[275] Zheng G, Patolsky F, Cui Y, Wang WU, Lieber CM. Multiplexed electrical detection of cancer markers with nanowire sensor arrays. Nat Biotech. 2005;23:1294-301.
[276] Wu J, Yan F, Tang J, Zhai C, Ju H. A Disposable Multianalyte Electrochemical Immunosensor Array for Automated Simultaneous Determination of Tumor Markers. Clinical Chemistry. 2007;53:1495-502.
[277] Tang D, Yuan R, Chai Y. Electrochemical immuno-bioanalysis for carcinoma antigen 125 based on thionine and gold nanoparticles-modified carbon paste interface. Analytica Chimica Acta. 2006;564:158-65.
[278] Zhuo Y, Yuan P-X, Yuan R, Chai Y-Q, Hong C-L. Bienzyme functionalized three-layer composite magnetic nanoparticles for electrochemical immunosensors. Biomaterials. 2009;30:2284-90.
[279] Rishpon J, Ivnitski D. An amperometric enzyme-channeling immunosensor. Biosensors and Bioelectronics. 1997;12:195-204.
[280] Yang H. Enzyme-based ultrasensitive electrochemical biosensors. Current Opinion in Chemical Biology.
[281] Posthuma-Trumpie G, Korf J, van Amerongen A. Lateral flow (immuno)assay: its strengths, weaknesses, opportunities and threats. A literature survey. Analytical and Bioanalytical Chemistry. 2009;393:569-82.
[282] von Lode P. Point-of-care immunotesting: Approaching the analytical performance of central laboratory methods. Clinical Biochemistry. 2005;38:591-606.
[283] Hudson MP, Christenson RH, Newby LK, Kaplan AL, Ohman EM. Cardiac markers: point of care testing. Clinica Chimica Acta. 1999;284:223-37.
[284] Chan C, Cheung Y-c, Renneberg R, Seydack M. New Trends in Immunoassays: Biosensing for the 21st Century. In: Renneberg R, Lisdat F, editors.: Springer Berlin / Heidelberg; 2008. p. 123-54.
[285] Warsinke A. Point-of-care testing of proteins. Analytical and Bioanalytical Chemistry. 2009;393:1393-405.

[286] Lauks IR. Microfabricated Biosensors and Microanalytical Systems for Blood Analysis. Accounts of Chemical Research. 1998;31:317-24.
[287] Care APo. http://www.i-stat.com/products/ctisheets/715595-00L.pdf. 2012.
[288] Lin Y-H, Chen S-H, Chuang Y-C, Lu Y-C, Shen TY, Chang CA, et al. Disposable amperometric immunosensing strips fabricated by Au nanoparticles-modified screen-printed carbon electrodes for the detection of foodborne pathogen Escherichia coli O157:H7. Biosensors and Bioelectronics. 2008;23:1832-7.
[289] Zhang X, Geng P, Liu H, Teng Y, Liu Y, Wang Q, et al. Development of an electrochemical immunoassay for rapid detection of E. coli using anodic stripping voltammetry based on Cu@Au nanoparticles as antibody labels. Biosensors and Bioelectronics. 2009;24:2155-9.
[290] Brandley BK, Schnaar RL. Cell-surface carbohydrates in cell recognition and response. Journal of Leukocyte Biology. 1986;40:97-111.
[291] Sela BA, Wang JL, Edelman GM. Antibodies reactive with cell surface carbohydrates. Proceedings of the National Academy of Sciences. 1975;72:1127-31.
[292] Rauvala H. Cell surface carbohydrates and cell adhesion. Trends in Biochemical Sciences. 1983;8:323-5.
[293] Muramatsu T. Alterations of cell-surface carbohydrates during differentiation and development. Biochimie. 1988;70:1587-96.
[294] Gorelik E, Galili U, Raz A. On the Role of Cell Surface Carbohydrates and their Binding Proteins (lectins) in Tumor Metastasis. Cancer and Metastasis Reviews. 2001;20:245-77.
[295] Varki A. Biological roles of oligosaccharides: all of the theories are correct. Glycobiology. 1993;3:97-130.
[296] Albersheim P, Anderson-Prouty AJ. Carbohydrates, Proteins, Cell Surfaces, and the Biochemistry of Pathogenesis. Annual Review of Plant Physiology. 1975;26:31-52.
[297] Reitter JN, Means RE, Desrosiers RC. A role for carbohydrates in immune evasion in AIDS. Nat Med. 1998;4:679-84.
[298] Apweiler R, Hermjakob H, Sharon N. On the frequency of protein glycosylation, as deduced from analysis of the SWISS-PROT database. Biochimica et Biophysica Acta (BBA) - General Subjects. 1999;1473:4-8.
[299] Spiro RG. Protein glycosylation: nature, distribution, enzymatic formation, and disease implications of glycopeptide bonds. Glycobiology. 2002;12:43R-56R.
[300] Parodi AJ. Protein Glucosylation and its Role in Protein Folding. Annual Review of Biochemistry. 2000;69:69-93.
[301] Wormald MR, Dwek RA. Glycoproteins: glycan presentation and protein-fold stability. Structure. 1999;7:R155-R60.
[302] Dwek RA, Edge CJ, Harvey DJ, Wormald MR, Parekh RB. Analysis of Glycoprotein-Associated Oligosaccharides. Annual Review of Biochemistry. 1993;62:65-100.
[303] Kiessling LL, Cairo CW. Hitting the sweet spot. Nat Biotech. 2002;20:234-5.
[304] Shin I, Park S, Lee M-r. Carbohydrate Microarrays: An Advanced Technology for Functional Studies of Glycans. Chemistry – A European Journal. 2005;11:2894-901.
[305] Feizi T, Fazio F, Chai W, Wong C-H. Carbohydrate microarrays — a new set of technologies at the frontiers of glycomics. Current Opinion in Structural Biology. 2003;13:637-45.

[306] Ratner DM, Adams EW, Su J, O'Keefe BR, Mrksich M, Seeberger PH. Probing Protein–Carbohydrate Interactions with Microarrays of Synthetic Oligosaccharides. ChemBioChem. 2004;5:379-83.
[307] Song E-H, Pohl NLB. Carbohydrate arrays: recent developments in fabrication and detection methods with applications. Current Opinion in Chemical Biology. 2009;13:626-32.
[308] Finklea HO, Snider DA, Fedyk J. Passivation of pinholes in octadecanethiol monolayers on gold electrodes by electrochemical polymerization of phenol. Langmuir. 1990;6:371-6.
[309] Rouya E, Cattarin S, Reed ML, Kelly RG, Zangari G. Electrochemical Characterization of the Surface Area of Nanoporous Gold Films. Journal of The Electrochemical Society. 2012;159:K97-K102.
[310] Chang B-Y, Park S-M. Electrochemical Impedance Spectroscopy. Annual Review of Analytical Chemistry. 2010;3:207-29.
[311] Macdonald DD. Review of mechanistic analysis by electrochemical impedance spectroscopy. Electrochimica Acta. 1990;35:1509-25.
[312] Orazem ME, Tribollet B. References. Electrochemical Impedance Spectroscopy: John Wiley & Sons, Inc.; 2008. p. 495-517.
[313] Retter U, Lohse H. Electrochemical Impedance Spectroscopy In: Scholz F, editor. Electroanalytical Methods: Springer Berlin Heidelberg; 2010. p. 159-77.
[314] Urquidi-Macdonald M, Real S, Macdonald DD. Applications of Kramers—Kronig transforms in the analysis of electrochemical impedance data—III. Stability and linearity. Electrochimica Acta. 1990;35:1559-66.
[315] Macdonald JR, Johnson WB. Fundamentals of Impedance Spectroscopy. Impedance Spectroscopy: John Wiley & Sons, Inc.; 2005. p. 1-26.
[316] Nicholson RS. Theory and Application of Cyclic Voltammetry for Measurement of Electrode Reaction Kinetics. Analytical Chemistry. 1965;37:1351-5.
[317] Mabbott GA. An introduction to cyclic voltammetry. Journal of Chemical Education. 1983;60:697.
[318] Widrig CA, Chung C, Porter MD. The electrochemical desorption of n-alkanethiol monolayers from polycrystalline Au and Ag electrodes. Journal of Electroanalytical Chemistry and Interfacial Electrochemistry. 1991;310:335-59.
[319] Hobara D, Miyake K, Imabayashi S-i, Niki K, Kakiuchi T. In-Situ Scanning Tunneling Microscopy Imaging of the Reductive Desorption Process of Alkanethiols on Au(111). Langmuir. 1998;14:3590-6.
[320] Ramaley L, Krause MS. Theory of square wave voltammetry. Analytical Chemistry. 1969;41:1362-5.
[321] O'Dea JJ, Osteryoung J, Osteryoung RA. Theory of square wave voltammetry for kinetic systems. Analytical Chemistry. 1981;53:695-701.
[322] Zachowski EJ, Wojciechowski M, Osteryoung J. The analytical application of square-wave voltammetry. Analytica Chimica Acta. 1986;183:47-57.
[323] Osteryoung J. Voltammetry for the future. Accounts of Chemical Research. 1993;26:77-83.
[324] Hu M, Chen J, Li Z-Y, Au L, Hartland GV, Li X, et al. Gold nanostructures: engineering their plasmonic properties for biomedical applications. Chemical Society Reviews. 2006;35:1084-94.

[325] Daniel M-C, Astruc D. Gold Nanoparticles: Assembly, Supramolecular Chemistry, Quantum-Size-Related Properties, and Applications toward Biology, Catalysis, and Nanotechnology. Chemical Reviews. 2003;104:293-346.
[326] Bain CD, Whitesides GM. Molecular-Level Control over Surface Order in Self-Assembled Monolayer Films of Thiols on Gold. Science. 1988;240:62-3.
[327] Cortés E, Rubert AA, Benitez G, Carro P, Vela ME, Salvarezza RC. Enhanced Stability of Thiolate Self-Assembled Monolayers (SAMs) on Nanostructured Gold Substrates. Langmuir. 2009;25:5661-6.
[328] Coskun A, Wesson PJ, Klajn R, Trabolsi A, Fang L, Olson MA, et al. Molecular-Mechanical Switching at the Nanoparticle−Solvent Interface: Practice and Theory. Journal of the American Chemical Society. 2010;132:4310-20.
[329] Browne KP, Grzybowski BA. Controlling the Properties of Self-Assembled Monolayers by Substrate Curvature†. Langmuir. 2010;27:1246-50.
[330] Detsi E, van de Schootbrugge M, Punzhin S, Onck PR, De Hosson JTM. On tuning the morphology of nanoporous gold. Scripta Materialia. 2011;64:319-22.
[331] Hitz C, Lasia A. Experimental study and modeling of impedance of the her on porous Ni electrodes. Journal of Electroanalytical Chemistry. 2001;500:213-22.
[332] Pell WG, Conway BE. Voltammetry at a de Levie brush electrode as a model for electrochemical supercapacitor behaviour. Journal of Electroanalytical Chemistry. 2001;500:121-33.
[333] Lang X, Qian L, Guan P, Zi J, Chen M. Localized surface plasmon resonance of nanoporous gold. Appl Phys Lett. 2011;98:093701-3.
[334] Cherevko S, Chung C-H. Direct electrodeposition of nanoporous gold with controlled multimodal pore size distribution. Electrochem Commun. 2011;13:16-9.
[335] Lang XY, Guan PF, Fujita T, Chen MW. Tailored nanoporous gold for ultrahigh fluorescence enhancement. PCCP. 2011;13:3795-9.
[336] Fujita T, Qian L-H, Inoke K, Erlebacher J, Chen M-W. Three-dimensional morphology of nanoporous gold. Applied Physics Letters. 2008;92:251902-3.
[337] Stine KJ, Jefferson K, Shulga OV. Nanoporous Gold for Enzyme Immobilization. In: Minteer SD, editor. Enzyme Stabilization and Immobilization: Humana Press; 2011. p. 67-83.
[338] Li X, Wang R, Zhang X. Electrochemiluminescence immunoassay at a nanoporous gold leaf electrode and using CdTe quantun dots as labels. Microchimica Acta. 2011;172:285-90.
[339] Yu C, Jia F, Ai Z, Zhang L. Direct Oxidation of Methanol on Self-Supported Nanoporous Gold Film Electrodes with High Catalytic Activity and Stability. Chem Mater. 2007;19:6065-7.
[340] Nagle LC, Rohan JF. Nanoporous gold anode catalyst for direct borohydride fuel cell. Int J Hydrogen Energy.In Press, Corrected Proof.
[341] Chen Z, Jiang J, Shen G, Yu R. Impedance immunosensor based on receptor protein adsorbed directly on porous gold film. Analytica Chimica Acta. 2005;553:190-5.
[342] Qiu H, Xu C, Huang X, Ding Y, Qu Y, Gao P. Adsorption of Laccase on the Surface of Nanoporous Gold and the Direct Electron Transfer between Them. The Journal of Physical Chemistry C. 2008;112:14781-5.
[343] Gooding JJ, Hibbert DB. The application of alkanethiol self-assembled monolayers to enzyme electrodes. TrAC Trends in Analytical Chemistry. 1999;18:525-33.

[344] Ispas C, Sokolov I, Andreescu S. Enzyme-functionalized mesoporous silica for bioanalytical applications. Analytical and Bioanalytical Chemistry. 2009;393:543-54.
[345] Mrksich M, Whitesides GM. Using Self-Assembled Monolayers to Understand the Interactions of Man-made Surfaces with Proteins and Cells. Annual Review of Biophysics and Biomolecular Structure. 1996;25:55-78.
[346] Laibinis PE, Whitesides GM, Allara DL, Tao YT, Parikh AN, Nuzzo RG. Comparison of the structures and wetting properties of self-assembled monolayers of n-alkanethiols on the coinage metal surfaces, copper, silver, and gold. Journal of the American Chemical Society. 1991;113:7152-67.
[347] Troughton EB, Bain CD, Whitesides GM, Nuzzo RG, Allara DL, Porter MD. Monolayer films prepared by the spontaneous self-assembly of symmetrical and unsymmetrical dialkyl sulfides from solution onto gold substrates: structure, properties, and reactivity of constituent functional groups. Langmuir. 1988;4:365-85.
[348] Hoogvliet JC, Dijksma M, Kamp B, van Bennekom WP. Electrochemical Pretreatment of Polycrystalline Gold Electrodes To Produce a Reproducible Surface Roughness for Self-Assembly:□ A Study in Phosphate Buffer pH 7.4. Analytical Chemistry. 2000;72:2016-21.
[349] Diao P, Jiang D, Cui X, Gu D, Tong R, Zhong B. Studies of structural disorder of self-assembled thiol monolayers on gold by cyclic voltammetry and ac impedance. Journal of Electroanalytical Chemistry. 1999;464:61-7.
[350] Kiani A, Alpuche-Aviles MA, Eggers PK, Jones M, Gooding JJ, Paddon-Row MN, et al. Scanning Electrochemical Microscopy. 59. Effect of Defects and Structure on Electron Transfer through Self-Assembled Monolayers. Langmuir. 2008;24:2841-9.
[351] Creager SE, Hockett LA, Rowe GK. Consequences of microscopic surface roughness for molecular self-assembly. Langmuir. 1992;8:854-61.
[352] Robinson DB, Wu C-AM, Ong MD, Jacobs BW, Pierson BE. Effect of Electrolyte and Adsorbates on Charging Rates in Mesoporous Gold Electrodes. Langmuir. 2010;26:6797-803.
[353] Hakamada M, Mabuchi M. Microstructural evolution in nanoporous gold by thermal and acid treatments. Materials Letters. 2008;62:483-6.
[354] Kim M, Jeong GH, Lee KY, Kwon K, Han SW. Fabrication of nanoporous superstructures through hierarchical self-assembly of nanoparticles. Journal of Materials Chemistry. 2008;18:2208-12.
[355] Mohl M, Kumar A, Reddy ALM, Kukovecz A, Konya Z, Kiricsi I, et al. Synthesis of Catalytic Porous Metallic Nanorods by Galvanic Exchange Reaction. The Journal of Physical Chemistry C. 2009;114:389-93.
[356] Losic D, Shapter JG, Gooding JJ. Influence of Surface Topography on Alkanethiol SAMs Assembled from Solution and by Microcontact Printing. Langmuir. 2001;17:3307-16.
[357] Delamarche E, Michel B, Gerber C, Anselmetti D, Guentherodt HJ, Wolf H, et al. Real-Space Observation of Nanoscale Molecular Domains in Self-Assembled Monolayers. Langmuir. 1994;10:2869-71.
[358] Biener J, Hodge AM, Hamza AV, Hsiung LM, Satcher JH. Nanoporous Au: A high yield strength material. Journal of Applied Physics. 2005;97:024301--4.

[359] Hodge AM, Biener J, Hsiung LL, Wang YM, Hamza AV, Satcher JH. Monolithic nanocrystalline Au fabricated by the compaction of nanoscale foam. Journal of Materials Research. 2005;20:554-7.
[360] Chu Y, Seo B, Kim J. Electrochemical Properties of Alkanethiol Monolayers Adsorbed on Nanoporous Au Surfaces. Bull Korean Chem Soc. 2010;31:3407-10.
[361] Guo Y-G, Zhang H-M, Hu J-S, Wan L-J, Bai C-L. Nanoarchitectured metal film electrodes with high electroactive surface areas. Thin Solid Films. 2005;484:341-5.
[362] Cao L, Yan P, Sun K, Kirk DW. Gold 3D Brush Nanoelectrode Ensembles with Enlarged Active Area for the Direct Voltammetry of Daunorubicin. Electroanalysis. 2009;21:1183-8.
[363] Janek RP, Fawcett WR, Ulman A. Impedance Spectroscopy of Self-Assembled Monolayers on Au(111):□ Sodium Ferrocyanide Charge Transfer at Modified Electrodes. Langmuir. 1998;14:3011-8.
[364] Lasia A. Impedance of Porous Electrodes. ECS Transactions. 2008;13:1-18.
[365] Lasia A. Impedance of porous electrodes. Journal of Electroanalytical Chemistry. 1995;397:27-33.
[366] Song H-K, Jung Y-H, Lee K-H, Dao LH. Electrochemical impedance spectroscopy of porous electrodes: the effect of pore size distribution. Electrochimica Acta. 1999;44:3513-9.
[367] Raistrick ID. Impedance studies of porous electrodes. Electrochimica Acta. 1990;35:1579-86.
[368] Devan S, Subramanian VR, White RE. Analytical Solution for the Impedance of a Porous Electrode. Journal of The Electrochemical Society. 2004;151:A905-A13.
[369] de Levie R. On the impedance of electrodes with rough interfaces. Journal of Electroanalytical Chemistry and Interfacial Electrochemistry. 1989;261:1-9.
[370] Pillay J, Ozoemena KI, Tshikhudo RT, Moutloali RM. Monolayer-Protected Clusters of Gold Nanoparticles: Impacts of Stabilizing Ligands on the Heterogeneous Electron Transfer Dynamics and Voltammetric Detection. Langmuir. 2010;26:9061-8.
[371] Mashazi PN, Westbroek P, Ozoemena KI, Nyokong T. Surface chemistry and electrocatalytic behaviour of tetra-carboxy substituted iron, cobalt and manganese phthalocyanine monolayers on gold electrode. Electrochimica Acta. 2007;53:1858-69.
[372] Shrikrishnan S, Sankaran K, Lakshminarayanan V. Electrochemical Impedance Analysis of Adsorption and Enzyme Kinetics of Calf Intestine Alkaline Phosphatase on SAM-Modified Gold Electrode. The Journal of Physical Chemistry C. 2012;116:16030-7.
[373] Boubour E, Lennox RB. Potential-Induced Defects in n-Alkanethiol Self-Assembled Monolayers Monitored by Impedance Spectroscopy. The Journal of Physical Chemistry B. 2000;104:9004-10.
[374] Song H-K, Hwang H-Y, Lee K-H, Dao LH. The effect of pore size distribution on the frequency dispersion of porous electrodes. Electrochimica Acta. 2000;45:2241-57.
[375] Protsailo LV, Fawcett WR. Studies of electron transfer through self-assembled monolayers using impedance spectroscopy. Electrochimica Acta. 2000;45:3497-505.
[376] Bisquert J, Compte A. Theory of the electrochemical impedance of anomalous diffusion. Journal of Electroanalytical Chemistry. 2001;499:112-20.
[377] Sur UK, Lakshminarayanan V. Effect of bulk structure of some non-aqueous solvents on the barrier properties of alkanethiol monolayer. Journal of Electroanalytical Chemistry. 2001;516:31-8.

[378] Diao P, Guo M, Tong R. Characterization of defects in the formation process of self-assembled thiol monolayers by electrochemical impedance spectroscopy. Journal of Electroanalytical Chemistry. 2001;495:98-105.
[379] Diao P, Guo M, Jiang D, Jia Z, Cui X, Gu D, et al. Fractional coverage of defects in self-assembled thiol monolayers on gold. Journal of Electroanalytical Chemistry. 2000;480:59-63.
[380] Sabatani E, Rubinstein I. Organized self-assembling monolayers on electrodes. 2. Monolayer-based ultramicroelectrodes for the study of very rapid electrode kinetics. The Journal of Physical Chemistry. 1987;91:6663-9.
[381] Aguiar FA, Campos R, Wang C, Jitchati R, Batsanov AS, Bryce MR, et al. Comparative electrochemical and impedance studies of self-assembled rigid-rod molecular wires and alkanethiols on gold substrates. Physical Chemistry Chemical Physics. 2010;12:14804-11.
[382] Finklea HO, Avery S, Lynch M, Furtsch T. Blocking oriented monolayers of alkyl mercaptans on gold electrodes. Langmuir. 1987;3:409-13.
[383] Sabatani E, Rubinstein I, Maoz R, Sagiv J. Organized self-assembling monolayers on electrodes: Part I. Octadecyl derivatives on gold. Journal of Electroanalytical Chemistry and Interfacial Electrochemistry. 1987;219:365-71.
[384] Cannes C, Kanoufi F, Bard AJ. Cyclic Voltammetric and Scanning Electrochemical Microscopic Study of Menadione Permeability through a Self-Assembled Monolayer on a Gold Electrode. Langmuir. 2002;18:8134-41.
[385] Finklea HO, Snider DA, Fedyk J, Sabatani E, Gafni Y, Rubinstein I. Characterization of octadecanethiol-coated gold electrodes as microarray electrodes by cyclic voltammetry and ac impedance spectroscopy. Langmuir. 1993;9:3660-7.
[386] Mortari A, Maaroof A, Martin D, Cortie MB. Mesoporous gold electrodes for sensors based on electrochemical double layer capacitance. Sensors and Actuators B: Chemical. 2007;123:262-8.
[387] Schlesinger M, Lasia A. Modeling of Impedance of Porous Electrodes. Modeling and Numerical Simulations: Springer New York; 2009. p. 67-137.
[388] Pajkossy T. Impedance of rough capacitive electrodes. Journal of Electroanalytical Chemistry. 1994;364:111-25.
[389] Bates JB, Chu YT, Stribling WT. Surface topography and impedance of metal-electrolyte interfaces. Physical Review Letters. 1988;60:627.
[390] Huang VM-W, Vivier V, Frateur I, Orazem ME, Tribollet B. The Global and Local Impedance Response of a Blocking Disk Electrode with Local Constant-Phase-Element Behavior. Journal of The Electrochemical Society. 2007;154:C89-C98.
[391] Brug GJ, van den Eeden ALG, Sluyters-Rehbach M, Sluyters JH. The analysis of electrode impedances complicated by the presence of a constant phase element. Journal of Electroanalytical Chemistry and Interfacial Electrochemistry. 1984;176:275-95.
[392] Fawcett WR, Kováčová Z, Motheo AJ, Foss Jr CA. Application of the ac admittance technique to double-layer studies on polycrystalline gold electrodes. Journal of Electroanalytical Chemistry. 1992;326:91-103.
[393] Sabatani E, Cohen-Boulakia J, Bruening M, Rubinstein I. Thioaromatic monolayers on gold: a new family of self-assembling monolayers. Langmuir. 1993;9:2974-81.
[394] Bandyopadhyay K, Vijayamohanan K. Formation of a Self-Assembled Monolayer of Diphenyl Diselenide on Polycrystalline Gold. Langmuir. 1998;14:625-9.

[395] Ozoemena KI, Mathebula NS, Pillay J, Toschi G, Verschoor JA. Electron transfer dynamics across self-assembled N-(2-mercaptoethyl) octadecanamide/mycolic acid layers: impedimetric insights into the structural integrity and interaction with anti-mycolic acid antibodies. Physical Chemistry Chemical Physics. 2010;12:345-57.
[396] Zhong C-J, Porter MD. Fine structure in the voltammetric desorption curves of alkanethiolate monolayers chemisorbed at gold. Journal of Electroanalytical Chemistry. 1997;425:147-53.
[397] Wong S-S, Porter MD. Origin of the multiple voltammetric desorption waves of long-chain alkanethiolate monolayers chemisorbed on annealed gold electrodes. J Electroanal Chem. 2000;485:135-43.
[398] Arihara K, Ariga T, Takashima N, Arihara K, Okajima T, Kitamura F, et al. Multiple voltammetric waves for reductive desorption of cysteine and 4-mercaptobenzoic acid monolayers self-assembled on gold substrates. Physical Chemistry Chemical Physics. 2003;5:3758-61.
[399] Leopold MC, Black JA, Bowden EF. Influence of Gold Topography on Carboxylic Acid Terminated Self-Assembled Monolayers. Langmuir. 2002;18:978-80.
[400] Chidsey CED, Loiacono DN. Chemical functionality in self-assembled monolayers: structural and electrochemical properties. Langmuir. 1990;6:682-91.
[401] Saxon E, Bertozzi CR. Chemical and Biological Strategies for Engeneering Cell Surface Glycosylation. Annual Review of Cell and Developmental Biology. 2001;17:1-23.
[402] Muramatsu T. Developmentally regulated expression of cell surface carbohydrates during mouse embryogenesis. Journal of Cellular Biochemistry. 1988;36:1-14.
[403] Dabelsteen E. Cell Surface Carbohydrates as Prognostic Markers in Human Carcinomas. The Journal of Pathology. 1996;179:358-69.
[404] Brandley B, Schnaar R. Cell-surface carbohydrates in cell recognition and response. Journal of Leukocyte Biology. 1986;40:97-111.
[405] Dube DH, Bertozzi CR. Glycans in cancer and inflammation [mdash] potential for therapeutics and diagnostics. Nat Rev Drug Discov. 2005;4:477-88.
[406] Porter, Robinson, Pickup, Edwards. An evaluation of lectin-mediated magnetic bead cell sorting for the targeted separation of enteric bacteria. Journal of Applied Microbiology. 1998;84:722-32.
[407] Pilobello KT, Krishnamoorthy L, Slawek D, Mahal LK. Development of a Lectin Microarray for the Rapid Analysis of Protein Glycopatterns. ChemBioChem. 2005;6:985-9.
[408] Ambrosi M, Cameron NR, Davis BG. Lectins: tools for the molecular understanding of the glycocode. Organic & Biomolecular Chemistry. 2005;3:1593-608.
[409] Smith EA, Thomas WD, Kiessling LL, Corn RM. Surface Plasmon Resonance Imaging Studies of Protein-Carbohydrate Interactions. Journal of the American Chemical Society. 2003;125:6140-8.
[410] Lee RT, Lee YC. Affinity enhancement by multivalent lectin–carbohydrate interaction. Glycoconjugate Journal. 2000;17:543-51.
[411] Jelinek R, Kolusheva S. Carbohydrate Biosensors. Chemical Reviews. 2004;104:5987-6016.

[412] Patel N, Davies MC, Hartshorne M, Heaton RJ, Roberts CJ, Tendler SJB, et al. Immobilization of Protein Molecules onto Homogeneous and Mixed Carboxylate-Terminated Self-Assembled Monolayers. Langmuir. 1997;13:6485-90.
[413] Horan N, Yan L, Isobe H, Whitesides GM, Kahne D. Nonstatistical binding of a protein to clustered carbohydrates. Proceedings of the National Academy of Sciences. 1999;96:11782-6.
[414] Ray S, Mehta G, Srivastava S. Label-free detection techniques for protein microarrays: Prospects, merits and challenges. Proteomics. 2010;10:731-48.
[415] Ruan C, Yang L, Li Y. Immunobiosensor Chips for Detection of Escherichia coli O157:H7 Using Electrochemical Impedance Spectroscopy. Analytical Chemistry. 2002;74:4814-20.
[416] Leteux C, Childs RA, Chai W, Stoll MS, Kogelberg H, Feizi T. Biotinyl-L-3-(2-naphthyl)-alanine hydrazide derivatives of N-glycans: versatile solid-phase probes for carbohydrate-recognition studies. Glycobiology. 1998;8:227-36.
[417] Yonzon CR, Jeoung E, Zou S, Schatz GC, Mrksich M, Van Duyne RP. A Comparative Analysis of Localized and Propagating Surface Plasmon Resonance Sensors: The Binding of Concanavalin A to a Monosaccharide Functionalized Self-Assembled Monolayer. Journal of the American Chemical Society. 2004;126:12669-76.
[418] Sun X-L, Stabler CL, Cazalis CS, Chaikof EL. Carbohydrate and Protein Immobilization onto Solid Surfaces by Sequential Diels−Alder and Azide−Alkyne Cycloadditions. Bioconjugate Chemistry. 2005;17:52-7.
[419] Loaiza OA, Lamas-Ardisana PJ, Jubete E, Ochoteco E, Loinaz I, Cabañero Gn, et al. Nanostructured Disposable Impedimetric Sensors as Tools for Specific Biomolecular Interactions: Sensitive Recognition of Concanavalin A. Analytical Chemistry. 2011;83:2987-95.
[420] Hone DC, Haines AH, Russell DA. Rapid, Quantitative Colorimetric Detection of a Lectin Using Mannose-Stabilized Gold Nanoparticles. Langmuir. 2003;19:7141-4.
[421] Seo JH, Adachi K, Lee BK, Kang DG, Kim YK, Kim KR, et al. Facile and Rapid Direct Gold Surface Immobilization with Controlled Orientation for Carbohydrates. Bioconjugate Chemistry. 2007;18:2197-201.
[422] Schlesinger L. Macrophage phagocytosis of virulent but not attenuated strains of Mycobacterium tuberculosis is mediated by mannose receptors in addition to complement receptors. The Journal of Immunology. 1993;150:2920-30.
[423] Zhi Z-l, Powell AK, Turnbull JE. Fabrication of Carbohydrate Microarrays on Gold Surfaces: Direct Attachment of Nonderivatized Oligosaccharides to Hydrazide-Modified Self-Assembled Monolayers. Analytical Chemistry. 2006;78:4786-93.
[424] Hernáiz MJ, de la Fuente JM, Barrientos ÁG, Penadés S. A Model System Mimicking Glycosphingolipid Clusters to Quantify Carbohydrate Self-Interactions by Surface Plasmon Resonance. Angewandte Chemie. 2002;114:1624-7.
[425] Ding L, Cheng W, Wang X, Ding S, Ju H. Carbohydrate Monolayer Strategy for Electrochemical Assay of Cell Surface Carbohydrate. Journal of the American Chemical Society. 2008;130:7224-5.
[426] Furukawa K, Iwamura K, Furukawa K. Blood Group Antigens: Blood Group Carbohydrate Antigens. In: Taniguchi N, Suzuki A, Ito Y, Narimatsu H, Kawasaki T, Hase S, editors. Experimental Glycoscience: Springer Japan; 2008. p. 363-5.

[427] Rasko DA, Sperandio V. Anti-virulence strategies to combat bacteria-mediated disease. Nat Rev Drug Discov. 2010;9:117-28.
[428] Lemichez E, Lecuit M, Nassif X, Bourdoulous S. Breaking the wall: targeting of the endothelium by pathogenic bacteria. Nat Rev Micro. 2010;8:93-104.
[429] Ling H, Boodhoo A, Hazes B, Cummings MD, Armstrong GD, Brunton JL, et al. Structure of the Shiga-like Toxin I B-Pentamer Complexed with an Analogue of Its Receptor Gb3. Biochemistry. 1998;37:1777-88.
[430] Stromberg N, Marklund BI, Lund B, Ilver D, Hamers A, Gaastra W, et al. Host-specificity of uropathogenic Escherichia coli depends on differences in binding specificity to Gal alpha 1-4Gal-containing isoreceptors. The EMBO journal. 1990;9:2001-10.
[431] Sylvester FA, Sajjan US, Forstner JF. Burkholderia (basonym Pseudomonas) cepacia binding to lipid receptors. Infection and Immunity. 1996;64:1420-5.
[432] Falguières T, Maak M, von Weyhern C, Sarr M, Sastre X, Poupon M-F, et al. Human colorectal tumors and metastases express Gb3 and can be targeted by an intestinal pathogen-based delivery tool. Molecular Cancer Therapeutics. 2008;7:2498-508.
[433] Zhu J, Wan Q, Ragupathi G, George CM, Livingston PO, Danishefsky SJ. Biologics through Chemistry: Total Synthesis of a Proposed Dual-Acting Vaccine Targeting Ovarian Cancer by Orchestration of Oligosaccharide and Polypeptide Domains. Journal of the American Chemical Society. 2009;131:4151-8.
[434] Kovbasnjuk O, Mourtazina R, Baibakov B, Wang T, Elowsky C, Choti MA, et al. The glycosphingolipid globotriaosylceramide in the metastatic transformation of colon cancer. Proceedings of the National Academy of Sciences of the United States of America. 2005;102:19087-92.
[435] Mangeney M, Lingwood CA, Taga S, Caillou B, Tursz T, Wiels J. Apoptosis Induced in Burkitt's Lymphoma Cells via Gb3/CD77, a Glycolipid Antigen. Cancer Research. 1993;53:5314-9.
[436] Kim M, Binnington B, Sakac D, Fernandes KR, Shi SP, Lingwood CA, et al. Comparison of detection methods for cell surface globotriaosylceramide. Journal of Immunological Methods. 2011;371:48-60.
[437] Johansson D, Kosovac E, Moharer J, Ljuslinder I, Brannstrom T, Johansson A, et al. Expression of verotoxin-1 receptor Gb3 in breast cancer tissue and verotoxin-1 signal transduction to apoptosis. BMC Cancer. 2009;9:67.
[438] Kitov PI, Railton C, Bundle DR. The synthesis of 16-mercaptohexadecanyl glycosides for biosensor applications. Carbohydrate Research. 1998;307:361-9.
[439] Blomberg E, Claesson PM, Konradsson P, Liedberg B. Globotriose- and Oligo(ethylene glycol)-Terminated Self-Assembled Monolayers: Surface Forces, Wetting, and Surfactant Adsorption. Langmuir. 2006;22:10038-46.
[440] Svedhem S, Öhberg L, Borrelli S, Valiokas R, Andersson M, Oscarson S, et al. Synthesis and Self-Assembly of Globotriose Derivatives: A Model System for Studies of Carbohydrate−Protein Interactions. Langmuir. 2002;18:2848-58.
[441] Kulkarni AA, Fuller C, Korman H, Weiss AA, Iyer SS. Glycan Encapsulated Gold Nanoparticles Selectively Inhibit Shiga Toxins 1 and 2. Bioconjugate Chemistry. 2010;21:1486-93.

[442] Chien Y-Y, Jan M-D, Adak AK, Tzeng H-C, Lin Y-P, Chen Y-J, et al. Globotriose-Functionalized Gold Nanoparticles as Multivalent Probes for Shiga-like Toxin. ChemBioChem. 2008;9:1100-9.
[443] Touhami A, Hoffmann B, Vasella A, Denis FA, Dufrêne YF. Probing Specific Lectin-Carbohydrate Interactions Using Atomic Force Microscopy Imaging and Force Measurements†. Langmuir. 2002;19:1745-51.
[444] Revell DJ, Knight JR, Blyth DJ, Haines AH, Russell DA. Self-Assembled Carbohydrate Monolayers: Formation and Surface Selective Molecular Recognition. Langmuir. 1998;14:4517-24.
[445] Mukherjee S, Maxfield FR. Membrane Domains. Annual Review of Cell and Developmental Biology. 2004;20:839-66.
[446] Anderson RGW. The Caveolae Membrane System. Annual Review of Biochemistry. 1998;67:199-225.
[447] Caldwell WB, Campbell DJ, Chen K, Herr BR, Mirkin CA, Malik A, et al. A Highly Ordered Self-Assembled Monolayer Film of an Azobenzenealkanethiol on Au(111): Electrochemical Properties and Structural Characterization by Synchrotron in-Plane X-ray Diffraction, Atomic Force Microscopy, and Surface-Enhanced Raman Spectroscopy. Journal of the American Chemical Society. 1995;117:6071-82.
[448] Flynn NT, Tran TNT, Cima MJ, Langer R. Long-Term Stability of Self-Assembled Monolayers in Biological Media. Langmuir. 2003;19:10909-15.
[449] Zolk M, Eisert F, Pipper J, Herrwerth S, Eck W, Buck M, et al. Solvation of Oligo(ethylene glycol)-Terminated Self-Assembled Monolayers Studied by Vibrational Sum Frequency Spectroscopy. Langmuir. 2000;16:5849-52.
[450] Kakiuchi T, Usui H, Hobara D, Yamamoto M. Voltammetric Properties of the Reductive Desorption of Alkanethiol Self-Assembled Monolayers from a Metal Surface. Langmuir. 2002;18:5231-8.
[451] Esplandiú MJ, Hagenström H, Kolb DM. Functionalized Self-Assembled Alkanethiol Monolayers on Au(111) Electrodes: 1. Surface Structure and Electrochemistry. Langmuir. 2001;17:828-38.
[452] Strutwolf J, O'Sullivan CK. Microstructures by Selective Desorption of Self-Assembled Monolayer from Polycrystalline Gold Electrodes. Electroanalysis. 2007;19:1467-75.
[453] Houseman BT, Mrksich M. The Role of Ligand Density in the Enzymatic Glycosylation of Carbohydrates Presented on Self-Assembled Monolayers of Alkanethiolates on Gold. Angewandte Chemie International Edition. 1999;38:782-5.
[454] Manimala JC, Roach TA, Li Z, Gildersleeve JC. High-Throughput Carbohydrate Microarray Analysis of 24 Lectins. Angewandte Chemie. 2006;118:3689-92.
[455] Ostuni E, Chapman RG, Holmlin RE, Takayama S, Whitesides GM. A Survey of Structure−Property Relationships of Surfaces that Resist the Adsorption of Protein. Langmuir. 2001;17:5605-20.
[456] Koc Y, de Mello AJ, McHale G, Newton MI, Roach P, Shirtcliffe NJ. Nano-scale superhydrophobicity: suppression of protein adsorption and promotion of flow-induced detachment. Lab on a Chip. 2008;8.
[457] Sun T, Qing G, Su B, Jiang L. Functional biointerface materials inspired from nature. Chemical Society Reviews. 2011;40.

[458] Wofsy C, Goldstein B. Effective Rate Models for Receptors Distributed in a Layer above a Surface: Application to Cells and Biacore. Biophysical journal. 2002;82:1743-55.
[459] Liang P-H, Wang S-K, Wong C-H. Quantitative Analysis of Carbohydrate−Protein Interactions Using Glycan Microarrays: Determination of Surface and Solution Dissociation Constants. Journal of the American Chemical Society. 2007;129:11177-84.
[460] Nahálková J, Švitel J, Gemeiner P, Danielsson B, Pribulová B, Petruš L. Affinity analysis of lectin interaction with immobilized C- and O- gylcosides studied by surface plasmon resonance assay. Journal of Biochemical and Biophysical Methods. 2002;52:11-8.
[461] Vijayendran RA, Leckband DE. A Quantitative Assessment of Heterogeneity for Surface-Immobilized Proteins. Analytical Chemistry. 2000;73:471-80.
[462] Schuck P. Kinetics of ligand binding to receptor immobilized in a polymer matrix, as detected with an evanescent wave biosensor. I. A computer simulation of the influence of mass transport. Biophysical journal. 1996;70:1230-49.
[463] Nishi N, Hobara D, Yamamoto M, Kakiuchi T. Chain-length-dependent change in the structure of self-assembled monolayers of n-alkanethiols on Au(111) probed by broad-bandwidth sum frequency generation spectroscopy. The Journal of Chemical Physics. 2003;118:1904-11.
[464] Weeraman C, Yatawara AK, Bordenyuk AN, Benderskii AV. Effect of Nanoscale Geometry on Molecular Conformation: Vibrational Sum-Frequency Generation of Alkanethiols on Gold Nanoparticles. Journal of the American Chemical Society. 2006;128:14244-5.
[465] Harder P, Grunze M, Dahint R, Whitesides GM, Laibinis PE. Molecular Conformation in Oligo(ethylene glycol)-Terminated Self-Assembled Monolayers on Gold and Silver Surfaces Determines Their Ability To Resist Protein Adsorption. The Journal of Physical Chemistry B. 1998;102:426-36.
[466] Jackson AM, Myerson JW, Stellacci F. Spontaneous assembly of subnanometre-ordered domains in the ligand shell of monolayer-protected nanoparticles. Nat Mater. 2004;3:330-6.
[467] Bast RC, Klug TL, John ES, Jenison E, Niloff JM, Lazarus H, et al. A Radioimmunoassay Using a Monoclonal Antibody to Monitor the Course of Epithelial Ovarian Cancer. New England Journal of Medicine. 1983;309:883-7.
[468] Reynolds MA, Kirchick HJ, Dahlen JR, Anderberg JM, McPherson PH, Nakamura KK, et al. Early Biomarkers of Stroke. Clinical Chemistry. 2003;49:1733-9.
[469] Fu Z, Shao G, Wang J, Lu D, Wang W, Lin Y. Microfabricated Renewable Beads-Trapping/Releasing Flow Cell for Rapid Antigen−Antibody Reaction in Chemiluminescent Immunoassay. Analytical Chemistry. 2011;83:2685-90.
[470] Wang C, Kong H, Guan Y, Yang J, Gu J, Yang S, et al. Plasma Phospholipid Metabolic Profiling and Biomarkers of Type 2 Diabetes Mellitus Based on High-Performance Liquid Chromatography/Electrospray Mass Spectrometry and Multivariate Statistical Analysis. Analytical Chemistry. 2005;77:4108-16.
[471] Lee IN, Chen C-H, Sheu J-C, Lee H-S, Huang G-T, Yu C-Y, et al. Identification of Human Hepatocellular Carcinoma-Related Biomarkers by Two-Dimensional Difference Gel Electrophoresis and Mass Spectrometry. Journal of Proteome Research. 2005;4:2062-9.

[472] Lee HJ, Nedelkov D, Corn RM. Surface Plasmon Resonance Imaging Measurements of Antibody Arrays for the Multiplexed Detection of Low Molecular Weight Protein Biomarkers. Analytical Chemistry. 2006;78:6504-10.
[473] Wu G, Datar RH, Hansen KM, Thundat T, Cote RJ, Majumdar A. Bioassay of prostate-specific antigen (PSA) using microcantilevers. Nat Biotech. 2001;19:856-60.
[474] Choi J-W, Kang D-Y, Jang Y-H, Kim H-H, Min J, Oh B-K. Ultra-sensitive surface plasmon resonance based immunosensor for prostate-specific antigen using gold nanoparticle–antibody complex. Colloids and Surfaces A: Physicochemical and Engineering Aspects. 2008;313-314:655-9.
[475] Escamilla-Gómez V, Hernández-Santos D, González-García MB, Pingarrón-Carrazón JM, Costa-García A. Simultaneous detection of free and total prostate specific antigen on a screen-printed electrochemical dual sensor. Biosensors and Bioelectronics. 2009;24:2678-83.
[476] Mani V, Chikkaveeraiah BV, Patel V, Gutkind JS, Rusling JF. Ultrasensitive Immunosensor for Cancer Biomarker Proteins Using Gold Nanoparticle Film Electrodes and Multienzyme-Particle Amplification. ACS Nano. 2009;3:585-94.
[477] Uludağ Y, Tothill IE. Development of a sensitive detection method of cancer biomarkers in human serum (75%) using a quartz crystal microbalance sensor and nanoparticles amplification system. Talanta. 2010;82:277-82.
[478] Gao X, Zhang Y, Chen H, Chen Z, Lin X. Amperometric immunosensor for carcinoembryonic antigen detection with carbon nanotube-based film decorated with gold nanoclusters. Analytical Biochemistry. 2011;414:70-6.
[479] Wu J, Tang J, Dai Z, Yan F, Ju H, Murr NE. A disposable electrochemical immunosensor for flow injection immunoassay of carcinoembryonic antigen. Biosensors and Bioelectronics. 2006;22:102-8.
[480] Lin Y-Y, Liu G, Wai CM, Lin Y. Bioelectrochemical immunoassay of polychlorinated biphenyl. Analytica Chimica Acta. 2008;612:23-8.
[481] La Gal La Salle A, Limoges B, Degrand C, Brossier P. Enzyme Immunoassays with an Electrochemical Detection Method Using Alkaline Phosphatase and a Perfluorosulfonated Ionomer-Modified Electrode. Application to Phenytoin Assays. Analytical Chemistry. 1995;67:1245-53.
[482] Tabatabai MA, Bremner JM. Use of p-nitrophenyl phosphate for assay of soil phosphatase activity. Soil Biology and Biochemistry. 1969;1:301-7.
[483] Bale JR, Huang CY, Chock PB. Transient kinetic analysis of the catalytic cycle of alkaline phosphatase. Journal of Biological Chemistry. 1980;255:8431-6.
[484] Bronstein I, Voyta JC, Thorpe GH, Kricka LJ, Armstrong G. Chemiluminescent assay of alkaline phosphatase applied in an ultrasensitive enzyme immunoassay of thyrotropin. Clinical Chemistry. 1989;35:1441-6.
[485] Tang HT, Lunte CE, Halsall HB, Heineman WR. p-aminophenyl phosphate: an improved substrate for electrochemical enzyme immnoassay. Analytica Chimica Acta. 1988;214:187-95.
[486] Lovrić M. Square-Wave Voltammetry Electroanalytical Methods. In: Scholz F, editor.: Springer Berlin Heidelberg; 2010. p. 121-45.
[487] Osteryoung JG, Osteryoung RA. Square wave voltammetry. Analytical Chemistry. 1985;57:101A-10A.

[488] Lyon JL, Stevenson KJ. Picomolar Peroxide Detection Using a Chemically Activated Redox Mediator and Square Wave Voltammetry. Analytical Chemistry. 2006;78:8518-25.
[489] Zhang F, Yang SH, Kang TY, Cha GS, Nam H, Meyerhoff ME. A rapid competitive binding nonseparation electrochemical enzyme immunoassay (NEEIA) test strip for microcystin-LR (MCLR) determination. Biosensors and Bioelectronics. 2007;22:1419-25.
[490] Yan X, Meng F, Cui S, Liu J, Gu J, Zou Z. Effective and rapid electrochemical detection of hydrazine by nanoporous gold. Journal of Electroanalytical Chemistry. 2011;661:44-8.
[491] Pariente F, Hernández L, Lorenzo E. Amperometric sensor based on the alkaline phosphatase activity. Bioelectrochemistry and Bioenergetics. 1992;27:73-87.
[492] Bradley CR, Rechnitz GA. Kinetic analysis of enzyme electrode response. Analytical Chemistry. 1984;56:664-7.
[493] Wilson MS, Rauh RD. Hydroquinone diphosphate: an alkaline phosphatase substrate that does not produce electrode fouling in electrochemical immunoassays. Biosensors and Bioelectronics. 2004;20:276-83.
[494] Porstmann B, Porstmann T, Nugel E, Evers U. Which of the commonly used marker enzymes gives the best results in colorimetric and fluorimetric enzyme immunoassays: Horseradish peroxidase, alkaline phosphatase or β-galactosidase? Journal of Immunological Methods. 1985;79:27-37.
[495] Li Y, Gao F, Wei W, Qu J-B, Ma G-H, Zhou W-Q. Pore size of macroporous polystyrene microspheres affects lipase immobilization. Journal of Molecular Catalysis B: Enzymatic. 2010;66:182-9.
[496] Bhatia RB, Brinker CJ, Gupta AK, Singh AK. Aqueous Sol−Gel Process for Protein Encapsulation. Chemistry of Materials. 2000;12:2434-41.
[497] DeLouise LA, Miller BL. Enzyme Immobilization in Porous Silicon: Quantitative Analysis of the Kinetic Parameters for Glutathione-S-transferases. Analytical Chemistry. 2005;77:1950-6.
[498] Rodkey FL. Direct Spectrophotometric Determination of Albumin in Human Serum. Clinical Chemistry. 1965;11:478-87.
[499] Dong Y, Abaci S, Shannon C, Bozack MJ. Self-Assembly and Electrochemical Desorption of Thioctic Acid Monolayers on Gold Surfaces. Langmuir. 2003;19:8922-6.
[500] Madoz J, Kuznetzov BA, Medrano FJ, Garcia JL, Fernandez VM. Functionalization of Gold Surfaces for Specific and Reversible Attachment of a Fused β-Galactosidase and Choline-Receptor Protein. Journal of the American Chemical Society. 1997;119:1043-51.
[501] Alkaline Phosphatase Labeling Kit-NH2. Dojindo.
[502] Device Technologies New Zealand Limited, PSAwatch™. Device Technologies New Zealand Limited.
[503] Human PSA ELISA Kit, For the Quantitative Determination of Human Prostate-Specific Antigen (PSA) Concentrations in Serum.: Abazyme, LLC.
[504] Gyurcsanyi RE, Bereczki A, Nagy G, Neuman MR, Lindner E. Amperometric microcells for alkaline phosphatase assay. Analyst. 2002;127:235-40.

[505] Niwa O, Xu Y, Halsall HB, Heineman WR. Small-volume voltammetric detection of 4-aminophenol with interdigitated array electrodes and its application to electrochemical enzyme immunoassay. Analytical Chemistry. 1993;65:1559-63.
[506] Wang J, Martinez T, Yaniv DR, McCormick LD. Scanning tunneling microscopic investigation of surface fouling of glassy carbon surfaces due to phenol oxidation. Journal of Electroanalytical Chemistry and Interfacial Electrochemistry. 1991;313:129-40.
[507] Frew JE, Foulds NC, Wilshere JM, Forrow NJ, Green MJ. Measurement of alkaline phosphatase activity by electrochemical detection of phosphate esters: Application to amperometric enzyme immunoassay. Journal of Electroanalytical Chemistry and Interfacial Electrochemistry. 1989;266:309-16.
[508] Lis H, Sharon N. Protein glycosylation. European Journal of Biochemistry. 1993;218:1-27.
[509] Ohtsubo K, Marth JD. Glycosylation in Cellular Mechanisms of Health and Disease. Cell. 2006;126:855-67.
[510] Cheng Y, Ni N, Peng H, Jin S, Wang B. Carbohydrate Biomarkers. Carbohydrate Recognition: John Wiley & Sons, Inc.; 2011. p. 133-56.
[511] Stevens MM, George JH. Exploring and Engineering the Cell Surface Interface. Science. 2005;310:1135-8.
[512] Dell A, Morris HR. Glycoprotein Structure Determination by Mass Spectrometry. Science. 2001;291:2351-6.
[513] Castric P, Cassels FJ, Carlson RW. Structural Characterization of the Pseudomonas aeruginosa 1244 Pilin Glycan. Journal of Biological Chemistry. 2001;276:26479-85.
[514] Campbell MP, Royle L, Radcliffe CM, Dwek RA, Rudd PM. GlycoBase and autoGU: tools for HPLC-based glycan analysis. Bioinformatics. 2008;24:1214-6.
[515] Balaguer E, Neusüss C. Glycoprotein Characterization Combining Intact Protein and Glycan Analysis by Capillary Electrophoresis-Electrospray Ionization-Mass Spectrometry. Analytical Chemistry. 2006;78:5384-93.
[516] Szabo A, Stolz L, Granzow R. Surface plasmon resonance and its use in biomolecular interaction analysis (BIA). Current Opinion in Structural Biology. 1995;5:699-705.
[517] Park S, Shin I. Fabrication of Carbohydrate Chips for Studying Protein–Carbohydrate Interactions. Angewandte Chemie International Edition. 2002;41:3180-2.
[518] Shen Z, Huang M, Xiao C, Zhang Y, Zeng X, Wang PG. Nonlabeled Quartz Crystal Microbalance Biosensor for Bacterial Detection Using Carbohydrate and Lectin Recognitions. Analytical Chemistry. 2007;79:2312-9.
[519] Sanchez-Pomales G, Zangmeister RA. Recent Advances in Electrochemical Glycobiosensing. International Journal of Electrochemistry. 2011;2011.
[520] La Belle JT, Gerlach JQ, Svarovsky S, Joshi L. Label-Free Impedimetric Detection of Glycan−Lectin Interactions. Analytical Chemistry. 2007;79:6959-64.
[521] Xue Y, Ding L, Lei J, Ju H. A simple electrochemical lectin-probe for in situ homogeneous cytosensing and facile evaluation of cell surface glycan. Biosensors and Bioelectronics. 2010;26:169-74.
[522] Gruber K, Horlacher T, Castelli R, Mader A, Seeberger PH, Hermann BA. Cantilever Array Sensors Detect Specific Carbohydrate−Protein Interactions with Picomolar Sensitivity. ACS Nano. 2011;5:3670-8.

[523] Guasch RM, Guerri C, O'Connor J-E. Study of surface carbohydrates on isolated Golgi subfractions by fluorescent-lectin binding and flow cytometry. Cytometry. 1995;19:112-8.
[524] Kuno A, Uchiyama N, Koseki-Kuno S, Ebe Y, Takashima S, Yamada M, et al. Evanescent-field fluorescence-assisted lectin microarray: a new strategy for glycan profiling. Nat Meth. 2005;2:851-6.
[525] Pei Z, Anderson H, Aastrup T, Ramström O. Study of real-time lectin–carbohydrate interactions on the surface of a quartz crystal microbalance. Biosensors and Bioelectronics. 2005;21:60-6.
[526] Schofield CL, Haines AH, Field RA, Russell DA. Silver and Gold Glyconanoparticles for Colorimetric Bioassays. Langmuir. 2006;22:6707-11.
[527] Gornik O, Lauc G. Enzyme linked lectin assay (ELLA) for direct analysis of transferrin sialylation in serum samples. Clinical Biochemistry. 2007;40:718-23.
[528] Rüdiger H, Gabius H-J. Plant lectins: Occurrence, biochemistry, functions and applications. Glycoconjugate Journal. 2001;18:589-613.
[529] Thompson R, Creavin A, O'Connell M, O'Connor B, Clarke P. Optimization of the enzyme-linked lectin assay for enhanced glycoprotein and glycoconjugate analysis. Analytical Biochemistry. 2011;413:114-22.
[530] Leriche V, Sibille P, Carpentier B. Use of an Enzyme-Linked Lectinsorbent Assay To Monitor the Shift in Polysaccharide Composition in Bacterial Biofilms. Applied and Environmental Microbiology. 2000;66:1851-6.
[531] Wu A, Wu J, Singh T, Chu K-C, Peumans W, Rougé P, et al. A novel lectin (morniga M) from mulberry (*Morus nigra*) bark recognizes oligomannosyl residues in N-Glycans. Journal of Biomedical Science. 2004;11:874-85.
[532] Gabius HJ. Glycans: bioactive signals decoded by lectins. Biochemical Society transactions. 2008;36:1491-6.
[533] Shankar SP, Chen II, Keselowsky BG, García AJ, Babensee JE. Profiles of carbohydrate ligands associated with adsorbed proteins on self-assembled monolayers of defined chemistries. Journal of Biomedical Materials Research Part A. 2010;92A:1329-42.
[534] Landberg E, Pahlsson P, Lundblad A, Arnetorp A, Jeppsson JO. Carbohydrate Composition of Serum Transferrin Isoforms from Patients with High Alcohol Consumption. Biochemical and Biophysical Research Communications. 1995;210:267-74.
[535] Yamashita K, Koide N, Endo T, Iwaki Y, Kobata A. Altered glycosylation of serum transferrin of patients with hepatocellular carcinoma. Journal of Biological Chemistry. 1989;264:2415-23.
[536] Malhotra R, Wormald MR, Rudd PM, Fischer PB, Dwek RA, Sim RB. Glycosylation changes of IgG associated with rheumatooid arthritis can activate complement via the mannose-binding protein. Nat Med. 1995;1:237-43.
[537] Eraso LH, Ginwala N, Qasim AN, Mehta NN, Dlugash R, Kapoor S, et al. Association of Lower Plasma Fetuin-A Levels With Peripheral Arterial Disease in Type 2 Diabetes. Diabetes Care. 2010;33:408-10.
[538] Komaba H, Fukagawa M. Fetuin-mineral complex: a new potential biomarker for vascular calcification[quest]. Kidney Int. 0000;75:874-6.

[539] Wanebo HJ, Rao B, Pinsky CM, Hoffman RG, Stearns M, Schwartz MK, et al. Preoperative Carcinoembryonic Antigen Level as a Prognostic Indicator in Colorectal Cancer. New England Journal of Medicine. 1978;299:448-51.
[540] Peracaula R, Tabarés G, Royle L, Harvey DJ, Dwek RA, Rudd PM, et al. Altered glycosylation pattern allows the distinction between prostate-specific antigen (PSA) from normal and tumor origins. Glycobiology. 2003;13:457-70.
[541] Geisbrecht ER, Montell DJ. Myosin VI is required for E-cadherin-mediated border cell migration. Nat Cell Biol. 2002;4:616-20.
[542] Edelman GM, Cunningham BA, Reeke GN, Becker JW, Waxdal MJ, Wang JL. The Covalent and Three-Dimensional Structure of Concanavalin A. Proceedings of the National Academy of Sciences. 1972;69:2580-4.
[543] Krusius T, Finne J, Rauvala H. The structural basis of the different affinities of two types of acidic N-glycosidic glycopeptides for concanavalin A--sepharose. FEBS letters. 1976;72:117-20.
[544] Shao Z, Li Y, Yang Q, Wang J, Li G. A novel electrochemical method to detect cell surface carbohydrates and target cells. Analytical and Bioanalytical Chemistry. 2010;398:2963-7.
[545] Zhang X, Teng Y, Fu Y, Xu L, Zhang S, He B, et al. Lectin-Based Biosensor Strategy for Electrochemical Assay of Glycan Expression on Living Cancer Cells. Analytical Chemistry. 2010;82:9455-60.
[546] Zhang J-J, Cheng F-F, Zheng T-T, Zhu J-J. Design and Implementation of Electrochemical Cytosensor for Evaluation of Cell Surface Carbohydrate and Glycoprotein. Analytical Chemistry. 2010;82:3547-55.
[547] Cheng W, Ding L, Lei J, Ding S, Ju H. Effective Cell Capture with Tetrapeptide-Functionalized Carbon Nanotubes and Dual Signal Amplification for Cytosensing and Evaluation of Cell Surface Carbohydrate. Analytical Chemistry. 2008;80:3867-72.
[548] Dai Z, Kawde A-N, Xiang Y, La Belle JT, Gerlach J, Bhavanandan VP, et al. Nanoparticle-Based Sensing of Glycan−Lectin Interactions. Journal of the American Chemical Society. 2006;128:10018-9.
[549] Andrade CAS, Oliveira MDL, de Melo CP, Coelho LCBB, Correia MTS, Nogueira ML, et al. Diagnosis of dengue infection using a modified gold electrode with hybrid organic–inorganic nanocomposite and Bauhinia monandra lectin. Journal of Colloid and Interface Science. 2011;362:517-23.
[550] Oliveira MDL, Correia MTS, Coelho LCBB, Diniz FB. Electrochemical evaluation of lectin–sugar interaction on gold electrode modified with colloidal gold and polyvinyl butyral. Colloids and Surfaces B: Biointerfaces. 2008;66:13-9.
[551] Oliveira MDL, Nogueira ML, Correia MTS, Coelho LCBB, Andrade CAS. Detection of dengue virus serotypes on the surface of gold electrode based on Cratylia mollis lectin affinity. Sensors and Actuators B: Chemical. 2011;155:789-95.
[552] Ding L, Cheng W, Wang X, Xue Y, Lei J, Yin Y, et al. A label-free strategy for facile electrochemical analysis of dynamic glycan expression on living cells. Chemical Communications. 2009:7161-3.
[553] Willey TM, Vance AL, Bostedt C, van Buuren T, Meulenberg RW, Terminello LJ, et al. Surface Structure and Chemical Switching of Thioctic Acid Adsorbed on Au(111) As Observed Using Near-Edge X-ray Absorption Fine Structure. Langmuir. 2004;20:4939-44.

[554] van der Schaal IAM, Logman TJJ, Díaz CL, Kijne JW. An enzyme-linked lectin binding assay for quantitative determination of lectin receptors. Analytical Biochemistry. 1984;140:48-55.
[555] McCoy Jr JP, Varani J, Goldstein IJ. Enzyme-linked lectin assay (ELLA): Use of alkaline phosphatase-conjugated Griffonia simplicifolia B4 isolectin for the detection of α-d-galactopyranosyl end groups. Analytical Biochemistry. 1983;130:437-44.
[556] Raju TS, Briggs JB, Borge SM, Jones AJS. Species-specific variation in glycosylation of IgG: evidence for the species-specific sialylation and branch-specific galactosylation and importance for engineering recombinant glycoprotein therapeutics. Glycobiology. 2000;10:477-86.
[557] Jamieson GA, Jett M, DeBernardo SL. The Carbohydrate Sequence of the Glycopeptide Chains of Human Transferrin. Journal of Biological Chemistry. 1971;246:3686-93.
[558] Chu TM, Holyoke ED, Murphy GP. The Reaction between Carcinoembryonic Antigen and Concanavalin A. Cancer Research. 1974;34:212-4.
[559] Yakovleva ME, Safina GR, Danielsson B. A study of glycoprotein–lectin interactions using quartz crystal microbalance. Analytica Chimica Acta. 2010;668:80-5.
[560] Safina G, Duran IB, Alasel M, Danielsson B. Surface plasmon resonance for real-time study of lectin–carbohydrate interactions for the differentiation and identification of glycoproteins. Talanta. 2011;84:1284-90.
[561] Borkowska Z, Tymosiak-Zielinska A, Nowakowski R. High catalytic activity of chemically activated gold electrodes towards electro-oxidation of methanol. Electrochimica Acta. 2004;49:2613-21.
[562] Kergaravat SV, Pividori MI, Hernandez SR. Evaluation of seven cosubstrates in the quantification of horseradish peroxidase enzyme by square wave voltammetry. Talanta. 2012;88:468-76.
[563] Bowers GN, McComb RB. A Continuous Spectrophotometric Method for Measuring the Activity of Serum Alkaline Phosphatase. Clinical Chemistry. 1966;12:70-89.
[564] Young NM, Leon MA. The affinity of concanavalin A and Lens culinaris hemagglutinin for glycopeptides. Biochimica et Biophysica Acta (BBA) - Protein Structure. 1974;365:418-24.
[565] Babac C, Yavuz H, Galaev IY, Pişkin E, Denizli A. Binding of antibodies to concanavalin A-modified monolithic cryogel. Reactive and Functional Polymers. 2006;66:1263-71.
[566] Chang JJ, Crowl CP, Schneider RS. Homogeneous enzyme immunoassay for digoxin. Clinical Chemistry. 1975;21:967.
[567] Mann DA, Kanai M, Maly DJ, Kiessling LL. Probing Low Affinity and Multivalent Interactions with Surface Plasmon Resonance: Ligands for Concanavalin A. Journal of the American Chemical Society. 1998;120:10575-82.